



UNIVERSIDAD
DE GRANADA



CSIC

CONSEJO SUPERIOR DE INVESTIGACIONES CIENTÍFICAS



INSTITUTO DE INVESTIGACIONES MARINAS



Jaw
09/23

Nitrogen Cycling in the Cape Verde Frontal Zone (NW Africa): Elemental and isotopic characterization.

Sara Valiente Rodríguez
PhD Thesis 2023



Nitrogen cycling in the Cape Verde Frontal Zone (NW Africa): Elemental and isotopic characterization

Sara Valiente Rodríguez

Ph.D. Thesis – Tesis Doctoral



Memoria de Tesis Doctoral presentada por la Licenciada en Ciencias del Mar Sara Valiente Rodríguez para optar al grado de Doctor por la Universidad de Granada

Granada, septiembre de 2023

Esta Tesis Doctoral ha sido dirigida por el Dr. Antonio Delgado Huertas, Profesor de Investigación de OPIs, y el Dr. Xosé Antón Álvarez Salgado, Profesor de Investigación de OPIs

Editor: Universidad de Granada. Tesis Doctorales
Autor: Sara Valiente Rodríguez
ISBN: 978-84-1195-117-3
URI: <https://hdl.handle.net/10481/88373>

Funding: This thesis has been developed at the Biogeoquímica de Isotopos Estables group, in the Departamento de Petrología y Geoquímica of the Instituto Andaluz de Ciencias de la Tierra (CSIC-UGR) and at the Organic Geochemistry Lab in the Departamento de Oceanografía of the Instituto de Investigaciones Marinas (CSIC). The research presented in this PhD thesis has been funded by the project Flujos de carbono en un sistema de afloramiento costero (Cabo Blanco, NO de Africa): Caracterización elemental, óptica, isotópica y molecular, FLUXES (CTM2015-69392-C3-2-R), Ministerio de Economía, Industria y Competitividad. Sara Valiente has been funded by an Ayuda para Contratos Predoctorales para la Formación de Doctores (BES-2016-079216) associated to the project CTM2015-69392-C3-2-R, extended with additional fundings provided by the Consejo Superior de Investigaciones Científicas.

A mi padre

Abstract

Despite the scientific interest on nitrogen (N) in the marine environment and its key role in global biogeochemical cycles, there are still uncertainties about the mechanisms that control its cycle and how to quantify them. N fluxes to and within the ocean are likely to increase in the future due to anthropogenic activities. To understand the consequences of these anthropogenic perturbations in the ocean, natural fluctuations in the N cycle must be understood. In this context, the general objective of this PhD thesis is to characterize elemental and isotopically the inorganic and organic (dissolved and suspended) N pools, in the Cape Verde Frontal Zone (CVFZ) from the information collected during two oceanographic cruises carried out in summer and autumn 2017. This highly dynamic zone is located at the southern end of the Eastern Boundary Upwelling Ecosystem of the Canary current. In the CVFZ, convergence of tropical and subtropical Atlantic waters occurs, forming the thermohaline Cape Verde front (CVF). In addition, this region is characterised by large vertical and horizontal export fluxes of organic matter and inorganic nutrients, due to the interaction of the CVF with the Mauritanian coastal upwelling and its Cape Blanc Giant Filament.

We observed that the distributions of inorganic and organic N species, and the $-O_2:N:Si:P$ stoichiometric ratios in the epipelagic layer of the CVFZ were dictated by the position of the CVF and its interaction with meso- and submeso-scale structures (meanders, eddies, filaments). This stoichiometry reflected severe N limitation at surface mixed layer, and preferential N mineralisation in the water below pycnocline and in meso- and bathypelagic layers. Geographical heterogeneity in dissolved (DON) and suspended particulate (PON) organic nitrogen distributions and their stoichiometry were also observed within each of the different water masses of contrasting origin present in the study area (North and South Atlantic Central Water, Subpolar Mode Water, Mediterranean Water, Antarctic Intermediate Water, Labrador Sea Water and North East Atlantic Deep Water). Nevertheless, our analysis indicates that DON and suspended PON have a minor impact on local mineralisation processes, suggesting that regenerated nitrate in CVFZ was mainly derived from sinking POM. This higher contribution of sinking POM was also supported by the distribution of $\delta^{15}N_{NO_3^-}$ and $\delta^{18}O_{NO_3^-}$ and the average values obtained for each water mass in the CVFZ.

Key Word: Inorganic N, organic N, dissolved N, suspended N, nitrate isotopes, N cycling, basin scale, mesoscale, submesoscale, water masses, Cape Verde Frontal Zone.

Resumen

A pesar del interés científico sobre el ciclo del nitrógeno (N) en el medio marino y su papel clave en los ciclos biogeoquímicos globales, aún existen ciertas lagunas sobre los mecanismos que controlan su ciclo y como cuantificarlos. Además, se pronostica que los flujos de nitrógeno hacia y dentro del océano aumenten debido a efectos antropogénicos. Para comprender las consecuencias de estas perturbaciones antropogénicas en el océano, debemos entender las fluctuaciones naturales en los procesos del ciclo del N. En este contexto, el objetivo general de esta tesis consiste en caracterizar elemental e isotópicamente el nitrógeno inorgánico y orgánico (disuelto y en suspensión), en la Zona Frontal de Cabo Verde (CVFZ), a partir de la información recopilada durante dos campañas oceanográficas realizadas en verano y en otoño del 2017. Esta zona de gran dinamismo está situada en el extremo Sur del ecosistema de afloramiento costero de la Corriente de Canarias. En la CVFZ se produce la convergencia de aguas tropicales y subtropicales del Atlántico, formando el Frente termohalino de Cabo Verde (CVF). Esta región, está caracterizada, además, por grandes flujos de exportación de materia orgánica y nutrientes inorgánicos, tanto verticales como horizontales, debidos a la interacción del CVF con el afloramiento costero de Mauritania y el filamento gigante de Cabo Blanco

En esta tesis se observó que las distribuciones de N orgánico e inorgánico, así como las relaciones estequiométricas de $-O_2:N:Si:P$, en la capa epipelágica del CVFZ, las dictan la posición del CVF y su interacción con las estructuras de meso- y submesoescala en la zona (meandros, remolinos, filamentos). La estequiometría obtenida refleja una severa limitación de N en la capa superficial, mientras que por debajo de la pínoclina y en las capas meso- y batipelágicas mostró una mineralización preferente de N. Las distribuciones de nitrógeno orgánico disuelto (DON) y particulado (PON) y sus estequiometrias mostraron cierta heterogeneidad geográfica en las diferentes masas de agua presentes en el CVFZ (Aguas Centrales del Atlántico Norte y Sur, Agua Modal Subpolar, Agua Mediterráneo, Agua Intermedia Antártica, Agua de Labrador y Agua Profunda del Atlántico Nororiental). Los análisis mostraron que tanto DON como PON, tienen un impacto pequeño en los procesos locales de mineralización, lo cual sugiere que el nitrato regenerado en la región de estudio, se deriva principalmente por la mineralización del material particulado en sedimentación. Esta mayor contribución por parte del material particulado en sedimentación, la corrobora la distribución obtenida de $\delta^{15}N_{NO_3^-}$ y $\delta^{18}O_{NO_3^-}$ y sus valores medios en cada masa de agua presente en la CVFZ.

Palabras Clave: N inorgánico, N orgánico, N disuelto, N particulado, ciclo de N, isótopos de nitrato, escala de cuenca, mesoescala, submesoescala, masas de agua, zona frontal de Cabo Verde,.

Acknowledgment

En primer lugar, me gustaría agradecer a mis directores de tesis Antonio y Pepe. Por la empatía, la paciencia infinita, la comprensión y especialmente por permitirme formarme con ellos y dedicarme durante estos años a algo que me apasiona. Me siento afortunada de haber tenido unos grandes directores, especialmente como personas.

A Antonio, por introducirme en el complejo mundo de los isótopos, por darme la oportunidad de trabajar y familiarizarme con cada uno de los equipos del laboratorio, por la confianza depositada para el desarrollo de la plena autonomía y por estar siempre dispuesto a echar un cable en el laboratorio, sea la hora y el día que sea.

A Pepe, por su pasión por la ciencia (es un placer escucharte hablar de cualquier tema), por su dedicación, por la motivación y la capacidad de convertir lo tedioso en interesante y en fácil lo difícil, por llevarlo “*to pa'lante*” y sacarme tiempo de donde no lo tiene. Por leer, y releer y releer... Por estar siempre al pie del cañón, por el apoyo constante y el buen humor perpetuo.

Al proyecto FLUXES y sus integrantes de ambas campañas. Tanto a los científicos como a la tripulación. Y a los compañeros del IIM, María José y a Vanesa, por todos los análisis de la gran parte de las muestras, que se han utilizado para elaborar esta tesis.

Al personal del IACT: a Arsenio y a su infinita paciencia, por ayudarme siempre y enseñarme tanto en el laboratorio. A los de la “alta alcurnia”: Paco, Ana, Carlota y Arantxa. A Huertas, quien me ha echado tantas firmas a tantos permisos, que si fuera famoso y las vendiese por 2€ ya podría jubilarme. A los que dan vida a los pasillos y han sido compañeros en esta aventura: Ceci, Ricardo, Álvaro, Jon, Manu, Alberto, Manolis, Bob, Javi de Estepa, Alejandro, Paloma, Santi, Mela, Mari Flor, Luis, Mela, Alpiste... A los que su estancia ha sido breve, pero han dejado huella para siempre: Jorgy, Luana, Iane y Stefano, a sus sonrisas perpetuas y a las carcajadas de quedarte sin aire. A Alex, Elsy Pablo, Andrea, Federica, Marianne, Susana... A Meri y Antonio (y tu infinidad de detalles), que son el corazón del IACT y van dejando una estela de alegría por donde pasan. A los porteros, Paco, el otro Paco, Jose, Roberto, Lola e Ignacio mis primeras risas por la mañana durante todos estos años y mi única compañía abriéndome las puertas del castillo los fines. Y, especialmente, a mis chicos del IACT Erwin, Adrián y Javi, por la amistad, por las noches de cervezas y por sus abrazos. Porque si de la ciencia he aprendido que el saber no

ocupa lugar, ellos me han dejado claro que el querer tampoco, ¡sois mejor que comerse la última croqueta!

A mi madre, la persona a que le debo TODO, a mi padre, cuya aportación también queda reflejada en esta tesis. A la familia que no escogí, pero de la cual me siento increíblemente orgullosa de pertenecer. Pues todo lo que soy, es la mezcla de lo que me han enseñado. La mentalidad de mi padre, la fortaleza de mi madre, la perseverancia de mi hermana, la empatía de Frozen, las ganas de vivir de la Sestra, la ilusión de mi tía Concha, la actitud de mi tía Mili, el carisma de mi padrino, la disposición de mi tía Uchi, la luz de mi tío Jesús, Pero sobre todo la resiliencia de toda la familia, y en particular, la a frase que siempre repetía mi abuelo “La clave está en hacer con una sonrisa, aquello que tienes que hacer de todos modos”. A Silvia (no sé en qué momento he pasado a ser yo la que aprende de ti). A la familia que, si escogí: Mis imprescindibles. Mis Carlis, mis *pussies*, Javishu y Pin, por los “vamos a hacer piña”, por la camaradería, por su fuerza inquebrantable, la capacidad de reiniciarte con una cerveza y un abrazo, y saber reírse de todo (A todos vosotros os estaré eternamente agradecida, y aprovecho para que se quede escrito para siempre, que OS QUIERO y OS ADMIRO).

A Mar que siempre está cerca estando lejos, a mis chicas de Granada, Sonia, Araceli, Eva y Cristina, ¿y a sus vamos? ¡Vamos! Sin duda me olvidaré de personas que me hayan ayudado y brindado apoyo durante estos años y ruego que me perdonen.

Y, por último, pero no por ello menos importante, a las personas que han hecho esto posible, a mi equipo: A Tao, porque el rescate fue mutuo. A Marcos por “salpimentarme los días, festejar mis alegrías, sufrir mis melancolías y acomodar sus pasos a mi caminar”. A mi *princess*, por llegar para quedarse, por ser la mejor amiga y compañera de piso, por todas las risas, los momentos de subidón, los de quejarnos de todo, por su energía, por ser el viento en la espalda, pero sobre todo por creer SIEMPRE en mí, especialmente en los momentos en los que dudaba yo (Eres una persona increíble, e increíblemente afortunada me siento yo por tenerte en mi vida). Y a Rubén, mi compañero de fatiga y mi pilar, por el apoyo moral, por el desahogo, por escucharme siempre, por haber recorrido este camino conmigo, por facilitarme la vida y por su amistad. A los cuatro, gracias. Qué bonito cuando la vida te sorprende con gente muy grande, que sin tener que pedirlo, está ahí, te apoya, te quiere, te cuida y te sigue al fin del mundo.

En resumen. A todos ellos, mi más sincera gratitud.

Contents

List of acronyms	1
-------------------------------	---

Chapter 1

1 Introduction

1.1 Nitrogen in the marine environment	5
1.1.1 Nitrogen reservoirs	5
1.1.2 Nitrogen in the ocean	6
1.1.3 Marine nitrogen cycle.	9
1.1.3.1 Atmospheric deposition and continental inputs	10
1.1.3.2 Assimilation	10
1.1.3.3 N ₂ Fixation	12
1.1.3.4 Ammonification	12
1.1.3.5 Nitrification	13
1.1.3.6 Denitrification	13
1.1.3.7 Anaerobic ammonium oxidation (anammox)	14
1.1.4 Oceanic nitrogen budgets	14
1.2 Stable isotopes in ocean biogeochemical nitrogen cycle.	18
1.2 The Cape-Verde Frontal Zone:	21
1.3.1 Eastern Boundary Ecosystem (EBUEs)	21
1.3.2 Main features of the Cape Verde Frontal Zone.	22
1.3.3 Water masses of the Cape Verde Frontal Zone.	25
1.3.4 Inorganic and organic N in the CVFZ	27
1.4. The project FLUXES.	28
1.5 Aim of this thesis	30
1.6 Structure of this thesis.	31

Chapter 2

2. Large-scale variability of nitrogen species in the Cape Verde Frontal Zone (NW Africa)

Abstract.	35
2.1 Introduction	37
2.2 Material and Methods	38
2.2.1 Sampling strategy	38
2.2.2 Analytical determination	40
2.2.3 Water mass analysis	41
2.2.4 WT proportion-weighted average values	45
2.2.5 Multiple regression models	46
2.2.6 Epipelagic layers	47
2.3 Results	47
2.3.1 Hydrography setting of the CVFZ.	47
2.3.1.1 Epipelagic layers	47
2.3.1.2 Meso- and bathypelagic layers	50

2.3.2 Biogeochemical variability in epi-, meso- and bathypelagic waters of the CVFZ	56
2.3.2.1 Epipelagic layers	56
2.3.2.2 Meso- and bathypelagic layers.	63
2.4 Discussion.	68
2.4.1 Variability in the epipelagic layers of the CVF	68
2.4.2 Impact of water mass mixing in meso- and bathypelagic layers . . .	70
2.4.3 Remineralisation of organic matter in the CVFZ	71
2.5 Conclusion	73

Chapter 3

3. Meso- and submeso-scale variability of nitrogen species in the Cape Verde Frontal Zone

Abstract.	77
3.1 Introduction.	79
3.2 Material and Methods	81
3.2.1 Sampling strategy and analytical determinations	81
3.2.2 Water mass analysis, water type proportion-weighted average values and multiple regression models.	84
3.3 Results.	85
3.3.1 Hydrography of the CVFZ in November 2017.	85
3.3.1.1 Epipelagic layers	86
3.3.1.2 Mesopelagic layers	90
3.3.2 Nitrogen biochemistry in the CVF in November 2017	93
3.3.2.1 Epipelagic layers	93
3.3.2.2 Mesopelagic layers	100
3.4 Discussion	103
3.4.1 Meso- and submeso-scale processes in epipelagic layers of the CVF.	103
3.4.2 Remineralization in the mesopelagic layers.	106
3.5 Conclusion.	107

Chapter 4

4. Nitrate in Cape Verde Frontal Zone: an isotopic approach

Abstract.	111
4.1 Introduction.	113
4.2 Material and Methods	114
4.2.1 Sampling strategy.	114
4.2.2 Analytical determinations.	116
4.2.3 Correction to calculate the true $\delta^{15}\text{N}$ and d^{18}O of nitrate.	118
4.2.4 Water mass analysis, WT proportion-weighted average values and multiple regression models.	119
4.3 Results.	120
4.3.1 $\delta^{15}\text{N}$ and d^{18}O in epipelagic water (30-200 dbar).	120
4.3.2 $\delta^{15}\text{N}$ and d^{18}O in the interior ocean (>200 dbar)	122

4.4 Discussion	128
4.4.1 $\delta^{15}\text{N}$ and $\delta^{18}\text{O}$ in CVFZ	128
4.4.2 Isotopic imprints in the nitrate of the different water masses of the CVFZ.	130
4.4.3 Dominant nitrogen cycle processes along the four transects of Fluxes I	131
4.5 Conclusion.	133

Chapter 5

5. General discussion

5.1 Water mass definitions in the Cape Verde Frontal Zone.	137
5.2 The importance of correcting water mass mixing to obtain reliable $-\text{O}_2:\text{N}:\text{P}:\text{Si}$ nutrient ratios	138
5.3 Differences in $-\text{O}_2:\text{N}:\text{P}:\text{Si}$ stoichiometry between FLUXES I and II.	140
5.4 Organic nitrogen contribution to NO_3^- production in the CVFZ	141
5.5 Revisiting the isotopic determination of NH_4^+	143

Chapter 6

6. Conclusions.	149
----------------------	-----

Supplementary Material	151
------------------------------	-----

Annexe.	161
--------------	-----

References.	167
------------------	-----

List of acronyms

AA	Modified Antarctic Intermediate Water
AC	Azores Current
AOU	Apparent oxygen utilization
CBGF	Cape Blanc Giant Filament
CC	Canary Current
Cd	Spongy Cadmium
Chl-a	Chlorophyll a
CCLME	Canary Current Large Marine Ecosystem
CUC	Canary Upwelling Current
CVC	Cape Verde Current
CVF	Cape Verde Front (when referring exclusively to the Front)
CVFZ	Cape Verde Frontal Zone (when referring to the entire study area)
DCM	Deep chlorophyll maximum
DIN	Dissolved inorganic nitrogen
DOC	Dissolved organic carbon
DOM	Dissolved organic matter
DON	Dissolved organic nitrogen
EBUE	Eastern Boundary Upwelling Ecosystem
ENACW	Eastern North Atlantic Central Water
ENACW_15	Eastern North Atlantic Central Water of 15 °C
ENACW_12	Eastern North Atlantic Central Water of 12 °C
IRMS	Isotope-ratio mass spectrometer
LNEADW	Lower North East Atlantic Deep Water
LSW	Labrador Sea Water
MC	Mauritanian Current
ME	Measurement error
MMW	Madeira Mode Water
MW	Mediterranean Water
N	Nitrogen
NASG	South-eastern North Atlantic subtropical gyre
NATG	North-eastern North Atlantic tropical gyre
NEADW	North East Atlantic Deep Water
NECC	North Equatorial Counter Current
NO	$\text{NO} = \text{O}_2 + R_N \cdot \text{NO}_3^-$
NWA	North-West Africa
ODR	Orthogonal Distance Regression
ODZ	Oxygen deficient zones
OM	Organic matter
OMP	Optimum multiparameter analysis
POC	Particulate organic carbon
POM	Particulate organic matter
PON	Particulate organic nitrogen
PUC	Poleward Under Current
R_N	Redfieldian stoichiometric ratio of oxygen consumption to nitrate production of 9.3 mol O_2 mol NO_3^-

SACW	South Atlantic Central Water
SACW_12	South Atlantic Central Water of 12°C
SACW_18	South Atlantic Central Water of 18°C
SE	Standard error
SPMW	Subpolar Mode Water
TDN	Total dissolved nitrogen
UNEADW	Upper North East Atlantic Deep Water
WT	Water type

Chapter 1

Introduction

Chapter 1:

1.1. Nitrogen in the marine environment

1.1.1 Nitrogen reservoirs

Nitrogen (N) is one of the most abundant elements in the biosphere and is essential for all life forms. The N cycle is the most complex of Earth's biogeochemical cycles, consisting of an unusually diverse set of transformations, which are mainly carried out by different specialized microorganisms (Gruber, 2008; Casciotti, 2016). Transformation of dinitrogen gas into combined forms of N in nature includes the formation of nitric oxide by lightning and ultraviolet rays, but the most significant processes consist on the formation of ammonia, nitrite, and nitrate by soil or aquatic microorganisms. N is a key component of the Earth's biogeochemistry, due to its critical role of N controlling primary production (Gruber, 2008; Gruber and Galloway, 2008).

N is present in a variety of forms with different states of matter (gas, dissolution, suspension, solid) and oxidation states: nitrate (NO_3^- , +5), nitrite (NO_2^- , +3), nitric oxide (NO , +2), nitrous oxide (N_2O , +1), dinitrogen (N_2 , 0), ammonium (NH_4^+ , -3) and organic nitrogen (ON, -3) (Gruber, 2008; Sipler and Bronk, 2015; Zhang et al., 2020).

The major N reservoir on Earth is the atmosphere, where it mostly occurs as N_2 (Fig. 1.1) (Gruber, 2008; Zhang et al., 2020). Despite the high concentration of combined N in the crust and ocean sediments (e.g., as ammonium in silica minerals and silt and as organic N in sedimentary rocks and sediments) (Fig. 1.1), its exchange with the ocean is smaller than ocean-atmosphere exchange of N_2 (Berner, 2006; Houlton et al., 2018; Zhang et al., 2020).

In the ocean the most abundant N form is also N_2 (20,000 Pg N) (Galloway et al., 2004). The ocean is also the largest reservoir of combined N on Earth, containing about 50 or 176 times more combined N than the biosphere (Fig. 1.1) (Moore et al., 2013; Zhang et al., 2020, and references there in).

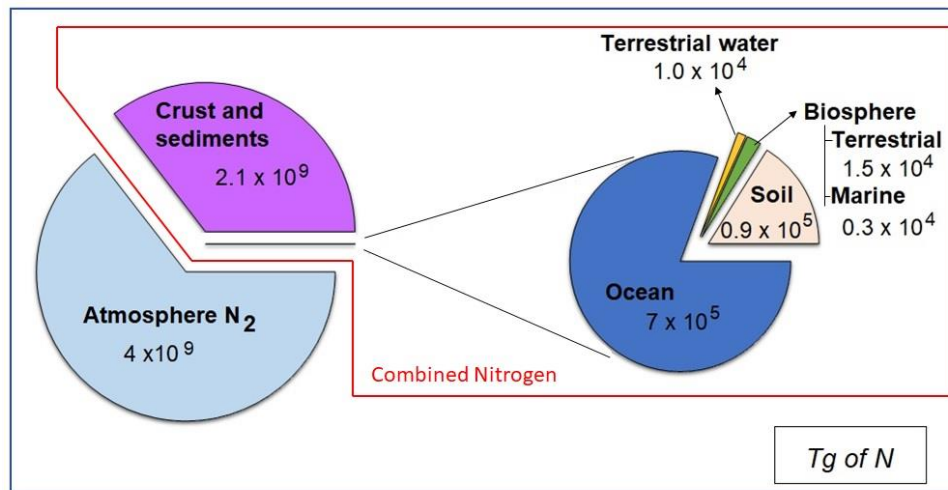


Figure 1.1. Estimated size of the main global combined N (available) reservoirs (red square), in comparison with the higher non-combined N reservoir on the Earth (Atmospheric N₂) in Tg of N ($= 1 \times 10^{12}$ g of N). Note that all numbers except atmospheric N₂ are reported as combined N. For this reason, the high N₂ reservoir in the ocean is non-reflected. (size values taken from Zhang et al., 2020).

1.1.2 Nitrogen in the ocean

N₂ represents about 95% of the total N in the ocean (Voss et al., 2013), due to its high partial pressure in the atmosphere and to the stability of the N triple bond. Despite the large amount of N in the form of N₂, it is almost considered an inert gas similar to Argon, biologically inaccessible except for diazotrophs (Gruber, 2008; Zhang et al., 2020).

The combined N reservoir is primarily composed of nitrate, nitrite, ammonia, and organic N, in the form of dissolved and particulate, suspended or sinking, organic compounds (Voss et al., 2013). Nitrate is the most abundant combined N form (about 88%), followed by dissolved organic nitrogen (DON) (12%), the leftover 0.3% being composed of particulate organic nitrogen (PON), NO₂⁻, NH₄⁺ and N₂O (Gruber, 2008; Canfield et al., 2010; Bertrand et al., 2015). The turnover time of these N forms ranges from minutes to thousands of years (Gruber, 2008), being about 400 years for NO₃⁻, 1-2 weeks for NH₄⁺ and PON, while for DON could range between a few minutes to hundreds of years depending on the variable reactivity of organic molecules (Gruber, 2008; Sipler and Bronk, 2015; Zhang et al., 2020).

Nitrate concentration in the ocean ranges from 0 to 10 μmol kg⁻¹ in surface waters, mainly due to consumption by phytoplankton, and from 20 to 50 μmol kg⁻¹ in deep waters, mainly due to remineralization of organic N and subsequent nitrification (Fig. 1.2); (Gruber, 2008; Voss et al., 2013; Ward, 2014; Zhang et al., 2020). Average nitrite

concentrations ranged from 6 nmol kg^{-1} in the euphotic zone to 100 nmol kg^{-1} at the base of the euphotic zone (primary nitrite maximum) and $> 5 \text{ } \mu\text{mol kg}^{-1}$ in oxygen-deficient zones (ODZs), characterized by low ventilation rates coupled with organic matter (OM) decomposition and consequently higher O_2 consumption (secondary nitrite maximum) (Fig. 1.2a,b and c) (Sarmiento and Gruber, 2006; Gruber, 2008; Casciotti, 2016; Kim, 2016). Ammonium concentrations in the open ocean range from undetectable to a few 100 nmol kg^{-1} , with maximum values associated with the sunlit and dark aphotic zone (Fig. 1.2) (Gruber, 2008).

The distribution of inorganic nitrogen below the euphotic zone is determined by physical and biogeochemical processes (Pelegrí and Benazzouz, 2015; Pelegrí et al., 2017). Physical processes are related with the vertical convective and diffusive fluxes between surface and subsurface layers and the lateral transport and biogeochemical processes are associated to remineralization, which is driven by the availability of OM, O_2 and inorganic nutrients.

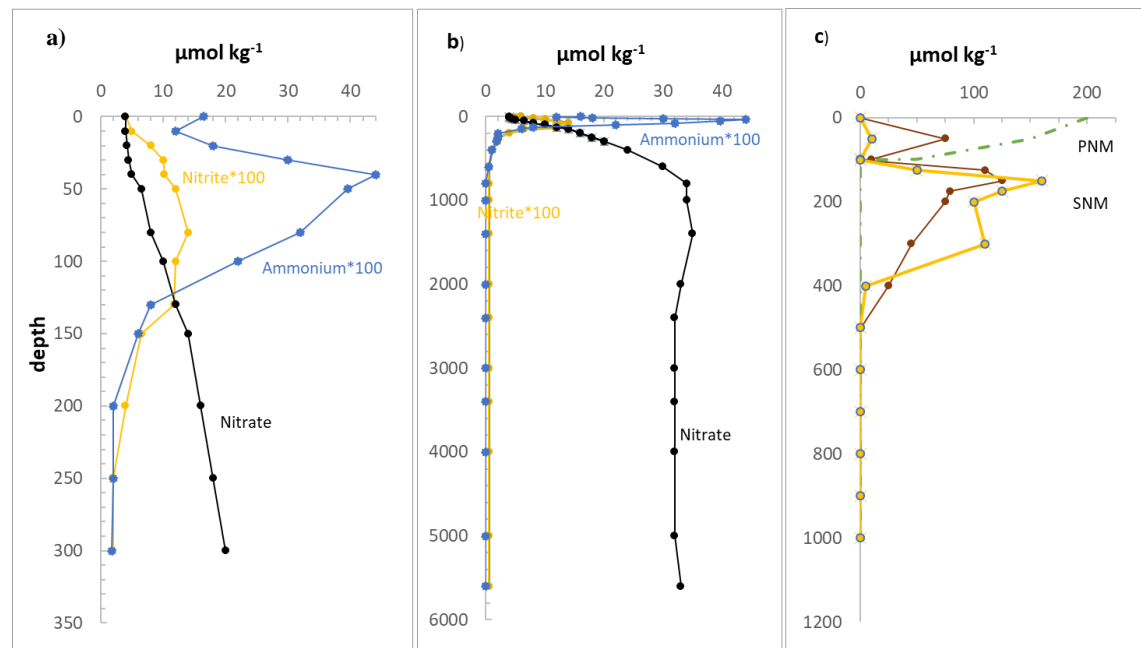


Figure 1.2. Global means profiles of nitrate, nitrite and ammonium for epipelagic waters (a) and entire water column (b) and nitrite and oxygen (green) concentrations in $\mu\text{mol kg}^{-1}$ profiles, in ODZ regions (c) Note that for a more intuitive visualization of the trends (compared to nitrate), nitrite and ammonium concentrations have been multiplied by 100. In (a) and (b), the nitrate profile is based on data from the World Ocean Atlas 2001. The nitrite profile by averaging all data from the World Ocean Circulation Experiment and ammonium profile was based on data from the Arabian Sea, the Southern Ocean, the North Atlantic, and the Equatorial Pacific While in (c) nitrite profiles are taken from the Eastern Tropical North Pacific (brown) and Arabian Sea (yellow) reflecting their primary nitrite maximum (PNM) and secondary nitrite maximum (SNM). (Taken from Gruber, 2008 and Casciotti, 2016b).

Chapter 1:

The major fraction of OM, dissolved OM (DOM), is classified according to its reactivity as labile, semi-labile and refractory (Hansell and Carlson, 2015). Labile DOM is produced and processed within the same water parcel, representing a minor fraction of the bulk DOM (0.1%); semi-labile DOM (1% of bulk DOM) is processed far from where it was produced because it is transported horizontally or vertically; and refractory DOM, which is the majority of the oceanic bulk DOM, remains in the ocean without being degraded by any organism for decades to thousands of years (Hansell and Carlson, 2013). In the ocean, DON is mostly produced in the water column (autochthonous sources; Fig. 1.3) and a minor part is supplied to the water column via surface (rivers) and ground waters and atmospheric inputs (allochthonous sources) (Sipler and Bronk, 2015). DON presents higher concentrations in surface waters, with a mean value of $4.4 \pm 0.5 \mu\text{mol L}^{-1}$ and decrease with depth to values around $\sim 2 \mu\text{mol L}^{-1}$ (Letscher et al., 2013; Sipler and Bronk 2015, Zhang et al., 2020). Surface DON concentrations increased closer to the coast, reaching a mean concentration up to $6 \pm 2 \mu\text{mol L}^{-1}$ (Letscher et al., 2013; Sipler and Bronk, 2015). Particulate OM (POM) is differentiated from DOM as the fraction of marine OM retained by a filter having a pore size from $0.2 \mu\text{m}$ (polycarbonate, polysulfone, or aluminium filters) to $0.7 \mu\text{m}$ (typically glass fiber filters; Repeta, 2015). POM is formed by living organisms and mainly their detritus, with different elemental (C, H, O, N, P) and biogeochemical composition, as phytoplankton is rich in proteins and carbohydrates, and their detritus in lipids (Ríos et al., 1998). POM is classified into suspended and sinking fractions as a function of their buoyancy, which is somewhat related to their size. Suspended POM consists of particles smaller than $100 \mu\text{m}$, with neutral buoyancy. On the contrary, particles larger than $100 \mu\text{m}$ are considered part of the sinking POM pool (Álvarez-Salgado and Arístegui, 2015).

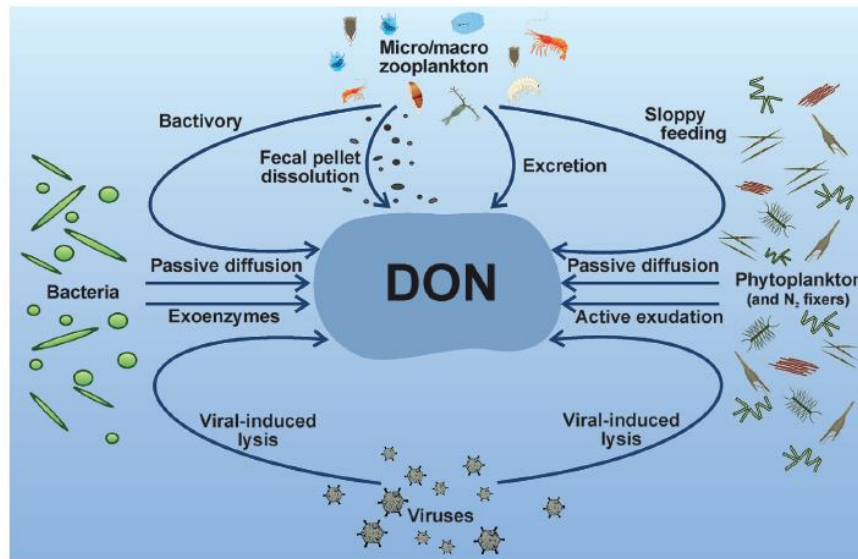


Figure 1.3. Conceptual diagram of the biogeochemical processes involved in *in situ* dissolved organic nitrogen (DON) production in aquatic systems. (Taken from Sipler and Bronk, 2015).

1.1.3 Marine nitrogen cycle

The marine N cycle consists of an assortment of redox reactions (Fig. 1.4) due to the ample range of possible oxidation states of N, mediated by enzymes, that transform one species to another (Fig. 1.5). These reactions, which comprises nitrogen assimilation, N_2 fixation, ammonification, nitrification, denitrification and anaerobic ammonium oxidation (Anammox), control the inventory, distribution and speciation of N (Fig. 1.5) (Gruber, 2008).

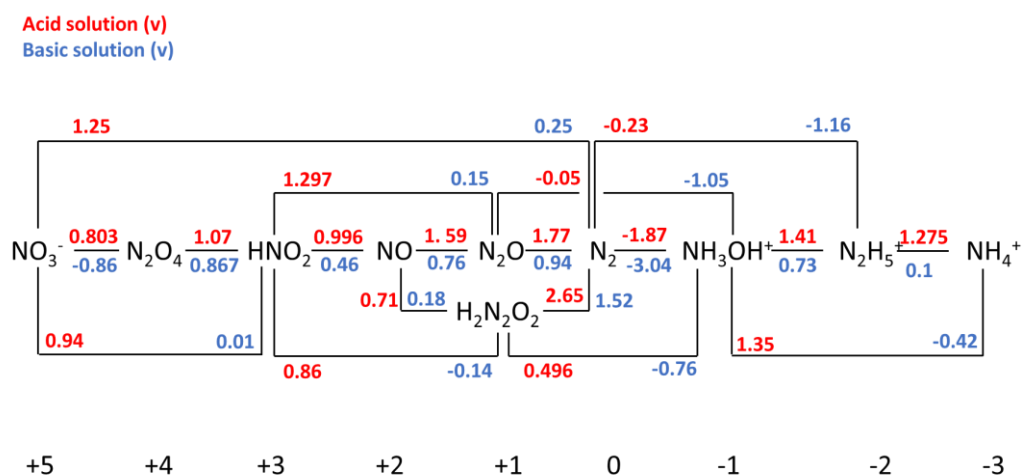


Figure 1.4. Standard reduction potentials of nitrogen in volts in acid solution at pH 0 (red) and in basic solution at pH 14 (Blue) (Modified from (Winter, 1999)

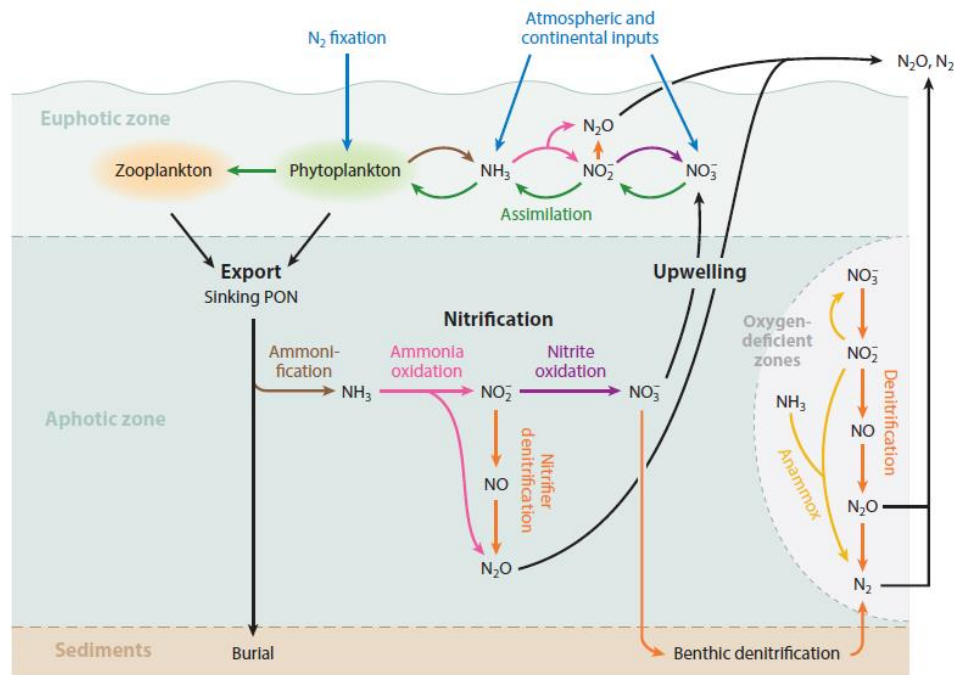


Figure 1.5. Overview of the marine N cycle, with N inputs shown in blue and losses in orange and yellow. Internal cycle processes are color-coded to distinguish steps of particulate organic nitrogen (PON) production [assimilation and grazing (green)] and remineralization [ammonification (brown) and nitrification, including ammonia oxidation (pink) and nitrite oxidation (purple)]. Physical processes (upwelling, export of sinking PON, air-sea gas exchange, and burial) are shown in black. The light-gray-shaded half circle represents oxygen-deficient regions of the water column. (Taken from Casciotti, 2016).

1.1.2.1 Atmospheric deposition and continental inputs

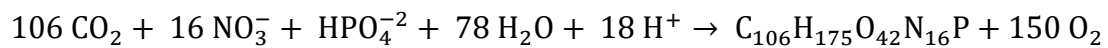
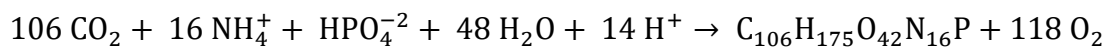
Atmospheric deposition is an important source of combined N to the open ocean. N is transported by air masses and released to the sea surface in the form of NO_x (34%), NH_x (36%), and organic N (30%) (Duce et al., 2008; Voss et al., 2013), occurring as wet and dry deposition. Continental inputs are important source of nitrate, PON and DON in coastal systems, being estimated for river inputs as nitrate (40%), PON (40%) and DON (20%) (Voss et al., 2013).

1.1.3.1 Assimilation

Because N is essential for phytoplankton growth, it is assimilated into biomass in the euphotic zone (Gruber, 2008). This process consists on the transformation of nitrate or ammonium into organic nitrogen by phytoplankton and dominates the marine N cycle (Fig. 1.5) (Gruber, 2008). NH_4^+ , which is at the same oxidation state than organic N (Fig. 1.4), and does not require active transport across the cell wall, is the preferred combined N form by phytoplankton (Mulholland and Lomas, 2008; Zouiten et al., 2013). Nevertheless,

nitrate can be also assimilated (Fig. 1.5), but this process involves a higher amount of energy, for the reduction of nitrate into ammonium (Fig. 1.4), which is catalyzed by the enzymes nitrate and nitrite reductase, and for active transport across the cell membrane (Campbell and Kinghorn, 1990; Solomonson and Barber, 1990; Gruber, 2008; Zouiten et al., 2013).

Due to the high requirement of carbon (C) and N by phytoplankton, the assimilation process is heavily linked to the photosynthetic C fixation (Gruber, 2008; Mulholland and Lomas, 2008), producing the synthesis of organic matter through the coupled assimilation of CO_2 , NH_4^+ or NO_3^- and HPO_4^{2-} , which can be written as:



where $\text{C}_{106}\text{H}_{175}\text{O}_{42}\text{N}_{16}\text{P}$ is the average composition of the products of synthesis and early degradation of marine phytoplankton (Redfield et al., 1963; Anderson, 1995).

OM has a rather constant elemental composition with ratios similar to those found in the inorganic forms, which reflect the relationship between biological production and export. The export of biogenic particles and their subsequent remineralization provided a consistent view of the distribution of these elements (Gruber, 2008).

Combined N is considered a limiting nutrient for biological productivity in most Earth surface environments (Elser et al., 2007; Moore et al., 2013; Du et al., 2020). To determine N limitation in the ocean, N and Phosphorus (P) ratios are compared with the canonical N:P molar ratio of 16 for phytoplankton biomass (i.e., the so called “Redfield ratio”). N:P ratios lower than 16 suggest potential N limitation (Redfield et al., 1963; Anderson and Sarmiento, 1994; Geider and La Roche, 2002; Zhang et al., 2020).

These “Redfield ratios” constitute an important tool for understanding ocean biogeochemistry and links between nutrient cycling, nutrient limitation, and other important oceanographic processes (Mills and Arrigo, 2010; Deutsch and Weber, 2012). Several studies have demonstrated that the N:P and C:N ratios vary in different ocean regions (Weber and Deutsch, 2010; Martiny et al., 2013) and between surface and deep waters. At the surface, labile DOM has average C:N:P molar ratio of 199:20:1, lower than the refractory DOM of the deep waters, with average C:N:P molar ratio of 3511:202:1 (Hopkinson and Vallino, 2005). While, POM molar ratios also show large spatial

variations, with higher molar ratios around 195:28:1 in low-latitude gyres (warm and nutrient-depleted), than in upwelling regions (warm, nutrient-rich) with molar ratios around 137:18:1 and in high-latitude regions (cold and nutrient-rich) with molar ratios of 78:13:1 (Martiny et al., 2013).

1.1.3.2 N₂ Fixation

Despite N₂ is an inert gas, there are certain organisms called N₂ fixers, with specific enzymes (nitrogenase) able to reduce dinitrogen to ammonium (Fig. 1.5) (Mulholland and Lomas, 2008). This process is denominated N₂ fixation and is the most important N source to the ocean to support biological production (Gruber, 2008; Voss et al., 2013).

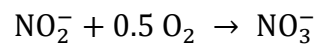
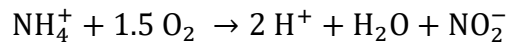
Traditionally, N₂ fixation has been associated to oligotrophic surface waters of the subtropical Atlantic and Pacific oceans (Capone et al., 1997; Mahaffey et al., 2005). Nonetheless, it has been shown that this process also occurs in marine sediments (Fulweiler et al., 2007), oxygen-deficient subsurface waters (ODZs) (Bonnet et al., 2013; Fernandez et al., 2011), nutrient-rich surface waters (Dekaezemacker et al., 2013; Hallstrøm et al., 2022) and actually, N₂ fixation also has been considered important in deep-sea environments (Dekas et al., 2009; Zehr and Capone, 2020; Hallstrøm et al., 2022). Mehta et al. (2003) described a diverse group of organisms with nitrogenase genes (the enzyme complex that catalyzes N fixation), and therefore potentially capable of fixing N₂. Hallstrøm et al. (2022) found N₂ fixation rates in meso- and bathypelagic layers of the Cape Verde Frontal Zone ranging from 0.03 ± 0.01 to 0.07 ± 0.01 nmol N l⁻¹ d⁻¹ by sinking cyanobacterial diazotrophs.

1.1.3.3 Ammonification

Ammonification is the reverse process of NH₄⁺ assimilation. During the excretion of organisms due to growth and metabolism recycling of macromolecules occurs. When organic compounds in biomass are degraded, while C is oxidized to CO₂, N remains in the same oxidation state, being released into the water column in the form of ammonia, which later reacts with H⁺ or H₂O to form ammonium (Fig. 1.4 and 1.5) (Gruber, 2008; Ward, 2014)

1.1.3.4 Nitrification

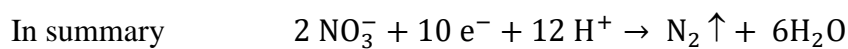
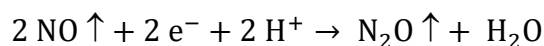
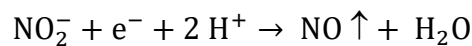
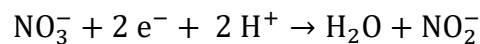
Nitrification consists on the biological oxidation of ammonium to nitrate (Fig 1.5), to produce energy by some bacteria and archaea which use oxygen as electron acceptor (Voss et al., 2013). It proceeds in two-step: ammonium is oxidized to nitrite by ammonium-oxidizing bacteria and archaea, which is followed by the oxidation of nitrite to nitrate by nitrite oxidizing bacteria (Kim, 2016).



Nitrification generally shows maximum rates closer to the bottom of the euphotic zone (Ward, 2008). Intermediary compounds such as hydroxylamine (NH_2OH), nitroxyl (NO) and nitrous oxide (N_2O) (Kim, 2016) are also formed during nitrification. Nitrification is limited by low O_2 levels; nitrifiers cease their activity at O_2 concentrations of 1 to 6 $\mu\text{mol kg}^{-1}$ (Henriksen et al., 1993; Ward, 2008). Furthermore, they tend to be inhibited by sunlight, specially nitrite oxidizers (Vanzella et al., 1989; Ward, 2008).

1.1.3.5 Denitrification

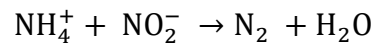
Denitrification is the conversion of NO_3^- to N_2 (Fig. 1.5). In anaerobic conditions, when O_2 is below about 2 $\mu\text{mol kg}^{-1}$, some heterotrophic anaerobic bacteria use nitrite and nitrate as electron donors (Kim, 2016). The process implies the reduction of nitrate to nitrite, followed by nitric oxide and nitrous oxide and finally N_2 , which is the principal end-product, accumulating nitrite and N_2O as intermediates (Devol, 2015).



This process requires anaerobic conditions, which are mainly associated to shelf sediments, coastal and ODZ (Kim, 2016).

1.1.3.6 Anaerobic ammonium oxidation (anammox)

Anammox is used for energy production (Gruber, 2008), and it consists in the oxidation of ammonium to N_2 using NO_2^- as oxidizing agent (Fig. 1.5). Anammox is produced under anaerobic conditions being inhibited in the presence of oxygen (Kim, 2016).



1.1.4 Ocean nitrogen budget

The main N inputs to the oceans are associated with atmospheric deposition, N_2 fixation and riverine flux (in the coastal zone). On the contrary, sediment burial, denitrification and anammox are considered the main sinks for combined N, with denitrification and anammox as the major sinks (Fig. 1.6) (Gruber, 2008; Voss et al., 2013; Zhang et al., 2020).

Global marine N_2 fixation is considered the major source of N to the oceans (Fig. 1.6), and has been estimated at 125 Tg N yr^{-1} (Gruber and Sarmiento, 1997). Many studies have focused on estimating marine N_2 fixation, through direct observation and models, finding values from 60 to 330 Tg N yr^{-1} (Gruber, 2004; Brandes et al., 2007; Deutsch et al., 2007; Eugster and Gruber, 2012; Grokopf et al., 2012; Fowler et al., 2015; Jickells et al., 2017; Wang et al., 2019). Duce et al. (2008) estimated N fluxes for atmospheric deposition of around 67 Tg N yr^{-1} of which 23, 24 and 20 Tg N yr^{-1} corresponded to NO_x , NH_x and N_{org} respectively. Finally, riverine N flux, are estimated around $40\text{-}60 \text{ Tg N yr}^{-1}$ (Fig. 1.6), as inorganic nitrogen (nitrate) (40%), PON (40%) and DON (20%) (Voss et al., 2013; Zhang et al., 2020).

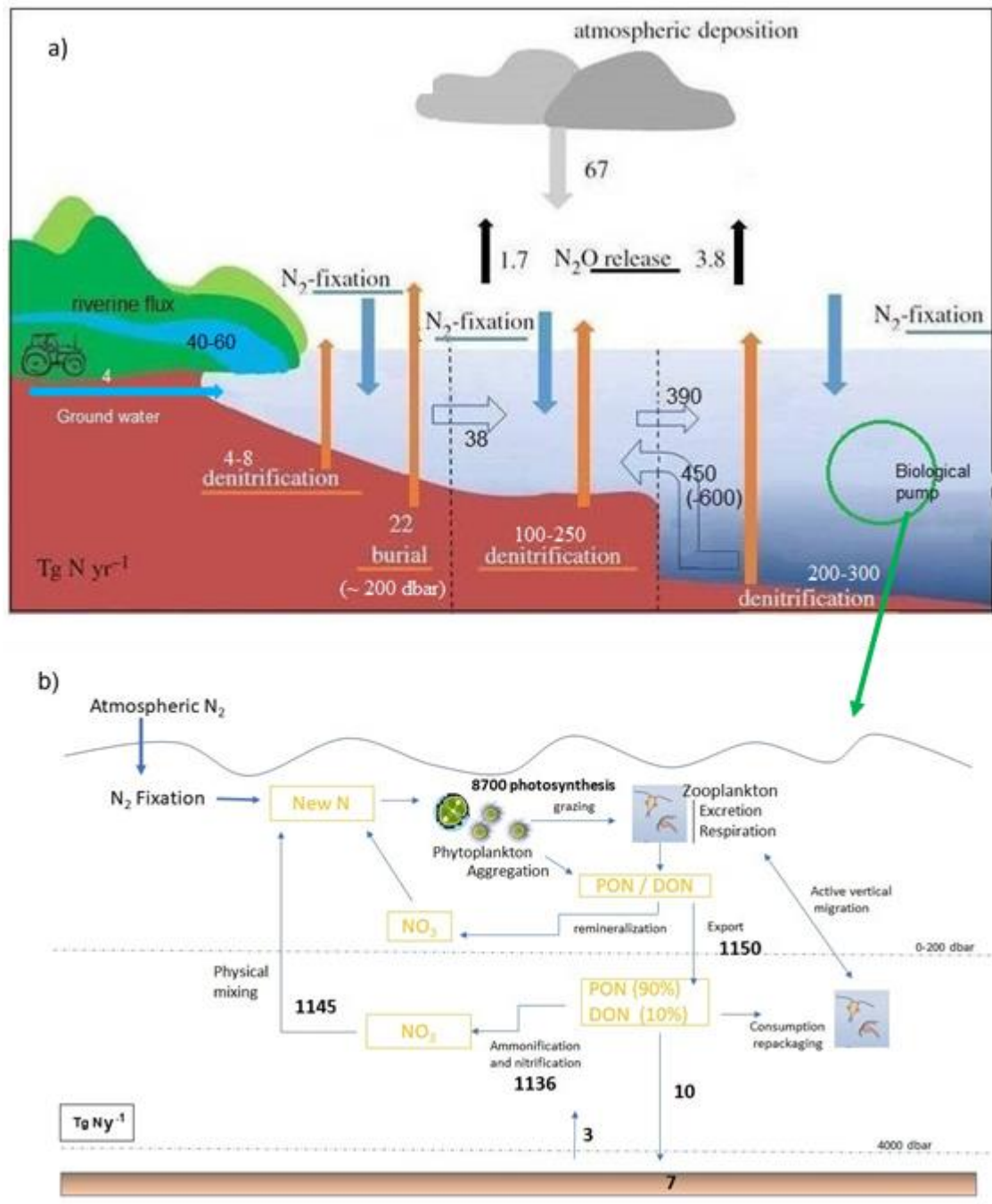


Figure 1.6. Nitrogen budget of the ocean (a) and simplified diagram of the N biological pump (b). In (a) the vertical dot lines separate the ocean in proximal, distal to coast and open ocean, the horizontal dot line represents 200 dbar deep, blue and black arrows represent inputs, orange and black arrows represent sinks, arrows with blue outline and transparent represent exported N between zone. Main numbers are given in the text. (Modified from Voss et al., 2013; reference values of biological pump are taken from Wollast et al., (1993) y Galloway et al., (2004).

Ocean N loss by N_2O emission and burial in marine sediments are estimated around 1-4 Tg N yr^{-1} and 22 Tg N yr^{-1} respectively (Fig. 1.6) (Voss et al., 2013; Zang et al., 2020). The N_2 fluxes to the atmosphere due the denitrification and anammox have been estimated

at 145-450 Tg N yr⁻¹ (Gruber, 2004; Codispoti, 2007; Devries et al., 2012; Eugster and Gruber, 2012; Hu et al., 2016; Jickells et al., 2017; Wang et al., 2019). Kuypers et al. (2003), suggested that in anoxic regions of the Black Sea anammox supports around 40% of the total N₂ production, while in the anoxic waters of Golfo Dulce (Pacific Coast of Central America), its account around 19-35% (Hort et al., 2003). The ocean has elevated denitrification fluxes (200 to 300 Tg N y⁻¹) compared with shelf sediment (100 to 250 Tg N y⁻¹) and terrestrial ecosystems (4 to 8 Tg N y⁻¹) (Fig.1.6) (Voss et al., 2013). Authors suggest that the ocean's N budget trends to loss N, as a consequence of a significantly imbalance with lower inputs than losses (Gruber and Galloway, 2008; Voss et al., 2013; Zhang et al., 2020).

Marine biological processes in interaction with oceanic transport and mixing, control the spatiotemporal variability of the various forms of combined N. In the euphotic layer, the main process driving N changes in the ocean is photosynthetic fixation when carbon and nutrients (nitrogen, phosphorus, iron, and others) are assimilated (Gruber, 2008). The organic nitrogen generated by assimilation can result in the form of biomass, detritus, or DON, which have different contributions to the efficiency and magnitude of the biological pump. In addition, the bulk of these organic materials decompose in the surface layer through dissolution, grazing and microbial hydrolysis but a small part survives and reaches the depths of the sea and sediments providing a source of inorganic N to deeper waters, highlighting the importance of understanding the mechanisms that control the partitioning of OM production between DOM, suspended and sinking POM.

It is estimated that ~9000 Tg N year⁻¹ are fixed by photosynthesis in the global ocean (Fig. 1.6b) (Galloway et al., 2004). Around 87% of this organic nitrogen is remineralized to inorganic N in the euphotic zone, contributing to the regenerated production of the ecosystem because the N returns to the same plankton population. The remaining 13% of these photoautotrophically fixed N, around 1150 Tg N year⁻¹, escapes rapid mineralization in the surface layers and sink into the ocean interior (Fig. 1.6b), contributing to export or new production as PON (90%) or DON (10%) (Galloway et al., 2004). The heterotrophic oxidation of PON back to inorganic N during sinking is highly efficient, around 1136 Pg N year⁻¹ and they are transported back to the upper layers by ocean circulation (Gruber, 2008). Therefore, less than 2%, around 10 Tg N year⁻¹ of the exported material, reaches the deepest layers and the seafloor of which 3 Tg N year⁻¹ is remineralized and 7 Tg N year⁻¹ remaining as reservoir (Fig. 1.6b).

In addition, it is also noticeable the large amount of anthropogenic new combined N introduced in the marine environment and the consequent alteration of the marine N cycle (Fig. 1.7). This is associated with food production and fossil fuel combustion, being important the use of fertilizers, accumulating oxidized forms of N in the atmosphere and in fresh surface and ground waters that end in the ocean (Galloway et al., 2004; Smil, 2004; Gruber, 2008; Zhang et al., 2020).

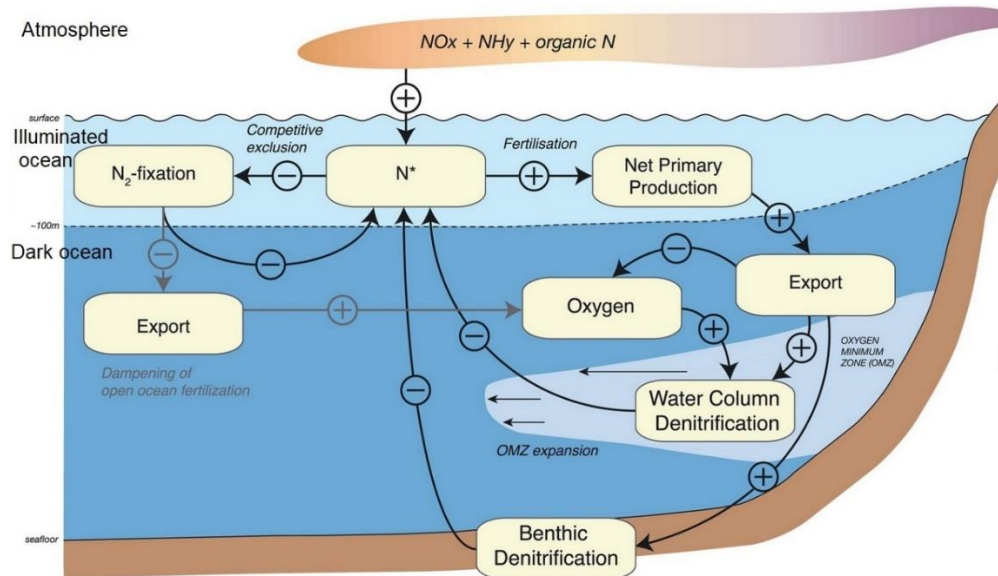


Figure 1.7. Representation of negative feedback induced for the increment of atmospheric N deposition associated to the anthropogenic effects. The sign of the response is given relative to a positive perturbation. An increase in N increases net primary production and export, producing a positive N^* perturbation, increasing water column and benthic denitrification. This positive perturbation also decreased the competitive advantage of diazotrophs decreasing N_2 fixation. Both processes compensate the initial perturbation constituting negative feedback. Lighter gray arrows show N_2 fixation damping reducing negative feedback from denitrification. (Taken from Yang and Gruber (2016)).

Capone et al., (2008) showed the current competition of the industrial and biological N_2 fixation as a consequence of the Haber-Bosch process. In 1860 atmospheric combined N input was estimated to be around 20 Tg N y^{-1} , 30% of which was anthropogenic. Currently, the atmospheric input has triplicated to 67 Tg N y^{-1} , 80% being anthropogenic (Duce et al., 2008). In the same way, human activities have roughly doubled river N flows since the pre-industrial period (25 Tg N y^{-1}) to nowadays ($40\text{-}70 \text{ Tg N y}^{-1}$) (Voss et al., 2013; Zhang et al., 2020). Furthermore, this anthropogenic input of combine N increased N_2O production in the ocean (Duce et al., 2008; Galloway et al., 2004; Zhang et al., 2020). At the same time, the N cycle is also reacting to a warmer and more acidic ocean, favouring nitrification processes in subsurface waters and reducing the N_2 assimilation in surface

waters, due the alteration of the physiological behaviour and evolutionary success of the N fixers (Capone and Hutchins, 2013; Zhang et al., 2020; Hutchins and Capone, 2022).

1.2. Stable isotopes in ocean biogeochemical nitrogen cycles

The utilization of stable isotopes of nitrogen and oxygen enables tracing of different processes associated with the N cycle in the ocean. There are two different stable isotopes of nitrogen, ^{14}N and ^{15}N . According to Mariotti (1983), their range of natural variation is 99.6-99.87% as ^{14}N , and 0.3-0.4% as ^{15}N . Oxygen has three stable isotopes with a range of natural variation of ^{16}O (99.7-99.8%), ^{17}O (0.03-0.04%), and ^{18}O (0.1-0.2%) (Dole, 1936; Epstein and Mayeda, 1953; Rosman and Taylor, 1998; Casciotti, 2016).

The N and O isotope ratios are generally expressed in delta notation ($\delta^{15}\text{N}$, $\delta^{18}\text{O}$), which indicates the natural abundance of ^{15}N or ^{18}O in a sample relative to the isotopic composition of a reference material (N from atmospheric AIR for nitrogen and Standard Mean Ocean Water (SMOW) for oxygen):

$$\delta^AX = \left[\frac{R_m}{R_{st}} - 1 \right] \times 1000 (\text{‰})$$

Where R_m and R_{st} represent the isotope ratio $^{15}\text{N}:^{14}\text{N}$ in a sample vs atmospheric AIR, or the isotope ratio $^{18}\text{O}:^{16}\text{O}$ and $^{17}\text{O}:^{16}\text{O}$ in a sample vs SMOW (Coplen, 1996).

$\delta^{15}\text{N}$ and $\delta^{18}\text{O}$ in nitrate, nitrite, ammonium, DON and PON are controlled by the areas where they originated and the biogeochemical processes by which they were formed and transformed. As a result, ^{15}N is a tracer, central to study the N biogeochemistry of marine ecosystems and its alteration by anthropogenic processes (Sigman et al., 1999; Altabet, 2006; Rafter et al., 2013). The biologically mediated N transformations impact in the N isotopic composition in unique ways. These different processes leave an unalterable signature on the stable-isotopic composition of the N products and remaining substrates, adjusting the abundance of ^{15}N and ^{14}N in oceanic N relative to the atmosphere (Sigman and Casciotti, 2001; Casciotti, 2016; Marconi et al., 2017). This provides a record of the sources that sustain biological productivity in the environment, which combined with circulation and biogeochemistry, provides new insights into the rates and distribution of marine N cycle processes (Glibert et al., 1982; Casciotti, 2016; Peters et al., 2018). Nevertheless, for the resolution of the N cycle through the use of N isotopes, an

understanding of the distribution of N isotopes and the nature of isotopic fractionation is required (Altabet, 2006; Casciotti, 2016; Peters et al., 2018)

$\delta^{15}\text{N}$ and $\delta^{18}\text{O}$ values of different materials vary as a result of different reaction rates for molecules containing each type of stable isotope during chemical, physical, and biological processes. This difference is known as isotopic fractionation (Urey, 1947; Lane and Dole, 1956). Isotopic fractionation occurs during chemical reactions, when nitrogen bonds are broken or formed, and relative to the initial value, will give rise to $\delta^{15}\text{N}$ depleted or enriched products. Most of the biologically mediated reactions involve discrimination of the heavy isotope ^{15}N due to a faster kinetic reaction rate for the 'lighter' ^{14}N , and it is a key to elucidate the ecosystem patterns of $\delta^{15}\text{N}$ of the marine N cycle (Fry, 2006).

One of the first studies on the isotopic composition of N in the marine environment was carried out by Miyake et al. (1967). They defined some of the key features of oceanic $\delta^{15}\text{N}_{\text{NO}_3^-}$ patterns, with values near 5‰ in deep waters. The average of $\delta^{15}\text{N}_{\text{NO}_3^-}$ in the marine environments is 4.7‰ (Sigman et al., 2009). Compared with the substrate, the products of an enzymatic reaction are normally depleted in heavy isotopes (Mariotti et al., 1981). It occurs due to the preferential reaction of the molecules containing light isotope (Altabet, 2006; Sigman et al., 2009; Casciotti, 2016a). The mean $\delta^{15}\text{N}_{\text{NO}_3^-}$ in the ocean is controlled by the global $\delta^{15}\text{N}$ budget, while the variability of $\delta^{15}\text{N}$ in a specific region is associated to N budgets fluxes and internal N cycle of that region (Altabet, 2006; Marconi et al., 2017)

In the marine N cycle, processes related with the N_2 fixation are accompanied by a reduction of $\delta^{15}\text{N}$ values close to 1‰ (Fig. 1.8). The introduction of O atoms occurs during nitrification and it is provided mainly by ocean water and dissolved oxygen (Fig. 1.8). On the contrary, the loss of light isotopes of nitrogen through denitrification, enriches in ^{15}N the residual nitrates. At depths characterised by intense denitrification, $\delta^{15}\text{N}$ can reach values of >20‰ (Fig. 1.8), generally associated with ODZ zones (Cline and Kaplan, 1975; Kendall and Caldwell, 1998; Altabet, 2006; Casciotti, 2016).

During assimilation processes, nitrate is transformed in NH_4^+ , and the light oxygen isotope (^{16}O) is preferentially removed from the combined N pool while N is retained (Casciotti, 2016). In a second step, as a consequence of the preference of phytoplankton towards ^{14}N of NH_4^+ , there is a progressive enrichment of ^{15}N in the NO_3^- of the euphotic

zone as it is consumed (Fig. 1.8) (Casciotti et al., 2002; Granger et al., 2004, 2008, 2010; Casciotti, 2016).

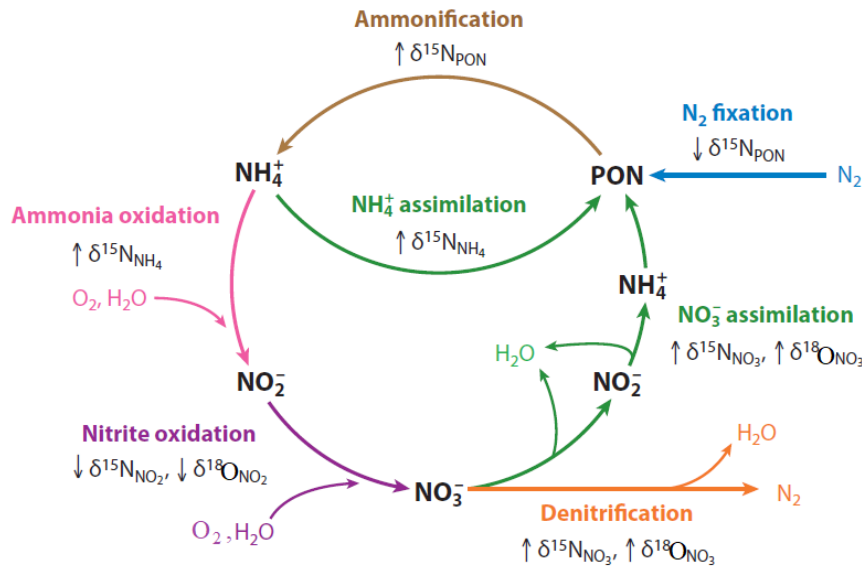


Figure 1.8. Overview of N and O fractionation processes in the microbial N cycle color-coded as in figure 1.5. The introduction of new N occurs through N_2 fixation (blue) with a low $\delta^{15}\text{N}$ value, whereas the introduction of new O from O_2 and H_2O occurs through nitrification (purple and pink arrows). The removal of both N and O occurs during denitrification (orange), whereas NO_3^- assimilation (green) removes O from the fixed N pool but retains N. Both processes increase the $\delta^{15}\text{N}$ and $\delta^{18}\text{O}$ of residual NO_3^- . (Modified from Casciotti, 2016))

The preservation of O isotopic signature in the analytic method in which NO_3^- and NO_2^- are converted to N_2O is critical. Since the combination of $\delta^{15}\text{N}$ and $\delta^{18}\text{O}$ values of nitrate and nitrite are of great interest for the interpretation of the processes in the N cycle in a specific region (such as denitrification or phytoplankton NO_3^- assimilation) (Fig. 1.8) (Sigman et al., 2009; Casciotti, 2016). Furthermore, $\delta^{15}\text{N}$ values can also be altered and controlled by water mass mixing. Mixing yields intermediate values of $\delta^{15}\text{N}$ with respect to the original constituents. Therefore, the separation of local NO_3^- isotopic signals versus those due to mixing and transport, will help to understand the N cycle and their changes on a global scale (Rafter et al., 2013; Yoshikawa et al., 2015; Rafter and Sigman, 2016; Peters et al., 2018)

1.3. The Cape-Verde Frontal Zone

1.3.1 Eastern Boundary Upwelling Ecosystems (EBUEs)

Eastern boundary upwelling ecosystems (EBUEs) comprise vast regions of the eastern margins of the Atlantic and Pacific oceans (Fig. 1.9) (Bakun, 1990; Bakun et al., 2010, 2015). They are defined by a front between coastal upwelled waters and the adjacent stratified ocean waters, regulated by equatorward coastal winds and Ekman dynamics (Mittelstaedt, 1991). Under these wind conditions, the offshore Ekman transport and upwelling of cold and nutrient-rich deep waters (Fig. 1.10) results in an intense biological activity, becoming the most productive ecosystem of the global ocean (Carr and Kearns, 2003; Chavez and Messié, 2009; Demarcq and Somoue, 2015; Pegliasco et al., 2015). In addition, the instabilities generated by the topography of the coast, the friction with the bottom and the difference of water densities, together with the Ekman mean circulation, favors the generation of mesoscale filaments and eddies near the coast that propagate towards the interior of the subtropical gyres (Morrow et al., 2004; Chaigneau et al., 2009; Lovecchio et al., 2017, 2018). The four major EBUEs are Peru-Chile and California-Oregon upwelling systems, located in the Pacific Ocean, and the Canary and Benguela upwelling systems, located in the Atlantic Ocean (Fig. 1.9) (Bakun and Nelson, 1991; Pegliasco et al., 2015).

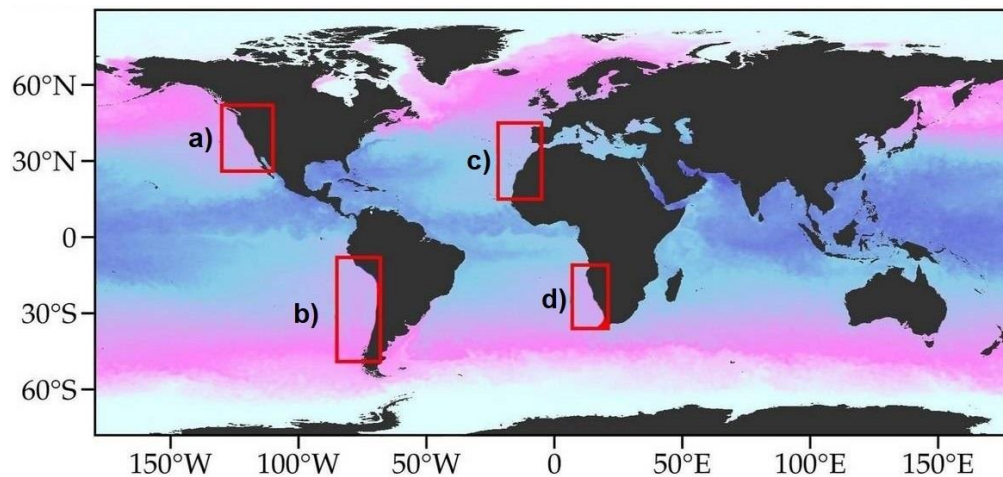


Figure 1.9. The four major EBUEs in the global ocean. The red rectangles delimit the EBUEs: California (a), Humboldt (b), Canary (c) and Benguela (d) current systems (Modified of Abrahams et al., 2021).

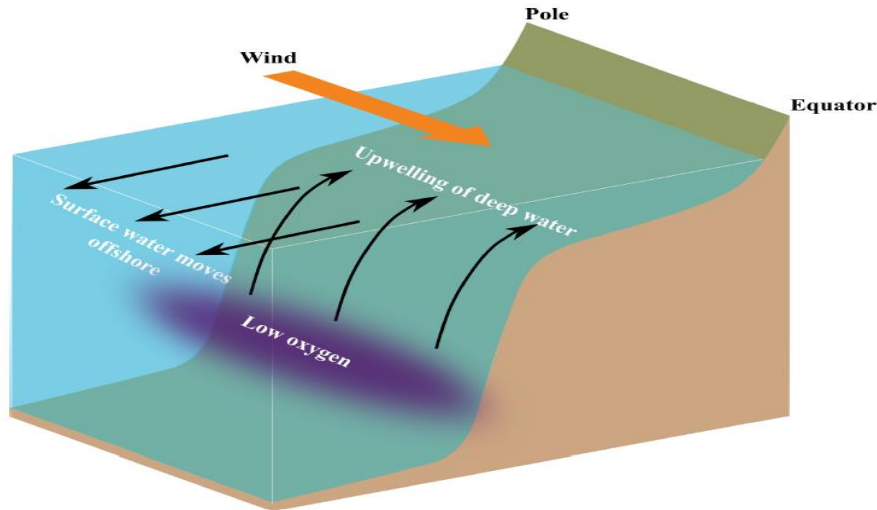


Figure 1.10. Coastal upwelling configuration, with Ekman offshore transport and upwelling of deep waters. (Taken from (Bettencourt et al., 2020)).

1.3.2 Main features of the Cape Verde Frontal Zone

The Canary Current EBUE is located at the eastern boundary of the North Atlantic, extending from the northern tip of the Iberian Peninsula at 43°N to south of Senegal at about 10°N (Arístegui et al., 2004). Due to the trade wind patterns, the Canary Current EBUE has year-round upwelling, except in the Iberian margin where upwelling occurs seasonally (Arístegui et al., 2004; Benazzouz et al., 2014; Faye et al., 2015). The strong short-time scale variability of trade winds, makes primary productivity especially spatial and seasonally variable (Carr and Kearns, 2003; Auger et al., 2016).

The Cape Verde Frontal Zone (CVFZ) is a highly dynamic region located in the southern boundary of the Canary Current EBUE, and may be divided in two major domains formed by surface and upper-thermocline waters subducted at higher latitudes of both Atlantic hemispheres: The South-eastern boundary of the North Atlantic subtropical gyre (NASG) and the North-eastern North Atlantic tropical gyre (NATG) (Fig. 1.11) (Pelegrí and Peña-Izquierdo, 2015). The anticyclonic NASG, comprises the Azores Current (AC), the Canary Current (CC) and Canary Upwelling Current (CUC) flowing southward (Fig. 1.11); while in the cyclonic NATG are present the eastward North Equatorial Counter Current (NECC) and the Cape Verde Current (CVC), which turn west south of the Cape Verde Front around the Guinea Dome, and Mauritanian Current (MC) which flows northward as a Poleward Under Current (PUC) (Fig. 1.11) (Klein and Siedler, 1989; Pelegrí

and Peña-Izquierdo, 2015; Pelegrí et al., 2017). Furthermore, the eastern margins of both gyres constitute the boundary current system of North-West Africa (NWA) (Pelegrí and Peña-Izquierdo, 2015).

The Cape Verde Front (CVF), was defined by Zenk et al. (1991) as the intersection of the 36 isohaline at 150 dbar depth, and separates the eastern margins of the subtropical and tropical Atlantic and associated water masses. Recently, Burgoa et al. (2021) extended this definition vertically and established an equation which define the front location at any depth from 100 to 650 dbar, based on an equal contribution (50%) of NACW and SACW. The interaction of the CVF and the Mauritanian coastal upwelling, makes the CVFZ mesoscale activity particularly intense (Lovecchio et al., 2018).

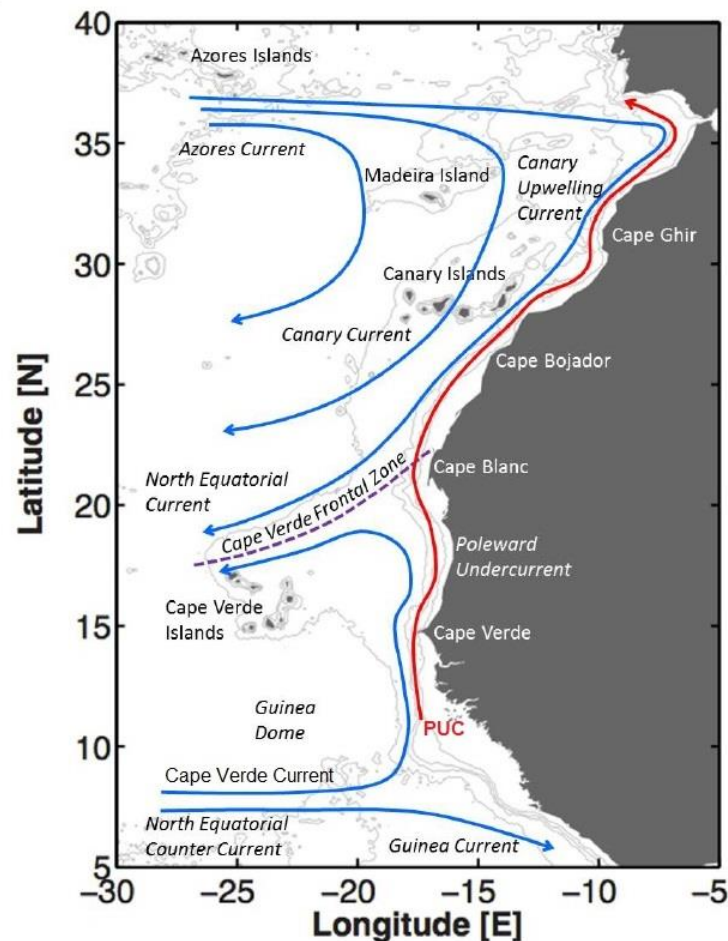


Figure 1.11. Map of the main features and mean oceanographic currents in the Canary Current Large Marine Ecosystem (CCLME) which coincides with the CC EBUE (Modified from Pelegrí and Peña Izquierdo, 2015)

In addition, the along-shore convergence produced by the confluence of south and northward currents along the CVF drives chlorophyll- and nutrient-rich waters, coming from the tropical gyre and the coastal upwelling region, into the south-eastern edge of the subtropical gyre. This favors the horizontal transport from the coast, and contributing to develop the Cape Blanc Giant Filament (CBGF) (21°N) (Pelegrí and Peña-Izquierdo, 2015). This shallow mesoscale structure can be seen in color satellite images and is associated with the offshore transport of upwelled waters. Around some prominent capes of the African coast, these filaments are able to extend offshore from 100-1000 km, exporting large amount of OM (Van Camp et al., 1991; Gabric et al., 1993; Helmke et al., 2005; Pelegrí et al., 2005; Álvarez-Salgado et al., 2007; Arístegui et al., 2009; Pastor et al., 2012; Álvarez-Salgado and Arístegui, 2015; Ohde et al., 2015; Sangrà, 2015). Upwelling filaments affect the distributions of OM (Fig. 1.12) in the sense that suspended POM and DOM are mainly exported horizontally offshore by the filament, while large fast-sinking POM settles over the continental shelf and slope (Álvarez-Salgado and Arístegui, 2015).

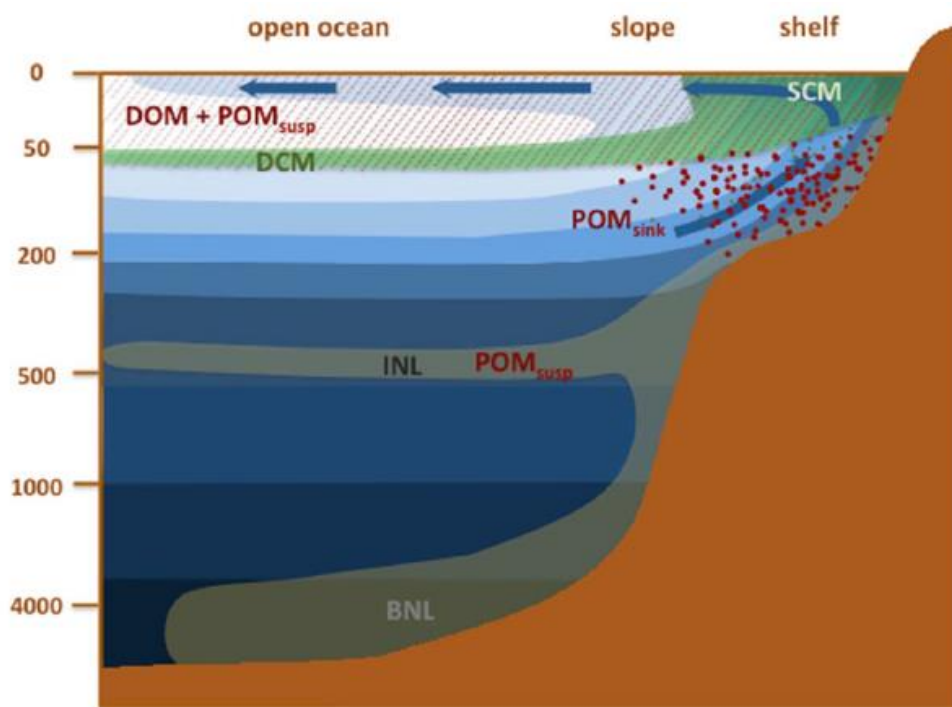


Figure 1.12. Schematic off-shelf export of dissolved (DOM), suspended POM (POM_{susp}) and sinking POM (POM_{sink}) organic matter by cold upwelling filaments and by intermediate (INL) and bottom (BNL) nepheloid layers in the Canary Current Large Marine Ecosystem (CCLME). The water temperature is represented by dark (colder) to light (warmer) blue. The blue arrows represent the uplift onto the shelf and offshore transport of cold upwelled water. Green shadow corresponds to the chlorophyll evolution distribution from a surface maximum (SCM) to a deep maximum (DCM) in the open ocean. oblique stripers, represent the DOM and POM_{susp} transported by the filament; The solid circles represent POM_{sink} over the shelf; grey shades, intermediate (INL) and bottom (BNL) nepheloid layers (Taken from Álvarez-Salgado and Arístegui, 2015).

1.3.3 Water masses of the Cape Verde Frontal Zone

Water masses of different origin converge in the CVFZ. Between 100 and 700 dbar, there are different central water masses such as the Madeira Mode Water (MMW), the Eastern North Atlantic Central Water (ENACW) and South Atlantic Central Water (SACW). ENACW converges with SACW, which is characterized by higher nutrient concentration and lower temperature, salinity and dissolved oxygen concentration than ENACW (Fig. 1.13) (Zenk et al., 1991; Pastor et al., 2015). At the CVF, due to the different characteristics of ENACW and SACW, intense interleaving occurs, as well as formation of meanders and eddies (Barton et al., 1998; Pérez-Rodríguez et al., 2001; Martínez-Marrero et al., 2008; Meunier et al., 2012; Alpers et al., 2013; Pastor et al., 2015; Barceló-Llull et al., 2017). The layer from 700 to 1500 dbar is occupied by the intermediate Subpolar Mode Water (SPMW), Antarctic Intermediate Water (AA) and the warmer and saltier Mediterranean Water (MW) (Bower et al., 2002; Machín and Pelegrí, 2009; Pastor et al., 2015; Jerusalén-Lleó et al., 2023). Finally, the Labrador Sea Water (LSW) and upper and lower North East Atlantic Deep Water (NEADW) occupy depths below 1500 dbar (Pérez-Rodríguez et al., 2001; Lønborg and Álvarez-Salgado, 2014; Pastor et al., 2015; Jerusalén-Lleó et al., 2023).

The North Atlantic subducting zone constitute the formation area of the ENACW, which is transported by the Portugal, Azores and Canary currents in the anticyclonic circulation of the North Atlantic subtropical gyre, to the Canary Current EBUE region (Fig. 1.13) (Sarmiento and Bryan, 1982; Pastor et al., 2015). On the contrary, the source of SACW is the subducting regions of the South Atlantic subtropical gyre, and is distributed to the tropical and equatorial upper ocean from the equatorial current system (Fig. 1.13) (Stramma and Schott, 1999; Pastor et al., 2015).

The low salinity AA is formed in the Sub-Antarctic region and is transported to the North Atlantic by the South Atlantic and South Equatorial currents and the equatorial currents system from the Subantarctic front to the CVFZ (Machín and Pelegrí, 2009; Pastor et al., 2015). SPMW originates in the eastern Subpolar gyre of the North Atlantic by the mixing of near-surface waters (Pérez-Rodríguez et al., 2001; Jerusalén-Lleó et al., 2023). The high salinity MW is formed in the Mediterranean Sea and flows into the Atlantic Ocean through the bottom of the Strait of Gibraltar. This MW mixes intensely with ENACW and then spreads along the Atlantic at about 1200 dbar (Fig. 1.13) (Bower et al., 2002; Pastor

et al., 2015). The MW has a higher dissolved oxygen concentration than AA while the latter is relatively rich in nutrients, particularly silicate (Peña-Izquierdo et al., 2012).

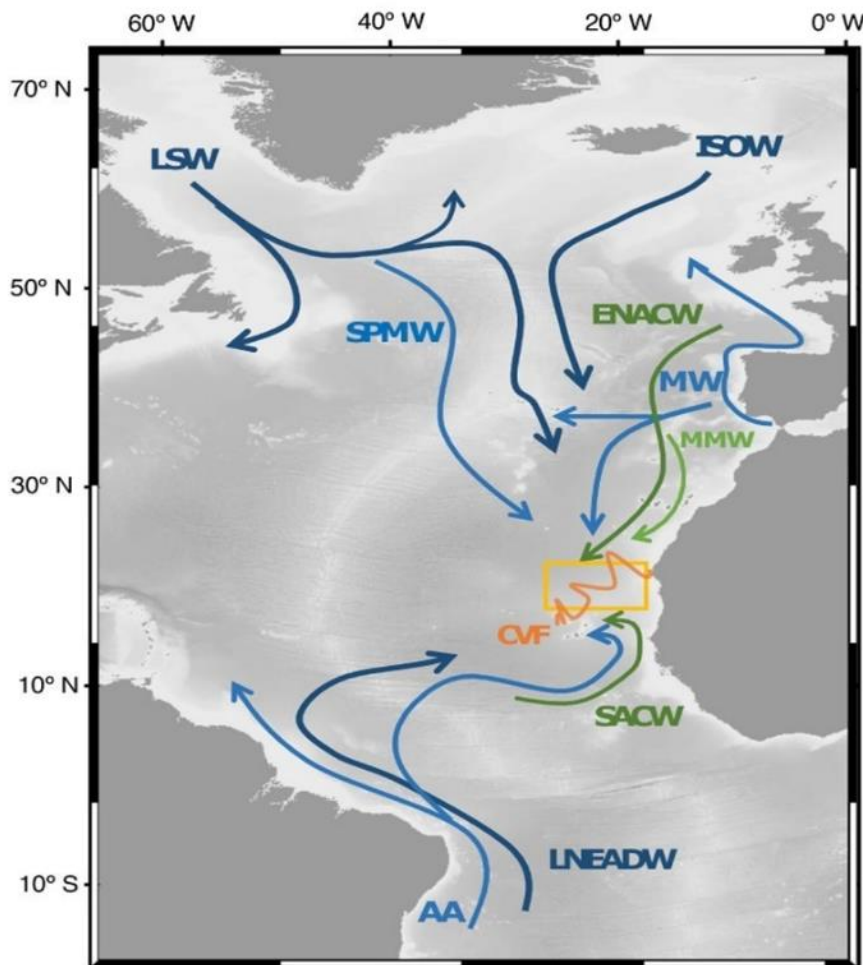


Figure 1.13. Main water masses present in the CVFZ. Arrows indicate the direction from its formation areas, corresponding to: Labrador Sea Water (LSW), Iceland Scotland Overflow Water (ISOW), Subpolar Mode Water (SPMW), Eastern North Atlantic Central Water (ENACW), Mediterranean Water (MW), Madeira Mode Water (MMW), Southern Atlantic Central Water (SACW), Antarctic Intermediate Water (AA) and Lower North East Atlantic Deep Water (LNEADW). The thickness and the color of the arrows indicate the bathymetric layer of each water mass. MMW: light green thin lines. Central waters: dark green thin lines. Intermediate waters: light blue thick lines. Deep waters: thicker dark blue lines. The yellow square represents the study area and the orange zigzag line is the position of the CVF at the time of sampling (taken from Burgoa et al., 2020) (Figure Taken of Jerusalén-Lleó et al., 2023).

LSW is formed in the central Labrador Sea by deep convection, spreading eastwards into the eastern North Atlantic, and south-eastwards with the deep western boundary current (Fig. 1.13) (Talley and McCartney, 1982; Sy et al., 1997; Jerusalén-Lleó et al., 2023). ENADW is a mixture between Iceland Scotland Overflow Water (ISOW), Labrador Sea Water (LSW) and Lower Deep Water (McCartney, 1992; Van Aken, 2000; Pastor et

al., 2015). It is classified into Upper and Lower North East Atlantic Deep Water (UNEADW and LNEADW). UNEADW, characterized by its high salinity, is composed mainly of ISOW with LSW and MW (Pérez-Rodríguez et al., 2001; Lønborg and Álvarez-Salgado, 2014) and LNEADW is characterized by high oxygen concentration and results from the mixing of ISOW and Antarctic Bottom Water (AABW) (Fig. 1.13) (Pérez-Rodríguez et al., 2001; Lønborg and Álvarez-Salgado, 2014).

1.3.4 Inorganic and organic N in the CVFZ

The CVFZ present a high physical and biogeochemical variability due to the confluence of water masses of different origin and ageing. These water masses had differences in nutrients and dissolved oxygen concentration. This makes the exchange of inorganic N nutrients and organic N particularly intense (Barth et al., 2002; Pelegrí et al., 2005; Benítez-Barrios et al., 2011) and affects to the metabolic balance of surface plankton communities (Álvarez-Salgado et al., 2001). In the CVFZ nutrient distributions are controlled by the cyclonic and anticyclonic gyres and by coastal upwelling. Upwelling systems supply nutrient-rich waters to the surface with a proportional enrichment of the essential nutrient concentrations that will be used by the phytoplankton in the form of nitrate, phosphate and silicate (Pelegrí and Benazzouz, 2015; Pelegrí and Peña-Izquierdo, 2015). These physical forcing with the large gradients in inorganic nutrients and dissolved oxygen present in the CVFZ constitutes the dynamic of inorganic N nutrients and organic N exports from the coastal margin (Helmke et al., 2005; Muller-Karger et al., 2005). The typical nutrient concentration observed in upwelled waters of NW Africa are summarize in Table 1.1.

Table 1.1. Nutrient concentrations (in $\mu\text{mol kg}^{-1}$) observed in waters upwelled in the NW Africa upwelling systems. (Aristegui et al., 2009)

	Latitude	T (°C)	NO_3^-	PO_4^{2-}	SiO_2	Upwelled Water
Cape Timiris-Nouakchott	~19° N	14	20	1.5	10	SACW
Cape Blanc- Cape Corveiro	~20° N	15.5	14-15.5	0.9-1	6.5-7.5	ENACW/SACW
Cape Sim, Cape Guir	~31° N	14.5	8-9	0.6-0.7	4-5	ENACW

Off Cape Blanc (at about 21°N), Von Appen et al. (2020) found very low nitrate concentration ($0.01 \mu\text{mol kg}^{-1}$) in the upper layer, but at 20.9°N they found significant

amounts (up to $5 \mu\text{mol kg}^{-1}$). In contrast, just below 100 dbar, especially in the southern part of the region of the northwest African upwelling system, they found high nitrate concentrations values ($20 \mu\text{mol kg}^{-1}$). They suggested that the spatial distribution of these nitrate values reflected the CBGF which came from the coast, which is cool and fresh and still had non-zero nitrate values in the mixed layer. In addition, they found phosphate ($0.06\text{--}0.31 \mu\text{mol kg}^{-1}$) and silicate ($1\text{--}2 \mu\text{mol kg}^{-1}$) concentrations in the upper mixed layer in line with the estimation by Bachmann et al. (2018) that phosphate and silicate are not thought to be the limiting nutrients in this region.

Concerning Organic matter, the sinking fraction of POM has been thoroughly studied at the CVFZ using sediments traps. Nowald et al. (2006), found maximum POM fluxes at around 200 dbar close to the coast, and at 400 dbar further offshore, likely due the lateral export by the CBGF. Schneider et al. (2003) found that even for large POM fluxes, $> 150 \text{ mg m}^{-2} \text{ d}^{-1}$, in the Northwest Africa upwelling region the average C:N molar ratio is 8.1, which was significantly higher than canonical Redfield's value of 6.7. Nowald et al. (2015) showed that the deposition of Sahara dust had an important impact on the dynamics of sinking POM due to their role in the aggregation of particles, indicating a close and fast coupling between dust input and sedimentation of the material. These observations have also been reported by other authors (Arístegui et al., 2004; Helmke et al., 2005; Fischer and Karakaş, 2009; Fischer et al., 2009; Iversen et al., 2010; Martiny et al., 2013; Martiny et al., 2013; Fischer et al., 2016, 2019; van der Jagt et al., 2018; Sanchez-Vidal et al., 2020). However, at the CVFZ there is a lack of information on suspended POM and DOM distributions and their C:N ratios, which will be ameliorated in this PhD thesis.

1.4. The project FLUXES

The project “Constraining organic carbon fluxes in an Eastern Boundary Upwelling system (Cape Blanc; NW Africa): role of non-sinking carbon in the context of the biological pump” (FLUXES, CTM2015-69392-C31, -C32, -C33), is a multidisciplinary effort, that encompasses physics, biogeochemistry and microbiology. In fact, the project was divided in three subprojects, which are deeply interconnected to produce a truly multidisciplinary study.

The first subproject “Constraining organic carbon fluxes in an Eastern Boundary Upwelling system (Cape Blanc; NW Africa): the role of non-sinking carbon in the context of the biological pump” is focused on the estimation of primary production, plankton community structure, biomass and metabolism, “active” and “gravitational” carbon fluxes and its association to the lithogenic ballast component.

The second subproject “Constraining organic carbon fluxes in an Eastern Boundary Upwelling system (Cape Blanc; NW Africa): submesoscale modulation of carbon production, export and consumption” is focused on describing large-, meso- and submeso-scale variability of the CVFZ and estimating carbon fluxes mediated by physical processes.

The third subproject, in which this PhD thesis is embedded, “Constraining organic carbon fluxes in an Eastern Boundary Upwelling system (Cape Blanc; NW Africa): elemental, optical, isotopic and molecular characterization” is focused on the study of the origin, fate and dynamics of inorganic nutrients and non-sinking organic matter (dissolved and particulate) in the CVFZ. Particularly, this PhD thesis is focused on inorganic and dissolved and particulate organic nitrogen.

The field work of FLUXES consisted of two cruises. The First cruise (Fig. 1.14), FLUXES I, in August 2017, consisted of four transects defining a box embracing the CVFZ (17°-23°N, 17°-26°W), which included 35 hydrographic stations 50 nautical miles apart. Three types of stations were occupied during FLUXES I: short (nocturnal), medium (diurnal) and long (full day), which lasted 3, 9 and 27 hours, respectively. Medium and long stations were sampled from the surface to 4000 dbar, whereas short stations were sampled down to 2000 dbar. The second cruise (Fig. 1.14), FLUXES II, in November 2017, consisted on two main activities. On the one hand, two SeaSoar grids for high-resolution characterization of the CVFZ and, on the other hand, two biogeochemical transects at high spatial resolution (5 NM). In the biogeochemical transects a total of 48 hydrographic stations were sampled from surface to 1500 dbar (Fig. 1.14). The first transect was made of 36 stations along 175 NM (324 km), while the remaining twelve stations were occupied during a second transect of 55 NM (102 km) perpendicular to the first one. Water samples were taken at each hydrographic station from a rosette equipped with 24 Niskin bottles, a conductivity, temperature and depth (CTD) probe, and sensors for dissolved oxygen, fluorescence of chlorophyll, turbidity, transmittance and nitrate, vessel-mounted Acoustic Doppler Current Profiler (ADCP) and turbulence data from a Turbomap. In addition, in

FLUXES I, a Marine Snow Catcher of 100 L was used to separate particles based on their sedimentation rates. From the view point of this PhD thesis, the aim of both cruises was to collect data to study the distributions of inorganic and organic (dissolved and particulate) nitrogen species at the large scale (30 NM) in FLUXES I and at meso- and submesoscale (5NM) during FLUXES II.

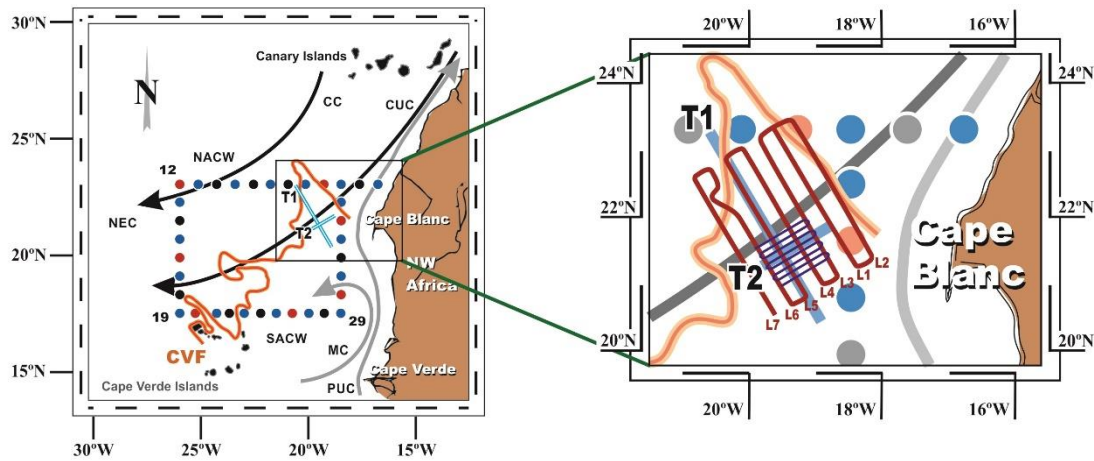


Figure 1.14. Map of the FLUXES I and II cruises. Dots represent the sampling stations. The box with dots in blue (diurnal stations), black (nocturnal stations) and red (long stations) correspond to the FLUXES I cruise; the numbers indicate the station number, from 1 to 35. The lines in cyan represent biogeochemical transects in FLUXES II cruise (T1 and T2). The blue and red lines in the square on the right, represent the Seasoar grids. The main geographic and oceanographic features and currents are represented. The black arrows correspond to the Canary Current (CC), Canary Upwelling Current (CUC) and North Equatorial Current (NEC), the grey arrows to the Mauritania Current (MC) and the Poleward Undercurrent (PUC) (taken from Pelegrí and Peña-Izquierdo, 2015). The orange line represents the approximate position of the CVF during the FLUXES I cruise (taken from Burgoa et al., 2021).

1.5. Aims of this PhD thesis

The overarching hypothesis of this PhD thesis is that the main hydrographic features at large-, meso- and submeso-scale present at the CVFZ dictate the distribution of organic and inorganic N forms in the region, with profound implications for dark-ocean remineralization and biological pump efficiency.

The general objective of this PhD thesis is to characterize elemental and isotopically the inorganic and organic (dissolved and suspended) N pools in the CVFZ in relation to the main hydrographic features of the study area (CVF, filaments, meanders, eddies, ...), the variety of water masses of contrasting origin that converge in the CVFZ, and the biogeochemical processes that take place in this transitional zone between the productive

Mauritanian upwelling and the oligotrophic adjacent ocean. This general objective has been divided into the following specific objectives:

- Study the influence of the CVF on the inorganic and organic, dissolved and particulate, N pools, and quantify the contribution of the organic N pools to water column remineralisation in the dark ocean of the CVFZ at the large/regional scale.
- Assess the impact of meso- and submeso-scale structures (meanders, eddies, filaments) on N distributions in the CVFZ, through the study of dissolved inorganic nitrogen and dissolved and suspended fractions of organic nitrogen in the CVFZ, and the O₂:C:N:P stoichiometry for inorganic nitrogen and C:N ratios for organic nitrogen.
- Assess the origin and biogeochemical transformations of nitrate (NO₃⁻) through their isotopic signatures of oxygen ($\delta^{18}\text{O}$) and nitrogen ($\delta^{15}\text{N}$).

1.6. Structure of this PhD thesis

This PhD thesis consists of 6 chapters. The first chapter includes a general introduction and presents the aims and structure of the thesis. In the second chapter, the large-scale dynamics of the dissolved inorganic and organic N and -O₂:C:N:P ratios relating them to the position of the CVF, were analysed, in epi, meso- and bathypelagic layers, in the CVFZ in August of 2017. The third chapter deals with the influence of meso- and submeso-scale structures on N species distribution in the CVFZ in November 2017. In the fourth chapter, the isotopic signatures of oxygen ($\delta^{18}\text{O}$) and nitrogen ($\delta^{15}\text{N}$) in nitrate are examined for the two cruises. Chapter 5 includes a general discussion and Chapter 6 the conclusions of the PhD thesis.

Chapter 2

**Large-scale variability of nitrogen species in
the Cape Verde Frontal Zone (NW Africa)**

The research work presented in this chapter is also a contribution to the paper published in Progress in Oceanography:

Valiente, S Fernández-Castro, B Campanero, R., Marrero-Díaz, Á., Rodríguez-Santana, Á., Gelado-Caballero, M.D., Nieto-Cid, M., Delgado-Huertas, A., Arístegui, J., Álvarez-Salgado, X.A., 2022. Dissolved and suspended organic matter dynamics in the Cape Verde Frontal Zone (NW Africa). *Progress in Oceanography*, doi: 10.1016/j.pocean.2021.102727

Abstract

In this chapter we study the role of dissolved inorganic and organic nitrogen species in the biogeochemistry of the highly dynamic Cape Verde Frontal Zone (CVFZ), located at the southern end of the Eastern Boundary Upwelling Ecosystem of the Canary current. This area is characterized by large vertical and horizontal export fluxes of organic matter and inorganic nutrients, due to the interaction of the Cape Verde Front (CVF) with the Mauritanian coastal upwelling. While the flux, composition and biogeochemical role of sinking organic matter have been thoroughly studied in the area, much less attention has been paid to the dissolved (DOM) and suspended particulate (POM) organic matter pools and particularly to dissolved (DON) and suspended organic nitrogen (PON). Full-depth profiles of inorganic nutrients, DOM and POM were sampled during an oceanographic cruise in the CVFZ, with four consecutive transects defining a box embracing the Cape Blanc giant filament and the CVF. The distributions of inorganic and organic nitrogen, and the stoichiometry of organic matter in the epipelagic layer were strongly influenced by the position of the transects relative to the giant filament and the front. Geographical heterogeneity in DON and PON distributions and their stoichiometry were also observed within each of the different water masses of contrasting origin present in the study area (North and South Atlantic Central Water, Subpolar Mode Water, Mediterranean Water, Antarctic Intermediate Water, Labrador Sea Water and North East Atlantic Deep Water). These facts suggest that water mass properties are re-shaped by transport and biogeochemical processes occurring within the CVFZ. Nevertheless, our analysis indicates that DON and PON have a minor impact on local mineralisation processes, representing only about 18% of the local nitrate production. Intense lateral export of POM and DOM out of the boundaries of the CVFZ is the likely reason behind these low contributions, which confirm the prominent role of sinking organic matter to mineralisation processes in this region. Remarkably, DOM distributions in the CVFZ are apparently affected by the dissolution/desorption from fast sinking particles ballasted with Sahara dust.

2.1 Introduction

The Eastern Boundary Upwelling Ecosystem (EBUE) associated with the Canary Current extends from the northern tip of the Iberian Peninsula at 43°N to South of Senegal at about 10°N (Arístegui et al., 2009). The intensity and persistence of upwelling-favorable winds increase with decreasing latitude, evolving from weak and seasonal to the North to strong and year-round to the South. The Canary Current EBUE is also characterized by an intense mesoscale activity in the form of upwelling filaments associated with prominent capes (Álvarez-Salgado et al., 2007; Lovecchio et al., 2018; Santana-Falcón et al., 2020) and island eddies (Barton et al., 1998; Sangrà et al., 2009; Cardoso et al., 2020). These mesoscale structures may export large amounts of inorganic nitrogen and organic matter produced over the shelf several hundreds of kilometres offshore (Gabric et al., 1993; Ohde et al., 2015; Lovecchio et al., 2018). Mesoscale activity is particularly intense in the southern boundary of the Canary Current EBUE due to the confluence of the Mauritanian upwelling and the Cape Verde Front (CVF). The CVF separates the eastern margins of the subtropical and tropical Atlantic regimes (Pelegrí and Peña-Izquierdo, 2015) and favors the horizontal transport from the coast, contributing to develop the Cape Blanc Giant Filament (CBGF) (21°N). This structure exports offshore massive amounts of biogenic organic matter produced in the Mauritanian coast (Van Camp et al., 1991; Gabric et al., 1993). At the CVF, Eastern North Atlantic Central Water (ENACW) encounters the slightly cooler, less saline, nutrient-rich and oxygen-poorer South Atlantic Central Water (SACW) (Zenk et al., 1991). In the frontal region, intense interleaving between the two water masses occurs (Pérez-Rodríguez et al., 2001; Martínez-Marrero et al., 2008), as well as the recurrent formation of meanders and eddies (Barton et al., 1998; Meunier et al., 2012; Alpers et al., 2013; Barceló-Llull et al., 2017).

Upwelling filaments, meandering fronts and eddies affect the metabolic balance and distribution of surface plankton communities in the Cape Verde Frontal Zone (CVFZ) (Olivar et al., 2016; Tiedemann et al., 2018; Arístegui et al., 2020). The CVFZ is characterized by the lateral export of organic matter from the coast to the open ocean not only in the surface nepheloid layer (SNL) but also in intermediate (INL) and bottom (BNL) nepheloid layers (Karakaş et al., 2006; Nowald et al., 2006; Fischer et al., 2009), which affects carbon fluxes in the adjacent deep ocean waters (Alonso-González et al., 2009; Arístegui et al., 2020).

The organic matter transported by these structures is dominated by slow sinking (hereby named “suspended”) particulate (POM) or dissolved (DOM) forms, while fast sinking POM (generally $>100\ \mu\text{m}$) is less susceptible to horizontal advection (Álvarez-Salgado and Arístegui, 2015). Differentiation between DOM, suspended and sinking POM is of fundamental importance. Information on the elemental composition of DOM, and suspended and sinking POM is crucial to understand the contrasting contribution of the three organic matter pools to the respiration in the ocean interior, which dictates the efficiency and magnitude of the biological carbon pump (Verdugo et al., 2004; Hopkinson and Vallino, 2005; Boyd et al., 2019).

While an important effort has been made to characterize the origin, elemental composition and fluxes of sinking POM in the CVFZ (Helmke et al., 2005; Iversen et al., 2010; Álvarez-Salgado and Arístegui, 2015 and references therein; Fischer et al., 2019), the suspended POM and DOM fractions have received much less attention (Alonso-González et al., 2009; Arístegui et al., 2020; Burgoa et al., 2020). The aim of this work is to study the dynamics of the dissolved inorganic nitrogen and dissolved and suspended organic nitrogen in the CVFZ, and quantify the contribution of these pools to the water column remineralisation in the dark ocean. Full-depth profiles of the dissolved inorganic nitrogen and organic nitrogen content of DOM and suspended POM were obtained in a box (17-23°N, 17-26°W) that embraced the CBGF and the CVF. Differences in dissolved inorganic nitrogen and dissolved (DON) and suspended particulate organic nitrogen (PON) stocks and their relative contribution to dissolved oxygen consumption and nitrate mineralisation between transects (Northern, NACW domain; Southern, SACW domain; Eastern, Coastal Transition Zone domain; and Western, open ocean domain) are examined for the surface, central, intermediate and deep water masses present in the study area.

2.2 Materials and Methods

2.2.1 Sampling strategy

The FLUXES I cruise (R/V Sarmiento de Gamboa; Las Palmas - Las Palmas, 12 July to 9 August 2017) consisted of four transects (Northern, Western, Southern and Eastern) defining a box crossing the CVFZ, including 35 hydrographic stations 50 nautical miles apart (Fig. 2.1). Three types of stations were occupied: short (nocturnal), medium (diurnal) and long (full day), which lasted 3, 9 and 27 hours, respectively (Fig. 2.1). Medium and long stations were sampled from the surface to 4000 dbar, whereas short stations were

sampled down to 2000 dbar. A rosette sampler carrying 24 Niskin bottles of 12 L was used. It was equipped with a conductivity, temperature and depth (CTD) probe (SeaBird SBE911 plus), and sensors for dissolved oxygen (SeaBird SBE43), fluorescence of chlorophyll (SeaPoint SCF), and turbidity (SeaPoint STM). Sampling depths were selected based on the continuous records of the sensors attached to the rosette. Fifteen levels were sampled in medium and long stations (down to 4000 dbar) and 10 levels in short stations (down to 2000 dbar).

CTD conductivity was calibrated with water samples taken from the rosette and analysed on board with a Guildline 8410-A Portasal salinometer. Samples for dissolved oxygen (O_2) determination were analysed on board by the Winkler potentiometric method following the procedure described by Langdon (2010). The apparent oxygen utilization (AOU) was calculated with the equation of Benson and Krause, $AOU = O_{2sat} - O_2$ (UNESCO, 1986), where O_{2sat} is the dissolved oxygen saturation. The fluorescence of chlorophyll (Chl) sensor was calibrated with water samples taken at 4 depths in the photic layer at each medium and long stations, where 500 mL of water was filtered and phytoplankton cells concentrated on 25 mm GF/F filters for chlorophyll a determination. Pigments were extracted with 10 mL of 90% acetone at 4°C in the dark for 24 h. The extracts were estimated fluorometrically by means of a Turner Designs bench fluorometer 10-AU, previously calibrated with pure chlorophyll a (Sigma Co.), as described in Holm-Hansen et al. (1965).

Water samples for the determination of inorganic nutrient concentrations were taken directly from the Niskin bottles in 25 mL polyethylene vials that were frozen at -20°C until analysis in the base laboratory. A similar procedure was followed for dissolved organic carbon / total dissolved nitrogen (DOC : TDN) samples, which were collected in 30 mL amber glass vials with Teflon stoppers. Although these samples were not filtered, they will be named as DOC and TDN, because they mainly represent DOM due to the low concentrations of POM in oceanic waters. For the analysis of the concentration of particulate organic carbon and nitrogen (POC and PON), 2 to 5 L of water were filtered onto pre-combusted (450°C, 4 hours) 25 mm Whatman GF/F filters in a filtration system with a mild vacuum (pressure difference <300 mm Hg). Filters were transferred to 2 mL Eppendorf vials and dried for 12 hours in a vacuum desiccator with silica gel. After drying, they were frozen at -20°C until analysis in the base laboratory. Dissolved oxygen, inorganic nutrients, DOC:TDN and POC:PON were collected at all stations and all sampling depths.

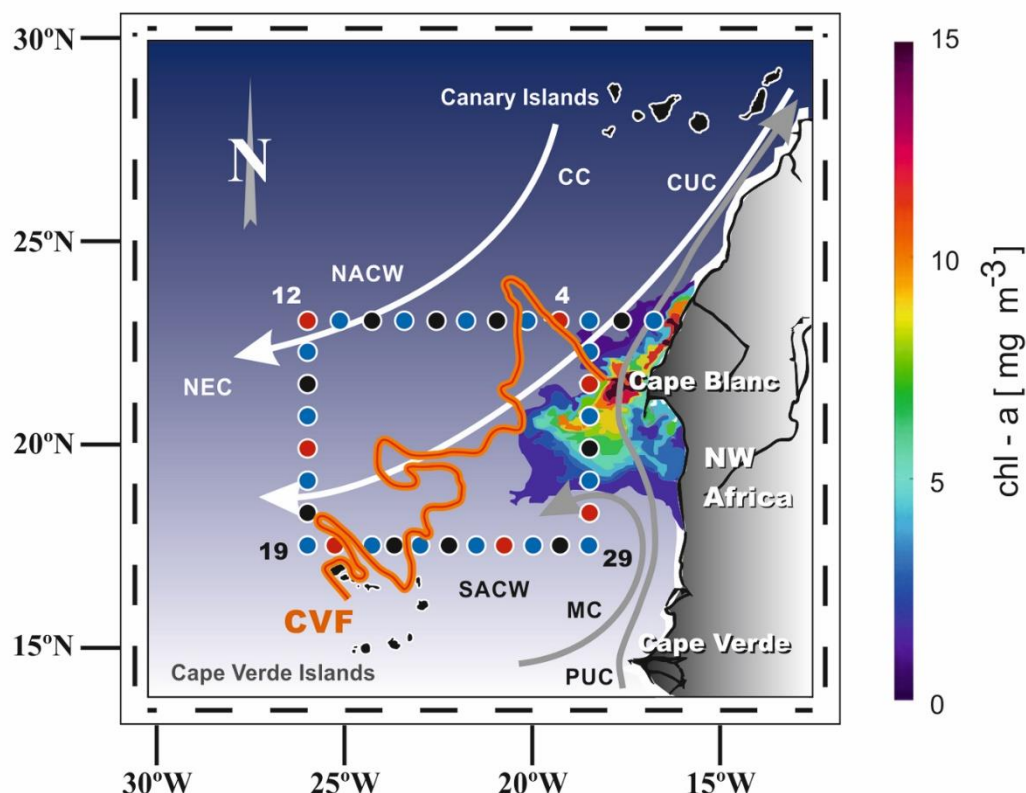


Figure 2.1. Map of the FLUXES I cruise. The dots represent the stations (blue: diurnal stations; black: nocturnal stations; red: long stations) the numbers indicate the station number, from 1 to 35. The main geographic and oceanographic features and currents are represented. White arrows correspond to the Canary Current (CC), Canary Upwelling Current (CUC) and North Equatorial Current (NEC), the grey arrows to the Mauritania Current (MC) and the Poleward Undercurrent (PUC) (taken from Pelegrí and Peña-Izquierdo, 2015). The orange line represents the approximate position of the CVF during the cruise (taken from Burgoa et al., 2021), and the colour contours near the coast represent the satellite chlorophyll *a* associated with the Cape Blanc filament on 24/07/2017 (from Copernicus Marine Service).

2.2.2 Analytical determination

Micromolar concentrations of nutrient salts (nitrate, nitrite, ammonium, phosphate and silicate) were determined simultaneously by segmented flow analysis in an Alliance Futura autoanalyser following the methods of Hansen and Koroleff (1999) except for the case of ammonium, which was measured by the fluorometric method of Kérouel and Aminot (1997). Frozen samples were gently melted in the dark overnight and vigorously shaken before analytical determination.

The determination of POC and PON in 25 mm GF/F filters was carried out by high temperature catalytic oxidation at 900°C in a Perkin Elmer 2400 elemental analyser. At two selected stations, one from the Eastern (coastal) and one from the Western (open ocean)

transects, the filters were divided into two parts; one part was measured directly and the other part was exposed to HCl fumes for 24 hours to remove CaCO_3 before determination. After checking that CaCO_3 represented <10% of carbon in these filters, the rest of the filters were analysed directly. Therefore, although we have measured total carbon, we will refer to these measurements as POC because of the low levels of CaCO_3 .

DOC and TDN were analysed by high temperature catalytic oxidation at 680°C with a Shimadzu TOC-V analyser connected in line with a TNM1 measuring unit. After melting, the samples were acidified to pH <2 and degassed with high purity N_2 to eliminate the CO_2 before measurement. Aliquots of 150 μL were injected in the analyser. Measurements were made in triplicate to quintuplicate. The accuracy was checked daily with the DOC:TDN reference materials (CRM) provided by D.A. Hansell (University of Miami, USA). Measured concentrations of the CRM were $44.9 \pm 1.7 \mu\text{mol C L}^{-1}$ ($n = 10$) and $31.7 \pm 1.4 \mu\text{mol N L}^{-1}$ ($n = 10$); the certified values are 43–45 $\mu\text{mol C L}^{-1}$ and 32–33 $\mu\text{mol N L}^{-1}$ (DSW Batch 16–2016*Lot 05-16). DON concentrations were calculated as $\text{DON} = \text{TDN} - \text{DIN}$ where DIN is the dissolved inorganic nitrogen (nitrate + nitrite + ammonium).

2.2.3 Water mass analysis

An optimum multiparameter (OMP) inverse method (Karstensen and Tomczak, 1998) has been used for the quantification of the water types (WTs) that contribute to the water samples collected in the CVFZ during FLUXES I. A water type (WT) is a body of water formed in a particular region of the ocean with certain thermohaline and chemical properties (Tomczak, 1999).

In our OMP, the variables used to define the WTs were potential temperature (θ), salinity (S), silicate (SiO_4H_4) and the conservative chemical parameter NO ($\text{NO} = \text{O}_2 + R_N \cdot \text{NO}_3^-$) (Broecker, 1974) where R_N was set to a constant value of 9.3 $\text{mol O}_2 \text{ mol NO}_3^{-1}$ (Anderson, 1995), and represents the Redfield ratio of dissolved oxygen consumption to nitrate production during the mineralisation of biogenic organic matter in the ocean. We identified 11 WT in the CVFZ: Madeira Mode Water (MMW); Eastern North Atlantic Central Water (ENACW) of 15°C and 12°C; South Atlantic Central Water of 18°C and 12°C; Subpolar Mode Water (SPMW); Antarctic Intermediate Water (AA); Mediterranean Water (MW); Labrador Sea Water (LSW); and upper and lower North East Atlantic Deep Water

Chapter 2:

(NEADW). The in-situ values of θ , S , SiO_4H_4 and NO from the rosette sampler collected during the cruise were used to calculate the contribution of each WT to every sample, by solving this set of mass balance equations per sample:

$$\begin{aligned}\sum_i X_{ij} \cdot \theta_i &= \theta_j + R\theta_j \\ \sum_i X_{ij} \cdot S_i &= S_j + RS_j \\ \sum_i X_{ij} \cdot (\text{SiO}_4\text{H}_4)_i &= (\text{SiO}_4\text{H}_4)_j + R(\text{SiO}_4\text{H}_4)_j \\ \sum_i X_{ij} \cdot \text{NO}_i &= \text{NO}_j + R\text{NO}_j \\ \sum_i X_{ij} &= 1 + R\end{aligned}$$

Where the subscript i corresponds to each WT and j to every sample; X_{ij} are the proportion of water type i in sample j ; θ_i , S_i , $(\text{SiO}_4\text{H}_4)_i$ and NO_i are the values of θ , S , SiO_4H_4 and NO for WT i ; θ_j , S_j , $(\text{SiO}_4\text{H}_4)_j$ and NO_j are the values for each variable in sample j ; and R are the residuals of each the mass balance equations and for the mass conservation equation for sample j .

These linear mixing equations were normalized and weighted. For normalization, the mean and standard deviation values of the parameters of most of these WTs were obtained from the literature (Table 2.1), except for AA and SACW of 18°C and 12°C, which were defined from the average characteristics of these WTs in the Eastern Equatorial Atlantic, between 5° N–5° S and 20–30° W (World Ocean Atlas, 2013). The equations were weighted considering the measurement error of each parameter in relation to its variability in the study area and its relative conservative nature. Weights of 10, 10, 2 and 1 were assigned to θ , S , NO and SiO_4H_4 , respectively. The weights assigned to the NO and SiO_4H_4 mass balance equations were lower because both variables are affected by non-conservative processes: SiO_4H_4 is influenced by silica dissolution and the R_N of NO is variable, which introduces more uncertainty in the mass balance equations. We assumed that the mass is accurately conserved, so a weight of 100 was assigned to the mass conservation equation.

Since we have 5 mass balance equations and 11 WTs, in order to solve the OMP it is necessary to define oceanographically consistent WT mixing groups, taking into account

that mixing occurs with adjacent WTs along or across isopycnals and a maximum of 4 WTs can mix simultaneously (Álvarez et al., 2014). The 5 groups of WTs defined, from surface to 4000 dbar were: 1) MMW - SACW18 - ENACW15; 2) SACW18 - ENACW15 - SACW12 - ENACW12; 3) SACW12 - ENACW12 - SPMW - AA; 4) SPMW - AA - MW - LSW; and 5) MW - LSW - LNEADW - UNEADW (Fig. 2.2). Each sample was assigned to a particular group according to its θ and S , and then the system of mass balance equations was solved for each sample.

Table 2.1. Thermohaline and chemical characteristics (average value \pm uncertainty) of the water types (WT) introduced in the OMP analysis of the water masses present in the CVFZ. Determination coefficient (R^2), standard error (SE) of the estimate and number of samples (n) of the multiple-regression of the measured and back-calculated variables.

WT	θ_i (°C)	S_i	SiO_4H_4 ($\mu\text{mol kg}^{-1}$)	NO_i ($\mu\text{mol kg}^{-1}$)
SACW_18 ^a	18.03 ± 0.05	35.82 ± 0.03	5.1 ± 0.1	260 ± 8
MMW ^b	20.0 ± 0.5	37.00 ± 0.04	0.4 ± 0.3	225 ± 10
ENACW_15 ^b	15.3 ± 0.4	36.10 ± 0.02	2.2 ± 1.7	264 ± 8
SACW_12 ^a	12.0 ± 0.1	35.16 ± 0.01	10.8 ± 0.1	345 ± 7
ENACW_12 ^c	12.2 ± 0.4	35.66 ± 0.02	4.9 ± 0.2	322 ± 8
SPMW ^c	8.2 ± 0.4	35.23 ± 0.01	14.5 ± 0.4	386 ± 7
AA ^a	4.89 ± 0.03	34.51 ± 0.02	30.3 ± 0.8	464 ± 8
MW ^c	11.8 ± 0.1	36.50 ± 0.01	7.2 ± 0.7	304 ± 9
LSW ^c	3.4 ± 0.2	34.89 ± 0.12	19.5 ± 0.4	446 ± 9
UNEADW ^d	2.500 ± 0.003	34.940 ± 0.003	34.8 ± 0.3	447 ± 7
LNEADW ^d	1.980 ± 0.002	34.884 ± 0.003	44.4 ± 0.3	462 ± 7
R^2	0.999	0.999	0.988	0.977
SE	0.04	0.005	1.2	11
N	307	307	307	307

^aThis work, taken from the WOA13 in the Equatorial Atlantic

^bÁlvarez and Álvarez-Salgado (2009); Lønborg and Álvarez-Salgado (2014)

^cPerez et al. (2001); Álvarez and Álvarez-Salgado (2009)

^dPerez et al. (2001); Lønborg and Álvarez-Salgado (2014)

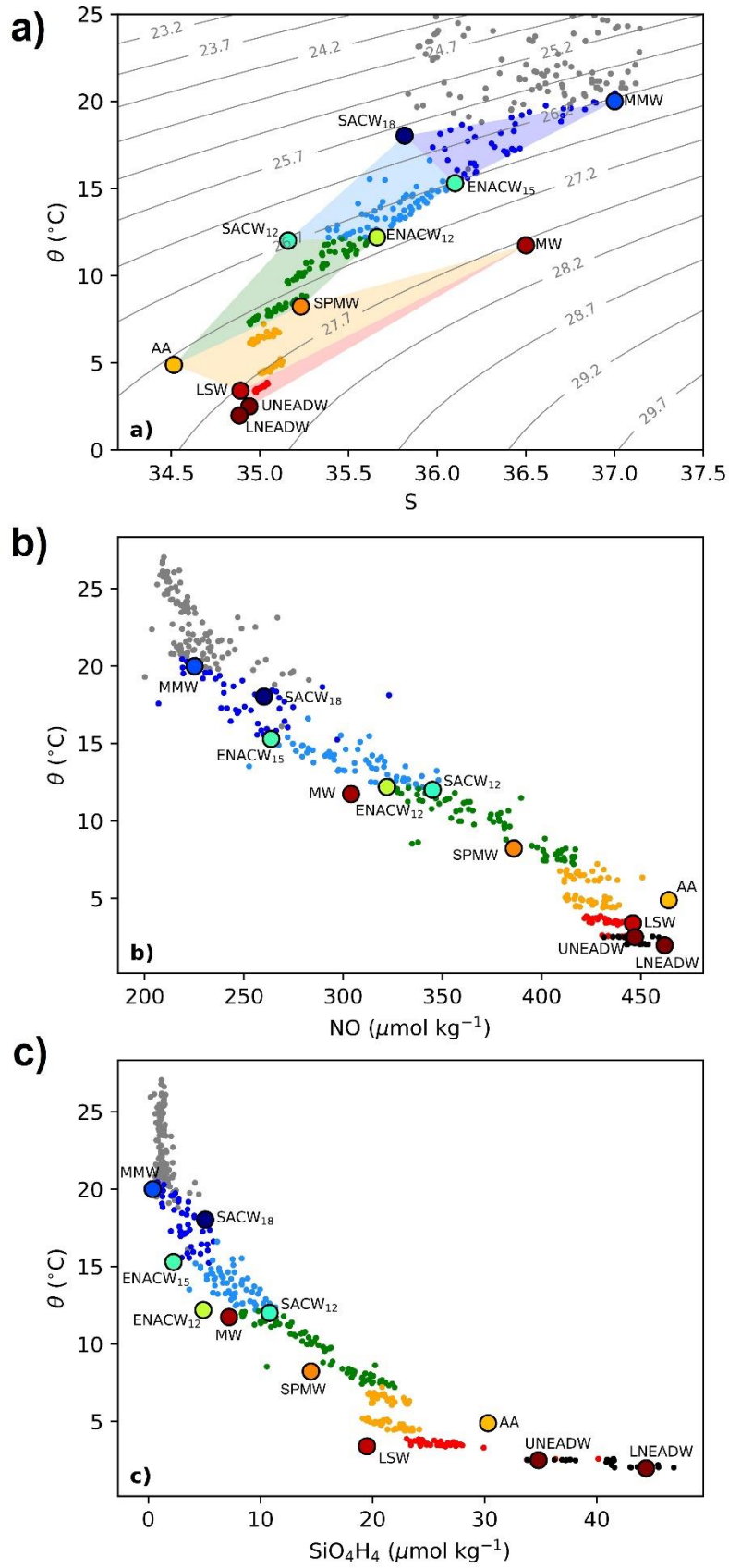


Figure 2.2. Potential temperature (θ) versus salinity (a), NO (b) and SiO_4H_4 (c) for FLUXES I. Dots represent the water samples collected and the shading colours in (a) identify the mixing group assigned to each sample. Potential density contours are also shown in (a).

The reliability of the OMP analysis was assessed with the determination coefficient (R^2) and standard error (SE) of the residuals of the linear regression between measured and back-calculated variables (θ , S, SiO_4H_4 and NO) (Álvarez et al., 2014). Note that our OMP reproduced the thermohaline and chemical fields during the cruise quite accurately, as demonstrated by the high R^2 (>0.977) and low SE of the linear regression of the measured and predicted values of θ , S, SiO_4H_4 and NO (Table 2.1).

Samples located between the surface and the base of the deep chlorophyll maximum (DCM) were excluded from the OMP analysis because the heat, freshwater and gas exchange with the atmosphere and the non-conservative behaviour of O_2 and nutrient salts would disprove the assumption of conservation of the mass balance equations. Therefore, the OMP was applied to 307 of the 419 samples of the FLUXES I cruise.

2.2.4 WT proportion-weighted average values

The WT proportion-weighted average value of any variable (N) in a given WT, henceforward archetype concentration of N , can be calculated using the X_{ij} obtained as detailed in section 2.2.3, and the concentration of N in each sample (Álvarez-Salgado et al., 2013). The equation is:

$$N_i = \frac{\sum_j X_{ij} \cdot N_j}{\sum_j X_{ij}}$$

Where N_i is the archetype value of N in water mass i ; X_{ij} is the proportion of WT i in sample j and N_j is the value of N in sample j . The standard error of the archetype value is obtained as:

$$SE_{N_i} = \frac{\sqrt{\sum_j X_{ij} (N_j - N_i)^2}}{\sum_j X_{ij}}$$

Finally, the proportion of the total volume of water sampled during the cruise that correspond to a given water mass (%VOL $_i$) can be calculated as:

$$\%VOL_i = 100 \cdot \frac{\sum_j X_{ij}}{n}$$

Where n is number of samples. In this study, we have calculated archetype values of Z , S , θ , AOU, HPO_4^{-2} , NO_3^- , DOC, DON, POC and PON for the 11 WT's identified in the study area. Moreover, N_i values were calculated also for the Northern (stns 3 to 12, excluding stations 1 and 2 over the continental shelf) and Southern transects (stns 19 to 29) -separated by the CVF- and the Western transect (stns 12 to 19) -located in the open ocean- and the Eastern transect (stns 29 to 35 and stn 3) near the coast (Fig. 2.1), to assess geographical differences between transects for a given WT.

2.2.5 Multiple regression models

The fraction of the total variability of a non-conservative variable (e.g. HPO_4^{-2} , NO_3^- , DOC, DON, POC, PON) explained by WT mixing can be calculated from a multiple linear regression of n mixing equations (one per sample) with m coefficients (one per WT). The explained variability is indicated by the determination coefficient (R^2) and the explanatory power by the standard error of the estimate (SE) of the multiple regression.

However, the distribution of HPO_4^{-2} , NO_3^- , DOC, DON, POC or PON depends not only on the conservative mixing of WT's but also on the biogeochemical processes that occur alongside mixing. The main biogeochemical process in the ocean interior is organic matter mineralisation and it can be traced with the AOU (Álvarez et al., 2014). The observed level of organic matter mineralisation is the result of the large-scale mineralisation from the formation area of each WT to the study area and the local mineralisation that occurs within the study area (Álvarez-Salgado et al., 2013), the CVFZ in our case. On the one hand, the large-scale mineralisation is assumed to be included in the archetype values of the different WT in the region and, therefore, accounted for by the multiple linear regression with X_{ij} . On the other hand, a multiple linear regression with X_{ij} and AOU (for DOC, DON, POC, PON, NO_3^- and HPO_4^{-2}) or NO_3^- (for DON, PON and HPO_4^{-2}) would quantify the effect of local mineralisation. In this multiple linear regression of n linear equations with $m + 1$ unknowns, the extra unknown is the coefficient that relates HPO_4^{-2} , NO_3^- , DOC, DON, POC or PON with AOU or NO_3^- and represents the rate of change of these variables with AOU or NO_3^- that does not depend on WT mixing (Álvarez-Salgado et al., 2013). Therefore, when calculating the multiple linear regression of DON or PON with X_{ij} and NO_3^- , the coefficient of DON or PON to NO_3^- would represent the contribution of DON or PON to local NO_3^- production. On the other hand, the coefficient

of AOU in the multiple linear regression of DOC or POC to AOU would represent the contribution of DOC or POC to the oxygen utilization once multiplied by the Redfield ratio of dissolved oxygen consumption to organic carbon mineralisation of $1.4 \text{ mol O}_2 \text{ mol C}^{-1}$ (Anderson, 1995).

2.2.6 Epipelagic layer

As indicated above, samples collected in the epipelagic layer were excluded from the OMP analysis because of the non-conservative behavior of θ , S, SiO_4H_4 and NO. Those samples have been used to study the impact of the CVFZ on the biogeochemistry of the epipelagic layer during the FLUXES I cruise. To do that, we have calculated average concentrations of the different variables (Z, S, θ , AOU, Chl-a, NO_3^- , NO_2^- , NH_4^+ , HPO_4^{2-} , SiO_4H_4 , DOC, DON, POC and PON) at the surface (5 dbar), and the deep chlorophyll maximum (DCM), as well as vertically-averaged from the surface to the base of the DCM. Vertical averages considered the uneven vertical sampling spacing by using the trapezoid rule to weight each sample. Average values were obtained for the whole cruise as well as for each individual transect. In the Northern transect, the first two stations were excluded because they are outside the box, and due to their position close to the continental shelf, they are affected by distinct processes from those observed in the oceanic waters, biasing the calculation of the average values of the Northern transect (Fig. 2.1).

2.3 Results

2.3.1 Hydrography settings of the CVF

2.3.1.1 Epipelagic layer

The relative position of the four transects with respect to the CVF during FLUXES I can be documented using the isohaline that defines the front (36 at 150 dbar) (Zenk et al., 1991) (Fig. 2.3a). According to this criterion, the Western and Northern transects were located to the North of the front, while the front intersected the Southern and Eastern transects at around stations 34 and 24, respectively (Fig. 2.1). Due to the dominance of saline waters of North Atlantic origin to the North of the front, the average salinity was significantly higher in the Northern and Western transects (36.7-36.8), than in the Southern and Eastern transects (36.2) ($p < 0.001$) (Fig. 2.3a, Table 2.2). Mesoscale variability was super-imposed over this large-scale pattern, notably due to the presence of a narrow

intrusion of relatively cold and less saline water of South Atlantic origin centred at stn 5 in the Northern transect. The mean depth-averaged temperature down to the base of the DCM was 22.3°C with non-significant differences between transects (Fig. 2.3b, Table 2.2). Nonetheless, the Southern transect was characterized by significantly higher ($p < 0.0005$) surface (5 dbar) temperatures (26.1°C) than the Northern transect (23.9°C).

Table 2.2. Average \pm SE depth, temperature, salinity, apparent oxygen utilization (AOU), and chlorophyll (Chl a), in the epipelagic layer during FLUXES I for the whole cruise and the Northern, Western, Southern and Eastern transects at surface (5 dbar), deep chlorophyll maximum (DCM) and 5 dbar-DCM base (5-DCM).

	Cruise	North	West	South	East
Depth (dbar)					
5 dbar	5.1 \pm 0.1	5.2 \pm 0.1	4.9 \pm 0.1	5.0 \pm 0.2	5.3 \pm 0.1
DCM	56.5 \pm 4.5	62.1 \pm 9.0	81.8 \pm 5.9	50.1 \pm 5.9	33.4 \pm 7.6
5-DCM	40.4 \pm 2.9	44.4 \pm 4.5	58.61 \pm 3.4	37.2 \pm 3.1	22.6 \pm 3.0
Temperature (°C)					
5 dbar	24.7 \pm 0.3	23.9 \pm 0.4	25.0 \pm 0.1	26.1 \pm 0.1	24.5 \pm 0.5
DCM	21.1 \pm 0.2	20.6 \pm 0.2	21.4 \pm 0.3	21.1 \pm 0.4	21.6 \pm 0.6
5-DCM	22.3 \pm 0.1	21.8 \pm 0.1	22.4 \pm 0.1	22.5 \pm 0.3	22.5 \pm 0.3
Salinity					
5 dbar	36.5 \pm 0.1	36.8 \pm 0.1	36.8 \pm 0.1	36.3 \pm 0.0	36.3 \pm 0.1
DCM	36.5 \pm 0.1	36.7 \pm 0.1	36.8 \pm 0.1	36.3 \pm 0.4	36.2 \pm 0.1
5-DCM	36.5 \pm 0.1	36.7 \pm 0.1	36.8 \pm 0.1	36.3 \pm 0.1	36.2 \pm 0.1
AOU ($\mu\text{mol kg}^{-1}$)					
5 dbar	-8.7 \pm 1.4	-11.1 \pm 2.5	-6.2 \pm 1.0	-4.4 \pm 0.7	-7.8 \pm 0.8
DCM	21.1 \pm 6.3	9.1 \pm 6.2	9.3 \pm 6.3	48.8 \pm 12.9	20.5 \pm 17.6
5-DCM	14.2 \pm 4.8	-1.1 \pm 4.5	4.5 \pm 5.2	37.1 \pm 9.0	21.6 \pm 13.0
Chl-a ($\mu\text{g L}^{-1}$)					
5 dbar	0.30 \pm 0.08	0.23 \pm 0.11	0.08 \pm 0.00	0.14 \pm 0.02	0.49 \pm 0.15
DCM	1.20 \pm 0.18	1.09 \pm 0.42	0.46 \pm 0.05	1.26 \pm 0.30	1.56 \pm 0.28
5-DCM	0.65 \pm 0.09	0.61 \pm 0.23	0.29 \pm 0.03	0.65 \pm 0.12	1.06 \pm 0.17

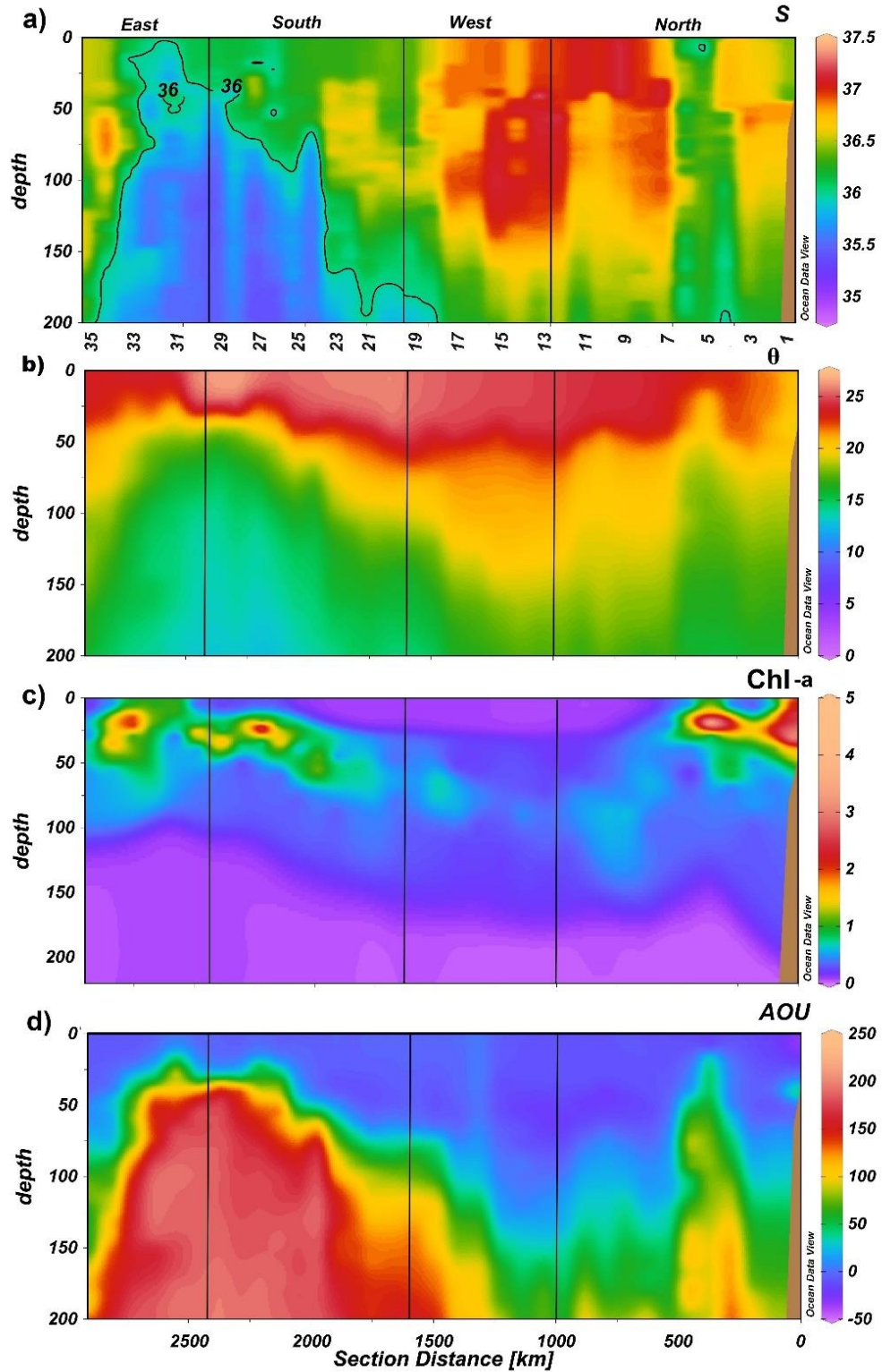


Figure 2.3. Distribution of salinity (S) (a), potential temperature (θ) in $^{\circ}\text{C}$ (b), Chl (chlorophyll a) in $\mu\text{g L}^{-1}$ (c) and apparent oxygen utilization (AOU) in $\mu\text{mol kg}^{-1}$ (d), in the epipelagic layer during the FLUXES I cruise. The black line in (a) represents the 36 isohaline defining the location of the CVF, and the vertical black lines represent the corners of the FLUXES I hydrographic box. The X-axis shows station number (a) or section distance (d). Produced with Ocean Data View (Schlitzer, 2017).

The DCM was shallower and with higher Chl-a levels towards the coast (Fig. 2.3c). The average depth of the DCM and average Chl-a levels in the Northern and Southern transects, were similar ($p > 0.3$) while the Western (oceanic) and Eastern (coastal) transects showed the highest differences, being the DCM deeper and with lower concentrations in the Western transect (Table 2.2).

AOU (Fig. 2.3d), increased significantly with depth (Table 2.2). As for salinity and temperature, marked differences were observed between the Northern and Southern transects: depth-averaged concentrations of AOU were significantly lower ($p < 0.05$) in the Northern and Western transects ($< 4.5 \mu\text{mol kg}^{-1}$) than in the Southern and Eastern transects ($> 20 \mu\text{mol kg}^{-1}$). The intrusion of water with South Atlantic origin at stn 5 was traced by higher AOU values in the upper 100 dbar (Fig. 2.3d).

2.3.1.2 Meso- and bathypelagic layer

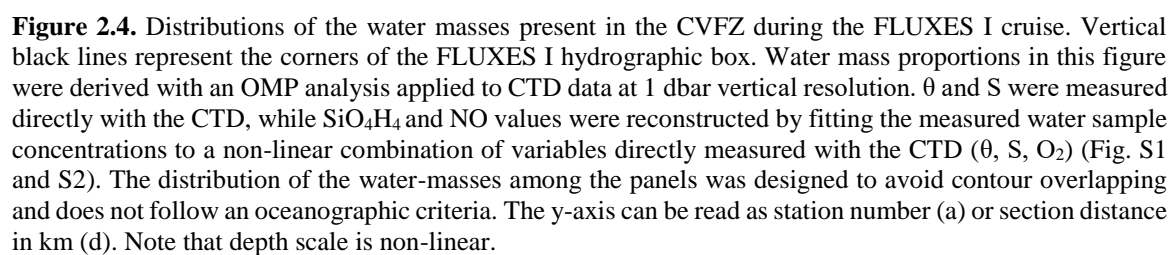
Below the epipelagic layer, in the depth range between 100-700 dbar, hydrographic variability was governed by the distribution of the central water types. SACW₁₈ and MMW, characterized by potential temperatures of 18°C and 20°C, respectively (Fig. 2.4ab, S1a; Table 2.1), and centred at about 110 dbar (Table 2.3) were the shallowest central water types. SACW₁₈ and MMW were defined by distinct salinity values, 35.82 and 37.00, respectively (Fig. 2.4ab, S1b. Table 2.1), as expected for two water masses of contrasting North and South Atlantic origin, and represented 4.78% and 5.48% of the total sampled water volume (Table 2.3) or 9.9% and 11.4% of the volume of central waters. ENACW₁₅ was located deeper, centred at 240 ± 14 dbar (Table 2.3) and represented 12.54% of the total sampled volume or 26.1% of the volume of central waters. Most of the ENACW₁₅ was present in the Northern and Western transects (42.8% and 25.0% of the volume of this WT, respectively), i.e. to the North of the CVF (Fig. 2.4c). SACW₁₂ and ENACW₁₂ were centred at 336 ± 28 dbar and 442 ± 19 dbar and were defined by a similar temperature of $\sim 12^\circ\text{C}$, but different values of salinity (35.16 and 35.66), SiO_4H_4 (10.8 and $4.9 \mu\text{mol kg}^{-1}$) and NO (345 and $322 \mu\text{mol kg}^{-1}$) values (Table 2.1). ENACW₁₂ was the most abundant WT sampled during the cruise with 18.09% (Fig. 2.4b. Table 2.3) or 37.6% of the volume of central waters and was present in the four transects (from a minimum of 17.8% of the total volume in the Western transect to a maximum of 28.6% in the Northern transect). Conversely, SACW₁₂ occupied a volume of 7.25% (or 15.1% of the central waters) and was mostly present in the stations of the Southern transect, where 57% of the volume of

this WT was found (Fig. 2.4a, Table 2.3). Again, in the Northern section, around stn 5, SACW_18 appears, although ENACW dominated in the rest of the transect (Fig. 2.4b, c).

Table 2.3. Percentage of the total volume of water sampled during FLUXES I that corresponded to each water type (%VOLi) and archetype values \pm SE of depth (Zi), apparent oxygen utilization (AOUi), nitrate (NO_3^- i), phosphate (HPO_4^{2-} i), dissolved organic carbon (DOCi), dissolved organic nitrogen (DONi), particulate organic carbon (POCi), particulate organic nitrogen (PONi), and C:N ratios of DOM and suspended POM for the water types intercepted during the cruise. Determination coefficient (R^2), standard error of the estimate (SE) of the multiple-regression of each variable; measurement error of each variable (ME).

WT	%VOLi	Zi (dbar)	AOUi ($\mu\text{mol kg}^{-1}$)	NO_3^- i ($\mu\text{mol kg}^{-1}$)	HPO_4^{2-} i ($\mu\text{mol kg}^{-1}$)	DOCi ($\mu\text{mol L}^{-1}$)
SACW_18	4.78%	102 \pm 19	120.2 \pm 15.4	16.9 \pm 2.1	0.44 \pm 0.09	58.9 \pm 2.5
MMW	5.48%	113 \pm 3	50.9 \pm 10.5	6.5 \pm 1.4	0.97 \pm 0.05	58.7 \pm 1.6
ENACW_15	12.54%	240 \pm 14	117.8 \pm 6.7	16.2 \pm 1.0	1.04 \pm 0.11	52.3 \pm 1.7
SACW_12	7.25%	336 \pm 28	191.7 \pm 5.4	28.7 \pm 1.0	1.56 \pm 0.05	49.9 \pm 1.5
ENACW_12	18.09%	442 \pm 19	171.2 \pm 4.8	27.2 \pm 0.8	1.65 \pm 0.06	48.5 \pm 0.6
SPMW	7.18%	809 \pm 32	175.7 \pm 4.2	30.9 \pm 0.7	1.92 \pm 0.04	44.8 \pm 0.6
AA	10.62%	873 \pm 54	172.6 \pm 5.7	31.3 \pm 0.6	1.91 \pm 0.04	45.1 \pm 0.6
MW	3.09%	1455 \pm 118	119.4 \pm 9.2	25.9 \pm 1.2	1.64 \pm 0.07	43.3 \pm 0.9
LSW	15.58%	1688 \pm 46	104.0 \pm 2.6	23.9 \pm 0.3	1.54 \pm 0.02	43.4 \pm 0.5
UNEADW	11.72%	2742 \pm 93	88.0 \pm 1.1	22.2 \pm 0.2	1.46 \pm 0.01	43.4 \pm 0.6
LNEADW	3.66%	3824 \pm 101	85.1 \pm 1.7	22.4 \pm 0.2	1.48 \pm 0.01	43.5 \pm 1
R^2			0.94	0.95	0.94	0.63
SE			12.9	1.8	0.1	4.0
ME			1.0	0.1	0.02	1.5

WT	DONi ($\mu\text{mol L}^{-1}$)	POCi ($\mu\text{mol L}^{-1}$)	PONi ($\mu\text{mol L}^{-1}$)	C:N DOM (mol C mol N $^{-1}$)	C:N POM (mol C mol N $^{-1}$)
SACW_18	4.6 \pm 0.4	3.2 \pm 1.2	0.33 \pm 0.13	12.7 \pm 1.1	9.9 \pm 1.6
MMW	5.1 \pm 0.3	2.7 \pm 1.0	0.25 \pm 0.10	11.6 \pm 0.7	10.9 \pm 1.3
ENACW_15	4.2 \pm 0.3	1.5 \pm 0.3	0.12 \pm 0.03	12.4 \pm 1.0	12.3 \pm 0.9
SACW_12	3.5 \pm 0.3	1.4 \pm 0.2	0.11 \pm 0.02	14.4 \pm 1.5	12.4 \pm 1.4
ENACW_12	3.4 \pm 0.2	1.2 \pm 0.1	0.09 \pm 0.01	14.4 \pm 1.1	12.5 \pm 0.8
SPMW	3.3 \pm 0.3	0.79 \pm 0.06	0.05 \pm 0.01	13.6 \pm 1.3	14.5 \pm 1.3
AA	3.1 \pm 0.3	0.81 \pm 0.06	0.06 \pm 0.01	14.6 \pm 1.3	14.2 \pm 1.3
MW	3.0 \pm 0.4	0.70 \pm 0.11	0.05 \pm 0.01	14.4 \pm 1.9	14.2 \pm 2.2
LSW	3.0 \pm 0.2	0.67 \pm 0.05	0.05 \pm 0.01	14.5 \pm 0.9	14.6 \pm 1.1
UNEADW	2.9 \pm 0.2	0.68 \pm 0.07	0.04 \pm 0.01	15.2 \pm 0.9	15.6 \pm 1.3
LNEADW	3.1 \pm 0.3	0.71 \pm 0.12	0.04 \pm 0.01	14.8 \pm 1.5	17.3 \pm 2.0
R^2	0.44	0.26	0.29		
SE	0.9	1.3	0.13		
ME	0.3	0.1	0.01		



The intermediate water domain, approximately between 700 dbar and 1500 dbar, was occupied by AA, SPMW and MW. These water masses, of contrasting sub-Antarctic, sub-Arctic and Mediterranean origin, have remarkable differences in θ , S , SiO_4H_4 and NO (Table 2.1). It is particularly noticeable the salinity minimum observed in the Southern transect at about 1000 dbar, which corresponds to AA (Fig. 2.4c, S1b). The shallowest intermediate WT was the SPMW, centred at 809 ± 32 dbar, with a temperature of 8°C and representing 7.18% of the sampled volume (or 34.3% of the intermediate waters).

SPWM was followed by AA at a depth of 873 ± 54 dbar, which had the lowest salinity (34.52) but the highest content of silicates ($30.3 \mu\text{mol kg}^{-1}$) and occupied a volume of 10.62% (or 50.8% of the intermediate waters). This water mass was mostly present to the South of the CVF (59.0% of the volume sampled in the Northern and Western transects) while SPMW predominated to the North of the front (56.8% of the sampled volume in the Eastern and Southern transects) (Fig. 2.4d). The deepest intermediate WT, MW, centred at 1455 ± 118 dbar, was much less represented with 3.09% (14.8% of the intermediate waters) and was almost absent in the Eastern transect (only 3.1% of the volume).

Finally, the deep waters domain was composed by three water types with similar salinity, yet different silicate content (Fig. S1c) due to their contrasting origin. While LSW is of pure North Atlantic origin, LNEADW and UNEADW are mixed with Antarctic waters that confer their higher silicate concentration. LSW was defined by a silicate concentration of $19.5 \mu\text{mol kg}^{-1}$, it was located at 1648 ± 46 dbar and represented 15.58% of the sampled volume (50.3% of the deep waters), being the second predominant water mass sampled during FLUXES I. LSW was found in the four transects, ranging from 19.9% of the total volume in the Eastern transect to 29.4% in the Northern transect (Fig. 2.4a). In contrast, UNEADW was located deeper at 2742 ± 93 dbar and had a silicate concentration of $34.8 \mu\text{mol kg}^{-1}$, with a volume sampled of 11.72% (37.9% of the deep waters). LNEADW was placed at 3824 ± 101 dbar, with a silicate concentration of $44.4 \mu\text{mol kg}^{-1}$ and a small representation of sampled volume of 3.66% (or 11.8% of deep waters). UNEADW was distributed in the four transects, ranging from 18.7% of the total volume in the Eastern transect to 29.0% in the Southern transect (Fig. 2.4d). In contrast, LNEADW concentrated in the Northern and Western transects (75% of the total volume of this WT) while it was practically absent in the Eastern transect. Bottom depth is the reason behind this difference (Fig. 2.4c).

AOU can be used to trace organic matter mineralisation in the meso- and bathypelagic layers of the CVFZ (Fig. 2.5). In the central waters, the lowest archetype AOU values (50 to 120 $\mu\text{mol kg}^{-1}$) were found in the shallowest WTs (MMW, ENACW_15 and SACW_18), while the highest archetype AOU (192 $\mu\text{mol kg}^{-1}$) corresponded to SACW_12 (Table 2.3). In intermediate and deep waters, AOU decreased significantly ($p < 0.0005$) with depth from an archetype value of 176 $\mu\text{mol kg}^{-1}$ in SPMW to 85 $\mu\text{mol kg}^{-1}$ in the LNEADW. WTs mixing explained 94% of the variability of AOU, but the SE of 12.9 $\mu\text{mol kg}^{-1}$ was an order of magnitude larger than the measurement error of $\sim 1 \mu\text{mol kg}^{-1}$ (Table 2.3).

Regarding the geographical variability within WTs, ENACW_12, the only central WT with significant presence in the four transects, showed significantly ($p < 0.01$) lower AOU levels in the Northern transect (144 $\mu\text{mol kg}^{-1}$) and higher in the Southern transect (204 $\mu\text{mol kg}^{-1}$; Table 2.4). In intermediate waters, AOU in SPMW and AA was also significantly higher in the Southern transect ($p < 0.05$). In deep waters, archetype AOU levels in LSW did not differ between transects, while in UNEADW, they were significantly ($p < 0.025$) higher in the Southern and Eastern transects (90–96 $\mu\text{mol kg}^{-1}$) as compared with the Northern and Western transects (83 $\mu\text{mol kg}^{-1}$).

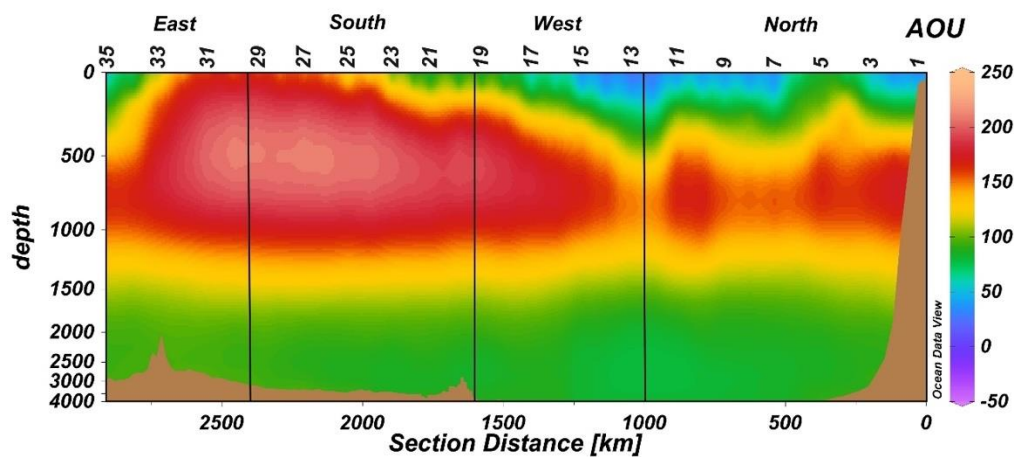


Figure 2.5. Distributions of AOU in $\mu\text{mol kg}^{-1}$ in the mesopelagic layer during the FLUXES I cruise. The vertical black lines represent the corners of the FLUXES I hydrographic box. The y-axis can be read as station number or section distance. Note that depth scale is non-linear Produced with Ocean Data View (Schlitzer, 2017).

Table 2.4. Percentage of the total volume of sampled water that corresponded to each water type (%VOL) and archetype \pm SE values of apparent oxygen utilization (AOU), dissolved organic carbon (DOC), dissolved organic nitrogen (DON), particulate organic carbon (POC), particulate organic nitrogen (PON), and C:N molar ratios of DOM and POM of the water types intercepted during FLUXES I in the Northern, Western, Southern and Eastern transects

	% VOL				AOU (μmol/kg)				DOC (μmol/L)			
	North	West	South	East	North	West	South	East	North	West	South	East
SACW_18	4.5%	2.3%	6.7%	4.7%	77 ± 24	87 ± 29	145 ± 17	155 ± 25	60.8 ± 4.5	56.3 ± 3.5	58.9 ± 2.1	55.1 ± 7.8
MMW	8.5%	8.3%	3.5%	1.6%	35 ± 12	46 ± 13	97 ± 15	45 ± 47	59.7 ± 2.7	55.8 ± 1.4	59.3 ± 1.5	61.4 ± 2.3
ENACW_15	18.3%	14.7%	7.3%	10.4%	99 ± 7	101 ± 11	160 ± 9	134 ± 15	51.4 ± 1.1	52.2 ± 1.3	53.4 ± 2.5	53.2 ± 5.4
SACW_12	1.95%	3.7%	14.3%	8.8%	149 ± 18	172 ± 15	199 ± 4	197 ± 9	47.9 ± 2.4	50.7 ± 1.8	49.9 ± 0.9	49.8 ± 5.4
ENACW_12	16.9%	14.5%	16.6%	24.2%	144 ± 7	156 ± 10	204 ± 3	174 ± 8	48.2 ± 1.1	48.3 ± 1.1	49.3 ± 0.9	48.1 ± 1.3
SPMW	8.1%	8.3%	6.6%	6.8%	164 ± 6	173 ± 8	190 ± 6	178 ± 7	44.4 ± 1.0	45.0 ± 1.0	45.7 ± 1.0	45.0 ± 1.6
AA	7.2%	9.4%	12.8%	12.2%	152 ± 11	161 ± 11	187 ± 9	173 ± 11	43.4 ± 1.1	44.9 ± 1.2	45.8 ± 0.9	45.4 ± 1.2
MW	3.6%	3.1%	2.2%	3.5%	113 ± 13	116 ± 18	126 ± 20	127 ± 19	41.8 ± 1.2	43.6 ± 1.9	44.1 ± 1.3	43.9 ± 2.6
LSW	15.1%	15.9%	15.1%	15.8%	99 ± 4	103 ± 6	109 ± 5	105 ± 4	41.8 ± 0.6	43.8 ± 0.9	44.1 ± 0.5	44.2 ± 5.2
UNEADW	11.2%	13.0%	11.9%	11.4%	85 ± 1	84 ± 2	88 ± 1	97 ± 1	42.6 ± 1.1	43.1 ± 1.7	44.1 ± 0.6	44.1 ± 1.4
LNEADW	4.7%	6.8%	3.0%	0.5%	83 ± 2	83 ± 2	90 ± 3	96 ± 4	41.4 ± 1.5	48.8 ± 5.9	44.5 ± 0.9	45.3 ± 8.8

	DON (μmol/L)				POC (μmol/L)				PON (μmol/L)			
	North	West	South	East	North	West	South	East	North	West	South	East
SACW_18	5.7 ± 0.6	4.2 ± 0.9	4.1 ± 0.4	4.2 ± 0.9	5.6 ± 3.0	1.4 ± 0.4	2.3 ± 0.5	1.8 ± 1.4	0.53 ± 0.31	0.12 ± 0.04	0.24 ± 0.09	0.20 ± 0.15
MMW	5.5 ± 0.3	4.7 ± 0.6	4.6 ± 0.3	4.9 ± 0.9	3.9 ± 2.1	1.2 ± 0.1	2.1 ± 0.4	2.8 ± 1.4	0.35 ± 0.21	0.11 ± 0.01	0.21 ± 0.07	0.19 ± 0.09
ENACW_15	4.7 ± 0.4	4.3 ± 0.7	3.8 ± 0.5	3.4 ± 0.5	1.7 ± 0.5	0.8 ± 0.1	1.6 ± 0.4	1.7 ± 0.5	0.13 ± 0.06	0.07 ± 0.01	0.11 ± 0.03	0.15 ± 0.04
SACW_12	4.0 ± 0.6	3.9 ± 0.7	3.4 ± 0.4	3.2 ± 0.5	1.1 ± 0.4	0.9 ± 0.3	1.3 ± 0.2	2.0 ± 0.6	0.08 ± 0.04	0.07 ± 0.02	0.11 ± 0.02	0.17 ± 0.04
ENACW_12	3.6 ± 0.3	3.8 ± 1.1	3.3 ± 0.4	3.0 ± 0.2	1.1 ± 0.2	0.8 ± 0.1	1.1 ± 0.1	1.5 ± 0.3	0.08 ± 0.01	0.06 ± 0.01	0.09 ± 0.02	0.14 ± 0.02
SPMW	3.5 ± 0.3	3.1 ± 0.7	3.6 ± 0.6	2.8 ± 0.3	0.8 ± 0.1	0.7 ± 0.1	0.8 ± 0.2	0.9 ± 0.1	0.05 ± 0.01	0.04 ± 0.01	0.05 ± 0.01	0.08 ± 0.01
AA	3.1 ± 0.3	3.0 ± 0.8	3.3 ± 0.5	3.0 ± 0.2	0.8 ± 0.2	0.6 ± 0.1	0.8 ± 0.1	1.0 ± 0.1	0.05 ± 0.01	0.04 ± 0.01	0.05 ± 0.01	0.08 ± 0.01
MW	3.0 ± 0.4	3.1 ± 1.0	3.0 ± 1.0	2.9 ± 0.4	0.7 ± 0.2	0.6 ± 0.1	0.6 ± 0.1	0.9 ± 0.3	0.05 ± 0.01	0.03 ± 0.01	0.04 ± 0.02	0.08 ± 0.02
LSW	3.1 ± 0.2	3.3 ± 0.5	2.9 ± 0.3	2.8 ± 0.2	0.6 ± 0.1	0.6 ± 0.1	0.6 ± 0.1	0.9 ± 0.2	0.05 ± 0.01	0.03 ± 0.00	0.03 ± 0.01	0.07 ± 0.01
UNEADW	3.1 ± 0.2	3.0 ± 0.3	2.8 ± 0.4	2.5 ± 0.2	0.7 ± 0.1	0.5 ± 0.1	0.6 ± 0.1	1.0 ± 0.3	0.04 ± 0.01	0.03 ± 0.00	0.04 ± 0.01	0.07 ± 0.01
LNEADW	3.2 ± 0.1	3.1 ± 0.2	2.9 ± 1.1	2.5 ± 0.6	0.9 ± 0.3	0.6 ± 0.04	0.6 ± 0.1	1.1 ± 1.0	0.05 ± 0.01	0.03 ± 0.00	0.03 ± 0.01	0.07 ± 0.04

	C:N DOM				C:N POM			
	North	West	South	East	North	West	South	East
SACW_18	10.7 ± 1.2	13.5 ± 3.3	14.5 ± 1.4	13.0 ± 2.8	10.4 ± 2.0	11.6 ± 1.9	9.5 ± 1.9	8.9 ± 6.8
MMW	10.9 ± 0.5	11.8 ± 1.5	13.0 ± 1.2	12.6 ± 2.6	11.2 ± 2.5	10.6 ± 0.8	9.9 ± 1.4	14.5 ± 6.3
ENACW_15	11.0 ± 1.0	12.2 ± 2.0	14.1 ± 2.0	15.9 ± 2.4	12.4 ± 1.3	11.5 ± 0.7	14.6 ± 2.5	11.1 ± 2.0
SACW_12	12.1 ± 2.2	13.2 ± 2.2	14.8 ± 2.2	15.5 ± 2.4	12.8 ± 4.6	11.8 ± 3.7	11.8 ± 1.7	12.2 ± 2.8
ENACW_12	13.4 ± 1.2	12.8 ± 4.0	15.1 ± 2.2	15.8 ± 1.0	13.6 ± 1.7	13.1 ± 1.0	12.6 ± 1.8	11.1 ± 1.2
SPMW	12.8 ± 1.4	14.5 ± 3.9	12.8 ± 2.2	16.1 ± 1.6	15.4 ± 2.0	15.8 ± 2.4	16.8 ± 3.9	11.5 ± 1.5
AA	14.2 ± 1.3	14.8 ± 4.2	14.0 ± 2.4	15.4 ± 1.3	14.3 ± 2.7	15.2 ± 1.4	15.9 ± 2.9	12.4 ± 1.5
MW	13.8 ± 1.9	14.1 ± 4.7	14.6 ± 4.8	15.4 ± 3.0	14.1 ± 3.5	17.4 ± 2.6	16.4 ± 6.9	12.4 ± 2.8
LSW	13.7 ± 1.0	13.5 ± 1.9	15.2 ± 1.7	15.7 ± 1.4	13.9 ± 1.9	18.1 ± 1.1	17.3 ± 2.7	12.3 ± 1.0
UNEADW	13.9 ± 1.1	14.6 ± 1.3	15.7 ± 2.3	17.6 ± 0.8	15.1 ± 1.5	19.4 ± 1.4	17.1 ± 3.1	13.9 ± 2.5
LNEADW	12.9 ± 0.6	15.7 ± 1.2	15.6 ± 6.2	18.1 ± 1.6	17.8 ± 2.0	18.1 ± 2.5	16.6 ± 5.0	15.5 ± 7.3

2.3.2 Biogeochemical variability in epi-, meso- and bathypelagic waters of the CVFZ

2.3.2.1 Epipelagic layer

The distribution of NO_3^- (Fig. 2.6a) matched with the distribution of AOU (Fig. 2.3d), showing a marked increase with depth. Differences were observed North and South of the CVF: depth-averaged concentrations of NO_3^- were significantly lower ($p < 0.05$) in the Northern and Western transects ($< 2.3 \mu\text{mol kg}^{-1}$) than in the Southern and Eastern transects ($> 4.6 \mu\text{mol kg}^{-1}$). As for the case of AOU, the intrusion of water of South Atlantic origin at stn 5 was also traced by higher NO_3^- values in the upper 100 dbar.

NO_2^- (Fig. 2.6b) and NH_4^+ (Fig. 2.6c) were, in general, very low (< 0.1 and $< 0.05 \mu\text{mol kg}^{-1}$) (Table 2.5), except in the surroundings of the DCM. The average concentration of NO_2^- at the DCM was $0.23 \pm 0.03 \mu\text{mol kg}^{-1}$, being significantly lower in the Western transect ($p < 0.025$). An average NH_4^+ concentration of $0.09 \pm 0.03 \mu\text{mol kg}^{-1}$ was observed at the DCM, with significantly ($p < 0.01$) lower values ($0.02 \pm 0.03 \mu\text{mol kg}^{-1}$) in the Western (oceanic) transect and higher values ($0.19 \pm 0.10 \mu\text{mol kg}^{-1}$) in the Eastern (coastal) transect. NO_2^- and NH_4^+ also showed relatively elevated concentrations at stn 5 in the Northern transect, coinciding with the relative maxima of temperature, Chl-a, AOU and NO_3^- , and minimum in salinity, reflecting the influence of the mesoscale variability of the CVF in the distribution of biogeochemical properties.

Below the DCM, the Orthogonal Distance Regression (ODR) of NO_3^- and salinity ($\text{NO}_3^- = -21 (\pm 1) \cdot S + 788 (\pm 38)$; $R^2 = 0.75$; $n = 107$) indicates that 75% of the variability of NO_3^- depends on the mixing of the nutrient-poorer saltier North Atlantic waters with the nutrient-rich fresher South Atlantic waters. The surface mixed layer was excluded from this analysis due to oxygen exchange with the atmosphere. To separate the contribution of mixing (traced by salinity) from mineralisation processes (traced by AOU), a multiple regression of NO_3^- with salinity and AOU was carried out, obtaining a R^2 of 0.97, and a NO_3^- :AOU molar slope of 0.110 ± 0.004 ($\text{NO}_3^- = -3.5 (\pm 0.6) \cdot S + 0.110 (\pm 0.004) \cdot \text{AOU} + 130 (\pm 22)$; $R^2 = 0.97$; $n = 106$).

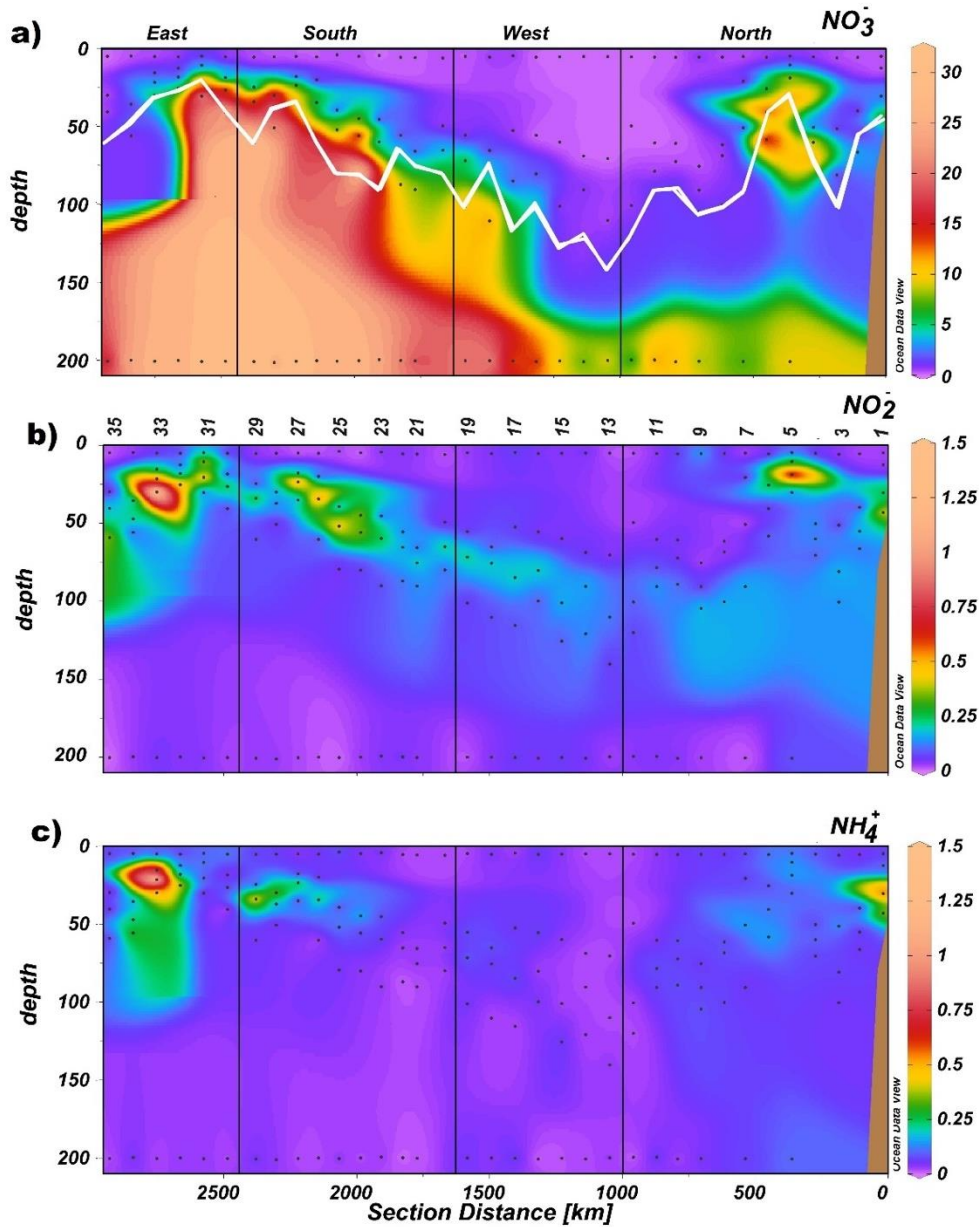


Figure 2.6. Distributions of nitrate (NO_3^-) in $\mu\text{mol kg}^{-1}$ (a), nitrite (NO_2^-) in $\mu\text{mol kg}^{-1}$ (b), and ammonium (NH_4^+) in $\mu\text{mol kg}^{-1}$ (c), in the epipelagic layer during the FLUXES I cruise. Dots represent samples, vertical back lines represent the corners of the FLUXES I hydrographic box and the white line in panel (a) represents the base of the DCM. The x-axis shows station number (a) or section distance (c). Produced with Ocean Data View (Schlitzer, 2017).

The concentration of HPO_4^{2-} (Fig. 2.7a) matched the predominant form of inorganic nitrogen, NO_3^- (Fig. 2.6a). Marked differences were observed North and South of the CVF: average concentrations of HPO_4^{2-} above the DCM were significantly lower ($p < 0.05$) in the Northern and Western transects ($< 0.3 \mu\text{mol kg}^{-1}$) than in the Southern and Eastern transects ($> 0.5 \mu\text{mol kg}^{-1}$) (Table 2.5). The intrusion of water with South Atlantic origin at stn 5 is also traced by higher HPO_4^{2-} values in the upper 100 dbar. Regarding SiO_4H_4 (Fig.

2.7b), a distribution parallel to NO_3^- and HPO_4^{2-} was also observed: significantly lower ($p < 0.005$) concentrations were found above the DCM in the Western and Northern transects ($< 1.9 \mu\text{mol kg}^{-1}$) than in the Eastern and Southern transects ($> 3.2 \mu\text{mol kg}^{-1}$) (Table 2.5).

Table 2.5. Average \pm SE of nitrate (NO_3^-), nitrite (NO_2^-), ammonium (NH_4^+), phosphate (HPO_4^{2-}), silicate (SiO_4H_4) dissolved organic carbon (DOC), dissolved organic nitrogen (DON), particulate organic carbon (POC), particulate organic nitrogen (PON), and C:N ratios of DOM and POM in the epipelagic layer during FLUXES I for the whole cruise and the Northern, Western, Southern and Eastern transects at surface (5 dbar), DCM and 5 dbar-DCM base (5-B DCM).

	Cruise	North	West	South	East
NO_3^- ($\mu\text{mol kg}^{-1}$)					
Surface	0.25 ± 0.04	0.30 ± 0.69	0.18 ± 0.09	0.20 ± 0.03	0.31 ± 10
DCM	3.93 ± 0.87	3.05 ± 1.24	1.20 ± 0.58	6.90 ± 1.88	4.71 ± 2.18
5-B DCM	3.2 ± 0.6	1.9 ± 0.8	0.95 ± 0.38	5.5 ± 1.3	4.6 ± 1.7
NO_2^- ($\mu\text{mol kg}^{-1}$)					
Surface	0.04 ± 0.01	0.04 ± 0.02	0.04 ± 0.01	0.02 ± 0.00	0.04 ± 0.02
DCM	0.23 ± 0.03	0.18 ± 0.07	0.14 ± 0.02	0.31 ± 0.07	0.27 ± 0.06
5-B DCM	0.14 ± 0.02	0.11 ± 0.04	0.08 ± 0.01	0.14 ± 0.02	0.21 ± 0.07
NH_4^+ ($\mu\text{mol kg}^{-1}$)					
Surface	0.03 ± 0.01	0.04 ± 0.01	0.02 ± 0.00	0.02 ± 0.00	0.04 ± 0.01
DCM	0.09 ± 0.03	0.05 ± 0.01	0.03 ± 0.01	0.10 ± 0.03	0.19 ± 0.10
5-B DCM	0.06 ± 0.01	0.05 ± 0.01	0.02 ± 0.00	0.06 ± 0.01	0.12 ± 0.06
HPO_4^{2-} ($\mu\text{mol kg}^{-1}$)					
Surface	0.09 ± 0.01	0.06 ± 0.02	0.10 ± 0.01	0.11 ± 0.01	0.1 ± 0.03
DCM	0.36 ± 0.06	0.26 ± 0.10	0.03 ± 0.01	0.60 ± 0.11	0.4 ± 0.14
5-B DCM	0.33 ± 0.03	0.20 ± 0.04	0.18 ± 0.00	0.40 ± 0.11	0.4 ± 0.19
SiO_4H_4 ($\mu\text{mol kg}^{-1}$)					
Surface	1.1 ± 0.06	0.9 ± 0.04	1.1 ± 0.1	1.2 ± 0.1	1.3 ± 0.1
DCM	1.6 ± 0.14	1.2 ± 0.10	1.2 ± 0.2	2.1 ± 0.3	1.9 ± 0.3
5-B DCM	1.8 ± 0.10	1.3 ± 0.10	1.4 ± 0.1	1.7 ± 0.5	2.0 ± 1.0
DOC ($\mu\text{mol L}^{-1}$)					
Surface	80.9 ± 1.7	73.2 ± 1.4	79.1 ± 1.9	84.7 ± 2.5	82.9 ± 3.1
DCM	69.8 ± 1.4	62.6 ± 1.4	67.1 ± 2.2	70.8 ± 1.3	77.7 ± 3.2
5-B DCM	72.2 ± 1.2	67.0 ± 1.5	71.0 ± 1.7	74.7 ± 1.4	79.2 ± 2.6
DON ($\mu\text{mol L}^{-1}$)					
Surface	6.7 ± 0.2	6.0 ± 0.3	6.5 ± 0.2	7.0 ± 0.2	7.0 ± 0.5
DCM	6.2 ± 0.2	5.8 ± 0.3	5.8 ± 0.2	6.1 ± 0.2	6.9 ± 0.5
5-B DCM	6.2 ± 0.1	5.9 ± 0.3	5.9 ± 0.2	6.2 ± 0.1	6.8 ± 0.3

Table 2.5. continuation

	Cruise	North	West	South	East
POC ($\mu\text{mol L}^{-1}$)					
Surface	6.1 ± 1.0	5.9 ± 2.1	2.8 ± 0.3	4.1 ± 0.6	8.9 ± 2.5
DCM	5.8 ± 0.9	4.6 ± 1.8	2.0 ± 0.3	5.1 ± 1.0	10.4 ± 2.0
5-B DCM	5.1 ± 0.8	5.5 ± 1.5	2.4 ± 0.2	4.5 ± 0.7	8.4 ± 2.4
PON ($\mu\text{mol L}^{-1}$)					
Surface	0.72 ± 0.12	0.67 ± 0.22	0.32 ± 0.01	0.45 ± 0.06	1.18 ± 0.31
DCM	0.72 ± 0.11	0.49 ± 0.15	0.24 ± 0.03	0.65 ± 0.14	1.49 ± 0.29
5-B DCM	0.61 ± 0.10	0.61 ± 0.18	0.26 ± 0.02	0.49 ± 0.10	1.25 ± 0.29
C : N DOM					
Surface	12.1 ± 0.2	12.2 ± 0.3	12.2 ± 0.5	12.1 ± 0.3	11.8 ± 0.6
DCM	11.3 ± 0.3	10.8 ± 0.4	11.6 ± 0.5	11.6 ± 0.5	11.2 ± 0.9
5-B DCM	11.9 ± 0.2	11.5 ± 0.4	12.1 ± 0.5	12.3 ± 0.4	11.6 ± 0.3
C : N POM					
Surface	8.5 ± 0.3	8.8 ± 0.4	8.8 ± 0.6	9.0 ± 0.4	7.5 ± 0.6
DCM	8.0 ± 0.4	9.5 ± 0.7	8.5 ± 0.4	7.8 ± 0.3	7.0 ± 0.9
5-B DCM	8.1 ± 0.4	9.8 ± 0.5	9.0 ± 0.2	7.3 ± 0.8	6.1 ± 0.9

In surface waters down to the base of DCM, the average N:P molar ratio was 7.9 ± 0.5 , ranging from 2.8 ± 0.1 at the surface to 10.9 ± 0.5 at the DCM. For the N:Si molar ratio, it ranged from 0.2 ± 0.1 at the surface to 2.4 ± 0.5 at DCM, with an average value above the DCM of 1.89 ± 0.3 . When each transect was considered separately, in surface waters, above DCM the N:P molar ratio ranged between 1.8 ± 1.7 in the Southern transect and 5.0 ± 3.5 in the Northern transect, being significantly higher in the Northern transect ($p < 0.05$). At the DCM it ranged from between 8.4 ± 0.3 in the Western transect and 11.6 ± 1.7 in the Northern and Southern transect, being significantly lower in Western transect ($p < 0.05$). Regarding the N:Si molar ratio, it ranged between 0.2 ± 0.1 (Western transect) and 0.3 ± 0.7 (Northern transect) at the surface and from 1.0 ± 0.5 (Western transect) to 3.3 ± 1.1 (Southern transect) at the DCM, without significantly differences between transects.

Below the DCM, the ODR of HPO_4^{-2} and salinity ($\text{HPO}_4^{-2} = -1.07 (\pm 0.04) \cdot S + 39 (\pm 1)$; $R^2 = 0.81$; $n = 107$) indicates that 81% of HPO_4^{-2} variability was due to water mass mixing. A multiple linear regression of NO_3^- with salinity and HPO_4^{-2} was also calculated ($\text{NO}_3^- = 20.0 (\pm 0.7) \cdot \text{HPO}_4^{-2} + 2.76 (\pm 0.6) \cdot S - 103 (\pm 27)$; $R^2 = 0.98$; $n = 102$) obtaining a

$\text{NO}_3^-:\text{HPO}_4^{2-}$ molar slope of 20.0 ± 0.7 . However, the $\text{NO}_3^-:\text{HPO}_4^{2-}$ slope is different between transects, being significantly lower in the Northern and Western transect ($p < 0.001$), 15.0 ± 0.4 and 17.1 ± 0.4 , respectively, than in Southern and Eastern transect with a higher slope of 19.5 ± 0.4 and 19.4 ± 0.7 respectively. Water mass mix explained 68% of SiO_4H_4 variability ($\text{SiO}_4\text{H}_4 = -4.9 (\pm 0.3) \cdot S + 184 (\pm 12)$; $R^2 = 0.68$; $n = 107$). As for the case of HPO_4^{2-} , a multiple linear regression of NO_3^- with salinity and SiO_4H_4 was also calculated ($\text{NO}_3^- = 2.6 (\pm 0.2) \cdot \text{SiO}_4\text{H}_4 - 5.5 (\pm 1.0) \cdot S + 202 (\pm 38)$; $R^2 = 0.92$; $n = 102$), obtaining a $\text{NO}_3^-:\text{SiO}_4\text{H}_4$ molar slope of 2.6 ± 0.17 . In addition, the multiple linear regression of NO_3^- with salinity and SiO_4H_4 , showed that the Northern transect had a significantly lower $\text{NO}_3^-:\text{SiO}_4\text{H}_4$ slope of 1.2 ± 0.4 ($p < 0.05$) than Western Southern and eastern transect (3.1 ± 0.3 , 2.5 ± 0.3 and 2.9 ± 0.4 respectively).

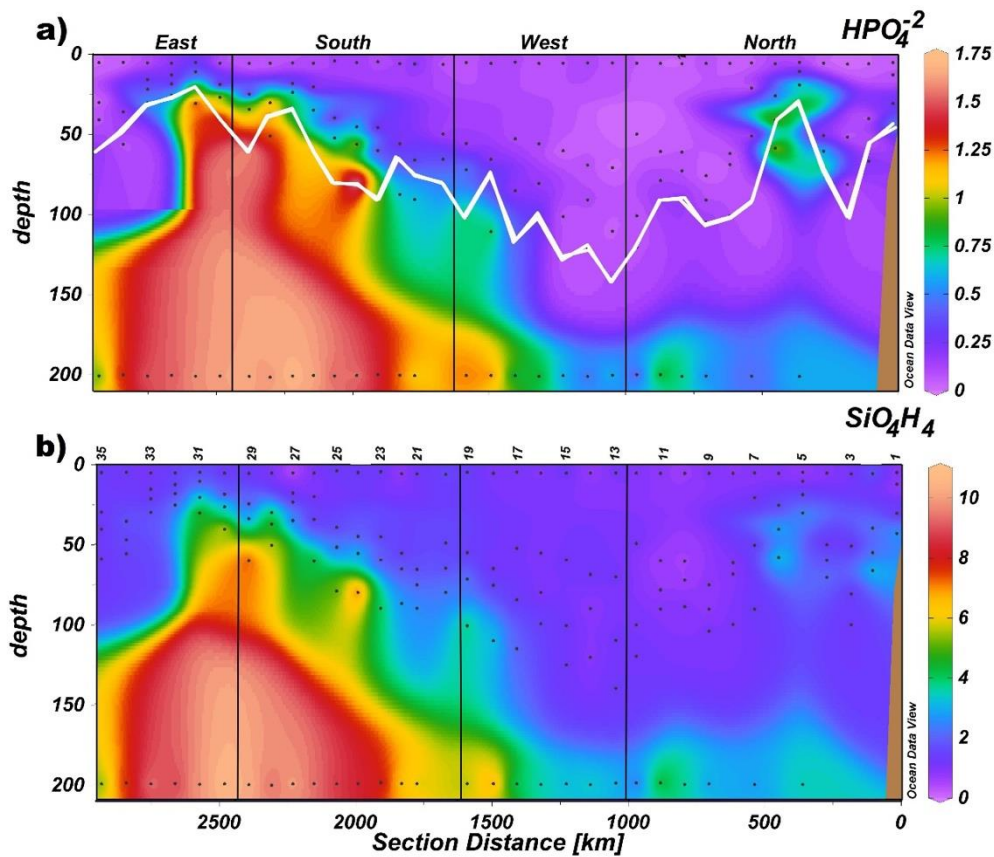


Figure 2.7. Distributions of phosphate (HPO_4^{2-}) in $\mu\text{mol kg}^{-1}$ (a), silicate (SiO_4H_4) in $\mu\text{mol kg}^{-1}$ (b) in the epipelagic layer during the FLUXES I cruise. Dots represent samples, vertical back lines represent the corners of the FLUXES I hydrographic box and the white line in panel (a) represents the base of the DCM. The x-axis shows the station number (b) or section distance (b). Produced with Ocean Data View (Schlitzer, 2017).

PON (Fig. 2.8a) and POC (Fig. S3a) concentrations showed similar distributions with a marked decrease below the DCM. Maximum concentrations of PON and POC were observed at the stations near the coast, in the Northern and Eastern transects. Maximum

PON coincided with the DCM in the Eastern ($1.49 \pm 0.3 \mu\text{mol L}^{-1}$) transect, while in the Western ($0.28 \pm 0.02 \mu\text{mol L}^{-1}$), Northern ($0.7 \pm 0.2 \mu\text{mol L}^{-1}$) and Southern ($0.55 \pm 0.1 \mu\text{mol L}^{-1}$) transects it was somewhat above the DCM (Table 2.5). In the upper 50 dbar, stn 5 shows very high values of POC and PON.

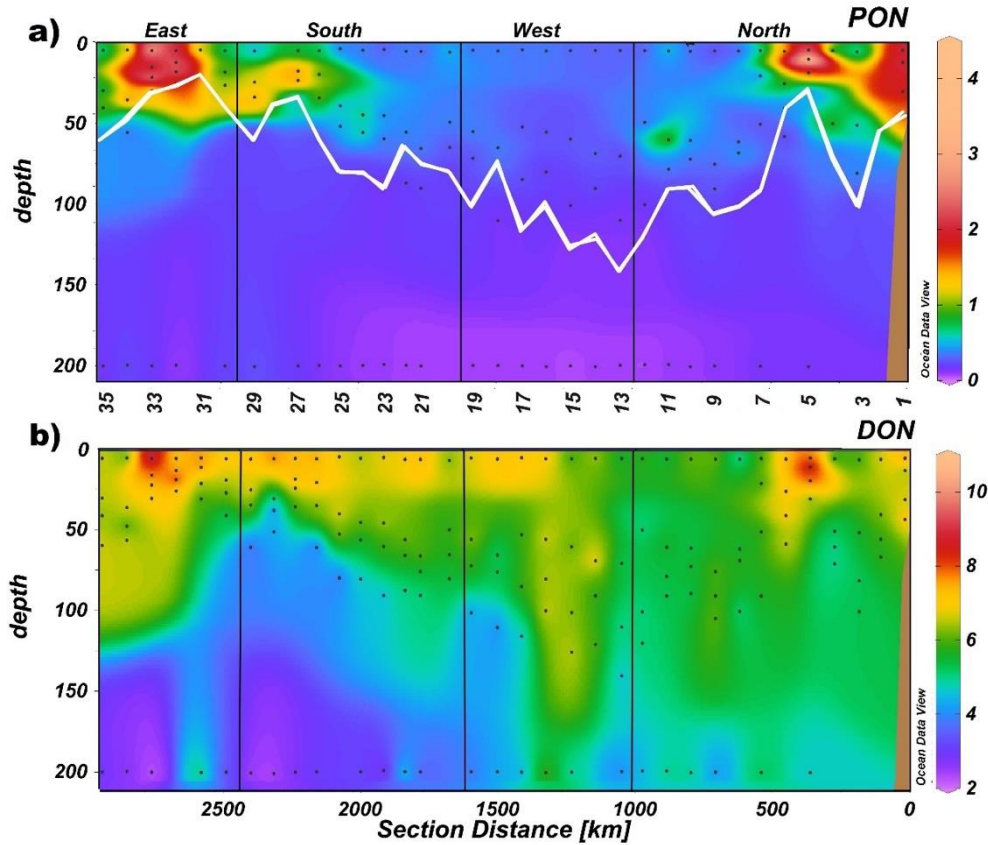


Figure 2.8. Distributions of PON in $\mu\text{mol L}^{-1}$ (a) and DON in $\mu\text{mol L}^{-1}$ (b) in the epipelagic layer during the FLUXES I cruise, dots represent samples, vertical black lines represent the corners of the FLUXES I hydrographic box and the white line in panel a represents the base of the DCM. The x-axis shows the station number (a) or section distance in km (b). Produced with Ocean Data View (Schlitzer, 2017).

Average C:N molar ratios of POM above DCM were significantly lower in the Eastern transect ($p < 0.01$) (Table 2.5). In the Western, Southern and Eastern transects, minimum values of the C:N molar ratio of POM were associated with the DCM (Table 2.5). Below the DCM average C:N molar ratios of POM were higher in the Northern and Western transects (>8.9) than in the Southern and Eastern transects (<7.3) ($p < 0.005$) (Table 2.5).

DON (Fig. 2.8b) and DOC (Fig. S3b) showed maximum average concentrations of $6.7 \pm 0.2 \mu\text{mol L}^{-1}$ and $80.9 \pm 1.7 \mu\text{mol L}^{-1}$ at the surface (Table 2.5), and decreased with

Chapter 2:

depth. DON and DOC levels were significantly higher in the Southern transect at the surface, while at the DCM, the highest DON and DOC concentrations were found in the Eastern (coastal) transect (Fig. 2.8a. Table 2.5). The average C:N molar ratio of DOM throughout the epipelagic layer (5 to 200 dbar) was 12.0 ± 0.3 , significantly higher than the average C:N molar ratio of POM, 8.1 ± 0.4 (Table 2.5). Above the DCM, at the DCM and below DCM average C:N molar ratio of DOM showed similar values in all transects ($p > 0.05$).

To quantify the contribution of DOC and POC to the oxygen demand and DON and PON to the local NO_3^- production, correlations with AOU (for DOC and POC) and with NO_3^- (for PON and DON) below the DCM were computed. DOC showed a significant correlation with AOU (ODR; $\text{DOC} = -0.07 (\pm 0.01) \cdot \text{AOU} + 67 (\pm 1)$; $R^2 = 0.29$; $n = 105$). The slope of the linear regression indicated that DOC supported around $10 \pm 1 \%$, of the oxygen demand in epipelagic waters assuming a Redfieldian $-\text{O}_2:\text{C}$ stoichiometric ratio of $1.4 \text{ mol O}_2 \text{ mol C}^{-1}$ (Anderson, 1995). When salinity was added to the multiple regression (ODR; $\text{DOC} = -0.17 (\pm 0.01) \cdot \text{AOU} - 17 (\pm 2) \cdot S + 725 (\pm 94)$; $R^2 = 0.52$; $n = 105$), a significantly higher DOC:AOU molar slope was obtained, with DOC supporting $24 \pm 1 \%$. For the case of POC with AOU (ODR; $\text{POC} = -0.014 (\pm 0.005) \cdot \text{AOU} + 4.4 (\pm 0.5)$; $R^2 = 0.07$; $n = 97$), inclusion of salinity increased the POC :AOU coefficient to -0.076 ± 0.007 (ODR; $\text{POC} = -0.076 (\pm 0.007) \cdot \text{AOU} - 11 (\pm 1) \cdot S + 411 (\pm 40)$; $R^2 = 0.55$; $n = 97$), indicating that POC supported around $10 \pm 1 \%$ of the oxygen demand of the epipelagic waters below the pycnocline. When each transect was considered separately, DOC supported similar percentage of the oxygen demand in all transects ($p > 0.1$). For the case of POC, significantly higher POC:AOU coefficients were obtained in the Northern and Eastern transect (0.11 ± 0.02 and 0.10 ± 0.01 , respectively) than in the Western and Southern transect (0.017 ± 0.006 and 0.038 ± 0.009 , respectively) ($p < 0.025$). These numbers indicate that in the Northern and Eastern transect, POC supports higher percentage of the oxygen demand ($>10 \%$ vs $<4\%$, respectively)

The simple correlation of DON with NO_3^- (ODR; $\text{DON} = -0.014 (\pm 0.001) \cdot \text{NO}_3^- + 6.2 (\pm 0.1)$; $R^2 = 0.48$ $n = 103$), would indicate that DON supported $1.4 \pm 0.1 \%$ of the NO_3^- production. However, when salinity was added to correct the water mass mixing the multiple regression ($\text{DON} = -0.17 (\pm 0.02) \cdot \text{NO}_3^- - 2.0 (\pm 0.4) \cdot S + 81 (\pm 14)$; $R^2 = 0.54$; $n = 103$), indicated that it really supported $17 \pm 2 \%$. For the case of PON the ODR with NO_3^- (ODR; $\text{PON} = -0.012 (\pm 0.005) \cdot \text{NO}_3^- + 0.52 (\pm 0.07)$; $R^2 = 0.04$ $n = 94$) indicates that PON

supported 1.2 ± 0.5 % of NO_3^- production, although when corrected for water mass mixing ($\text{PON} = -0.081 (\pm 0.008) \cdot \text{NO}_3^- - 1.6 (\pm 0.1) \cdot S + 61 (\pm 6)$; $R^2 = 0.53$; $n = 94$), it resulted that PON really contributed 8.1 ± 0.8 % to nitrate production. Furthermore, when each transect was considered separately, the multiple regression of DON and PON with NO_3^- and salinity, showed that DON supported similar percentage of the NO_3^- production in each transect ($p > 0.2$), while PON had significantly higher PON: NO_3^- coefficient in the Northern and Eastern transect (0.14 ± 0.03 and 0.10 ± 0.01 , respectively) than in the Western and Southern transect (0.018 ± 0.005 and 0.04 ± 0.01 , respectively) ($p < 0.025$).

2.3.2.2 Meso- and bathypelagic layer

NO_3^- (Fig. 2.9a) showed maximum values between 500 and 1000 dbar. Archetype NO_3^- was the lowest ($6.5 \pm 1.4 \mu\text{mol kg}^{-1}$) in the shallowest WT, MMW (Table 2.6), while the highest values corresponded to SPMW and AA, with 30.9 ± 0.7 and $31.3 \pm 0.6 \mu\text{mol kg}^{-1}$, respectively. WTs mixing explained 94% of the variability of NO_3^- , but SE of $\pm 1.81 \mu\text{mol kg}^{-1}$ was larger than the measurement error of about $\pm 0.1 \mu\text{mol kg}^{-1}$. Inclusion of AOU as explanatory variable increased the explained variability of the NO_3^- distribution to 98% (Table 2.6), with a NO_3^- :AOU coefficient independent of WT mixing of 0.109 ± 0.005 (Table 2.6). In addition, the Northern and Eastern transects have significantly higher NO_3^- :AOU coefficient than the Western and Southern transects ($p < 0.025$) (Table 2.7). The concentrations of NO_2^- and NH_4^+ in meso- and bathypelagic layers were extremely low with mean values of 0.03 ± 0.01 and $0.03 \pm 0.02 \mu\text{mol kg}^{-1}$, respectively.

HPO_4^{2-} (Fig. 2.9b) showed a distribution parallel to NO_3^- (Fig. 2.9a). Archetype values of HPO_4^{2-} ranged from $0.4 \pm 0.1 \mu\text{mol kg}^{-1}$ in SACW₁₈ to $1.90 \pm 0.04 \mu\text{mol kg}^{-1}$, in the intermediate AA and SPMW, and then decreased with depth until reaching a value of $1.50 \pm 0.01 \mu\text{mol kg}^{-1}$ in LNEADW (Table 2.3). WT mixing explained 96% of the variability of HPO_4^{2-} with a SE of $\pm 0.08 \mu\text{mol kg}^{-1}$ which was larger than the measurement error about $\pm 0.02 \mu\text{mol kg}^{-1}$. In addition, when AOU was added the explained variability was 95% and a significant HPO_4^{2-} :AOU molar coefficient of 0.0051 ± 0.0002 was obtained (Table 2.6). When each transect was considered separately, the Eastern transect showed significantly higher HPO_4^{2-} :AOU coefficient than the Western and Southern transects ($p < 0.001$) (Table 2.7). In addition, when HPO_4^{2-} was added as explanatory variable to NO_3^- the explained variance was 98% with a SE of $\pm 1.1 \mu\text{mol kg}^{-1}$ and with a NO_3^- : HPO_4^{2-} molar

coefficient of 18 ± 0.7 (Table 2.6). However, the Southern transect showed significantly lower $\text{NO}_3^-:\text{HPO}_4^{2-}$ coefficients than the Northern and Western transects (Table 2.7).

PON (Fig. 2.9c) decreased with depth down to the MW level and then remained almost constant to the bottom. The highest concentrations of PON, 0.33 ± 0.1 and $0.25 \pm 0.1 \mu\text{mol L}^{-1}$, were found in the shallowest central waters SACW_18 and MMW, respectively (Table 2.3). The multiple regression of PON with X_{ij} explained 29% of its variability (Table 2.3) and the inclusion of AOU as explanatory variable increased the explained variability to 44% with a SE reduction of 23%, while inclusion of NO_3^- increased the explained variability to 34%. The PON:AOU coefficient was -0.0034 ± 0.001 , while the PON: NO_3^- coefficient was -0.021 ± 0.004 , meaning that PON contributes only $2.1 \pm 0.4\%$ to the production of NO_3^- (Table 2.6).

The lowest PON concentrations were found in the Western (ocean) transect, while the Northern transect presented two PON maxima in SACW_18 and MMW (Table 2.4). In the intermediate and deep WTs, the highest concentrations were observed in the Eastern (coastal) transect ($p < 0.01$). The variability of PON explained with the multiple regression including X_{ij} and AOU or NO_3^- as explanatory variables was lower in the Southern than in the Northern transect (Table 2.7), with NO_3^- coefficients of -0.014 ± 0.002 and -0.039 ± 0.010 respectively, indicating that PON represented $1.4 \pm 0.2\%$ and $3.9 \pm 1.0\%$ of the mineralised NO_3^- .

POC (Fig. S4a) generally mirrored the PON distribution in central and intermediate waters. WTs mixing explained only 26% of the POC variability in the CVFZ (Table 2.3), which increased to 38% when AOU was included in the multiple linear regression, accompanied by a SE reduction of 46% (Table 2.6). The AOU coefficient of the multiple regression $-0.032 \pm 0.005 \text{ mol C mol O}_2^{-1}$ (Table 2.6), represents the average stoichiometric ratio of POC to O_2 consumption for the meso- and bathypelagic waters in the CVFZ. This ratio is independent of water mass mixing and indicates that POC covers only $4.5 \pm 0.7\%$ of the oxygen demand during water mass mixing in the area, assuming a $\text{O}_2:\text{C}$ Redfield ratio of $1.4 \text{ mol O}_2 \text{ mol C}^{-1}$ (Anderson, 1995).

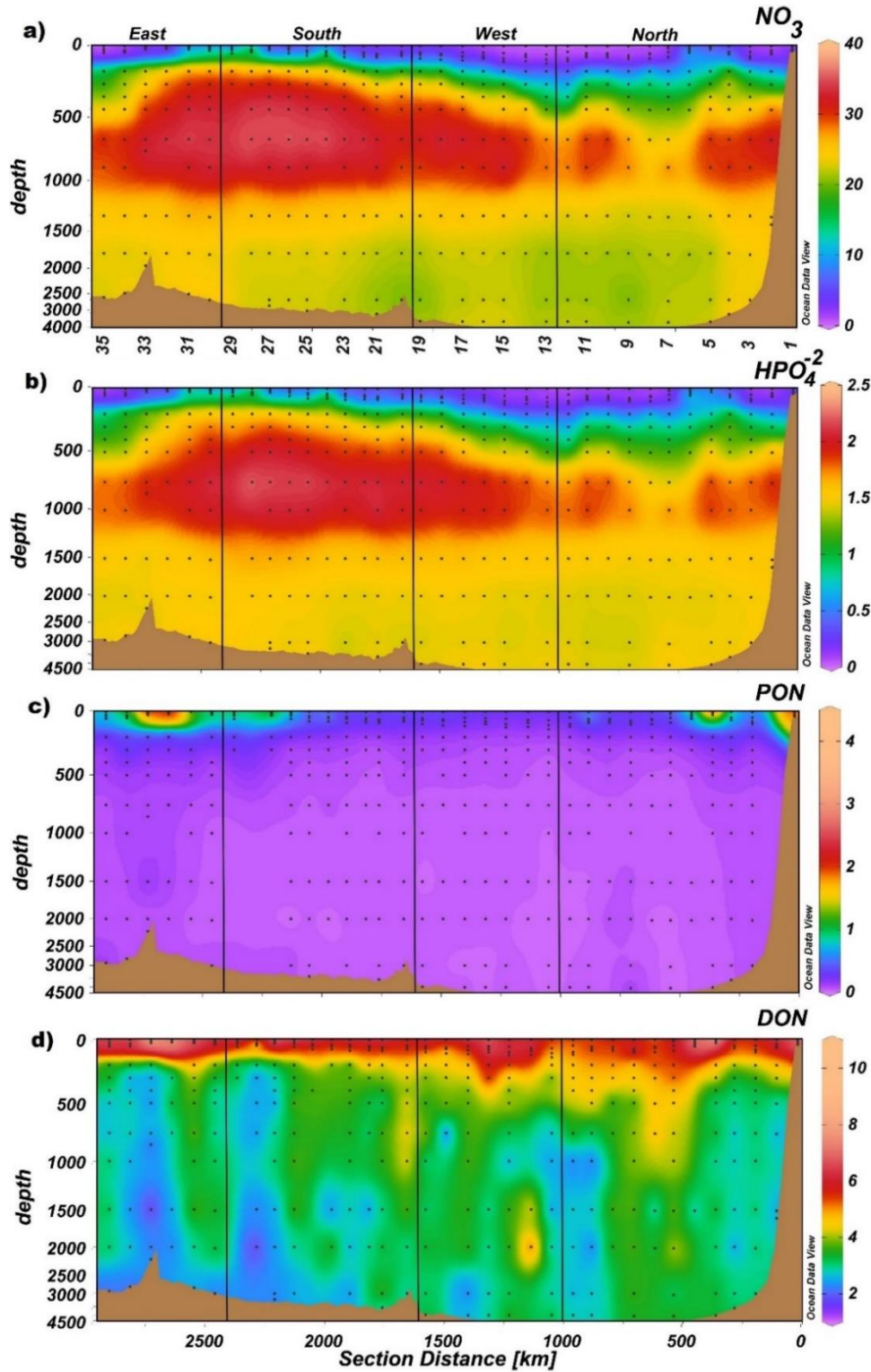


Figure 2.9. Full depth distributions of NO_3^- in $\mu\text{mol kg}^{-1}$ (a), HPO_4^{2-} in $\mu\text{mol kg}^{-1}$ (b) DON in $\mu\text{mol L}^{-1}$ (c) and PON in $\mu\text{mol L}^{-1}$ (d) during the FLUXES I cruise. Dots represent samples and vertical black lines represent the corners of the FLUXES I hydrographic box. Note that depth scale is not linear. The x-axis shows the station number (a) or section distance in km (d). Note that depth scale is non-linear. Produced with Ocean Data View (Schlitzer, 2017).

Table 2.6. Multiple linear regressions of DOC, DON, POC, PON and NO_3^- with the water type proportions (X_{ij}) and AOU, NO_3^- or HPO_4^{2-} . Determination coefficient (R^2_{+1}), standard deviation (SE_{+1}), percentage of R^2 increase (% R^2) and percentage of SE reduction (%SE) between the multiple linear regression with X_{ij} (Table 2.3) and the multiple linear regression with X_{ij} and AOU or NO_3^- , regression coefficient of each variable with AOU, NO_3^- or HPO_4^{2-} (β), and standard error of the estimate (SE_β) and p -value of β .

	DOC vs. AOU	DON vs. AOU	POC vs. AOU	PON vs. AOU	NO_3^- vs AOU
R^2_{+1}	0.70	0.46	0.38	0.44	0.98
SE_{+1}	3.4	0.7	1.0	0.10	1.1
% R^2	11	5	46	52	3.5
% SE	15	22	23	23	38
β	-0.0260	-0.0130	-0.0325	-0.0034	0.109
SE_β	0.0154	0.0035	0.0049	0.0005	0.005
p-level	0.09	0.0003	2.1E-10	4.1E-11	3.7E-63

	HPO_4^{2-} vs AOU	PON vs. NO_3^-	DON vs. NO_3^-	NO_3^- vs. HPO_4^{2-}
R^2_{+1}	0.98	0.34	0.50	0.98
SE_{+1}	0.05	0.13	0.73	1.03
% R^2	4	17	14	3
% SE	50	0	19	42
β	0.0051	-0.0210	-0.1568	18
SE_β	0.0002	0.0004	0.0246	0.7
p-level	7.9E-66	2.99E-06	8.4E-10	4E-74

Table 2.7. AOU or NO_3^- coefficients of the multiple linear regressions of NO_3^- , HPO_4^{2-} , DOC, DON, POC, PON with the WT proportions (X_{ij}) and AOU, NO_3^- or HPO_4^{2-} for each transect. β , AOU, NO_3^- or HPO_4^{2-} coefficients of the multiple linear regression; SE_β , standard error and p -value of the estimation of β .

	North			West		
	β	SE_β	p	B	SE_β	p
DOC vs AOU	-0.061	0.032	0.06	n.s	n.s	n.s
DON vs AOU	n.s	n.s	n.s	n.s	n.s	n.s
POC vs AOU	-0.044	0.015	0.006	n.s	n.s	n.s
PON vs AOU	-0.004	0.002	0.020	n.s	n.s	n.s
DON vs NO_3^-	-0.120	0.030	0.001	n.s	n.s	n.s
PON vs NO_3^-	-0.039	0.011	0.001	0.074	0.032	0.022
NO_3^- vs AOU	0,11	0,01	4 E-20	0,15	0,02	2 E-10
HPO_4^{2-} vs AOU	0,006	0,0004	6 E-24	0,005	0,001	9 E-09
NO_3^- vs HPO_4^{2-}	18,8	1,005	7 E-33	21,2	1,6	3 E-19

	South			East		
	β	SE_β	P	B	SE_β	p
DOC vs AOU	-0.150	0.038	0.0001	n.s	n.s	n.s
DON vs AOU	-0.030	0.007	6 E-05	n.s	n.s	n.s
POC vs AOU	-0.017	0.005	0.002	n.s	n.s	n.s
PON vs AOU	-0.003	0.001	6 E-09	n.s	n.s	n.s
DON vs NO_3^-	-0.160	0.030	2 E-06	n.s	n.s	n.s
PON vs NO_3^-	-0.014	0.002	5 E-08	n.s	n.s	n.s
NO_3^- vs AOU	0,140	0,011	5 E-21	0,09	0,01	7 E-12
HPO_4^{2-} vs AOU	0,007	0,0005	9 E-24	0,004	0,0005	1 E-9
NO_3^- vs HPO_4^{2-}	14,7	1,40	4 E-17	18,2	1,96	9 E-13

The C:N molar ratio of POM increased significantly with depth from 9.9 ± 1.6 in SACW_18 to 17.3 ± 2.0 in LNEADW (Table 2.3). In central waters, the maximum C:N molar ratio of POM was observed in SACW_12 and ENACW_12, 12.4–12.5, while in the intermediate waters the ratio was similar for the three water masses, ranging from 14.2 to 14.5. In the deep waters, LNEADW presented the highest C:N molar ratio of POM. Concerning differences between transects, there were not significant differences in the C:N ratio of POM for ENACW_12 (Table 2.4). In the deep waters, the LSW presented the largest differences ($p < 0.0005$) being higher in the Western transect (Table 2.4).

DON (Fig. 2.9d) decreased with depth from $5.1 \pm 0.3 \mu\text{mol L}^{-1}$ in MMW to $3.1 \pm 0.3 \mu\text{mol L}^{-1}$ in the deepest WT, LNEADW (Table 2.3). The multiple regression with X_{ij} explained 44% of the variability of the distribution of DON in the CVFZ with a SE of $0.90 \mu\text{mol L}^{-1}$, 3 times the measurement error (Table 2.3). Addition of AOU to the multiple linear regression increased the explained variability to 46% and SE reduced by 22%. When NO_3^- was included as an explanatory variable, R^2 increased to 55% and SE reduced by 19%. In this case, the NO_3^- coefficient of -0.16 ± 0.02 indicated that DON supports $16 \pm 2\%$ of the NO_3^- production in the CVFZ (Table 2.6). When analysing the DON to NO_3^- coefficient of the multiple linear regression with X_{ij} and NO_3^- transect by transect, we obtained significant values only for the Northern (-0.12 ± 0.03) and Southern (-0.16 ± 0.03) transects (Table 2.7).

Archetype DOC values (Fig. S4b) ranged from $58.9 \pm 2.5 \mu\text{mol L}^{-1}$ in SACW_18 to $43.4 \pm 0.6 \mu\text{mol L}^{-1}$ in LNEADW (Table 2.3). The multiple regression with X_{ij} explained 63% of the DOC variability with a SE of $4.0 \mu\text{mol L}^{-1}$. The addition of AOU to the multiple linear regression increased the explained variability to 70% and produced a 15% reduction of SE (Table 2.6). The AOU coefficient of the multiple regression, $-0.026 \pm 0.015 \text{ mol C mol O}_2^{-1}$, indicates that DOC covers only $3.6 \pm 2.1\%$ of the oxygen demand during water mass mixing in the area, assuming a - $\text{O}_2\text{:C}$ Redfield ratio of $1.4 \text{ mol O}_2 \text{ mol C}^{-1}$.

Finally, the C:N molar ratio of DOM increased significantly ($p < 0.0005$) with depth from 11.6 ± 0.7 in the MMW to 15.2 ± 0.9 in the UNEADW (Table 2.3). In central waters, ENACW_12, which was present in the four transects, had a higher DOM C:N ratio in the Southern and Eastern transects, i.e. to the South of the CVF, than in the Northern and Western transects ($p < 0.025$) (Table 2.4). In intermediate waters, the C:N ratio was similar

for all transects, while in deep waters, the NEADW had significantly higher C:N ratio of DOM in the Eastern transect (Table 2.4).

2.4 Discussion

2.4.1 Variability in the epipelagic layer of the CVFZ

The relative position of the four transects in relation to the CVF and the proximity of the Mauritanian coast explains the large differences observed in Chl-a levels and depth of the DCM between transects. The depth of the DCM ranged from 33 to 82 dbar, being deeper and with lower Chl-a concentration in the Western transect, as expected in oligotrophic open ocean waters (Antoine et al., 1996; Mignot et al., 2014; Iuculano et al., 2019). Conversely, the DCM was shallower and with higher Chl-a concentration in the Eastern transect, because of the impact of the offshore export of coastal plankton communities by the CBGF (Gabric et al., 1993; Lovecchio et al., 2017; Santana-Falcón et al., 2020). The easternmost part of the Northern transect is dynamically very complex, with both cyclonic and anticyclonic eddies to the West and East of stn 5, respectively (Burgoa et al., 2021). The presence of these eddies produces a convergence in stn 5 that generates the displacement of the CVF to the North through this station (Fig. A10, (Burgoa et al., 2021)). This mesoscale variability at stn 5 is reflected in the higher concentration of Chl-a. The front interacts with the CBGF, which brought organic matter across the sampling point and generated a hydrographic anomaly around this station, which presents characteristics closer to those observed to the South of the front.

NH_4^+ and NO_2^- concentrations exhibited several maxima in the surroundings of the DCM. These maxima are associated with the enhanced microbial degradation processes of ammonification and nitrification at the DCM (Ward et al., 1982; Meeder et al., 2012). It has also been suggested that this primary nitrite maximum could be related to inefficient nitrate assimilative reduction by phytoplankton at the low light levels of the DCM (Lomas and Lipschultz, 2006). The mean concentrations of NH_4^+ ($0.06 \mu\text{mol kg}^{-1}$) and NO_2^- ($0.14 \mu\text{mol kg}^{-1}$) found throughout the epipelagic layer of the CVFZ were very low, as expected for oligotrophic waters (Twomey et al., 2007; Li et al., 2008). Higher levels of $0.8 \mu\text{mol kg}^{-1}$ for NH_4^+ and $1.5 \mu\text{mol kg}^{-1}$ for NO_2^- were found in the Eastern (coastal) transect, coinciding again with the offshore export of coastal waters by the CBGF. These levels are

comparable with those found by Clark et al. (2016) in the mixed layer of a filament in the Mauritanian upwelling.

The multiple correlation of nitrate with AOU and salinity below the DCM explained 97% of nitrate variability, showing a clear dependence with the mixing of SACW and ENACW. The inverse of the NO_3^- :AOU coefficient, 9.1 ± 0.3 , represents the $-\text{O}_2$:N ratio of organic matter mineralization in the epipelagic layer, which was similar than the 9.4 proposed by Redfield for the products of synthesis and early degradation of phytoplankton organic matter (Redfield et al., 1963; Anderson, 1995).

The low N:P molar ratio found above DCM denote nitrogen limitation to primary production in surface waters, while the N:P molar ratio below the DCM was 20.0 ± 0.7 , being higher than the canonical Redfield molar ratio of 16, showing a preferential remineralization of P. The N:Si molar ratio above the DCM of 0.2 ± 0.1 was lower than N:Si Redfield ratio (1:1), reflecting the N limitation in surface waters. On the contrary, the higher N:Si molar ratio of 3.0 ± 0.5 below DCM than Redfield ratios, reflects the expected faster regeneration of N than Si during mineralization of sinking POM in the ocean (Kudela and Dugdale, 2000; Álvarez-Salgado et al., 2014).

DON concentrations in surface waters are similar to those found by Letscher et al. (2013) in the Atlantic Ocean at 30°W. Higher DON concentrations in the Eastern and Southern transect, i.e. near the coast and South of the CVF, were especially noticeable. It is expected that DON levels are higher when approaching to the coastal ocean (Gattuso et al., 1998; Del Giorgio and Duarte, 2002) and can exceed $>7 \mu\text{mol L}^{-1}$ in highly productive areas such as in EBUEs (Hill and Wheeler, 2002; Hansell et al., 2009). These high DON levels can extend offshore due to the horizontal export by the CBF (Gabric et al., 1993; Lovecchio et al., 2017, 2018). The C:N ratio of DOM was also higher in the Eastern and Southern transects. The mean C:N molar ratio of DOM in epipelagic waters of the CVFZ (11.7) was significantly higher than the value of 10 mol C mol N⁻¹ found by Church et al. (2002) and Hopkinson and Vallino (2005) in coastal and offshore regions of the North Atlantic and North Pacific central gyre. However, Letscher et al. (2013) found higher values around 16 in the upper 50 dbar of Eastern Subtropical North Atlantic (10-40°N 10-50°W) and South Atlantic (10-40°S 10-50°W).

The highest concentrations of suspended POM were also observed near the coast. Van Camp et al. (1991) and Gabric et al. (1993) estimated that the offshore currents

associated with the giant filament could export around 50% of the POM produced in the coastal area around Cape Blanc (21°N). Furthermore, the maximum of suspended POM concentration in the Northern transect could be explained by the convergence at stn 5 produced by eddies. The location of the POM maxima in the Eastern transects coincided with the DCM, while in the Western transect POM maxima were observed at the surface because DCM is deeper which is related with the stratification and the higher nutrient concentration and production of the Eastern Transect.

The C:N molar ratio of POM was very variable, being the lowest near the coast i.e. along the Eastern transect (7.6 ± 0.4), because of the intense production of fresh organic matter with a lower C:N ratio in coastal waters and subsequent offshore export by the CBGF. Furthermore, C:N molar ratios to the North of the CVF were higher than to the South and always higher than the canonical Redfield ratio of 6.7 (Redfield et al., 1963). In fact, Martiny et al. (2013) showed large spatial variations in the C:N molar ratio of POM in the epipelagic ocean that differed substantially from the classical Redfield ratio, proposing a C:N:P ratio of 137:18:1 in warm, nutrient-rich upwelling zones. This C:N molar ratio of 7.6 is lower than the average value of 8.5 that we found down to the base of the DCM in the CVFZ.

2.4.2 Impact of water mass mixing in meso- and bathypelagic layers

We have applied a water mass analysis to obtain archetype inorganic nutrients, DOM and POM concentrations for the 11 WT's identified during the FLUXES I cruise, for the entire cruise and for each transect. Our water mass analysis followed Pastor et al. (2012). With regard to the central waters, ENACW and SACW differ in their thermohaline and chemical characteristics as a result of their different origin and history from their respective formation areas to the CVFZ (Stramma and Schott, 1999). ENACW is relatively more ventilated and, therefore, well oxygenated, which explains the contrasting dissolved oxygen concentrations in relation to their position with respect to the CVF. The coexistence of the different ENACW and SACW types was evident in the large-scale distribution of water properties in the FLUXES I hydrographic box, as well as at the mesoscale range, with the meandering of the CVF tracing the presence of low salinity central waters of southern origin in some stations of the Northern transect.

Archetype DON concentration in ENACW (3.0 to $4.2 \mu\text{mol L}^{-1}$) are lower than those found in the Eastern North Atlantic by Álvarez-Salgado et al. (2013) at 40°N . This difference could be explained because ENACW at 40°N is closer to the formation area of this water mass and, therefore younger and DON-rich, compared to the same water mass at 20°N . Furthermore, in intermediate and deep waters, DON concentrations also were lower to those found by these authors. Archetype DON concentrations explained an important fraction (44%) of the total DON variability in the CVFZ, however the SE of $0.90 \mu\text{mol L}^{-1}$, was 3 times higher than the measurement error, suggesting that basin-scale processes occurring from the formation area to the CVFZ are the main drivers of the DON variability

PON concentrations in the mesopelagic layer of the CVFZ are low, with an average value of $0.11 \pm 0.1 \mu\text{mol L}^{-1}$. Baltar et al. (2009) reported similar concentrations of suspended PON in the mesopelagic and bathypelagic layer of the Subtropical North Atlantic (35°N to 5°N) ($0.1 \mu\text{mol L}^{-1}$). Despite the low contribution of PON, as expected, it shows slightly higher concentrations near the coast and lower in open ocean.

The C:N ratios of suspended POM and DOM are higher than the canonical Redfield ratio and increase with depth indicating PON and DON depletion with respect to POC and DOC due to preferential remineralisation of nitrogen-rich compounds (Hopkinson and Vallino, 2005; Letscher et al., 2013; Lønborg and Álvarez-Salgado, 2014). Previous research in the study area found elevated, and sometimes depth dependent, C:N ratios of sinking POM, higher than the Redfield ratio (Fischer et al., 2009; Nowald et al., 2015), but always lower than our C:N ratios of suspended POM. The large residence time of small size suspended particles in the water column exacerbates the impact of preferential nitrogen mineralisation, explaining the higher C:N molar ratios observed. The same trend of higher C:N ratios of suspended compared to sinking POM was observed by Schneider et al. (2003) in the subtropical gyre of the North Pacific.

2.4.3 Remineralisation of organic matter in the CVFZ

The inverse of the coefficient of the multiple linear regression of NO_3^- or HPO_4^{2-} with AOU ($\text{NO}_3^-:\text{AOU}$ and $\text{HPO}_4^{2-}:\text{AOU}$, respectively) represent the $-\text{O}_2:\text{N}$ and $-\text{O}_2:\text{P}$ ratios of organic matter mineralization (Redfield et al., 1963; Anderson and Sarmiento, 1994;

Anderson, 1995). In epipelagic waters below DCM, the inverse of the NO_3^- :AOU and HPO_4^{2-} :AOU coefficient (9.1 ± 0.2 and 153 ± 6) were in line with the Redfield ratio. Conversely, in meso- and bathypelagic waters, the inverse of the NO_3^- :AOU coefficient (9.12 ± 0.01) was in agreement with the Redfield ratio, but the inverse of the HPO_4^{2-} :AOU coefficient (196 ± 7) was significantly higher than the Redfield ratio of 150 to 170 (Anderson and Sarmiento, 1994; Anderson 1995), suggesting preferential remineralization of P, which has also been proposed by others studies (Sambrotto et al., 1993; Anderson and Sarmiento, 1994; Hupe and Karstensen, 2000; Osterroht and Thomas, 2000). In addition, the NO_3^- : HPO_4^{2-} coefficient of 18.0 ± 0.7 was also slightly higher than the canonical Redfield value of 16, which also indicates preferential remineralization of P.

The DON to NO_3^- coefficient indicates that in epipelagic layer below DCM, DON supported 18 ± 2 % of the NO_3^- production, while in meso- and bathypelagic waters represented 16 ± 2 %. Álvarez-Salgado et al. (2006) found that in NW Iberian upwelling (42°N) that the contribution of DOM to the mineralisation of organic nitrogen was 30%, while in deep open oceans waters of the North Pacific, the contribution of DON to the mineralised nitrate varied from 10% to 25% (Jackson and Williams, 1985; Maita and Yanada, 1990). In epipelagic waters below DCM, PON represented 8.1 ± 0.8 % of the NO_3^- production. While in meso- and bathypelagic waters it represents only $2.1 \pm 0.4\%$. The maximum contribution of PON to NO_3^- mineralisation in mesopelagic waters was $3.9 \pm 1.1\%$ in the Northern transect.

The DOC to AOU ratio obtained from the multiple linear correlation of DOC with the WT proportions and AOU indicates that DOC explains only $3.6 \pm 2.1\%$ of the oxygen demand of the meso- and bathypelagic waters of the CVFZ. This surprisingly low contribution is well below the 10-20% found by Aristegui et al. (2002) for the World Ocean, and the range of contributions (9- 28%) found for other authors in different region of the Atlantic Ocean (26.5% to the south of the Canary Islands, 9-19% in the deep North Atlantic; $28 \pm 3\%$ in the subpolar North Atlantic; $26 \pm 3\%$ in the Eastern North Atlantic) (Aristegui et al., 2003; Carlson et al., 2010; Alvarez-Salgado et al., 2013; Lønborg and Alvarez-Salgado, 2014). This result could be explained by the fact that most of the water masses in this region are far away from their formation areas, where the proportion of labile DOC is higher (Hansell et al., 2012; Hansell and Carlson, 2013) and by the massive flux of biodegradable sinking POM produced in the coast, which is subjected to the lateral export by the CBGF in the area, and the divergence below the surface to depth as the filament is

moving away from continental shelf, ballasted lithogenic materials (Iversen et al., 2010; Lovecchio et al., 2018). In the same way in the case of POC, it represents $4.5 \pm 0.7\%$ of the oxygen demand of the meso- and bathypelagic waters of the CVFZ. As for the case of PON with NO_3^- mineralisation, the maximum contribution of POC to the oxygen demand was in the Northern transect.

The low contribution of DON and suspended PON to the respiratory demand and NO_3^- regeneration in the euphotic zone and the dark ocean of the CVFZ indicates that mineralization processes were mainly supported by sinking POM. DOM and suspended POM may be exported rapidly offshore in this area of strong offshore zonal flow (Arístegui and Alvarez-Salgado, 2015), leaving a minor imprint in the biogeochemistry of the study area. This situation contrasts with the Northern location in Alonso-González et al. (2009), where the dominant mean flow is Southward and along-shore with the Canary Current, and the zonal transport is localized in mesoscale filaments and eddies (Álvarez-Salgado et al., 2007; Lovecchio et al., 2017). In addition, the higher contributions of DON to NO_3^- mineralisation (15.7%) than DOC to oxygen demand (3.6%) support the idea that the preferential N remineralisation explains the higher Redfield DOM C:N ratios in the CVFZ.

2.5 Conclusions

The distribution of inorganic nitrogen, DON and suspended PON in the CVFZ is dictated by 1) the position of the front, which separates surface and central waters of contrasting North and South Atlantic origin, and 2) the intersection with meanders of the frontal system associated with mesoscale structures and their interaction with the Cape Blanc giant upwelling filament. In the intermediate and deep waters, which are very distant from their respective source regions, the distributions are dictated by water mass mixing and remineralization from the source regions to the CVFZ. DON and suspended PON mineralisation in the study hydrographic box represent about 18% of the nitrogen mineralisation but higher than the 8.1% contribution of DOC and POC to the oxygen demand, suggesting that 1) the local nitrogen demand is mainly supported by sinking POM and 2) N-containing organic compounds are mineralised faster than C-containing organic compounds. The results obtained in this field study confirm a latitudinal gradient in the importance of the vertical vs. horizontal flows of organic matter in the Canary Current

Chapter 2:

EBUE, and suggest that the offshore regions of EBUEs act as a buffer zone that modifies the stoichiometry of the organic matter exported to the gyres, making it nitrogen poorer.

Chapter 3

**Meso- and submesoscale variability of
nitrogen species in the Cape Verde Frontal
Zone (NW Africa)**

The results presented in this chapter are also a manuscript in preparation.

Abstract

The FLUXES II cruise was conducted at high spatial resolution (< 10 km) in the Cape Verde Frontal Zone (CVFZ) during fall 2017. The aim was to investigate the impact of meso- and submesoscale physical structures on inorganic and organic N species distributions in epipelagic waters and the contribution of organic N pools to water column remineralisation processes in mesopelagic waters. The distributions of inorganic and organic N species and the $-O_2:N:Si:P$ stoichiometric ratios in the epipelagic layer were dictated by the presence of cyclonic and anticyclonic eddies in the area. In epipelagic waters above the pycnocline, low NO_2^- and NH_4^+ concentration $< 0.1 \mu\text{mol kg}^{-1}$ were found associated to nitrate and nitrite reduction by phytoplankton and microbial degradation processes. N:P molar ratios between 4.6 ± 1.7 and 6.4 ± 3.5 and N:Si molar ratio between 0.4 ± 0.1 and 0.9 ± 0.5 , in the surface mixed layer pointed to N limitation to net primary production in the region. This is also reflected in the high C:N molar ratios (> 8) of particular organic matter (POM). In epipelagic waters below the pycnocline, most of the variability ($R^2 > 0.79$) of inorganic nutrient distributions (nitrate, phosphate and silicate) was mainly explained by the mixing of central waters of contrasting North and South Atlantic origin, but local mineralization processes contributed to increase the explained variability ($R^2 > 0.88$). The observed $-O_2:N:P:Si$ molar ratios indicate that there was a preferential mineralization of N- and P-rich compounds, corroborated by the high C:N ratios (> 11) of POM. Dissolved organic nitrogen (DON) supported 33% of the nitrogen demand of epipelagic waters below the pycnocline, while suspended organic nitrogen (PON) supported only 2.4%, suggesting that the surface DON is removed via vertical mixing and subsequent mineralization below the mixed layer. In the mesopelagic layer, water mass mixing explained 54% of the variability of PON and most of its mineralization occurred mainly during the transit of the water masses from the formation sites to the CVFZ, suggesting that local mineralization seems to be essentially due to fast-sinking POM produced *in situ* or imported from the Mauritanian upwelling. The differences in C:N molar ratios of POM and the $-O_2:N:Si:P$ mineralization ratios with depth are of considerable importance for modelling the biological pump in C and N biogeochemical cycles and predicting its feedback mechanisms due to global change.

3.1 Introduction

In the marine environment, the combined nitrogen reservoir is composed of dissolved inorganic (DIN) (NO_3^- , NO_2^- , NH_4^+) and dissolved (DON) and particulate (PON) organic nitrogen. The mean vertical profiles of the three combined inorganic nitrogen forms show different patterns (Gruber, 2008; Zhang et al., 2020). Combined inorganic nitrogen is mostly present in the form of NO_3^- , which is the most oxidized form of nitrogen, generally presents near-surface depletion (depending, however, on the geographical area and the time of year) and enrichment at depth driven by the biological pump (McCarthy et al., 1998; Sarmiento and Gruber, 2006; Brandes et al., 2007; Zhang et al., 2020). NO_3^- is dominant in oxic environments below the pycnocline. In contrast, NH_4^+ and NO_2^- , accumulate at the base of the euphotic layer, and rapidly decrease their concentrations above and below this depth (Gruber, 2008; Smith et al., 2014; Zakem et al., 2018; Zhang et al., 2020). This distribution reflects their role as intermediary nitrogen forms that are rapidly produced and consumed through the water column (Gruber, 2008). NH_4^+ accumulation occurs because phytoplankton is limited by light, and organic nitrogen is rapidly remineralized (Gruber, 2008; Mulholland and Lomas, 2008; Glibert et al., 2016; Zhang et al., 2020), while the accumulation of NO_2^- to significant levels is mainly due to the inhibition by light of nitrifying bacteria and the low light levels for phytoplankton growth. In addition, NO_2^- is the least abundant N form, except in suboxic zones, while in anoxic environments, the most abundant N form is the most reduced natural form NH_4^+ (McCarthy et al., 1998; Sarmiento and Gruber, 2006; Brandes et al., 2007; Zhang et al., 2020).

Organic nitrogen is part of the dissolved (DOM), suspended (POM) and sinking fractions of organic matter, which contribute differently to the biological pump (Sanders et al., 2014; Boyd et al., 2019). The largest pool of organic nitrogen in the oceans is DON (Letscher et al., 2013; Hansell and Carlson, 2015; Zhang et al., 2020). Despite most of the DOM is recalcitrant, a small fraction is photo-reactive and/or bioavailable, contributing to the biological pump through the recycling and export of marine primary production (Hansell and Carlson, 2014). DON is the second-most abundant form of combined N with significant concentrations in the open ocean, especially in surface waters (Gruber, 2008). DON concentrations are elevated in eastern boundary current regions, where the increase of NO_3^- result in net production of DON (Lestcher et al., 2013; Sipler and Bronk, 2015). DON is produced in the surface ocean, where the fraction that escapes rapid microbial degradation

accumulates, being subsequently transported downwards by physical process such as advection and turbulent diffusion (Lévy et al., 2012; Nagai et al., 2015). PON represents a small proportion of the total organic nitrogen pool and exists in different sizes, ranging from very fine suspended particles to large aggregates, such as marine snow or fecal pellets (Gruber, 2008). Nitrogen is preferentially consumed compared to carbon, which produces an increase of the C:N molar ratio with depth (Schneider et al., 2003; Álvarez-Salgado et al., 2014). On the other hand, sinking POM is mainly controlled by solubilization (throughout the water column), the setting velocity of the aggregates of marine snow, mineralization and/or disaggregation, being able to sink at tenths to hundreds of meters per day (Nowald et al., 2009; Riley et al., 2012; Boyd et al., 2019). Vertical profiles of DOM and POM, and their C:N ratios, becomes useful to quantify the export from the upper ocean and to characterize the coupled nutrient and carbon cycling in the oceans (Letscher et al., 2015). Sinking POM usually present a C:N ratio close to the canonical Redfield value of 6.7 (Redfield et al., 1963; Anderson and Sarmiento, 1994), while suspended POM and DOM are characterized by much higher C:N ratios, particularly in the case of DOM (Letscher et al., 2015; Hansell and Carlson, 2015).

There is growing evidence that the three physical processes that drive the Biological Pump (BP) (lateral advection, vertical advection and turbulent mixing) occur at the submesoscale range (Omand et al., 2015; Boyd et al., 2019; Hernández-Hernández et al., 2020). The relevance of submesoscale processes is also important for the vertical transport of nutrients to the euphotic layer that control primary production, nitrogen fixation and the BP (Lévy et al., 2012; Hosegood et al., 2017; Hernández-Hernández et al., 2020). They are also relevant for the subduction of particle-rich surface waters on timescales of days and across spatial scales of 1–10 km, driven by strong vertical circulation associated with fronts and eddies, i.e. the so-called eddy-subduction pump (Niewiadomska et al., 2008; Estapa et al., 2015; Boyd et al., 2019). All these mesoscale processes have a significant effect on the distribution and metabolism of microorganisms and the presence of maxima of organic matter in the mesopelagic layer (Aristegui et al., 2003; Baltar et al., 2009). In fact, Sangrà et al. (2015) showed that submesoscale onshore flows in an upwelling filament may greatly reduce the impact of the overall offshore transport of carbon and other biogeochemical properties.

The interaction of the Cape Verde Front (CVF) with the Cape Blanc Giant Filament (CBGF), and the mixing processes between SACW and ENACW, produce an intense

meso- and submesoscale activity in the Cape Verde Frontal Zone (CVFZ) in the form of meanders and eddies (Arístegui et al., 2009; Lovecchio et al., 2018). The FLUXES II cruise was conducted in the season when upwelling was most intense in this area. High-resolution (< 10 km) vertical profiles of inorganic (NH_4^+ , NO_2^- and NO_3^-) and organic (DON and PON) nitrogen forms through the upper 1500 dbar were sampled. The aim of this chapter is using the data from this cruise to study: 1) the variability of organic and inorganic nitrogen species in the epipelagic CVFZ at the meso- and submesoscale range; and 2) assess the contribution of the dissolved, suspended and sinking organic nitrogen pools to water column remineralisation processes in the mesopelagic CVFZ.

3.2 Materials and Methods

3.2.1 Sampling strategy and analytical determinations

The FLUXES II cruise (Fig. 3.1) (R/V Sarmiento de Gamboa; Las Palmas - Las Palmas, 2-24 November 2017) consisted of two main activities: on the one hand, two SeaSoar grids for high-resolution characterization of the study area; and, on the other hand, two high spatial resolution biogeochemical transects (5 nautical miles, NM, 9.3km). The SeaSoar (MKII, Chelsea Instruments) was equipped with sensors for conductivity-temperature-depth (CTD, SBE 911 plus), oxygen (SBE 43), fluorescence (SeaPoint SCF) and turbidity (SeaPoint STM) determination. During the SeaSoar grids the speed was constant (8 knots), covering a depth range from sea surface to 450 dbar. In this PhD Thesis have used the data from the SeaSoar grids in order to contextualize the two high-resolution biogeochemical transects. The first SeaSoar grid consisted of 7 transects covering a box of 120×90 NM (222.2×166.7 km) carried out from November 5 to 10, while the second consisted of 8 transects that covered a box of 45×35 NM (83.3×64.8 km) from 19 to 20 November (Fig. 3.1). Furthermore, current velocities were measured with a 75 kHz RDI ship Acoustic Doppler Current Profiler (sADCP) configured in narrow band (long range). The sADCP provided along track raw data every 5 minutes from 36 to 800 dbar.

In the biogeochemical transects, a total of 48 hydrographic station were sampled at 10 levels each from surface to 1500 dbar. The first transect (long section) consisted of 36 station along 175 NM (324 km) with a horizontal resolution of 5 NM (9.3 km) (November 10th to 16th). The second transect, perpendicular to the first one and with the same

horizontal resolution, consisted of 12 stations along 55 NM (102 km) (November 19th to 20th) (Fig. 3.1). As in the FLUXES I cruise, the high resolution biogeochemical transects were sampled using a rosette sampler. The rosette carried 24 Niskin bottles of 12 L and it was equipped with a conductivity, temperature and depth (CTD) probe (SeaBird SBE911 plus), and sensors for dissolved oxygen (SeaBird SBE43), fluorescence of chlorophyll (SeaPoint SCF), turbidity (SeaPoint STM) transmittance (WetLabs C-Star) and nitrate (SUNA V2, SeaBird). Salinity was calibrated using a Guildline 8410-A Portasal salinometer, and conductivity measurements were converted into practical salinity units using the (UNESCO, 1985) equation. Dissolved oxygen was determined following Langdon (2010). The apparent oxygen utilization (AOU) was calculated following Benson and Krause (UNESCO, 1986), where $AOU = O_{2sat} - O_2$, with O_{2sat} being the oxygen saturation. The method of Holm-Hansen et al. (1965) was used to determine Chl-a. Nutrient concentrations were determined by segmented flow analysis. Nitrate, nitrite, phosphate, and silicate were determined colorimetrically as described in Hansen and Koroleff (1999). Ammonium was determined using the fluorometric method of K  rouel and Aminot (1997). POC and PON samples were filtered through 25 mm Whatman GF/F pre-combusted filters (450   C, 4h) using a vacuum filtration system, dried overnight in a vacuum dessicator under silicagel, and determined by high temperature catalytic oxidation (900  C) with a Perkin Elmer 2400 elemental analyser. DOC and TDN samples were not filtered due to the low concentration of particulate matter, frozen at -20  C and analysed by high temperature catalytic oxidation at 680  C with a Shimadzu TOC-V analyser connected in line with a TNM1 measuring unit (  lvarez-Salgado and Miller, 1998). For more details about sampling strategy and analytical determination see Chapter 2 of this PhD Thesis.

The analysis of TDN involves the transformation of all combined dissolved nitrogen species in the sample into nitric oxide (NO), which is subsequently determined by chemiluminescence (  lvarez-Salgado et al., 2022). Note that while nitrogen in DON and NH_4^+ (oxidation state, 3) is more reduced than in NO (oxidation state, +2), in NO_2^- (oxidation state, +3) and NO_3^- (oxidation state, +5) nitrogen is more oxidized. Since the sample is subjected to high temperature catalytic oxidation, the conditions are ideal for DON and NH_4^+ oxidation, but not so favorable for NO_2^- and NO_3^- reduction to NO. Consequently, a tight conditioning of the Pt-catalyst is essential to efficiently transform NO_2^- and NO_3^- into NO in the furnace of the Shimadzu TOC-V analyzer. When this conversion is not efficient, DON values are not reliable for samples with high NO_3^-

concentration. This was the case of the samples collected during the FLUXES II cruise, and therefore, in this chapter only DON values for the surface layer have been reported, due to generally low concentration of NO_3^- at the surface. This is an analytical issue faced by chemical oceanographers involved in the determination of TDN worldwide. The most recent compilation of DOC and TDN concentration in the open ocean (Hansell et al., 2021) highlighted the problem by restricting the TDN database to the upper 200 dbar.

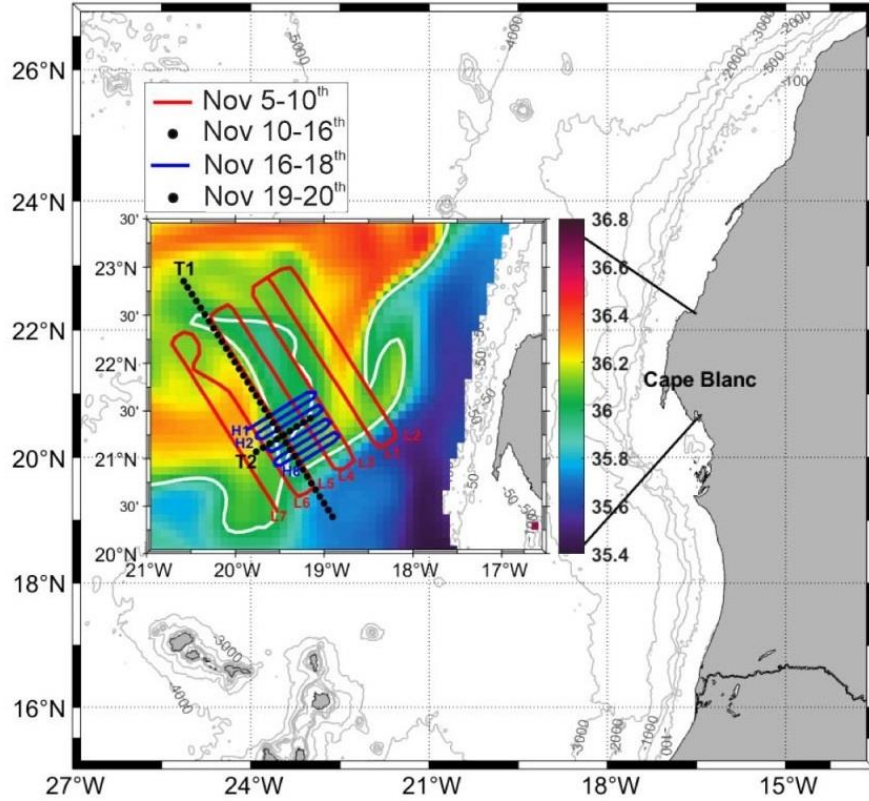


Figure 3.1. Map of the FLUXES II cruise presenting the low-resolution (red line) and high-resolution (blue line) SeaSoar grids and the biogeochemical transects T1 and T2 (black dots) over a plot of the average salinity during the cruise (Nov 5th – 20th) at 156 dbar depth obtained from GLORYS reanalysis. The white line represents the position of the Cape Verde Front (CVF) in FLUXES II, as identified by the 36.0 isohaline.

The pycnocline, which separates the surface mixed layer from the waters immediately below, has been identified as the depth of maximum stability (squared Brunt-Väisälä frequency, N^2_{max}) (Doval et al., 2001). It was calculated as follows:

$$N^2 = g \times \frac{\ln(\rho_z/\rho_{z-1})}{z - (z - 1)}$$

where g is the gravity acceleration (9.81 m s^{-2}), and ρ_z is the density at atmospheric pressure at depth z (in kg m^{-3}), calculated from salinity and temperature using the equation of UNESCO (1985).

3.2.2 Water mass analysis, water type proportion-weighted average values and multiple regression models

For the quantification of the proportions (X_{ij}) of the water types (WTs) that contribute to the water samples collected in the mesopelagic layer (200–1500 dbar) during the FLUXES II cruise, an optimum multiparameter (OMP) inverse method (Karstensen and Tomczak, 1998) has been used. This OMP method is the same that was developed for the FLUXES I cruise samples and has been explained in detail in Chapter 2. Note that during FLUXES II the maximum sampling depth was 1500 dbar and, therefore, UNEADW and LNEADW were not sampled. To run the OMP analysis, the following 4 oceanographically consistent WT mixing groups were defined (Fig. 3.2): 1) MMW - SACW18 - ENACW15; 2) SACW18 - ENACW15 - SACW12 - ENACW12; 3) SACW12 - ENACW12 - AA - SPMW; and 4) AA - SPMW - MW - LSW (Fig. 3.2). Since the samples from the epipelagic layer were excluded because of the non-conservative behavior of θ , S , SiO_4 and NO , the OMP was applied to 290 of the 480 samples collected during FLUXES II.

Once the WT proportions (X_{ij}) were obtained, we calculated: 1) the WT proportion weighted-average (hereafter, archetype) concentrations of AOU and the different nitrogen species; 2) the multiple linear regressions of the nitrogen species with X_{ij} (mixing model); and 3) with $X_{ij} + \text{AOU}$ (mixing + biogeochemical model) as already detailed in Chapter 2.

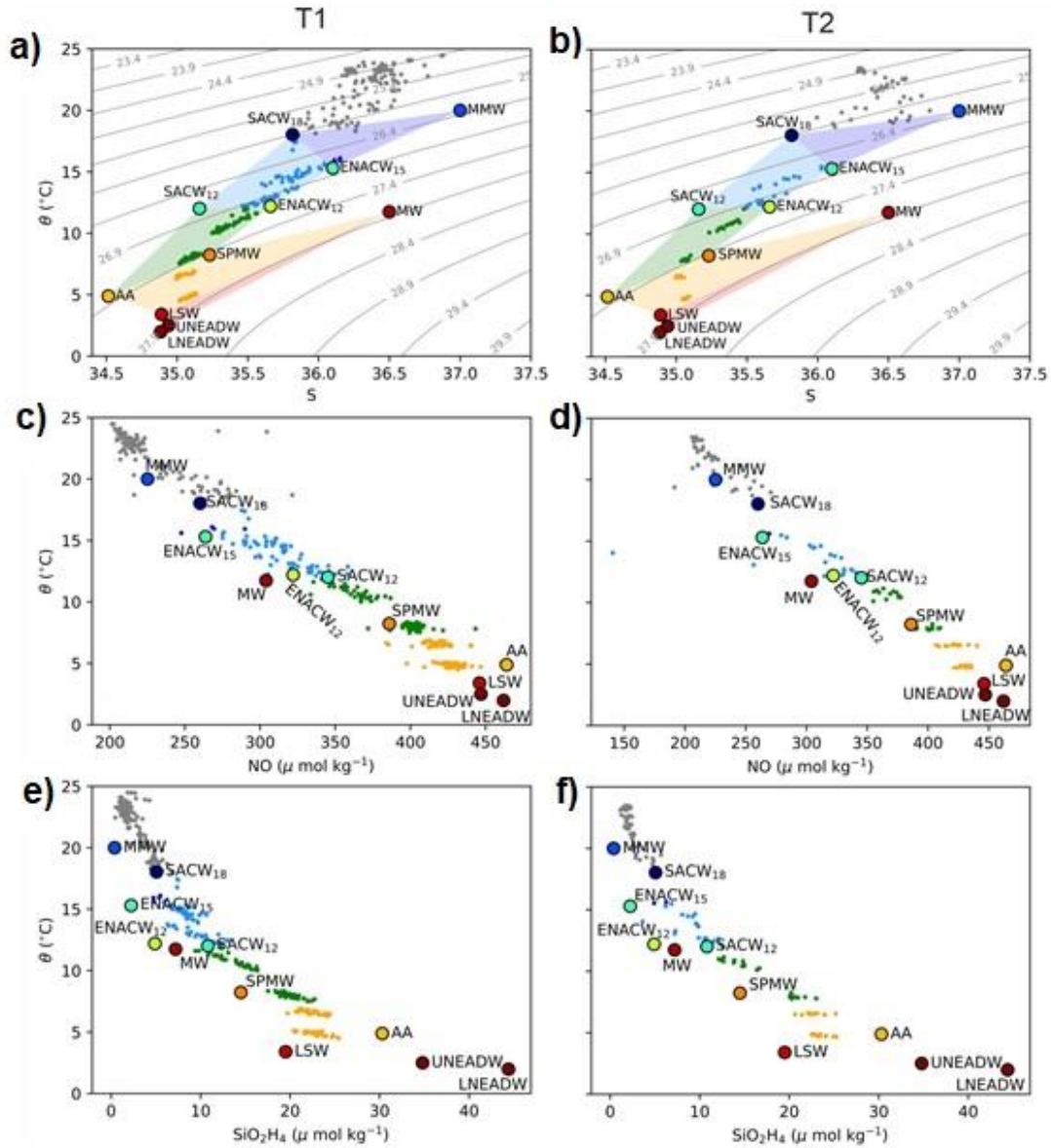


Figure 3.2. Potential temperature versus salinity (a, b), NO (c, d) and SiO_4H_4 (e, f) for the T1 (left) and T2 (right) during the FLUXES II cruise. Dots represent the water samples collected and the coloured shadow areas in (a) and (b) identify the mixing group assigned to each sample. Potential density contours are also shown in (a) and (b).

3.3 Results

3.3.1 Hydrography of the CVF in November 2017

Based on satellite altimetry images (Fig. 3.3), changes occurred in the mesoscale activity of the area between the two biogeochemical transects. When T1 was occupied (November 10th to 16th), while the first stations of the transect (stn 1-13) were affected by

Chapter 3:

a cyclonic eddy with the core at stn 4-5, most of the transect (stn 13-36) bordered the southwestern front of an anticyclonic eddy located immediately to the northeast (Fig. 3.3a). In contrast, when T2 was occupied (November 19th to 20th) the anticyclonic eddy displaced slightly to the northwest, changed its shape and intensified while the cyclonic eddy moved slightly to the south and weakened its intensity (Fig. 3.3b).

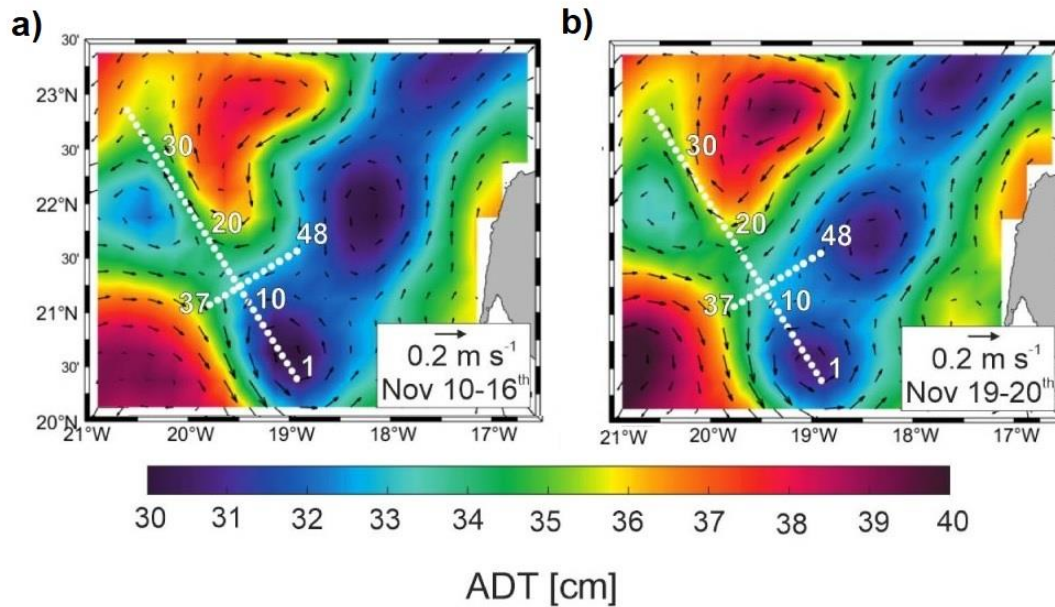


Figure 3.3. Average absolute dynamic topography with the derived geostrophic field superimposed at the time of T1 (a) and T2 (b). Made with GLORYS reanalysis. White dots represent the two biogeochemical transects occupied during the FLUXES II cruise, T1 and T2. Numbers are station numbers.

3.3.1.1 *Epipelagic layer*

In the upper 40 dbar of the southern part of T1, a shallow intrusion of low salinity ($S < 36.2$) surrounded by a water body of higher salinity ($S > 36.2$) was observed (Fig. 3.4a). Below, in the 40-200 dbar layer, this low salinity intrusion was also noticeable in the southern and northern parts of T1, producing a narrow zone with higher salinity located between them, at stations 19-22 (Fig. 3.4b).

Three hydrographic domains can be identified along T1, on basis of the position of the CVF, which was defined by the 36.0 isoline crossing the 150 dbar isobar (Zenk et al., 1991). The depth of the 36.0 isohaline showed a marked variability, from 40 dbar at stns 6-8 to more than 200 dbar at stns 23-27 (Fig. 3.5). The CVF was crossed at two stations (9 and 28), defining the three hydrographic domains as: A (stn 1-9), B (stn 9-28), and C (stn

28-36) (Fig. 3.5a). In addition, along T1 a well-marked pycnocline was observed (thick black line in Figure 3.5a) ranging from 24 to 64 dbar (average, 42 dbar), which separates the warmer surface mixed layer from the colder sub-surface waters below.

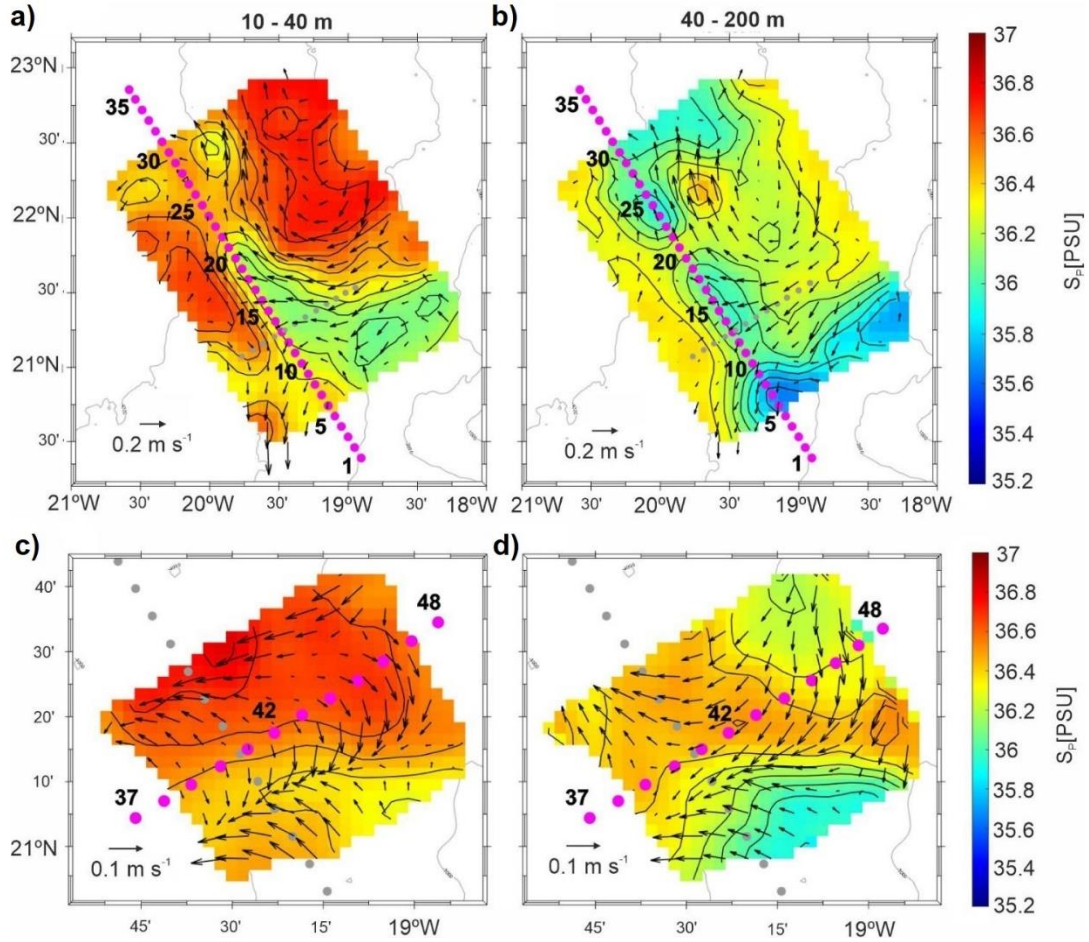


Figure 3.4. Average interpolated grids of salinity and horizontal velocity fields between 10-40 dbar and 40-200 dbar at the time when T1 (a, b) and T2 (c, d) were occupied. Current velocities were measured with the ship mounted ADCP. Purple dots represent the stations occupied during the biogeochemical transects.

Above the pycnocline, domains A and B showed similar salinities, while domain C presented an intrusion of high salinity water ($S > 36.5$) (Fig. 3.5a) that produces a marked salinity gradient across the pycnocline. Furthermore, this high salinity intrusion coincided with the highest surface temperatures ($p < 0.0005$) of 23.30 ± 0.04 °C (Fig. 3.5b; Table 3.1). Below the pycnocline, domains A and C, showed less salinity than domain B (Fig. 3.5a), reflecting the predominance of the less saline SACW, versus the predominance of the more saline ENACW in domain B. Nevertheless, along domain B from 50 to 80 dbar, a filament-

shaped low salinity intrusion of water with $S < 36$ was observed. This intrusion was associated to a SACW uplift in domain A which is inserted in domain B (Fig. 3.5a. horizontal dotted line) being slightly below the pycnocline. Temperatures below the pycnocline down to 200 dbar, were significantly different between the three domains, with domain B showing the highest values as expected when ENACW was the dominant water mass ($p < 0.0005$; Table 3.1).

The deep chlorophyll maximum (DCM) roughly coincided with the pycnocline depth (Fig. 3.5c). In domains A and C, the DCM was at 33.8 and 45.5 dbar respectively, while in domain B high Chl-a values reached the surface. Maximum values of Chl-a were found at the boundary between domains A and B, at stn 8-13, with concentrations above $1 \mu\text{g L}^{-1}$. The lowest values ($p < 0.0005$) of Chl-a, $0.37 \pm 0.01 \mu\text{g L}^{-1}$ coincided with the intrusion of high salinity water observed in domain C (Table 3.1).

Above the pycnocline, AOU was significantly different between the three domains, being the highest in domain A with $1.7 \pm 1.4 \mu\text{mol kg}^{-1}$ ($p < 0.05$, Table 3.1). In contrast, significantly lower values ($p < 0.0005$) of $-4.6 \pm 0.6 \mu\text{mol kg}^{-1}$ were found in domain B, which suggest higher net primary production in this domain. Below the pycnocline, domain B presented significantly lower values, which coincided with the warmer and saltier ENACW. The intrusion of SACW in this domain at 50-80 dbar was also traceable by the slightly higher levels of AOU (Fig. 3.5d).

Salinity distribution along T2 differed from T1, as expected from the satellite altimetry observations (Fig. 3.3) and SeaSoar surveys (Fig. 3.4). During T2, the low salinity water intrusion disappeared, being occupied with a high salinity surface water body (Fig. 3.4c), while between 40-200 dbar the less saline water was displaced to the south (Fig. 3.4d). This displacement in the upper 40 dbar was also noticeable in Figure 3.5a, with higher salinity below the pycnocline than at T1. The Chl-a distribution in the surface mixed layer showed higher values at both ends of T2, and lower in the middle, where Chl-a was higher below the pycnocline (Fig. 3.5c). The distribution of AOU showed higher concentrations at 100 dbar, similar to the levels found in domain A during T1. (Fig. 3.5d).

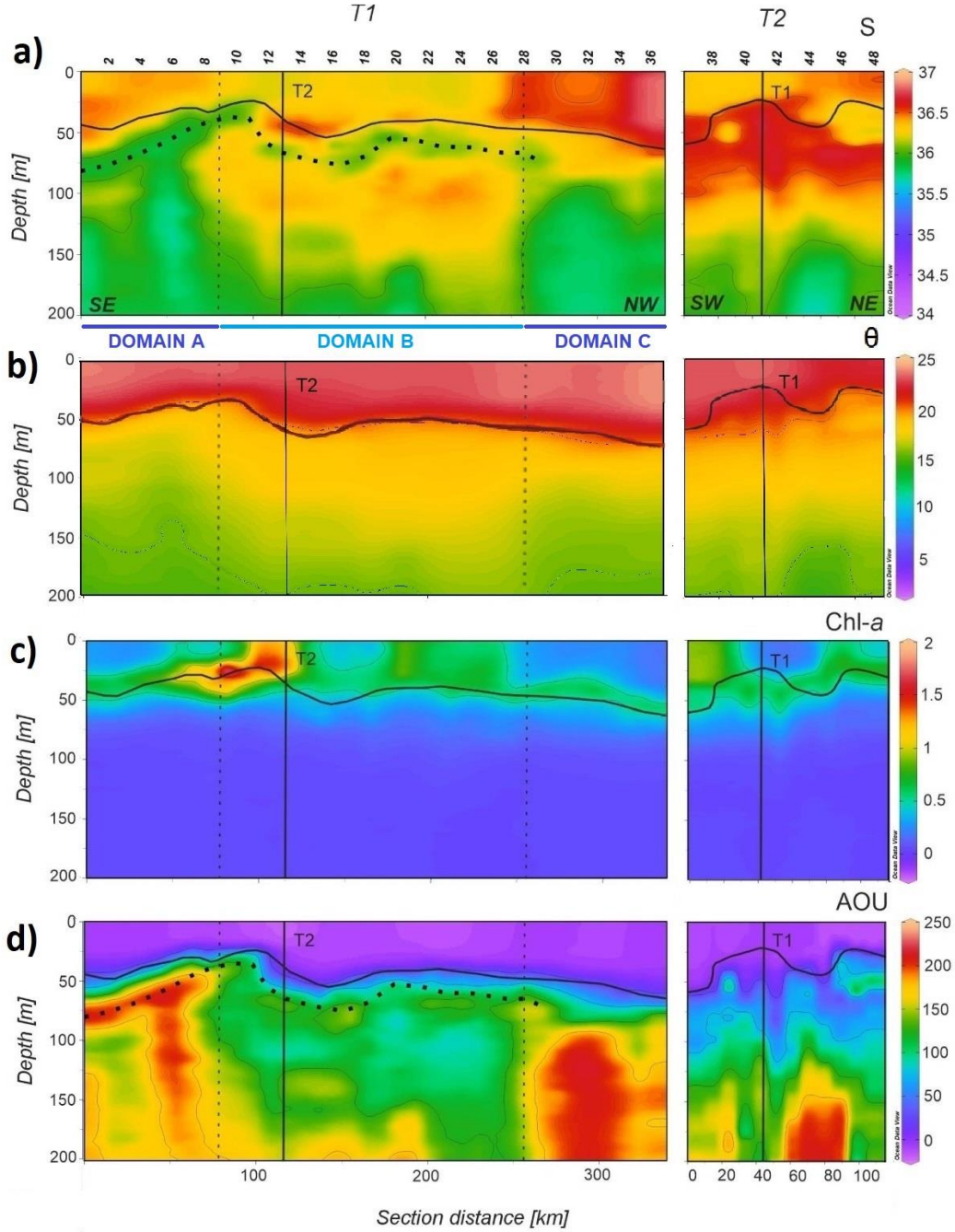


Figure 3.5. Distribution of salinity (S) (a), potential temperature (θ) in $^{\circ}\text{C}$ (b), Chl-a (chlorophyll a) in $\mu\text{g L}^{-1}$ (c) and apparent oxygen utilization (AOU) in $\mu\text{mol kg}^{-1}$ (d), in the epipelagic layer during the FLUXES II cruise along T1 (left) and T2 (right). All measurements were obtained at 1 dbar vertical resolution. T1 is divided into three domains (A-C) separated by vertical dotted lines at stn 9 and 28. Vertical black lines show the position of the orthogonal transects T2 and T1, respectively. Horizontal black line shows the position of the pycnocline and horizontal black dotted line in (a) and (d) show the position of the low salinity intrusion (see text). Section distance is counting from southeast (SE) to northwest (NW) in T1 and from southwest (SW) to northeast (NE) in T2 (labelled at the bottom of the first panel). Produced with Ocean Data View (Schlitzer, 2017).

Table 3.1. Thermohaline and chemical characteristics (average value \pm SE) (Salinity, θ in $^{\circ}\text{C}$, Chl-a in $\mu\text{g L}^{-1}$, AOU in $\mu\text{mol kg}^{-1}$) of epipelagic waters above and below the pycnocline and at the deep chlorophyll maximum (DCM) along the biogeochemical transect T1. The depth of DCM was 34.0 ± 2.7 , 39.6 ± 1.6 and 45.7 ± 2.9 dbar in domains A, B and C respectively.

Domain	Salinity			Temperature		
	Above pyc.	DCM	Below pyc.	Above pyc.	DCM	Below pyc.
A	36.38 ± 0.01	36.28 ± 0.06	35.95 ± 0.01	23.00 ± 0.05	21.33 ± 0.57	16.08 ± 0.04
B	36.31 ± 0.01	36.34 ± 0.05	36.19 ± 0.00	22.99 ± 0.02	21.84 ± 0.27	17.30 ± 0.03
C	36.58 ± 0.01	36.56 ± 0.04	35.96 ± 0.01	23.30 ± 0.04	22.75 ± 0.18	16.65 ± 0.06

Domain	AOU			Chl a		
	Above pyc.	DCM	Below pyc.	Above pyc.	DCM	Below pyc.
A	1.7 ± 1.4	53.6 ± 15.9	165.4 ± 1.1	0.63 ± 0.03	1.57 ± 0.30	0.15 ± 0.01
B	-4.6 ± 0.6	35.7 ± 8.8	120.0 ± 0.6	0.66 ± 0.01	1.17 ± 0.25	0.12 ± 0.00
C	-1.5 ± 0.6	15.3 ± 2.9	170.4 ± 1.5	0.37 ± 0.01	0.83 ± 0.09	0.11 ± 0.00

3.3.1.2 Mesopelagic layer

SACW₁₈, centred at 165 ± 25 dbar, was the shallowest central WT. It represented 3.2% of the total volume of water sampled during the FLUXES II cruise (Fig. 3.6, Table 3.2). Below SACW₁₈, MMW was found, centred at 201 ± 1 dbar. Nevertheless, this water type represented only 0.1% of the total volume sampled during the cruise. ENACW₁₅ was located deeper, at 232 ± 11 dbar, and represented 12.3% of the total sampled volume. Finally, SACW₁₂ and ENACW₁₂, were centred at 339 ± 24 and 453 ± 17 dbar respectively. ENACW₁₂ was the most abundant WT sampled during the cruise with 26.1%. Conversely SACW₁₂ represented a total sampled volume of 8.6% (Fig. 3.6, Table 3.2). The distribution of the central waters was similar between T1 and T2 (Fig. 3.6) and every water mass were present in all domains of T1 and T2, except SACW₁₂ being mostly present in domains B and C in T1, and was not present in T2.

Intermediate waters were occupied by AA, SPMW, MW and LSW (Fig. 3.6). The shallowest intermediate water was SPMW, centred at 813 ± 20 dbar, and representing a total volume of sampled water of 10.4%. SPWM was followed by AA at a depth of 904 ± 36 dbar, representing 20.2% of the volume, being the most representative intermediate water (Fig. 3.6, Table 3.2). MW, centred at 1225 ± 62 dbar, was much less representative with 5.6% of the volume. Finally, LSW, centred at 1443 ± 26 dbar, represented 13.4% of the sampled volume (Fig. 3.6, Table 3.2).

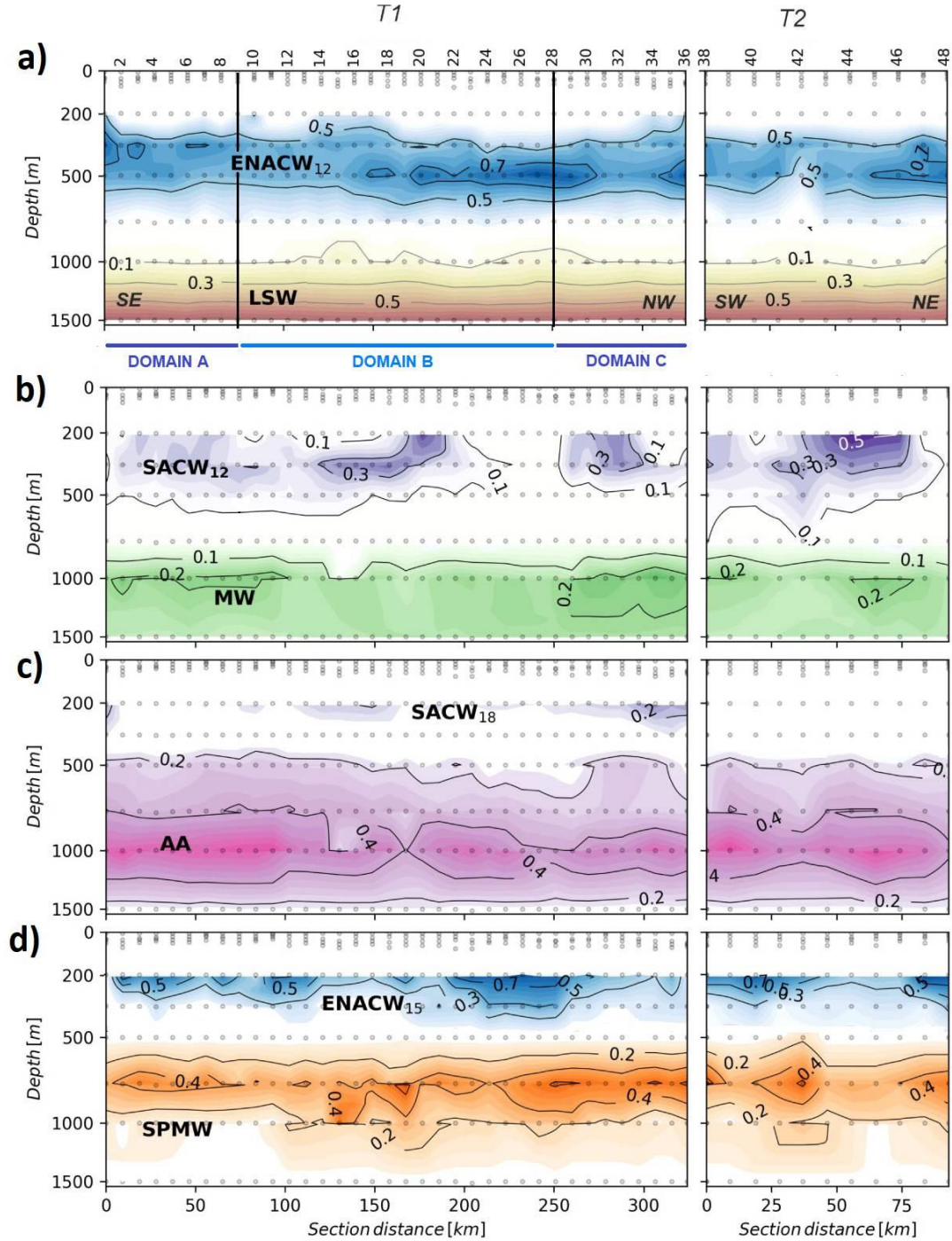


Figure 3.6. Distributions of the water masses present in the CVFZ during the FLUXES II cruise. Water mass proportions in this figure were derived from an OMP analysis applied to CTD data at 1 dbar vertical resolution. θ and S were measured directly with the CTD, while SiO_4H_4 and NO values were reconstructed by fitting the measured water sample concentrations to a non-linear combination of variables directly measured with the CTD (θ , S , O_2). The distribution of the water-masses among the panels was designed to avoid contour overlapping and does not follow an oceanographic criterion. In panel (a) the three domains of T1 (A-C) are reflected separated by vertical black lines at stn 9 and 28. the Section distance is counting from southeast (SE) to northwest (NW) in T1 and from southwest (SW) to northeast (NE) in T2 (labelled at the bottom of the first panel).

Table 3.2. Percentage of the total volume of water sampled during the FLUXES II cruise that corresponded to each water type (%VOLi) and archetype values \pm SE of depth (Zi, dbar), apparent oxygen utilization (AOUi, $\mu\text{mol kg}^{-1}$), nitrate (NO_3^{-}i , $\mu\text{mol kg}^{-1}$), phosphate ($\text{HPO}_4^{2-}\text{i}$, $\mu\text{mol kg}^{-1}$) dissolved organic carbon (DOCi, $\mu\text{mol L}^{-1}$), particulate organic carbon (POCi, $\mu\text{mol L}^{-1}$), particulate organic nitrogen (PONi, $\mu\text{mol L}^{-1}$), and C:N molar ratio (mol C mol N^{-1}) of suspended POM for the water types sampled during the cruise. Determination coefficient (R^2), standard error of the estimate (SE) of the multiple-regression and the measurement error (ME) of each variable.

WT	%VOLi	Zi (dbar)	AOUi ($\mu\text{mol kg}^{-1}$)	NO_3^{-}i ($\mu\text{mol kg}^{-1}$)	$\text{HPO}_4^{2-}\text{i}$ ($\mu\text{mol kg}^{-1}$)
SACW_18	3.20%	165 ± 25	173.2 ± 8.1	24.6 ± 1.2	1.32 ± 0.07
MMW	0.10%	201 ± 1	112.0 ± 13.6	15.4 ± 2.7	0.80 ± 0.14
ENACW_15	12.30%	232 ± 11	155.3 ± 4.8	21.8 ± 0.8	1.15 ± 0.04
SACW_12	8.60%	339 ± 24	191.0 ± 4.2	28.2 ± 0.9	1.51 ± 0.05
ENACW_12	26.10%	453 ± 17	186.2 ± 2.6	29.3 ± 0.5	1.59 ± 0.03
SPMW	10.40%	813 ± 20	187.1 ± 2.3	32.4 ± 0.3	1.92 ± 0.02
AA	20.20%	904 ± 36	176.9 ± 3.2	31.5 ± 0.3	1.84 ± 0.02
MW	5.60%	1225 ± 62	148.6 ± 6.2	29.1 ± 0.8	1.71 ± 0.05
LSW	13.40%	1443 ± 26	127.8 ± 6.2	26.6 ± 0.32	1.56 ± 0.02
R^2			0.96	0.97	0.93
SE			6.6	1.72	0.08
ME			1.0	0.1	0.02

WT	DOCi ($\mu\text{mol L}^{-1}$)	POCi ($\mu\text{mol L}^{-1}$)	PONi ($\mu\text{mol L}^{-1}$)	C:N POM (mol C mol N^{-1})
SACW_18	52.8 ± 1.9	1.9 ± 0.2	0.16 ± 0.02	12.2 ± 0.9
MMW	53.1 ± 7.3	1.3 ± 0.4	0.09 ± 0.02	14.7 ± 2.2
ENACW_15	51.2 ± 0.9	1.5 ± 0.1	0.11 ± 0.01	13.9 ± 0.6
SACW_12	47.8 ± 1.0	1.6 ± 0.1	0.12 ± 0.01	14.4 ± 0.7
ENACW_12	46.6 ± 0.6	1.4 ± 0.1	0.10 ± 0.01	15.4 ± 0.4
SPMW	43.5 ± 1.0	1.1 ± 0.1	0.06 ± 0.00	18.3 ± 0.7
AA	43.1 ± 0.6	1.1 ± 0.1	0.06 ± 0.01	17.7 ± 0.6
MW	41.2 ± 1.0	0.9 ± 0.1	0.05 ± 0.01	19.1 ± 1.1
LSW	41.8 ± 0.7	0.9 ± 0.1	0.05 ± 0.00	19.5 ± 0.7
R^2	0.40	0.38	0.54	
SE	4.54	0.44	0.03	
ME	1.5	0.1	0.01	

The distribution of AOU in the central waters presented the lowest values ($100\text{--}150 \mu\text{mol kg}^{-1}$) in the shallowest WTs between stn 8 and 28 (domain B), related with the dominant presence of ENACW (Fig. 3.7). Conversely, the highest archetype AOU values ($191.0 \pm 4.2 \mu\text{mol kg}^{-1}$) corresponded to SACW_12 (Table 3.2). In intermediate waters, AOU decreased significantly ($p < 0.005$) with depth from an archetype value of $187 \mu\text{mol kg}^{-1}$ for SPMW to $128 \mu\text{mol kg}^{-1}$ for LSW. WTs mixing explained 96% of the variability of AOU, but the SE of $6.6 \mu\text{mol kg}^{-1}$ was larger than the measurement error of AOU, about $1 \mu\text{mol kg}^{-1}$ (Table 3.2). This indicates that, although the R^2 is high, mixing is not able to

explain satisfactorily the distribution of AOU because the SE is about an order of magnitude larger than the measurement error (Álvarez-Salgado et al., 2013).

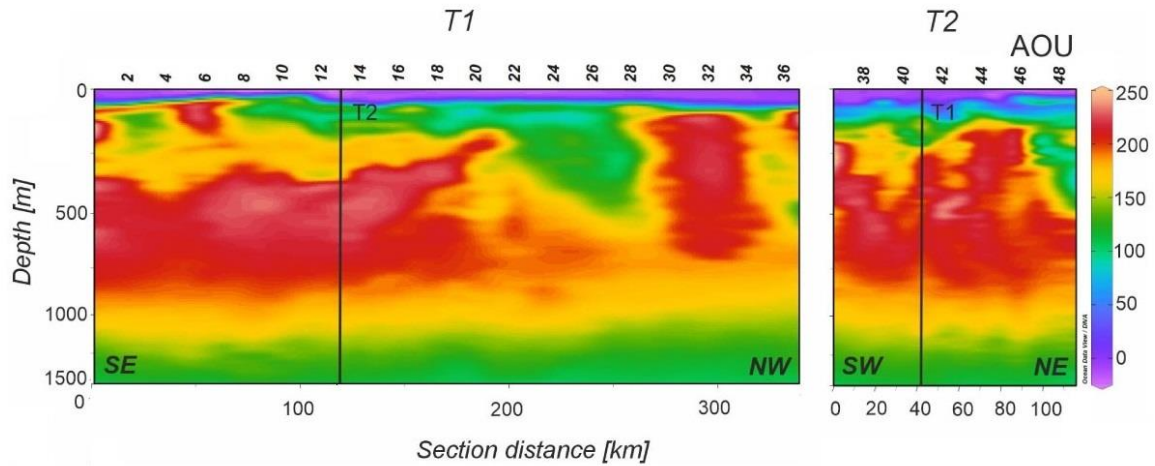


Figure 3.7. Distributions of AOU in $\mu\text{mol kg}^{-1}$ during the FLUXES II cruise, along T1 (left) and T2 (right). Vertical black lines show the position of the orthogonal transects T2 and T1, respectively. Section distance is counting from southeast (SE) to northwest (NW) in T1 and from southwest (SW) to northeast (NE) in T2. Produced with Ocean Data View (Schlitzer, 2017).

3.3.2 Nitrogen biogeochemistry in the CVF in November 2017

3.3.2.1 Epipelagic layer

Along T1, the distribution of the predominant form of inorganic nitrogen, NO_3^- (Fig. 3.8a), was parallel to the distributions of salinity (Fig. 3.5a) and AOU (Fig. 3.5d). The shallow intrusion of low salinity in domain B, was also noticeable in the high concentration of NO_3^- observed just below the pycnocline. Below the pycnocline, average values of NO_3^- were non significantly different between the three domains (Table 3.3). Concentrations of NO_2^- and NH_4^+ (Fig. 3.8b, c) were low, usually less than $0.1 \mu\text{mol kg}^{-1}$, with maximum values in the surroundings of the DCM and specifically in domain B, where the average concentrations of NO_2^- and NH_4^+ were 0.38 ± 0.08 and $0.30 \pm 0.06 \mu\text{mol kg}^{-1}$, respectively (Table 3.3). These high values coincided with the high levels of Chl-a present in domain B.

When T2 was occupied, the distribution of NO_3^- showed higher concentrations at 100 dbar, similar to the concentration found in domain A during T1 (Fig. 3.8a). NO_2^- and NH_4^+ concentrations showed similar distributions than in T1 but with slightly higher values around the pycnocline, with NO_2^- showing a peak at stn 47 (Fig. 3.8b, c). The distributions of NO_2^- and NH_4^+ were parallel to the distribution of Chl-a.

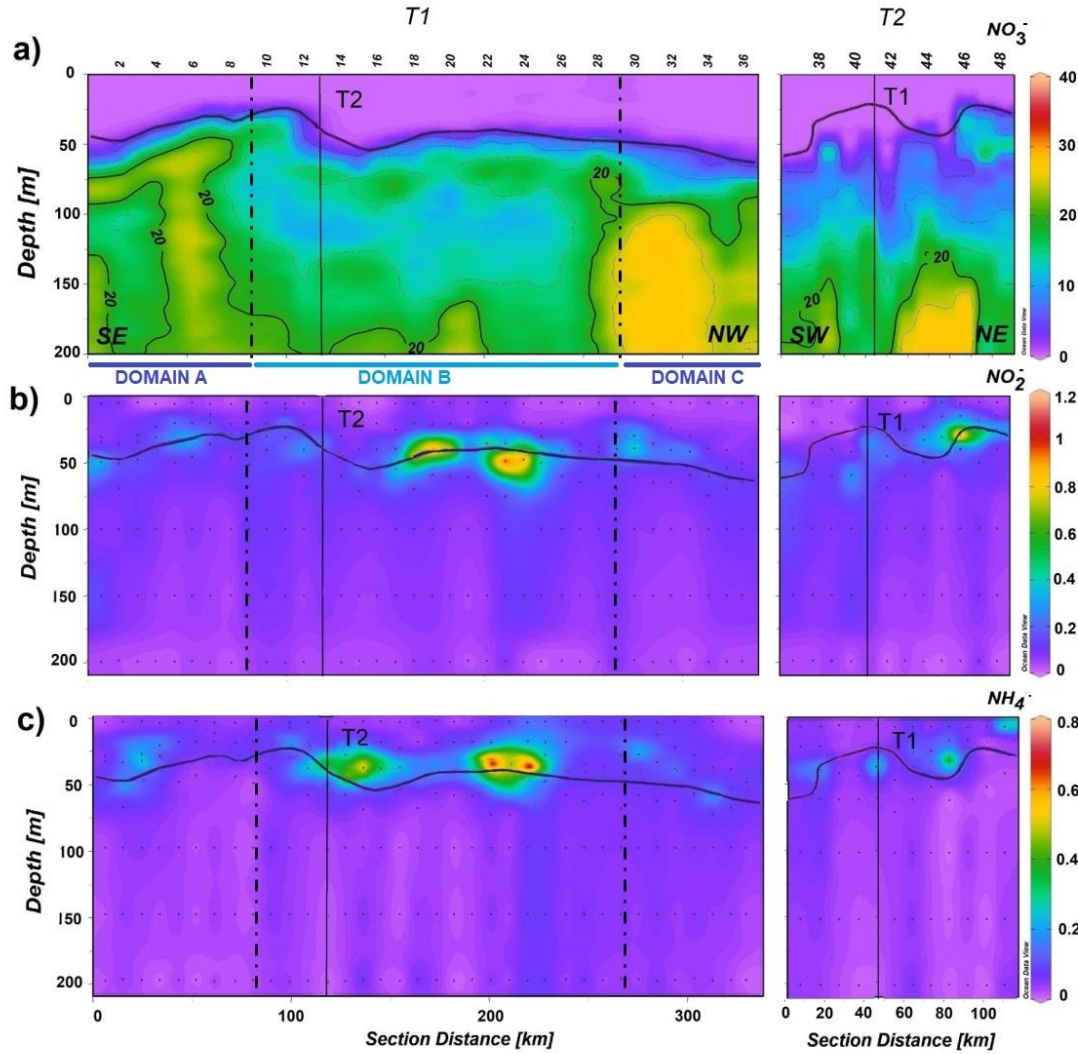


Figure 3.8. Distributions of nitrate (NO_3^-) in $\mu\text{mol kg}^{-1}$ (a), nitrite (NO_2^-) in $\mu\text{mol kg}^{-1}$ (b), and ammonium (NH_4^+) in $\mu\text{mol kg}^{-1}$ (c), in the epipelagic layer during the FLUXES II cruise, along T1 (left) and T2 (right). T1 is divided into three domains (A-C) separated by vertical dotted lines at stn 9 and 28. Vertical black lines show the position of the orthogonal transects T2 and T1, respectively. Horizontal black line shows the position of the pycnocline. Section distance is counting from southeast (SE) to northwest (NW) in T1 and from southwest (SW) to northeast (NE) in T2. Produced with Ocean Data View (Schlitzer, 2017).

Below the pycnocline, The Orthogonal Distance Regression (ODR) of NO_3^- and salinity, ($\text{NO}_3^- = -25 (\pm 1) \cdot S + 946 (\pm 40)$; $R^2 = 0.83$; $n = 116$) indicates that 83% of the variability of NO_3^- depends on the mixing of the nutrient-poorer and saltier North Atlantic waters with the nutrient-richer and fresher South Atlantic waters, showing that the $20 \mu\text{mol kg}^{-1}$ nitrate isoline coincided with the 36 isohaline that defines the position of the CVF. We excluded from these correlations the surface mixed layer samples because of the impact of phytoplankton photosynthesis on the concentration of NO_3^- and the precipitation-evaporation balance on salinity. To separate the contribution of mixing (traced by salinity) from mineralisation processes (traced by AOU), a multiple correlation of NO_3^- with salinity

and AOU was carried out, obtaining a $R^2 = 0.97$, and a NO_3^- :AOU molar coefficient of 0.120 ± 0.006 ($\text{NO}_3^- = -3.84 (\pm 1.2) \cdot S + 0.120 (\pm 0.006) \cdot \text{AOU} + 142 (\pm 42)$; $R^2 = 0.97$; $n = 112$), without significantly differences between the three domains.

Table 3.3. Depth of DCM (Z) in dbar, inorganic nutrients in $\mu\text{mol kg}^{-1}$, DOM and POM in $\mu\text{mol L}^{-1}$ and C:N ratios, characteristic of the epipelagic waters above and below the pycnocline and DCM along the biogeochemical transect T1, in domains A, B and C.

	Z			NO_3^-		
	Above pc.	DCM	Below pc.	Above pc.	DCM	Below pc.
Domain A		34.0 ± 2.7		1.43 ± 0.63	6.82 ± 1.92	19.28 ± 1.76
Domain B		39.6 ± 1.6		0.83 ± 0.31	4.21 ± 1.09	16.47 ± 0.95
Domain C		45.7 ± 2.9		0.65 ± 0.21	1.80 ± 1.53	17.22 ± 2.00
	NO_2^-			NH_4^+		
	Above pc.	DCM	Below pc.	Above pc.	DCM	Below pc.
Domain A	0.05 ± 0.01	0.22 ± 0.05	0.12 ± 0.03	0.09 ± 0.02	0.12 ± 0.05	0.04 ± 0.01
Domain B	0.03 ± 0.01	0.38 ± 0.08	0.20 ± 0.04	0.17 ± 0.03	0.30 ± 0.06	0.06 ± 0.01
Domain C	0.09 ± 0.03	0.24 ± 0.06	0.08 ± 0.01	0.08 ± 0.01	0.11 ± 0.03	0.06 ± 0.02
	HPO_4^{2-}			SiO_4H_4		
	Above pc.	DCM	Below pc.	Above pc.	DCM	Below pc.
Domain A	0.26 ± 0.04	0.55 ± 0.10	1.11 ± 0.08	1.73 ± 0.14	2.96 ± 0.39	6.40 ± 0.50
Domain B	0.24 ± 0.02	0.42 ± 0.06	0.97 ± 0.04	1.39 ± 0.09	2.46 ± 0.26	5.44 ± 0.29
Domain C	0.17 ± 0.02	0.25 ± 0.03	1.04 ± 0.09	1.94 ± 0.12	2.50 ± 0.20	6.31 ± 0.66
	DOC			DON		
	Above pc.	DCM	Below pc.	Above pc.	DCM	Below pc.
Domain A	75.3 ± 1.3	69.4 ± 2.0	60.1 ± 1.6	6.1 ± 0.28	6.9 ± 1.17	4.9 ± 1.20
Domain B	77.2 ± 1.2	69.0 ± 1.9	57.5 ± 1.2	7.1 ± 0.19	5.9 ± 0.48	3.3 ± 0.34
Domain C	74.8 ± 1.3	70.8 ± 2.2	58.4 ± 2.1	6.8 ± 1.7	6.5 ± 0.25	3.67 ± 0.43
	C:N DOM			POC		
	Above pc.	DCM	Below pc.	Above pc.	DCM	Below pc.
Domain A	12.7 ± 0.59	11.8 ± 1.69	17.6 ± 0.97	5.9 ± 0.4	6.0 ± 0.7	3.0 ± 0.4
Domain B	11.2 ± 0.27	14.1 ± 1.99	15.9 ± 2.37	7.0 ± 0.4	6.3 ± 0.7	3.0 ± 0.3
Domain C	11.1 ± 0.26	11.1 ± 0.57	16.5 ± 1.02	3.9 ± 0.2	3.6 ± 0.2	2.1 ± 0.2
	PON			C:N POM		
	Above pc.	DCM	Below pc.	Above pc.	DCM	Below pc.
Domain A	0.69 ± 0.05	0.71 ± 0.08	0.28 ± 0.04	8.74 ± 0.26	8.56 ± 0.32	11.20 ± 0.54
Domain B	0.86 ± 0.05	0.68 ± 0.07	0.30 ± 0.04	8.24 ± 0.14	9.39 ± 0.54	11.24 ± 0.41
Domain C	0.48 ± 0.03	0.42 ± 0.04	0.20 ± 0.02	8.30 ± 0.22	8.93 ± 0.50	11.25 ± 0.71

The concentration of HPO_4^{2-} (Fig. 3.9a) decreased from southeast to northwest in the surface mixed layer, being significantly lower in domain C (Table 3.3). Below the pycnocline, higher values were observed in domain A with an average concentration of $1.11 \pm 0.08 \mu\text{mol kg}^{-1}$ and non-significant differences between the three domains. Regarding SiO_4H_4 (Fig. 3.9b), a distribution parallel to NO_3^- was also observed, although the lowest concentrations ($p < 0.01$) were found in domain B above the pycnocline (Table 3.3) and there were no significant differences in the three domains below the pycnocline.

Above the pycnocline the N:P molar ratio of inorganic nutrients ranged between 4.6 ± 1.7 and 6.4 ± 3.5 and increased with depth, reaching values of 16.3 ± 0.9 below pycnocline with no significant differences between domains. The N:Si ratio above the pycnocline ranged between 0.4 ± 0.1 and 0.9 ± 0.5 . Conversely, below the pycnocline an average ratio of 3.0 ± 0.5 was found in the three domains with no significant differences between them.

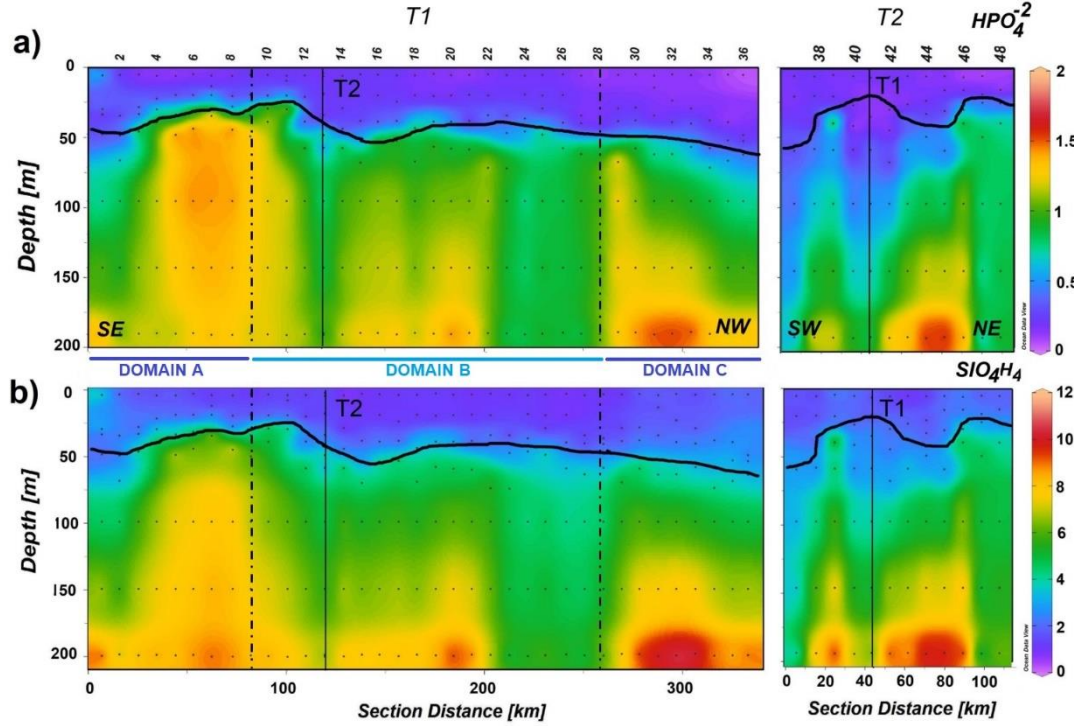


Figure 3.9. Distributions of phosphate (HPO_4^{2-}) in $\mu\text{mol kg}^{-1}$ (a), and silicate (SiO_4H_4) in $\mu\text{mol kg}^{-1}$ (b) in the epipelagic layer during the FLUXES II cruise along T1 (left) and T2 (right). T1 is divided into three domains (A-C) separated by vertical dotted lines at stn 9 and 28. Vertical black lines show the position of the orthogonal transects T2 and T1, respectively. Horizontal black line shows the position of the pycnocline. Section distance is counting from southeast (SE) to northwest (NW) in T1 and from southwest (SW) to northeast (NE) in T2. Produced with Ocean Data View (Schlitzer, 2017).

Below the pycnocline the ODR of HPO_4^{2-} with salinity ($\text{HPO}_4^{2-} = -1.23 (\pm 0.05) \cdot S + 45 (\pm 1.9)$; $R^2 = 0.82$; $n = 116$) indicates that 82% of the variability depends on water mass mixing. A multiple correlation of HPO_4^{2-} with salinity and AOU was carried out, obtaining a $R^2 = 0.97$, and a $\text{HPO}_4^{2-}:\text{AOU}$ molar coefficient of 0.0049 ± 0.0004 ($\text{HPO}_4^{2-} = -0.38 (\pm 0.8) \cdot S + 0.0049 (\pm 0.0004) \cdot \text{AOU} + 14 (\pm 3)$; $R^2 = 0.93$; $n = 112$). To differentiate between mixing and mineralisation processes in the relationship between nitrate and phosphate, a multiple regression model of NO_3^- with salinity and HPO_4^{2-} was calculated ($\text{NO}_3^- = 18 (\pm 1) \cdot \text{HPO}_4^{2-} - 3.6 (\pm 1.3) \cdot S + 130 (\pm 47)$; $R^2 = 0.95$; $n = 116$) obtaining a $\text{NO}_3^-:\text{HPO}_4^{2-}$ molar slope of 18 ± 1 . When each domain was considered separately, the $\text{NO}_3^-:\text{HPO}_4^{2-}$ molar slope did not show significant differences between them. The ODR of SiO_4H_4 with salinity ($\text{SiO}_4\text{H}_4 = -7.4 (\pm 0.4) \cdot S + 271 (\pm 12.8)$; $R^2 = 0.79$; $n = 116$) indicates

that 79% of its variability depends on the mixing. Again, a multiple regression model of NO_3^- with salinity and SiO_4H_4 was applied ($\text{NO}_3^- = 2.3 (\pm 0.2) \cdot \text{SiO}_4\text{H}_4 - 9 (\pm 2) \cdot S + 316 (\pm 60)$; $R^2 = 0.92$; $n = 116$) obtaining a $\text{NO}_3^-:\text{SiO}_4\text{H}_4$ molar slope of 2.3 ± 0.2 . In addition, when considered the three domains separately in the multiple linear regression of NO_3^- with salinity and SiO_4H_4 , domain A and B showed similar $\text{NO}_3^-:\text{SiO}_4\text{H}_4$ molar slope around 2.4 ± 0.4 , while domain C showed a significantly lower $\text{NO}_3^-:\text{SiO}_4\text{H}_4$ molar slope of 0.88 ± 0.4 ($p < 0.05$).

PON along T1 showed the highest values above the pycnocline (Fig. 3.10a), particularly in domain B with an average concentration of $0.86 \pm 0.05 \mu\text{mol L}^{-1}$ (Table 3.3), while the lowest values were found in domain C with an average concentration of $0.48 \pm 0.03 \mu\text{mol L}^{-1}$. Below the pycnocline, an average value of $0.26 \pm 0.03 \mu\text{mol L}^{-1}$ was obtained decreasing significantly ($p < 0.05$) from domain A and B to domain C (Table 3.3). In epipelagic waters, PON correlated significantly with Chl-a (ODR; $\text{PON} = 0.54 (\pm 0.02) \cdot \text{Chl a} - 0.15 (\pm 0.02)$; $R^2 = 0.50$; $n = 237$; $p < 0.005$). When T2 was occupied PON presented higher values at both ends of T2 and slightly lower at the middle of the section (Fig. 3.10a). The values were similar to those found along T1 but being significantly lower at the DCM ($p < 0.05$). In addition, as in T1, higher PON values coincided with higher values of Chl-a.

The C:N molar ratio of POM increased significantly with depth ($p < 0.005$). T1 showed values from > 8 in the surface mixed layer to > 11 below the pycnocline, being the average value of C:N molar ratio of POM similar between the three domains. In T2, above the pycnocline and at the DCM, significantly lower C: N molar ratio than T1 were observed ($p < 0.05$), around 7. In epipelagic waters, POC (Fig. S5a) resembled the distribution of PON (ODR; $\text{POC} = 7.4 (\pm 0.1) \cdot \text{PON} + 0.6 (\pm 0.1)$; $R^2 = 0.92$; $n = 235$; $p < 0.005$).

In T1, DON (Fig. 3.10b) showed maximum average concentrations of $6.8 \pm 0.3 \mu\text{mol L}^{-1}$ above the pycnocline (Table 3.3), and decreased with depth to an average value of $3.5 \pm 0.3 \mu\text{mol L}^{-1}$ below the pycnocline. At the surface, domain A showed significantly lower values, than domains B and C ($p < 0.05$) (Table 3.3), while at the DCM and below the pycnocline all domains presented similar values ($p > 0.05$).

DOC (Fig. S5b) maximum concentration of $97 \mu\text{mol L}^{-1}$ was found at the surface layer of stn 21, coinciding with high values of Chl-a found above the pycnocline between stn 19-27. Average concentrations of DOC in the surface mixed layer were $76.0 \pm 0.8 \mu\text{mol}$

L^{-1} and decreased significantly with depth (Table 3.3). Nevertheless, the distribution of DOC below the pycnocline showed columns with relatively high DOC values, which extended up to 200 dbar and were surrounded by areas of lower concentration, in the three domains. In T2, DOC presented higher values in the surface at stn 39 with a maximum of $116.7 \mu\text{mol L}^{-1}$, coinciding with high values of Chl-a found in T2.

Above the pycnocline, the average C:N molar ratio of DOM was around 11.4 ± 0.2 , increasing with depth to 17 ± 1 ($p < 0.005$), showing similar averages values in both transects (T1 and T2) ($p > 0.05$). When the average values of the C:N ratio of DOM below the pycnocline in each transect were analysed, T1 showed significantly higher values ($p > 0.005$). In T1, above the pycnocline considering the three domains separately, domain A presented an average C:N molar ratio of 12.7 ± 0.6 , significantly higher than average values of domains B and C ($p < 0.05$) (Table 3.3).

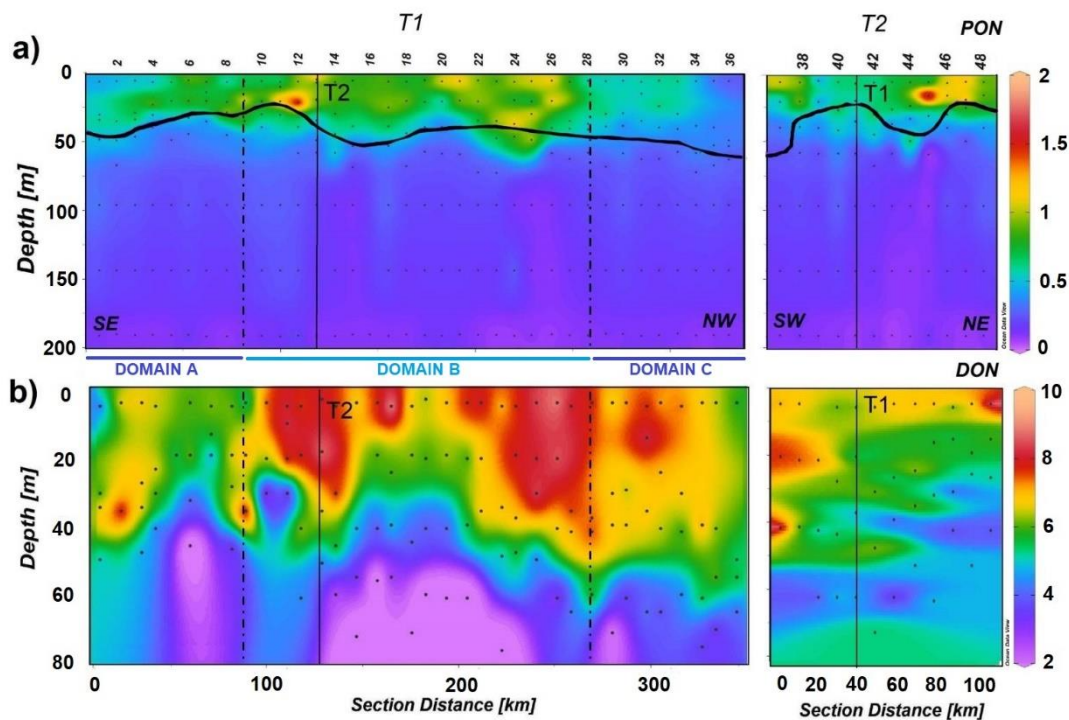


Figure 3.10. Distributions of PON in $\mu\text{mol L}^{-1}$ (a) and DON in $\mu\text{mol L}^{-1}$ (b) in the epipelagic layer during the FLUXES II cruise, along T1 (left) and T2 (right). T1 is divided into three domains (A-C) separated by vertical dotted lines at stn 9 and 28. Vertical black lines show the position of the orthogonal transects T2 and T1, respectively. Horizontal black line in (a) shows the position of the pycnocline. Note that the depth scale in (a) and (b) is different. Section distance is counting from southeast (SE) to northwest (NW) in T1 and from southwest (SW) to northeast (NE) in T2. Produced with Ocean Data View (Schlitzer, 2017).

Correlations with AOU (for DOC and POC) and with NO_3^- (for PON and DON) below the pycnocline were examined to quantify the contribution of DOC and POC to local oxygen consumption, and the contribution of DON and PON to local NO_3^- production. DOC showed a significant correlation with AOU (ODR; $\text{DOC} = -0.15 (\pm 0.01) \cdot \text{AOU} + 75.5 (\pm 1.3)$; $R^2 = 0.49$; $n = 116$). The slope of the linear regression indicated that DOC supported around $21 \pm 1 \%$, of the oxygen demand in the epipelagic waters assuming a Redfieldian $-\text{O}_2:\text{C}$ stoichiometric ratio of $1.4 \text{ mol O}_2 \text{ mol C}^{-1}$ (Anderson, 1995). Furthermore, when T1 was examined considering the three domains separately, domain B presented a significantly more negative slope (-0.18 ± 0.02) than domains A and C (-0.13 ± 0.04 and -0.15 ± 0.03 , respectively). Therefore, while DOC supported $25.3 \pm 2.8 \%$ of the oxygen demand in domain B, this value decreased to $18.5 \pm 5.6 \%$ and $21.0 \pm 4.2 \%$ in domains A and C, respectively. A multiple regression model of DOC with salinity and AOU was applied, but it was not significant.

Table 3.4. AOU or NO_3^- coefficients of DOC, POC, PON and DON for each domain in T1, in the epipelagic layer, below the pycnocline. β , AOU or NO_3^- coefficients of the regression; SE- β , standard error and p-value of the estimation of β .

	Domain A			Domain B			Domain C		
	β	SE- β	p	B	SE- β	P	B	SE- β	p
DOC vs AOU	-0.13	0.023	0.001	-0.180	0.018	1.3E-09	-0.136	0.0214	0.0002
POC vs AOU	-0.034	0.006	0.025	-0.045	0.006	0.002	-0.015	0.003	0.015
PON vs NO_3^-	-0.025	0.005	0.005	-0.037	0.005	0.0005	-0.011	0.001	0.0002
DON vs NO_3^-	-0.430	0.105	0.018	-0.334	0.055	0.004	-0.219	0.047	0.0056

For the case of POC (ODR; $\text{POC} = -0.030 (\pm 0.006) \cdot \text{AOU} + 6.3 (\pm 0.8)$; $R^2 = 0.23$ $n = 110$), its represented only the $4.4 \pm 0.8 \%$ of the oxygen demand. When salinity was added to the multiple regression (ODR; $\text{POC} = -0.030 (\pm 0.006) \cdot \text{AOU} - 4.2 (\pm 1.2) \cdot S + 157 (\pm 46)$; $R^2 = 0.28$; $n = 110$), a similar POC:AOU molar slope was obtained. When each domain was studied separately, again, domain B presented a significantly more negative

slope (-0.045 ± 0.006) for POC vs AOU correlation than domains A (-0.034 ± 0.006) and C (-0.015 ± 0.003) (Table 3.4), suggesting that POC supported 6.3 ± 0.8 % of the oxygen demand in domain B.

DON supported 33 ± 10 % of the NO_3^- production (ODR; $\text{DON} = -0.33 (\pm 0.1) \cdot \text{NO}_3^- + 8.96 (\pm 1.7)$; $R^2 = 0.39$ $n = 75$). As for DOC, when salinity was added to the multiple regression there was not a significant improvement of the explained variability and the coefficient with salinity was not significant. For the case of PON the ODR with NO_3^- (ODR; $\text{PON} = -0.014 (\pm 0.001) \cdot \text{NO}_3^- + 0.45 (\pm 0.03)$; $R^2 = 0.29$ $n = 110$) indicates that PON supported only $1.4\% \pm 0.1$ % of the NO_3^- production, although when corrected for water mass mixing ($\text{PON} = -0.027 (\pm 0.004) \cdot \text{NO}_3^- - 0.42 (\pm 0.12) \cdot S + 16 (\pm 4)$; $R^2 = 0.34$; $n = 110$), a PON: NO_3^- a molar slope of -0.027 ± 0.004 was obtained, indicating that PON really contributed 2.7 ± 0.4 % to nitrate production. Furthermore, when T1 was examined, DON supported significantly lower ($p < 0.05$) NO_3^- production in domain C ($22 \pm 5\%$) than in domain A (43 ± 10 %) and B (33 ± 5 %) (Table 3.4). For the case of PON, domain B presented a significantly more negative slope (-0.037 ± 0.005) than domains A and C (-0.025 ± 0.005 and -0.011 ± 0.001 , respectively), suggesting that PON supported significantly higher ($p < 0.05$) NO_3^- mineralisation in domain B ($3.7 \pm 0.5\%$) versus the 1.1 ± 1.3 % in domain C (Table 3.4). The inclusion of salinity to the DON and PON regression in three domains it was not significant or with same coefficients, so the domains coefficients were presented as the lineal regression.

3.3.2.2 Mesopelagic layer

The distribution of NO_3^- (Fig. 3.11a) showed maximum values between 500 and 1000 dbar. The lowest archetype values of NO_3^- (15.4 ± 2.7 and $21.8 \pm 0.8 \mu\text{mol kg}^{-1}$) were observed in the shallowest WTs, MMW and ENACW_15 (Table 3.2), while the highest values between 500 and 1000 dbar corresponded to SPMW and AA, 32.4 ± 0.3 and $31.5 \pm 0.3 \mu\text{mol kg}^{-1}$, respectively. WTs mixing explained 87% of the variability of NO_3^- , but the SE of $1.72 \mu\text{mol kg}^{-1}$ was larger than the measurement error of $0.1 \mu\text{mol kg}^{-1}$ (Table 3.2). Inclusion of AOU as explanatory variable increased the explained variability of the NO_3^- distribution to 90% (Table 3.2), with a significant NO_3^- :AOU coefficient independent of WT mixing of 0.13 ± 0.01 (Table 3.5).

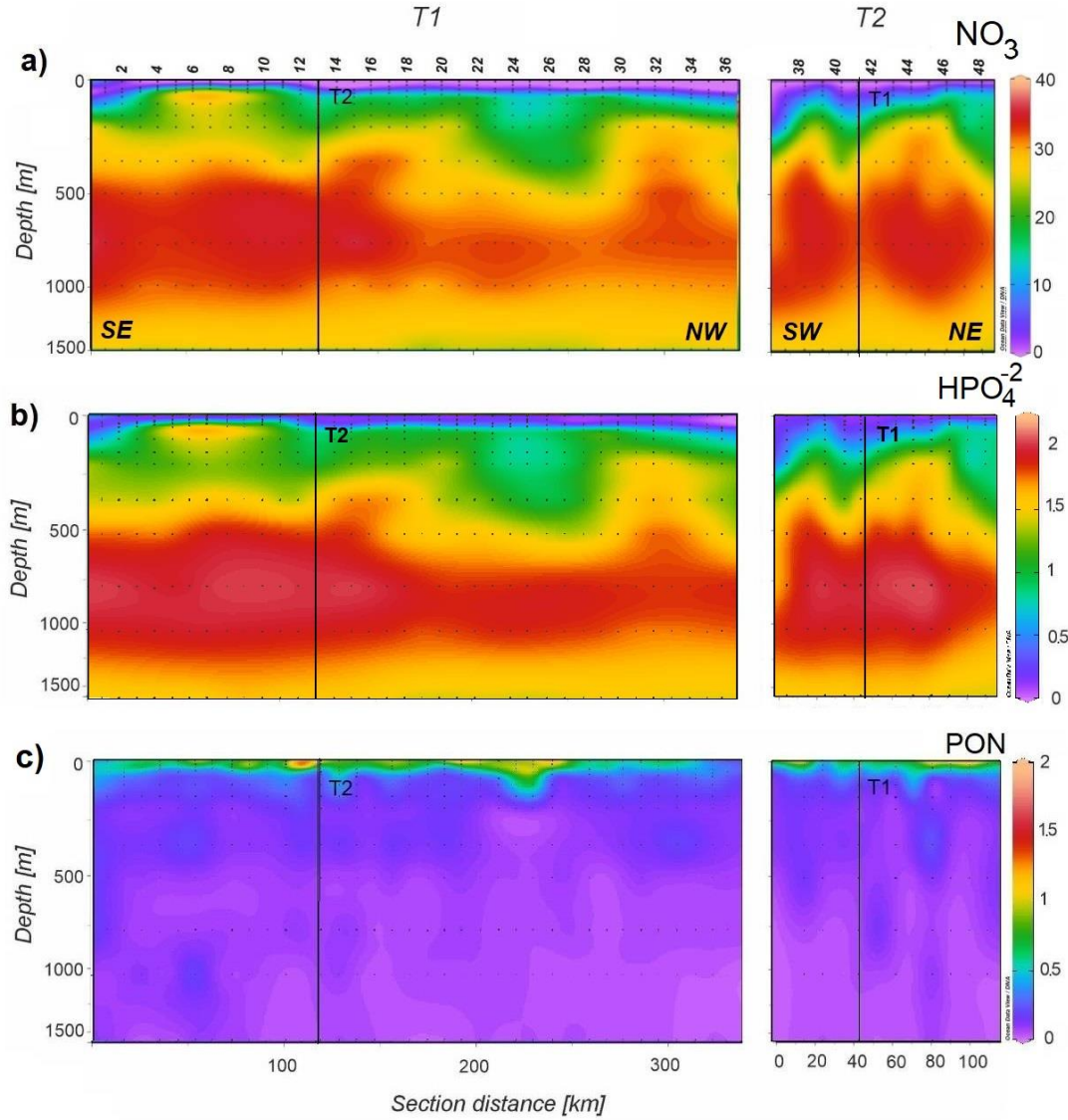


Figure 3.11. Distributions of NO_3^- in $\mu\text{mol kg}^{-1}$ (a), HPO_4^{2-} in $\mu\text{mol kg}^{-1}$ (b) and PON in $\mu\text{mol L}^{-1}$ (c) in the mesopelagic layer during the FLUXES II cruise along T1 (left) and T2 (right). Vertical black lines show the position of the orthogonal transects T2 and T1, respectively. Section distance is counting from southeast (SE) to northwest (NW) in T1 and from southwest (SW) to northeast (NE) in T2. Produced with Ocean Data View (Schlitzer, 2017).

HPO_4^{2-} showed a similar distribution than NO_3^- (Fig. 3.11b). Archetype values of HPO_4^{2-} ranged from $1.15 \pm 0.04 \mu\text{mol kg}^{-1}$ in ENACW_15 to $1.92 \pm 0.02 \mu\text{mol kg}^{-1}$, in the intermediate SPMW, and then decreased with depth until reaching a value of $1.56 \pm 0.02 \mu\text{mol kg}^{-1}$ in LSW (Table 3.2). WT mixing explained 93% of the variability of HPO_4^{2-} with a SE of $0.08 \mu\text{mol kg}^{-1}$, being this SE 4 times the measurement error of $0.02 \mu\text{mol kg}^{-1}$ (Table 3.2). In addition, when AOU was added to the multiple regression the explained variance was 95% and a significant HPO_4^{2-} :AOU coefficient of 0.0066 ± 0.0006 was

obtained (Table 3.5). Furthermore, when HPO_4^{-2} was added as an explanatory variable to NO_3^- the explained variance was 95% with a SE of $1.1 \mu\text{mol kg}^{-1}$ and with a $\text{NO}_3^-:\text{HPO}_4^{-2}$ coefficient of 16.1 ± 0.8 (Table 3.5).

PON (Fig. 3.11c) showed a similar distribution along T1 and T2, with a general decreased of concentration with depth. Archetype PON values ranged from $0.16 \pm 0.02 \mu\text{mol kg}^{-1}$ in the shallowest SACW_18 to $0.05 \pm 0.00 \mu\text{mol kg}^{-1}$ in LSW (Table 3.2). WTs mixing explained 54% of the variability of the distribution of PON in the CVFZ with a SE of $0.03 \mu\text{mol L}^{-1}$ higher than the measurement error of $0.01 \mu\text{mol L}^{-1}$ (Tables 3.2 and 3.5). In addition, when adding AOU or NO_3^- to the multiple regression model the PON:AOU and PON: NO_3^- coefficients were not significant (Table 3.5).

The distribution of POC (Fig. S6a) was parallel to PON with a general decreased of concentration with depth. The highest concentrations of POC $1.9 \pm 0.2 \mu\text{mol L}^{-1}$, was found in the shallowest central water SACW_18 (Table 3.2). WTs mixing explained only 38% of the POC with a SE of $0.4 \mu\text{mol L}^{-1}$ variability in the CVFZ (Table 3.5). As for the case of PON when adding AOU to the multiple regression model the POC–AOU coefficient were not significant (Table 3.5).

Table 3.5. Multiple linear regressions of DOC, POC, PON and NO_3^- with the water type proportions (X_{ij}) and AOU or NO_3^- . Determination coefficient (R^2_{+1}) and standard deviation (SE_{+1}), between the multiple linear regression with X_{ij} (Table 3.2) and the multiple linear regression with X_{ij} and AOU or NO_3^- , regression coefficient of each variable with AOU or NO_3^- (β), and standard error of the estimate (SE_β), p -value of β and total of samples (n).

	DOC vs. AOU	POC vs. AOU	PON vs. AOU	PON vs. NO_3^-	NO_3^- vs AOU	HPO_4^{-2} vs AOU	HPO_4^{-2} vs. NO_3^-
R^2_{+1}	0.40	0.38	0.54	0.59	0.90	0.95	0.95
SE_{+1}	4.55	0.44	0.03	0.03	1.5	0.07	1.11
β	-	-	-	-	0.13	0.0066	16.4
SE_β	-	-	-	-	0.01	0.0006	0.80
p-level	-	-	-	-	6.8×10^{-19}	1.3×10^{-22}	5.34×10^{-56}
n	288	288	287	287	290	290	290

The C:N molar ratio of POM increased significantly with depth, from an archetype value of 12.2 ± 0.9 in SACW_18 to 19.5 ± 0.7 in LSW (Table 3.2). The highest C:N ratios were found in the northern part of T1 from stn 24 to 36, in the depth range of 750-1500 dbar with a maximum local value of 27.5 in stn 32 at 1500 dbar. When PON was added to

the multiple regression of POC and WT mixing the explained variance was 96% with a significant POC:PON molar coefficient of 9.8 ± 0.2 .

As previously explained, DON values in the mesopelagic layers were not reliable and are not showed. Therefore, for organic nitrogen, we only quantify the contribution of PON to oxygen utilization and local NO_3^- mineralization. For this reason, in the case of DOM, only was showed the distribution of DOC. Archetype DOC values (Table 3.2) ranged from $52.8 \pm 1.9 \mu\text{mol L}^{-1}$ in SACW_18 to $41.8 \pm 0.7 \mu\text{mol L}^{-1}$ in LSW (Table 3.2), showing a gradual decrease with depth. The multiple regression with X_{ij} explained 40% of the DOC variability with a SE of $4.5 \mu\text{mol L}^{-1}$ (Table 3.5) When adding AOU to the multiple linear regression the DOC-AOU slope was not significant (Table 3.5).

3.4 Discussion

3.4.1 Meso- and submeso-scale processes in epipelagic layer of the CVF

The distribution of the different forms of dissolved inorganic and organic nitrogen are clearly influenced by the meso- and submesoscale physical processes observed in the CVFZ such as meanders and eddies. The cyclonic eddy, which affected the southern sector of T1 transported SACW, being the responsible for the uplift of the pycnocline in domain A. In addition, this explains the connection with the low salinity intrusion observed below the pycnocline in the southern part of T1 along domain B. On the contrary, the northernmost part of T1 was affected by an anticyclonic eddy that deepened the pycnocline, being especially noticeable in domain C. The distribution of salinity and temperature at 150 dbar clearly reflects the distribution of SACW and ENACW due to their different thermohaline and chemical characteristics as a result of their different origin and history from their respective formation areas to the CVFZ (Stramma and Schott, 1999). Hosegood et al. (2017) brought the importance of mesoscale process for the injection of nutrients to the euphotic zone which stimulate higher levels of primary production. This importance is also reflected in the CVF, in this nutrient-rich lens extended along the first 250 km of T1 and about 20-30 m thick which provided nutrients to the immediately above surface waters, contributing to the observed high values of Chl-a (Fig. 3.5c).

The NO_2^- and NH_4^+ maxima at the DCM are associated with the interplay of nitrate and nitrite reduction by phytoplankton and microbial degradation processes of ammonification and nitrification at the DCM (Ward et al., 1982; Meeder et al., 2012).

Accumulation of NH_4^+ around the DCM occurs as a result of the ammonification of organic nitrogen but the resulting NH_4^+ is slowly removed by nitrifying bacteria (Gruber, 2008; Meeder et al., 2012). For the case of NO_2^- , it should be distinguished between a phytoplankton and a microbial mechanism of formation of the maxima. Due the low light levels, phytoplankton have enough available energy to reduce NO_3^- to NO_2^- but it is insufficient to reduce NO_2^- to NH_4^+ , leading to the observed accumulation of NO_2^- (Gruber, 2008 Mulholland and Lomas, 2008, Ward, 2008). Light levels also affect nitrifying bacteria in such a way that while the first step of nitrification (i.e., NH_4^+ to NO_2^-) is not light inhibited, the second step (i.e., NO_2^- to NO_3^-) experiences some photoinhibition, leading also to the accumulation of NO_2^- (Ward et al., 1982; Gruber, 2008, Ward, 2008).

The correlation of NO_3^- with salinity below the pycnocline indicate that 83% of the variability of nitrate depends on the mixing of the nutrient-poorer saltier North Atlantic waters with the nutrient-rich fresher South Atlantic waters, raising the explained variability to 97% when AOU was added, indicating that local mineralization processes were also necessary to explain the nitrate distributions. In addition, the AOU: NO_3^- slope independent of water mass mixing of 8.3 ± 0.4 , being slightly lower than the 9–10 proposed by Redfield (Redfield et al., 1963; Anderson, 1995), suggests that in epipelagic waters below the pycnocline organic matter mineralisation does not follow the Redfield stoichiometry, but there is a preferential mineralization of the more labile N-rich molecules as already observed in other ocean regions (Brea et al., 2004; Alvarez-Salgado et al., 2014; Fernández-Castro et al., 2019).

Average N:P molar ratios between 4.6 ± 1.7 and 6.4 ± 3.5 were obtained in the surface mixed layer. This low N:P ratio indicates a severe N limitation to primary production in the upper mixed layer of the CVFZ at the time of sampling. Below the pycnocline, the N:P molar ratio obtained (18 ± 1) was slightly higher than the Redfield molar ratio of 16, indicating preferent remineralization of P over N (Sambrotto et al., 1993; Hupe and Karstensen, 2000; Osterroht and Thomas, 2000). Furthermore, the origin intercept of the linear regression between NO_3^- : HPO_4^{2-} below the pycnocline (-3.6 ± 1.3) also reflects the N limitation.

The N:Si molar ratio in the surface mixed layer, 0.7 ± 0.3 , points again to N limitation to net primary production in the region, considering the N:Si Redfield ratio of 1:1 for diatoms growing under silicate-replete conditions (Brzezinski, 1985). Conversely,

below the pycnocline, the ratio of 2.3 (± 0.2) indicates the expected faster mineralization of N compared to Si during mineralization of sinking POM in the ocean (Kudela and Dugdale, 2000; Álvarez-Salgado et al., 2014). In addition, domains A and B also showed faster remineralization of N, with similar N:Si molar ratio of mineralisation of 2.3 ± 0.6 and 2.8 ± 0.3 , respectively. However, domain C showed significantly lower molar ratio than domain A and B, of 0.88 ± 0.4 , not significantly different than Redfield ratio of 1.

The surface mean concentration of DON was slightly higher than those found in the Atlantic Ocean of $>5 \mu\text{mol kg}^{-1}$ to the east to $\sim 4.5 \mu\text{mol kg}^{-1}$ to the west (Mahaffey et al., 2004; Roussenov et al., 2006; Torres-Valdés et al., 2009; Letscher et al., 2013). The linear correlation between DON and NO_3^- indicates that DON supported about 32% of the nitrogen demand of epipelagic waters, while PON supported only 2.7%. It is noticeable the significant differences in the DON: NO_3^- and PON: NO_3^- slope in epipelagic waters between domains A, B and C, (43%, 33% and 21% for DON and 2.5%, 3.7% and 1.1% for PON), suggesting that DON mineralization below the mixed layer in domain A, supports a larger fraction of nitrate production. Due the low contribution of DON and PON to the nitrogen demand, the remaining should therefore be supported by the sinking OM fraction.

The mean C:N molar ratio of DOM in surface waters of the CVFZ is similar to previously reported in other areas; for example 11.5-15.5 in the Sargasso Sea; 15.1 in a Equatorial Pacific, 13.6 in North Sea and 15.3 in Western Subtropical North Atlantic (Hansell and Carlson, 2001) being significantly higher than the Redfield ratios. And was compatible with the C: N ratio reported by Hopkinson and Vallino (2005) for refractory marine DOM, 3511: 202. However, the C:N ratios of POM are significantly higher than reported values in the northeast Atlantic Ocean, by Körtzinger et al. (2001) which found mean C:N molar ratios of 6.1 ± 0.8 , near Redfield ratios, and also higher than values reported in other works (see compilation by Schneider et al., 2003), which are explained by preferential N remineralisation. Although these ratios for POM also exceeded the Redfield value, they were closer to it than DOM. When the three domains are considered separately, the C:N ratios of DOM were higher in domain A, suggesting faster remineralization of N than in domain B and C, which was in consonance with the higher percentage of DON remineralization.

3.4.2 Remineralization in the mesopelagic layer

In the multiple regression models of NO_3^- with water mass proportions and AOU, the inverse of the NO_3^- :AOU coefficient 7.7 (± 0.6), represents the $-\text{O}_2$:N ratio of organic matter mineralization in the mesopelagic layer, being lower than the Redfield ratio (Redfield et al., 1963; Anderson and Sarmiento, 1994; Anderson 1995) showing a marked deviation from the Redfield stoichiometry with a strong preferential N remineralization that suggests the regeneration of the labile fraction of organic matter. Conversely, the inverse of the HPO_4^{2-} :AOU coefficient (Table 3.5), 152 ± 14 , representing the $-\text{O}_2$:P ratio of organic matter mineralization in the mesopelagic layer, was quite consistent with the Redfield ratio of 150 to 170 (Anderson and Sarmiento, 1994; Anderson 1995). In addition, the N:P ratios (16.8 ± 0.4) was similar to the canonical Redfield value of 16. This preferential remineralization of N has also been proposed by studies based on dissolved nutrient fields (Sambrotto et al., 1993; Anderson and Sarmiento, 1994; Hupe and Karstensen, 2000; Osterroht and Thomas, 2000).

Due to the production in the surface layers and subsequent mineralization at depth, DOC, POC and PON in mesopelagic waters showed the expected distribution decreasing with depth. The analysis of the C:N ratios of POM in the mesopelagic layer showed systematic deviations from the C:N Redfield ratio. In the epipelagic layer they are higher than the canonical Redfield ratio of 6.7 (Redfield et al., 1963; Anderson and Sarmiento, 1994), and also higher than values reported in other works (see compilation by Schneider et al., 2003). However, They were similar to the C:N ratio in upwelling-influenced systems (A. C. Martiny et al., 2013). The increase of the C:N molar ratio with depth indicates a preferential degradation of N compounds at shallower depths, increasing the relative abundance of carbon over nitrogen with depth and it is consistent with the low $-\text{O}_2$:N ratio obtained from the dissolved oxygen and nutrient distributions (e.g., Álvarez et al., 2014) also observed in this study. In addition, suspended particles are very small and have longer residence time than the sinking particles (Bacon and Anderson, 1982). This long residence time may be the cause for the predominant nutrient depletion, explaining the systematic higher C:N ratios. Conversely sinking particles, with a mean sinking velocity of about 10–280 dbar per day (Diercks and Asper, 1997; Pilskaln et al., 1998), have a short residence time on the order of weeks to months.

The water mass mixing model explained 54% of the variability of PON, and no significant increase of the variability explained by the model occurs when adding AOU or NO_3^- as explanatory variables. This indicates that the imprint of PON mineralization observed in mesopelagic waters of the CVFZ does not occur locally but during the pathway of the water masses from their respective formation sites to the CVFZ. The low contribution of DOC and POC to local mineralization also suggests that sinking POM should be the primary support for the local oxygen demand. Nevertheless, other works further north in the Canary Current system (Aristegui et al., 2003, 2020), where the concentration of suspended POM is much higher, found that this fraction was the main support for mesopelagic respiration there. They argued that the reason behind this behaviour is the advection of this suspended POC from the adjacent coastal productive waters.

3.5 Conclusions

A tight coupling between physical and biogeochemical parameters was observed in the CVFZ, being the distribution of DIN, DON and PON, dictated by meso- and submesoscale structures such as meanders and eddies. The N:P:Si molar ratio in the surface mixed layer points to severe N limitation to net primary production in the region. The low contribution to the local oxygen demand suggests that mineralization of POM in mesopelagic layers mainly occurs during the transit of the water masses from their respective formation sites to the CVFZ. Local mineralization is favoured by the well-known ballasting effect of lithogenic material that have been studied previously in the NW African upwelling system, and is drives fast-sinking POM. This local mineralization leads to an increase of the C:N ratios due to preferential consumption of N compounds, which is reflected in the deviations of the C:N ratio from the classical Redfield stoichiometry. Significant differences between the three domains suggest that near the coast, in domain A and B, faster N remineralization occurs. DON contributed more to nitrate production in domain A, while PON remineralization was higher in domain B, where the pycnocline was shallower and the concentrations of PON and Chl a in the upper mixed layer higher.

Chapter 4

Nitrate in the Cape Verde Frontal Zone: an isotopic approach

Chapter 4:

The results presented in this chapter are also a manuscript in preparation.

Abstract

In this chapter we report the dual isotopic signature $\delta^{15}\text{N}$ and $\delta^{18}\text{O}$ of nitrate during the cruises FLUXES I and II to provide insights on the biogeochemical cycling of N in the Cape Verde Frontal Zone (CVFZ) during summer and fall 2017. Low values of $\delta^{15}\text{N}$ of nitrate (2-3‰) were observed at depths below 200 dbar, likely associated to the mineralization of organic N produced from N_2 fixation, which is characterised by low $\delta^{15}\text{N}$ values. During FLUXES I, at 200 to 300 dbar, South of the Cape Verde Front (CVF), $\delta^{18}\text{O}$ of nitrate increases while $\delta^{15}\text{N}$ of nitrate remained constant, suggesting a tight coupling between nitrification and assimilation processes. The high $\delta^{15}\text{N}$ of nitrate observed in intermediate waters accompanied by low values of $\delta^{18}\text{O}$ of nitrate, suggests that the high $\delta^{15}\text{N}$ signal was not produced locally but imported with the Antarctic Intermediate Water (AA) that arrives to the study area in significant volumes. The characteristic isotopic signal of AA is due to the partial assimilation of nitrate that occurs during the formation of this water mass in the Subantarctic front. Average $\delta^{15}\text{N}$ and $\delta^{18}\text{O}$ of nitrate in the deep water masses of the CVFZ were in consonance with the previously estimated deep ocean values of $\delta^{15}\text{N}$ (3-6 ‰) and $\delta^{18}\text{O}$ (~2‰) of nitrate. The isotopic signals in central and intermediate waters masses in the CVFZ were different than the corresponding isotopic signals in their respective formation areas. In addition, $\delta^{15}\text{N}$ and $\delta^{18}\text{O}$ of nitrate in the CVFZ were similar for different water masses suggesting that the regenerated nitrate was primarily derived from sinking PON, which highlights the major importance of sinking PON over DON and suspended PON at CVFZ.

4.1 Introduction

Nitrate is the dominant form of bioavailable N in the ocean, and its local availability is determined by the interplay between nitrate generation and consumption processes (Sigman et al., 1999; Marconi et al., 2019). Nitrate can be supplied to phytoplankton from different sources: new N imported from the atmosphere or upwelled subsurface waters below, and locally regenerated nitrate produced from ammonium and nitrite oxidation (Bode et al., 1997; Hooper et al., 1997; Fawcett et al., 2015). The different biogeochemical processes of generation/transformation/consumption related with the N cycle (mentioned below and explained in Chapter 1 in more detail) generate different isotopic signatures on the $^{15}\text{N}:^{14}\text{N}$ and $^{18}\text{O}:^{16}\text{O}$ ratios of nitrate, reported as $\delta^{15}\text{N}_{\text{NO}_3^-}$ and $\delta^{18}\text{O}_{\text{NO}_3^-}$ (Kendall and Caldwell, 1998; Rafter et al., 2019). These isotopic signatures on $\delta^{15}\text{N}_{\text{NO}_3^-}$ and $\delta^{18}\text{O}_{\text{NO}_3^-}$ are preserved for time scales ranging from years to millennia, being shorter for nitrate in surface waters and longer in the deep ocean (Marconi et al., 2019; Deman et al., 2021).

The dual isotopic signature of $\delta^{15}\text{N}_{\text{NO}_3^-}$ and $\delta^{18}\text{O}_{\text{NO}_3^-}$ of different nitrate sources is specific, preserving the characteristics of the processes from which they were originated (Kendall and Caldwell, 1998; Rafter et al., 2019). Consequently, $\delta^{15}\text{N}_{\text{NO}_3^-}$ and $\delta^{18}\text{O}_{\text{NO}_3^-}$ values provide the opportunity of studying specific deviations related with N_2 fixation, nitrate assimilation by phytoplankton, denitrification and nitrification (Miyake and Wada, 1967; Wada and Hattori, 1978; Liu, 1979; Carpenter et al., 1997; Casciotti et al., 2013; Rafter et al., 2013, 2019; Sigman and Fripiat, 2019). In this sense, and considering the discrimination of phytoplankton for the heavy ^{15}N isotope, it has been demonstrated that assimilation and denitrification processes, raise $\delta^{15}\text{N}_{\text{NO}_3^-}$ and $\delta^{18}\text{O}_{\text{NO}_3^-}$, in an approximate ratio of 1:1, generating trend lines (Brandes and Devol, 2002; Casciotti, 2016; Peters et al., 2018; Sigman and Fripiat, 2019).

The process producing new combined nitrogen in the marine environment and its subsequent transformation to NO_3^- has different effects in $\delta^{15}\text{N}$ and $\delta^{18}\text{O}$, decoupling the two isotope systems: $\delta^{15}\text{N}$ of the new nitrate is controlled by the dissolved N_2 ratio, and the fixation and organic matter remineralization processes, the degree of nitrate assimilation in euphotic zone and by the $\delta^{15}\text{N}_{\text{NO}_3^-}$ from below the pycnocline. On the contrary, $\delta^{18}\text{O}$ has greater variability since it is affected by the $^{18}\text{O}:^{16}\text{O}$ ratio of dissolved O_2 , which is much more variable than dissolved N_2 , since it is a mixture of atmospheric O_2 and new O_2 from

photosynthesis. Additionally, a fractionation occurs in the process of incorporation of the oxygen atoms in the NO_2^- and NO_3^- (Fawcett et al., 2015; Casciotti, 2016; Sigman and Fripiat, 2019). The preservation of the isotopic oxygen signal in nitrate is guaranteed since at the pH of seawater the rate of oxygen isotope exchange between water and NO_3^- is extremely slow (millions of years) (Kaneko and Poulson, 2013). However, there is evidence for oxygen isotope exchange between H_2O and NO_2^- , and this intermediate step of the nitrification process affects the final isotopic value of nitrate. This last step aims to homogenize oxygen isotopic values. The competition for ammonium between phytoplankton and nitrifying bacteria, causes lower $\delta^{15}\text{N}$ values in the photic zone than in the dark waters below, where nitrification predominates (Kemeny et al., 2016). Finally, theoretical enzymatic isotopic exchange reactions between nitrate and nitrite are related to opposite trends in $\delta^{18}\text{O}$ and $\delta^{15}\text{N}$ values of nitrates (Kemeny et al., 2016; Chen et al., 2022).

Apart from biogeochemical processes, the distribution of NO_3^- isotopes can also be altered by physical processes, such as mixing (Peters et al., 2018). In this sense, the intense meso- and submesoscale activity in the CVFZ makes the area especially interesting for an isotopic approach. In this chapter, we used data from the FLUXES I and II cruise, and the water mass proportions calculated with an Optimum Multiparameter analysis, to gain new insights on the distribution, interactions of the marine N cycle and isotopic characterization of nitrate in the different water masses present in CVFZ using the $\delta^{15}\text{N}_{\text{NO}_3^-}$ and $\delta^{18}\text{O}_{\text{NO}_3^-}$ signatures.

4.2 Materials and Methods

4.2.1 Sampling strategy

As explained in Chapter 2 and Chapter 3 of this PhD Thesis, two cruises were carried out. FLUXES I (R/V Sarmiento de Gamboa; Las Palmas - Las Palmas, 12 July to 9 August 2017) consisted of four transects (Northern, Western, Southern and Eastern) defining a box crossing the CVFZ, including 35 hydrographic stations 50 nautical miles apart (Fig. 4.1) sampled from the surface to 4000 dbar. FLUXES II (Fig. 4.1) (R/V Sarmiento de Gamboa; Las Palmas - Las Palmas, 2-24 November 2017), consisted of two biogeochemical transects, where a total of 48 hydrographic station were sampled at 10 levels each from surface to 1500 dbar. In this Chapter, we will only use the first

biogeochemical transect of FLUXES II, which consisted of 36 sampling station along of 175 NM (324 km) with a horizontal resolution of 5 NM (9.3 km).

Seawater samples collection along the transects were carried out using a rosette sampler with 24 Niskin bottles of 12 L and equipped with a conductivity, temperature and depth (CTD) probe (SeaBird SBE911 plus), and sensors for dissolved oxygen (SeaBird SBE43), fluorescence of chlorophyll (SeaPoint SCF), turbidity (SeaPoint STM) transmittance (WetLabs C-Star) and nitrate (SUNA V2, SeaBird). Salinity was calibrated using a Guildline 8410-A Portasal salinometer, and conductivity measurements were converted into practical salinity units using the (UNESCO, 1985) equation.

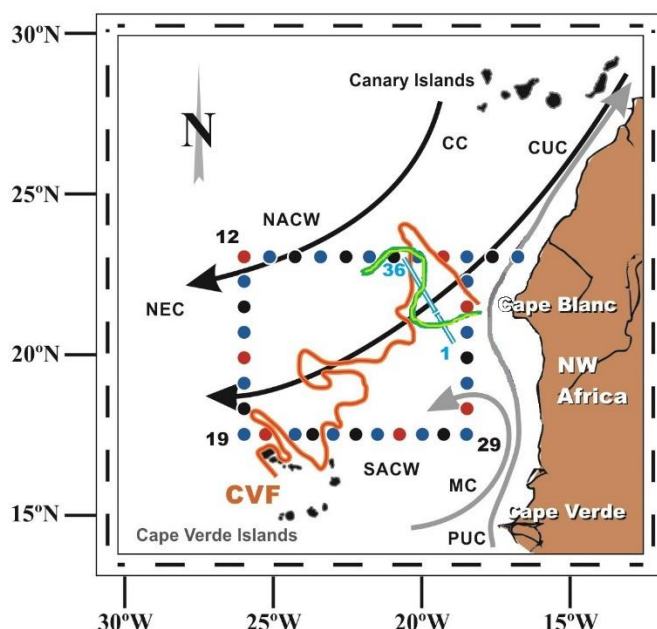


Figure 4.1. Map of FLUXES I (dots) and II (light blue line) cruises. In FLUXES I, dots represent the stations (blue: diurnal stations; black: nocturnal stations; red: long stations) the black numbers indicate the station number, from 1 to 35. In FLUXES II, the biogeochemical transect is represented by a light blue line, blue numbers indicate station number from 1 to 36. The main geographic and oceanographic features and currents are represented. The orange and green line represents the approximate position of the CVF during the FLUXES I cruise (taken from Burgoa et al., 2021) and FLUXES II respectively.

Water samples for the determination of $\delta^{15}\text{N}_{\text{NO}_3^-}$ and $\delta^{18}\text{O}_{\text{NO}_3^-}$, were taken directly from the Niskin bottles, in borosilicate vials of 12 mL, in which HgCl_2 were previously added in the laboratory to prevent microbial activity, and were refrigerated at 4 °C for their conservation until analysis in the Laboratory of Biogeochemistry of Stable Isotopes of the Instituto Andaluz de Ciencias de la Tierra (CSIC-UGR).

4.2.2 Analytical determinations

The determination of $\delta^{15}\text{N}_{\text{NO}_3^-}$ and $\delta^{18}\text{O}_{\text{NO}_3^-}$ was carried out following the routinary method of the Laboratory of Biogeochemistry of Stable Isotopes of the Instituto Andaluz de Ciencias de la Tierra (CSIC-UGR) based on a modified protocol of the procedure described by McIlvin and Altabet (2005). Sample preparation before $^{15}\text{N}:^{14}\text{N}$ and $^{18}\text{O}:^{16}\text{O}$ analysis as N_2O consisted in two steps, which involves two primary reduction reactions: first NO_3^- to NO_2^- , followed by NO_2^- to N_2O .

12 mL headspace glass (borosilicate) vials were used as reaction vials. For the first step of conversion of nitrate into nitrite, the sponge cadmium method was used (Margeson et al., 1980). A volume of 10 mL of sample was placed in 12 mL borosilicate vials, 1 mL of 0.5 M EDTA was added to obtain a pH close to 8.5, followed by one gram of spongy cadmium (Cd) (Fig. 4.2). The samples were closed and shaken at room temperature. Then, these 5 mL, were injected with a syringe in two 12 mL headspace borosilicate reaction vials, to have two replicates and had enough headspace to the produced N_2O (Fig. 4.2). Prior to this step, the borosilicate reaction vials were primarily filled with He and capped tightly with Teflon-line septa, to minimize the oxygen exchange in the final product N_2O , and maximize the precision and consistency of the $\delta^{18}\text{O}$ of nitrate of the samples.

The second step consisted on the addition of 1 mL of an azide/acetic acid buffer to each vial with a syringe to reduce the pH to 4.5 and carry out the reduction of nitrite to N_2O (Fig. 4.2). The azide/acetic acid buffer was prepared daily. McIlvin and Altabet (2005) mixed in 1:1 volume proportion 20% acetic acid and 2 M sodium azide, and then purged with He to remove any trace of N_2O in the mixture. Here, a mixture in 3:1 volume proportion (20% acetic acid and 3 M sodium azide) was used, adding also 1:1 volume proportion of sodium acetate 3 M with the acetic acid, to increase the pH stability and minimize the oxygen exchange. McIlvin and Altabet (2005) performed all reactions at room temperature. They considered that 15 minutes were the optimal reaction time, and then 0.5 mL of 6 M NaOH was injected to rise the pH to 12 to stop the reaction. However, they observed that incubating the samples for hours beyond the required reaction time did not have negative effects. Therefore, in this PhD thesis, to decrease the N_2O solubility, the reaction took place on a thermostatic bath at 50°C , and 6 hours was the reaction time (Fig. 4.2). After use, the decanted spongy cadmium in the discarded vials was collected and

washed with HCl 6M and then repeatedly rinsed with deionized water until pH was neutral, so it could be reused again.

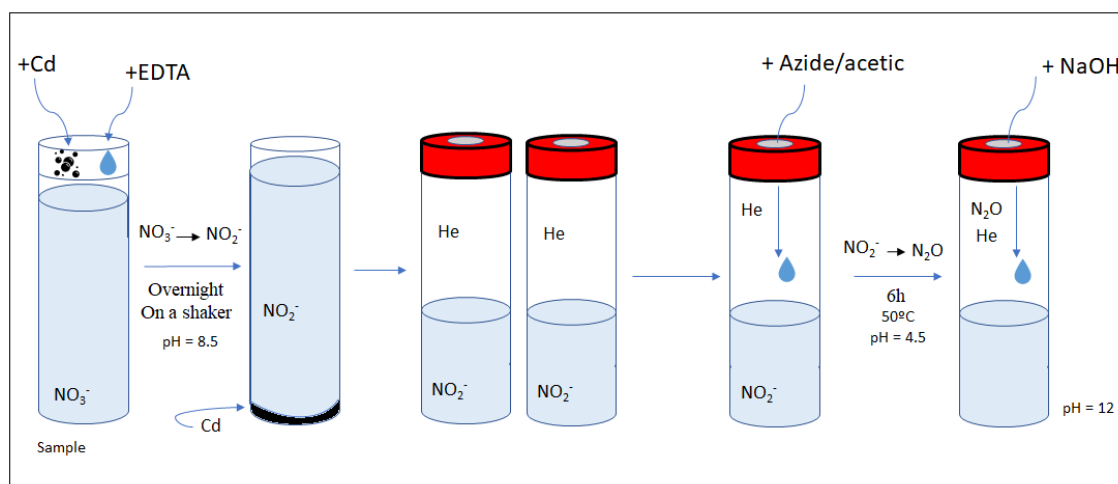


Figure 4.2. Brief schematic summary of the method. Note that in the first step, in which the vials were closed with caps and a shaken overnight, the necessary He purge of azide/acetic reagent and the Cd recollection in discarded vials were not drawing.

Nitrite showed very low concentrations compared with NO_3^- in most samples. Thus, samples can be analysed without interference and unaltered for NO_3^- isotopic composition.

Prior to use, the $\delta^{18}\text{O}$ of the water used for reagents preparation was determined with a laser spectroscopy analyzer (Picarro L2140-i, USA). Five international standards with known $\delta^{15}\text{N}_{\text{NO}_3^-}$ and $\delta^{18}\text{O}_{\text{NO}_3^-}$ were used (see Table 4.1), to check the consistency of the method, to correct analytical variations associate to the Isotope-Ratio Mass Spectrometer (IRMS), and finally for the calculation of the true $\delta^{15}\text{N}_{\text{NO}_3^-}$ and $\delta^{18}\text{O}_{\text{NO}_3^-}$. These standards were treated with the same protocol than seawater samples. For this, 10 mL of $15 \mu\text{mol L}^{-1}$ international standard solution prepared in deionized water were added into 12 mL reaction vials. In the same way, laboratory standards of NaNO_2 named IACT 9 and IACT 10 ($\delta^{15}\text{N}$ -8.08‰ and -37.8‰ determined by IRMS, respectively) were run to check the efficiency of the second step (NO_2^- to N_2O). For this, 5 mL of 5, 10 and $15 \mu\text{mol L}^{-1}$ solution prepared in deionized water were added into the 12 mL vials filled with He.

Finally, for the analysis of the final product (N_2O), the samples were run on an automated purge and trap system, Gas Bench II, coupled to an IRMS, Deltaplus XP (ThermoFisher scientific). The samples were run in an automatic autosampler (Combipal de CTC Analytics). After 800 seconds purge time, the trap was released from the liquid nitrogen and the gas sample was then diverted to the GS-Q GC column, for separating the

N₂O from any remaining CO₂ and O₂. Finally, by a capillary from an open split directly to the ion source the sample entered to the mass spectrometer.

Table 4.1. International standard used and their known $\delta^{15}\text{N}$ and $\delta^{18}\text{O}$.

	Reagent	$\delta^{15}\text{N}$ (‰)	$\delta^{18}\text{O}$ (‰)
EEZ-30	KNO ₃	14.38	27.10
EEZ-31	NaNO ₃	-0.22	14.16
USGS 34	KNO ₃	-1.8	-27.9
USGS 35	NaNO ₃	2.7	57.5
IAEA-NO3	KNO ₃	4.7	25.6

4.2.3 Correction to calculate the true $\delta^{15}\text{N}$ and $\delta^{18}\text{O}$ of nitrate

As described by McIlvin and Altabet (2005), assuming that the two-step reactions goes to completion, one of the two N atoms in the produced N₂O is provided by the NO₃⁻ of the sample and the other by the azide reagent. This fact is reflected in the slope of the relationship between the $\delta^{15}\text{N}_{\text{NO}_3^-}$ international standards and the $\delta^{15}\text{N}$ of the produced N₂O, which is 0.5. On the other hand, the oxygen isotopic composition of the produced N₂O reflects that of the NO₃⁻ in the sample, the oxygen exchange with water and the isotopic fractionation during the Cd or azide reduction. Most of these oxygen exchange occurs during the step of nitrite to nitrous oxide reduction, when the incorporation of oxygen atoms from water could account for around 20% of the measured N₂O (McIlvin and Altabet, 2005). So, the $\delta^{18}\text{O}$ slope should be 1 if no oxygen exchange with water occurs while if complete exchange occurs the slope should be 0 (McIlvin and Altabet, 2005).

To correct samples for oxygen exchange, the $\delta^{18}\text{O}_{\text{NO}_3^-}$ in the sample is divided by the slope of the curve made with the nitrate standards, with know $\delta^{18}\text{O}$:

$$\delta^{18}\text{O}_{\text{NO}_3^-} = \frac{(\delta^{18}\text{O}_{\text{N}_2\text{O}} - b)}{m_{std}}$$

Where b is the y-intercept and m_{std} is the slope of the linear regression obtained between the measured $\delta^{18}\text{O}$ in final N_2O product and the theoretical $\delta^{18}\text{O}$ of the standards, all reported relative to Vienna Standard Mean Ocean Water (V-SMOW). In the same way, to correct the $\delta^{15}\text{N}_{\text{NO}_3^-}$ of samples, the linear fitting is performed between the $\delta^{15}\text{N}$ measured in the final N_2O product and the theoretical $\delta^{15}\text{N}$ associated to each standard:

$$\delta^{15}\text{N}_{\text{NO}_3^-} = \frac{(\delta^{15}\text{N}_{\text{N}_2\text{O}} - b)}{m_{std}}$$

4.2.4 Water mass analysis, WT proportion-weighted average values and multiple regression models

An optimum multiparameter (OMP) inverse method (Karstensen and Tomczak, 1998) was used for the quantification of the proportions (X_{ij}) of the water types (WTs) that contribute to the water samples collected in the meso- and bathypelagic layers (200–4000 dbar) during FLUXES I and mesopelagic layer (200–1500 dbar) during FLUXES II. This OMP method has been explained in detail in the previous chapters (see Chapter 2 for the OMP of FLUXES I; and Chapter 3 for the OMP for FLUXES II). Once the WT proportions were obtained, we calculated the WT proportion weighted-average (hereafter, archetype) value $\delta^{15}\text{N}_{\text{NO}_3^-}$ and $\delta^{18}\text{O}_{\text{NO}_3^-}$.

To consider the combined effect of mixing and biogeochemical processes, through the multiple linear regression (as already detailed in Chapter 2), with X_{ij} (mixing model) and with $X_{ij} + \text{AOU}$ (mixing + biogeochemical model), the delta notation ($\delta^{15}\text{N}_{\text{NO}_3^-}$), were first converted into a concentration value of $^{15}\text{NO}_3^-$ concentration. To calculate these $^{15}\text{NO}_3^-$ concentration, the equation of delta notation and nitrate concentration was used, by obtaining the $^{15}\text{N}:^{14}\text{N}$ ratio of each sample (R_s) following the equation:

$$R_m = \left(\frac{\delta^A X}{1000} + 1 \right) * R_{St}$$

and multiplying then by its NO_3^- concentration. Where $\delta^A X$ represent $\delta^{15}\text{N}_{\text{NO}_3^-}$, and R_{St} represent the isotope ratio $^{15}\text{N}:^{14}\text{N}$ in a sample and in atmospheric N_2 ($0.36765 \pm 0.00081\%$).

Low nitrate concentrations in the surface layer (< 30 dbar) of the CVFZ (see Figures 2.6a and 3.8a in Chapter 2 and 3 respectively), were generally below the limit of detection of the isotopic method, producing unreliably high N and O isotopic fractionation values. For this reason, surface waters were omitted in this chapter, and the nitrate isotope distribution was studied in the following domains: 1) in the 30 to 200 dbar layer, the four transects of FLUXES I (Northern (stn 3-12), Western (stn 12-19), Southern (stn 19-29) and Eastern (stn 29-35), and the three domains of FLUXES II (A (stn 1-9), B (stn 9-28) and C (stn 28-36)) were considered. In addition, due to the generally low nitrate concentrations above and at the DCM, the epipelagic layer was divided in two layers: 30 to 100 dbar, and 200 dbar, which is different from the approach used in chapters 2 and 3; and 2) below 200 dbar, the central, intermediate and deep water masses identified in CVFZ.

4.3 Results

4.3.1 $\delta^{15}\text{N}_{\text{NO}_3^-}$ and $\delta^{18}\text{O}_{\text{NO}_3^-}$ in epipelagic waters (30 - 200 dbar)

During the FLUXES I cruise lowest values of the $\delta^{15}\text{N}_{\text{NO}_3^-}$ were found in the epipelagic layer (30 to 200 dbar) without significant differences between the average value from 30 to 100 dbar and the base of the epipelagic layer (200 dbar), 4.1‰ and 4.6‰ (AIR) respectively (Table 4.2). On the contrary $\delta^{18}\text{O}_{\text{NO}_3^-}$ showed higher average values from 30 to 100 dbar than at 200 dbar, +5.4 and +3.6‰ (V-SMOW) respectively ($p < 0.005$). When each transect was considered separately, $\delta^{15}\text{N}_{\text{NO}_3^-}$ from 30 to 100 dbar showed similar values without significant differences between transect (Table 5.2). On the contrary, significant differences were found between all transects in $\delta^{18}\text{O}_{\text{NO}_3^-}$ ($p < 0.0005$). The Southern transect showed the highest $\delta^{18}\text{O}_{\text{NO}_3^-}$ values around +7‰ (V-SMOW), reaching a maximum of +15‰ (Table 5.2), while the Northern transect showed the lowest $\delta^{18}\text{O}_{\text{NO}_3^-}$ mean value of +2.5‰ (Table 5.2). At the base of euphotic zone at 200 dbar showed similar $\delta^{15}\text{N}_{\text{NO}_3^-}$ mean values ($p > 0.1$) in the different transects, while on the contrary, significant differences were found in $\delta^{18}\text{O}_{\text{NO}_3^-}$ mean values, with the lowest mean value in the Northern transect around 2.1‰ vs V-SMOW ($p < 0.025$). (Table 5.2).

Below pycnocline, the Orthogonal Distance Regression (ODR) of $^{15}\text{NO}_3^-$ concentration and salinity ($^{15}\text{NO}_3^- = -0.076 (\pm 0.006) \cdot S + 2.8 (\pm 0.2)$; $R^2 = 0.71$; $n = 50$)

indicates that 71% of the variability of $^{15}\text{NO}_3^-$ depends on the mixing of North and South Atlantic waters. A multiple correlation of $^{15}\text{NO}_3^-$ with salinity and AOU was also calculated to separate the contribution of mixing (traced by salinity) from mineralisation processes (traced by AOU), obtaining a $R^2 = 0.94$.

As explained in Chapter 2, the mixing and mixing + biogeochemical regression models explained a similar percentage of variability of NO_3^- than of $^{15}\text{NO}_3^-$ (75 vs 71% for the mixing, and 96 vs 94% for the mixing+biogeochemical model). As expected, the SE of the estimate was larger for the NO_3^- than for the $^{15}\text{NO}_3^-$ regressions because of the minor proportion of ^{15}N compare with ^{14}N .

FLUXES II showed significantly lower mean values of $\delta^{15}\text{N}_{\text{NO}_3^-}$ in the 30-100 dbar depth range than at 200 dbar ($p < 0.005$). The lowest $\delta^{15}\text{N}_{\text{NO}_3^-}$ mean values at 30-100 dbar were found in domain C (+4.7‰ vs AIR), being significantly lower than in domain B ($p < 0.05$). $\delta^{18}\text{O}_{\text{NO}_3^-}$ showed a high variability along the transect, being significantly different between the three domains ($p < 0.0005$), with higher $\delta^{18}\text{O}_{\text{NO}_3^-}$ mean values in domain A (4.9‰) (Table 4.2). At 200 dbar, $\delta^{15}\text{N}_{\text{NO}_3^-}$ was not significantly different between the three domains. However, $\delta^{18}\text{O}_{\text{NO}_3^-}$ showed high variability at 200 dbar, with domain A presenting significantly higher $\delta^{18}\text{O}_{\text{NO}_3^-}$ mean values than domain C (4.2‰ and 2‰ respectively) ($p < 0.0005$).

Below the pycnocline, the Orthogonal Distance Regression (ODR) of $^{15}\text{NO}_3^-$ concentration and salinity, ($^{15}\text{NO}_3^- = -0.107 (\pm 0.006) \cdot S + 3.9 (\pm 0.2)$; $R^2 = 0.81$; $n = 50$) indicated that mixing explained 81% of the variability of $^{15}\text{NO}_3^-$ concentration. The correlation of $^{15}\text{NO}_3^-$ with AOU explained 92% of $^{15}\text{NO}_3^-$ concentration. The multiple correlation of $^{15}\text{NO}_3^-$ with salinity and AOU was not significant. The simple regression model with salinity and with AOU, explained similar percentage of the variability of NO_3^- than $^{15}\text{NO}_3^-$ (83 vs 81%, and 98 vs 92% respectively) (Chapter 3).

Chapter 4:

Table 4.2. Mean, maximum and minimum values of $\delta^{15}\text{N}_{\text{NO}_3^-}$ and $\delta^{18}\text{O}_{\text{NO}_3^-}$ (‰) in epipelagic waters from 30 to 100 dbar; and at 200 dbar during FLUXES I (Total, Northern, Western, Southern and Eastern transects) and FLUXES II (Total, domain A, domain B and domain C) cruise

	$\delta^{15}\text{N}_{\text{NO}_3^-}$ (‰)				$\delta^{18}\text{O}_{\text{NO}_3^-}$ (‰)			
	30-100	200	Max	Min	30-100	200	Max	Min
FLUXES I								
Total	4.1 ± 0.1	4.6 ± 0.3	6.4	1.5	5.4 ± 0.3	3.6 ± 0.5	15.6	0.3
North	3.9 ± 0.2	3.8 ± 0.4	6.2	1.5	2.5 ± 0.3	2.3 ± 0.5	6.1	0.3
West	3.9 ± 0.2	4.6 ± 0.4	5.9	2.8	6.1 ± 0.4	3.7 ± 0.6	7.2	2.1
South	4.3 ± 0.2	4.5 ± 0.3	6.4	2.6	7.0 ± 0.5	4.9 ± 0.8	15.6	2.8
East	3.9 ± 0.2	4.7 ± 0.4	5.6	2.8	3.9 ± 0.3	3.5 ± 0.7	7.2	1.5
FLUXES II								
Total	5.1 ± 0.2	5.6 ± 0.2	6.9	1.9	3.9 ± 0.2	3.3 ± 0.3	8.5	0.5
Domain A	5.1 ± 0.2	5.9 ± 0.3	6.5	1.9	4.9 ± 0.2	4.2 ± 0.5	8.5	2.3
Domain B	5.2 ± 0.2	5.4 ± 0.2	6.9	3.0	3.6 ± 0.2	3.1 ± 0.4	8.5	0.5
Domain C	4.7 ± 0.2	6.0 ± 0.2	6.4	4.1	1.7 ± 0.1	2.0 ± 0.4	2.7	0.6

4.3.2 $\delta^{15}\text{N}_{\text{NO}_3^-}$ and $\delta^{18}\text{O}_{\text{NO}_3^-}$ in the interior ocean (> 200 dbar)

The $\delta^{15}\text{N}_{\text{NO}_3^-}$ values during FLUXES I from 200 to 1500 dbar (Fig. 4.3a) and the archetype $\delta^{15}\text{N}_{\text{NO}_3^-}$ for the central and intermediate water masses of the CVFZ (Table 4.3), were characterised by lower values in shallower waters, which increased with depth until reaching a maximum at around 700 dbar and then it decreased down to 1500 dbar, from which it remained constant (Fig. 4.4a). On the contrary, the $\delta^{18}\text{O}_{\text{NO}_3^-}$ values (Fig. 4.3b) and the corresponding archetype values of $\delta^{18}\text{O}_{\text{NO}_3^-}$ (Table 4.3) showed higher values in shallower waters, decreasing with depth up to 1000 dbar, and remaining quite constant from 1000 to 4000 dbar.

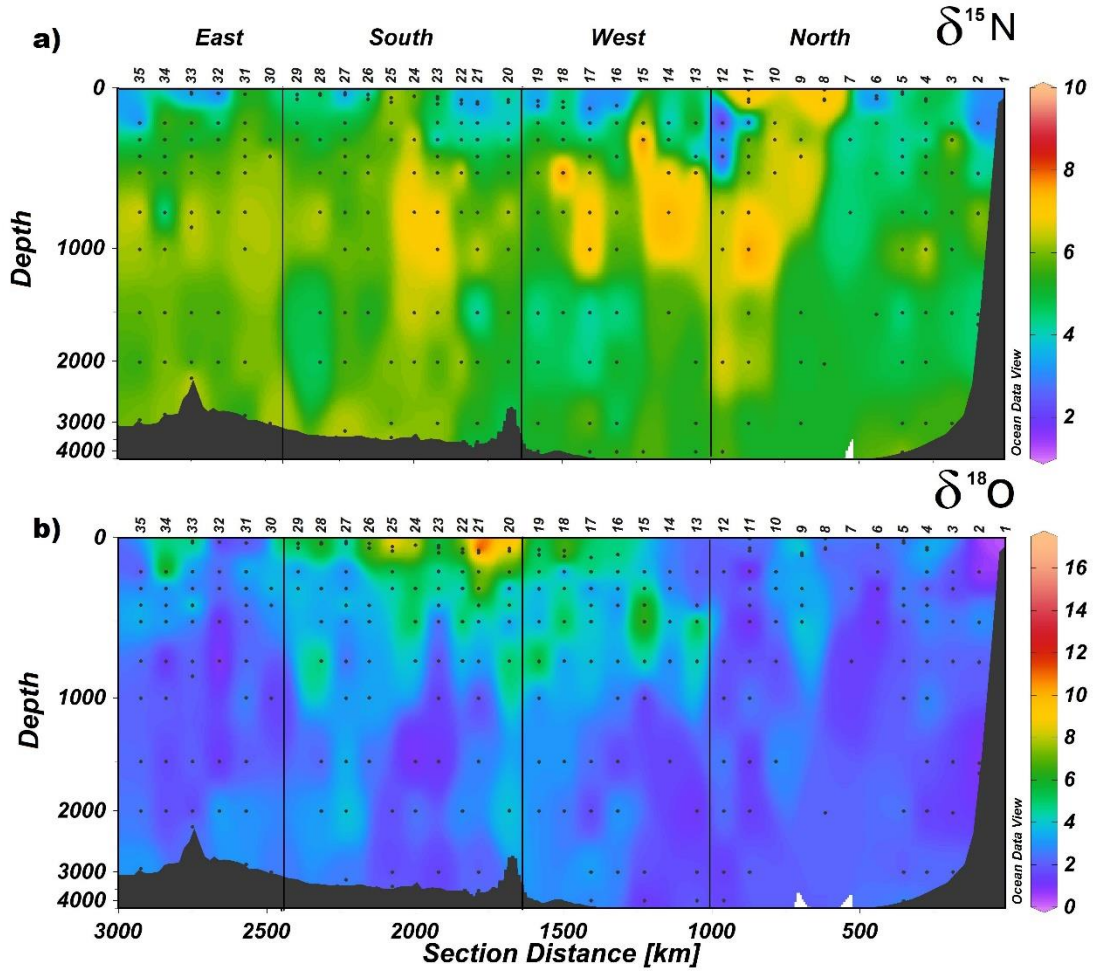


Figure 4.3. Distributions of the $\delta^{15}\text{N}$ (a) and $\delta^{18}\text{O}$ (b) of NO_3^- during the FLUXES I cruise. Dots represent samples and vertical black lines represent the corners of the FLUXES I hydrographic box. Note that depth scale is not linear. The x-axis shows the station number (a,b) or section distance in km (b). Produced with Ocean Data View (Schlitzer, 2017).

During FLUXES I, in the depth range of central waters (100-700 dbar) non-significantly different archetype values of $\delta^{15}\text{N}_{\text{NO}_3^-}$ and $\delta^{18}\text{O}_{\text{NO}_3^-}$ were found with an average value of 4.7‰ and 3.6‰, respectively (Fig. 4.4, Table 4.3). In intermediate waters, the salinity minimum is associated with higher nitrate concentration and $\delta^{15}\text{N}_{\text{NO}_3^-}$, and corresponded to AA and SPMW, characterised by the same archetype $\delta^{15}\text{N}_{\text{NO}_3^-}$ of 5.9‰ and $\delta^{18}\text{O}_{\text{NO}_3^-}$ of 2.7‰ (Fig. 4.4, Table 4.3). In the deep layer, the three deep water types, LSW, UNEADW and LNEADW, showed similar archetype $\delta^{15}\text{N}_{\text{NO}_3^-}$ around 5.3‰ and a mean archetype $\delta^{18}\text{O}_{\text{NO}_3^-}$ of 2.4‰ respectively (Fig. 4.4, Table 4.3).

The multiple regression with X_{ij} explained 94% of the $^{15}\text{NO}_3^-$ concentration variability with a SE of $0.006 \mu\text{mol kg}^{-1}$. When AOU was added to the multiple regression

Chapter 4:

of $^{15}\text{NO}_3^-$ concentration, the explained variability increased to 97% with SE of $0.0042 \mu\text{mol kg}^{-1}$.

WTs mixing explained the same variability of NO_3^- (see Chapter 2) than $^{15}\text{NO}_3^-$. But due the minor proportion of the heavy isotope, the SE of $1.81 \mu\text{mol kg}^{-1}$ of NO_3^- , was larger than the SE of $^{15}\text{NO}_3^-$. In the same way, when AOU was added the mixed+biogeochemical regression model explained same the same percentage of the variability (~97%).

Table 4.3. Average \pm SE of nitrate $\delta^{15}\text{N}$ and $\delta^{18}\text{O}$ (‰) and nitrate concentration ($\mu\text{mol kg}^{-1}$) in FLUXES I and FLUXES II cruise.

	FLUXES I			FLUXES II		
WT	$\delta^{15}\text{N}_{\text{NO}_3^-}$	$\delta^{18}\text{O}_{\text{NO}_3^-}$	NO_3^-	$\delta^{15}\text{N}_{\text{NO}_3^-}$	$\delta^{18}\text{O}_{\text{NO}_3^-}$	NO_3^-
SACW_18	4.3 ± 0.9	4.2 ± 1	16.9 ± 2.1	5.6 ± 0.3	4.1 ± 0.5	24.6 ± 1.2
MMW	3.8 ± 1.4	4.0 ± 1.6	6.5 ± 1.4	n.s.	n.s.	15.4 ± 2.7
ENACW_15	4.5 ± 0.5	3.1 ± 0.5	16.2 ± 1.0	5.4 ± 0.2	3.2 ± 0.4	21.8 ± 0.8
SACW_12	5.4 ± 0.6	3.7 ± 0.5	28.7 ± 1.0	5.8 ± 0.2	3.0 ± 0.5	28.2 ± 0.9
ENACW_12	5.6 ± 0.3	3.3 ± 0.3	27.2 ± 0.8	5.8 ± 0.1	3.0 ± 0.2	29.3 ± 0.5
SPMW	5.9 ± 0.8	2.7 ± 0.4	30.9 ± 0.7	5.9 ± 0.3	2.6 ± 0.4	32.4 ± 0.3
AA	5.9 ± 0.7	2.8 ± 0.4	31.3 ± 0.6	6.2 ± 0.2	2.8 ± 0.3	31.5 ± 0.3
MW	5.4 ± 1.4	2.2 ± 0.6	25.9 ± 1.2	6.1 ± 0.2	2.5 ± 0.5	29.1 ± 0.8
LSW	5.3 ± 0.5	2.2 ± 0.3	23.9 ± 0.3	5.9 ± 0.1	2.5 ± 0.3	26.6 ± 0.32
UNEADW	5.3 ± 0.8	2.3 ± 0.4	22.2 ± 0.2			
LNEADW	5.5 ± 1.4	2.6 ± 0.9	22.4 ± 0.2			

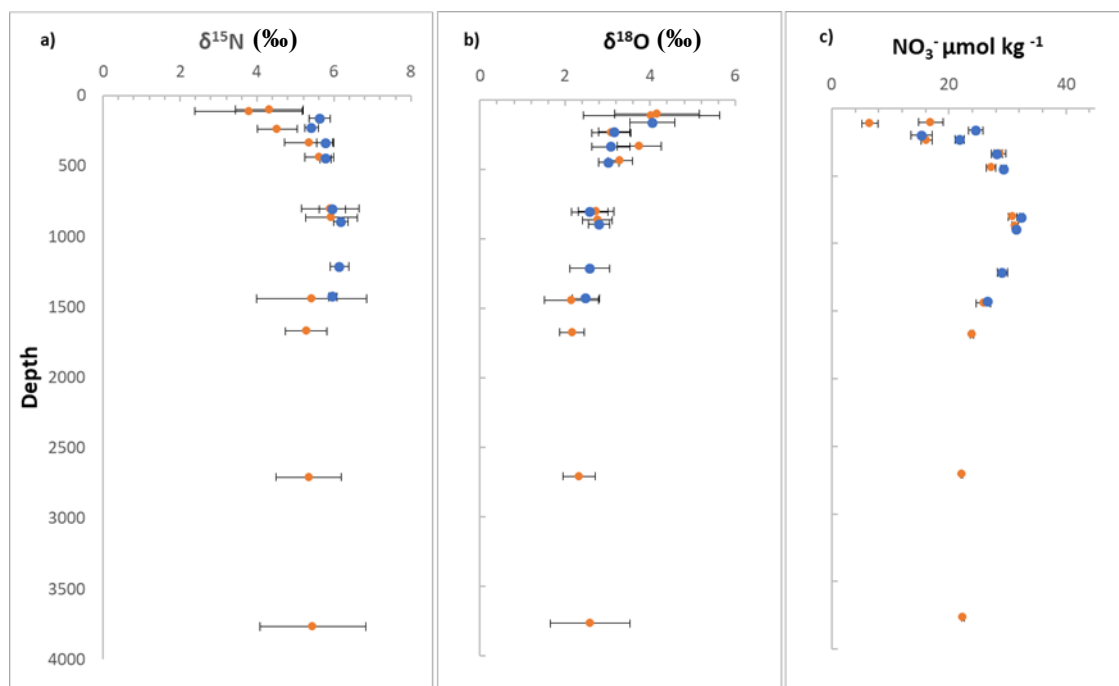


Figure 4.4. Distributions of the $\delta^{15}\text{N}_{\text{NO}_3^-}$ (a) and $\delta^{18}\text{O}_{\text{NO}_3^-}$ (b) (‰) and NO_3^- concentration in ($\mu\text{mol kg}^{-1}$) (c) with SE, of the water masses present in the CVFZ during the FLUXES I (blue dots) and FLUXES II (orange dots) cruises.

Regarding the variability for the different water masses, $\delta^{15}\text{N}_{\text{NO}_3^-}$ showed similar archetype values in all transects ($p > 0.2$) during FLUXES I, except for ENACW_12, which was significantly higher in the Southern than in the Northern and Eastern transects ($p < 0.025$) (Fig. 4.5a, Table S1). On the contrary, archetype $\delta^{18}\text{O}_{\text{NO}_3^-}$ showed significant differences between transects. The shallower SACW_18, showed significantly lower archetype values in the Northern and Eastern transects (2.5 ± 1 and 3.2 ± 1 ‰, respectively) ($p < 0.01$) than in the Southern transects (6.8 ± 0.5 ‰) (Fig. 4.5b, Table S1). The ENACW_15 showed significantly higher archetype values in the Southern Transect (6.8 ± 1.6 ‰) than in the Northern, Western and Eastern transects (1.9 ± 0.4 , 2.9 ± 0.5 and 2.5 ± 0.7 ‰, respectively) ($p < 0.0005$) (Fig. 4.5b, Table S1). SACW_12 also showed significantly lower values in the Northern and Eastern transects ($p < 0.025$) (Fig. 4.5b, Table S1). ENACW_12, which was the only central WT with significant presence in the four transects (as reported in Chapter 2), had significantly higher values in the Western and Southern transect (4.1 ± 0.6 and 4.6 ± 0.3 ‰, respectively), than in the Northern transect (2.1 ± 0.3 ‰) ($p < 0.001$) (Fig. 4.5b, Table S1). In the same way, the intermediate SPMW and AA showed significantly higher values in the Western and Southern transect (> 3.3 ‰) than in the Northern and Eastern transect (< 2.1 ‰) ($p < 0.025$). In deep waters, LSW showed significantly lower $\delta^{18}\text{O}_{\text{NO}_3^-}$ archetype value in the Northern than in the Southern transect

Chapter 4:

(1.8 ± 0.3 and $2.7 \pm 0.3\%$, respectively) ($p < 0.025$). No isotopic differences were observed in LNEADW and UNEADW (Fig. 4.5b, Table S1).

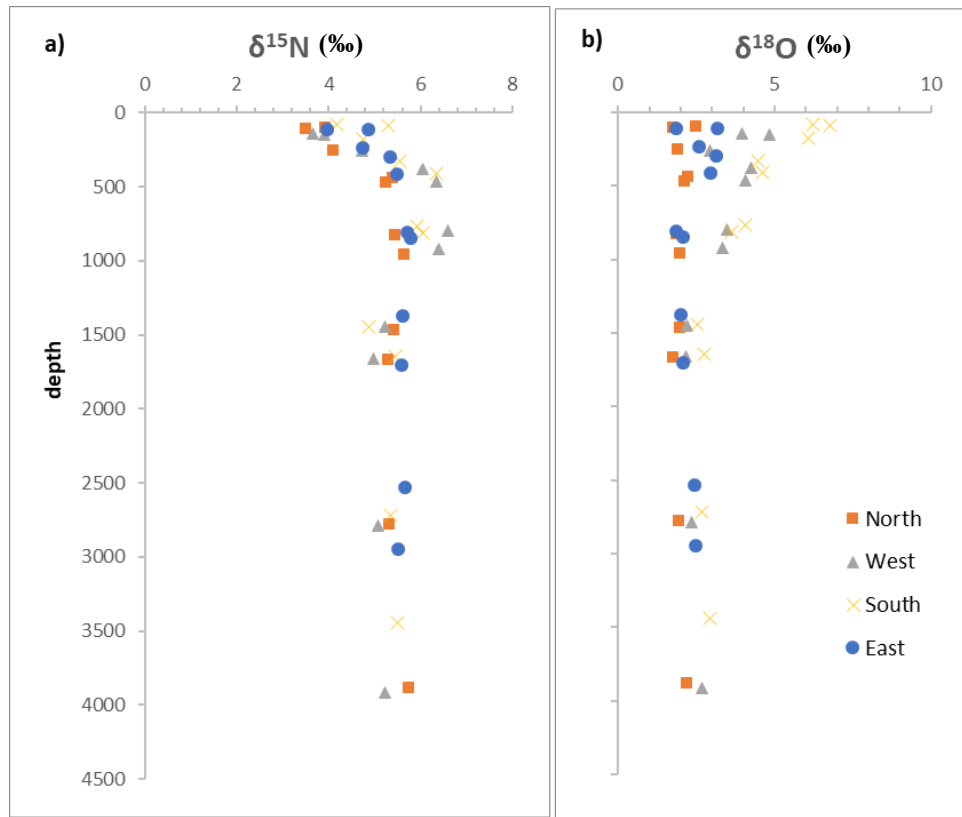


Figure 4.5. Distributions of the $\delta^{15}\text{N}_{\text{NO}_3^-}$ (a) and $\delta^{18}\text{O}_{\text{NO}_3^-}$ (‰) of the water masses present in the Northern, Western, Southern and Eastern transects in CVFZ during FLUXES I cruise. Note that for optimize dots visualization the SE, were non-presented. They are shown in table S1 and figure S7.

In FLUXES II, $\delta^{15}\text{N}_{\text{NO}_3^-}$ values (Fig. 4.6a) below 200 dbar varied from 4-7‰ and $\delta^{18}\text{O}_{\text{NO}_3^-}$ (Fig. 4.6b) ranged between ~2 and 6‰. Generally, in FLUXES II all WT showed similar ($p > 0.1$) values than in FLUXES I (Fig. 4.4).

In central waters non-significantly differences were found, with average archetype values of $\delta^{15}\text{N}_{\text{NO}_3^-}$ and $\delta^{18}\text{O}_{\text{NO}_3^-}$ of 5.6‰ and 3.3‰ respectively (Table 4.3). In intermediate waters, archetype values of $\delta^{15}\text{N}_{\text{NO}_3^-}$ and $\delta^{18}\text{O}_{\text{NO}_3^-}$ were similar without significantly differences, between the three water types, SPMW, AA and MW, with average archetype values of 6.1‰ and 2.7‰ respectively (Fig 4.4, Table 4.3).

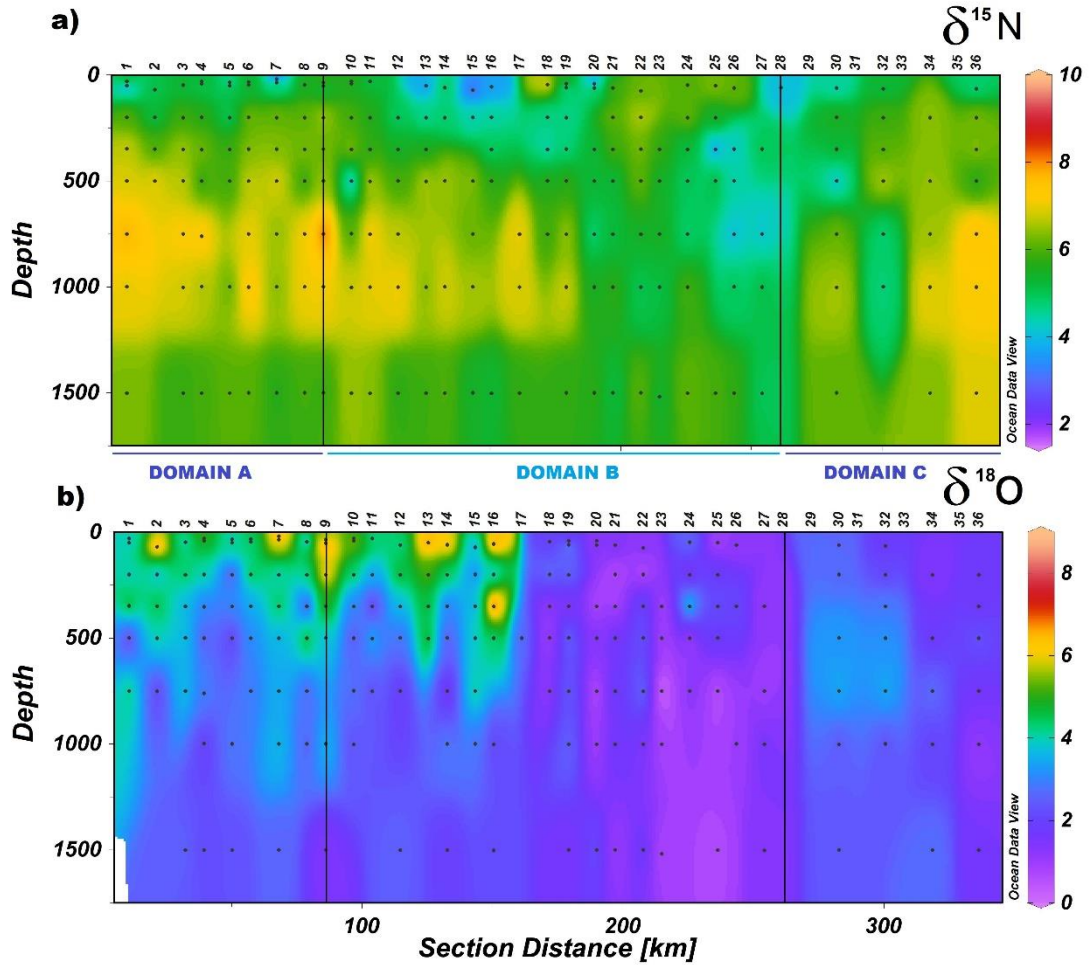


Figure 4.6. Distributions of the $\delta^{15}\text{N}$ (a) and $\delta^{18}\text{O}$ (b) of NO_3^- during the FLUXES II cruise. Dots represent samples. The x-axis shows the station number (a, b) or section distance in km counting from southeast (SE) to northwest (NW) (b). Produced with Ocean Data View (Schlitzer, 2017).

The multiple regression with X_{ij} explained 91% of the observed variability of $^{15}\text{NO}_3^-$ concentration with a SE of $0.005 \mu\text{mol kg}^{-1}$. When AOU was added to the multiple regression of $^{15}\text{NO}_3^-$ concentration it explained 95% of variability with a SE of $0.004 \mu\text{mol kg}^{-1}$.

WTs mixing in FLUXES II explained a lower percentage of the variability of NO_3^- (87%; see Chapter 3) than the 91% of $^{15}\text{NO}_3^-$. Furthermore, the SE of $1.72 \mu\text{mol kg}^{-1}$ was also larger than the SE of $^{15}\text{NO}_3^-$. In the same way, when AOU was added to the mixing + biogeochemical regression model $^{15}\text{NO}_3^-$ increase the explained variability to 90 and 95%, being also higher in $^{15}\text{NO}_3^-$.

4.4 Discussion

4.4.1 $\delta^{15}\text{N}$ and $\delta^{18}\text{O}$ in CVFZ

N_2 fixation drives the entry in the ocean of N with $\delta^{15}\text{N}$ values near to 0 ‰ (AIR), in agreement with the isotopic signature of dissolved N_2 around +0.7 ‰ (AIR). Therefore, when POM derived from N_2 fixation is remineralized below the DCM produces nitrate with relatively low $\delta^{15}\text{N}$ values around 2-3‰ (Peters et al., 2018). Altabet (1988) also suggest that low values of $\delta^{15}\text{N}$ of nitrate in waters below the DCM may also occur due to the transformation of suspended into sinking POM, as a result of active processes such as macrozooplankton feeding, removing isotopically heavy N. Another origin for this anomaly can be related with the competition for NH_4^+ in the photic zone: phytoplankton (assimilation) vs oxidation process. Light inhibits nitrification and NH_4^+ is predominantly consumed by phytoplankton. Consequently, NH_4^+ oxidation is being restricted to the dark waters below the photic zone (Kemeny et al., 2016).

The low $\delta^{15}\text{N}_{\text{NO}_3^-}$ in epipelagic waters (30 – 200 dbar) found at the CVFZ during FLUXES I are in agreement with the low $\delta^{15}\text{N}$ values around 2-3‰ found in the North Atlantic by Knapp et al. (2005) and Marconi et al. (2015; 2019) (20-40°N) as a result of the mineralization of organic nitrogen with low $\delta^{15}\text{N}$ added by N_2 fixation (Knapp et al., 2005, 2008; Marconi et al., 2015, 2017; Peters et al., 2018; Rafter et al., 2019). Hallstrøm et al. (2022) investigated the N_2 fixation rates in the CVFZ during FLUXES I, finding that they displayed marked spatial differences. The regions where higher N_2 fixation rates were detected coincided with areas of low $\delta^{15}\text{N}_{\text{NO}_3^-}$ at 30 - 200 dbar in our study. In fact, they found that the contribution of N_2 fixation rates to the N required for new production ranged from 0.03 to 2.77%, being the highest percentage at the surface and 50 dbar of stn 12, which could explain the lower $\delta^{15}\text{N}_{\text{NO}_3^-}$ values found in this stn at 300 dbar. In addition, many authors found low values of $\delta^{15}\text{N}$ -PON at the surface (2-4‰) in the Atlantic Ocean between 7°N and 32°N associated with a large impact of diazotrophic activity (Montoya et al., 2002; Mahaffey et al., 2003; Landrum et al., 2011; Fernandez et al 2014; Piñago et al., 2023).

$\delta^{15}\text{N}_{\text{NO}_3^-}$ is influenced by nitrate consumption and the isotopic composition of the source nitrogen (Altabet, 1988; Altabet and Francois, 1994; Montoya et al., 2002; Marconi et al., 2019; Piñago et al., 2023). Nitrate assimilation discriminates for the heavy isotope raising the $\delta^{15}\text{N}_{\text{NO}_3^-}$ of surface waters. This high $\delta^{15}\text{N}$ of non-consumed nitrate could enter

the ocean interior by mixing, leaving waters with higher $\delta^{15}\text{N}$ (Rafter et al., 2013; Marconi et al., 2015). In addition, assimilation processes also raise the $\delta^{18}\text{O}$ (Rafter et al., 2013; Casciotti, 2016; Sigman and Fripiat, 2019). The time-series of $\delta^{15}\text{N}_{\text{NO}_3^-}$ by Rafter and Sigman (2016) in the Eastern Equatorial Pacific showed that the variability of nitrate assimilation deviated the $\delta^{15}\text{N}$ around $+2.5\text{‰}$. This deviation is expected to affect minimally subsurface nitrate in the Atlantic Ocean, due to the consumption of all nitrate supplied to the euphotic zone by phytoplankton assimilation (Rafter et al., 2013; Marconi et al., 2015). However, this deviation is known to occur in AA water due to the drawdown of nitrate in Antarctic surface waters (Rafter et al., 2013; Marconi et al., 2015; Peters et al., 2018), where the partial assimilation of NO_3^- leads to increases in both $\delta^{15}\text{N}_{\text{NO}_3^-}$ and $\delta^{18}\text{O}$ of nitrate (Marconi et al., 2015, 2019). In the CVFZ, deviation of $\delta^{15}\text{N}_{\text{NO}_3^-}$ and $\delta^{18}\text{O}_{\text{NO}_3^-}$ appeared at deeper central and intermediate layers, with high $\delta^{15}\text{N}_{\text{NO}_3^-}$ and moderately elevated $\delta^{18}\text{O}_{\text{NO}_3^-}$. The lack of parallelism between both increases suggests that $\delta^{15}\text{N}_{\text{NO}_3^-}$ was imported, and has been associated with samples in which the Optimum Multiparameter water mass analysis revealed that AA had a contribution to the total volume sampled higher than 30%.

Marconi et al. (2019) used a three-dimensional map of surface water contribution to the ocean interior (Total Matrix Intercomparison (TMI) method) (Gebbie and Huybers, 2010), finding that the $\delta^{15}\text{N}$ of sinking PON between 19 and 25°N had similar values of $\delta^{15}\text{N}$ estimates for deep Atlantic nitrate. The mid- to low latitudes of the Atlantic Ocean are characterized by nutrient limitation, being all upwelled nitrate consumed by assimilation. This produces that the $\delta^{15}\text{N}$ of sinking PON increases to an average value of 6.2‰ (Marconi et al., 2019). The addition of regenerated nitrate from this PON, also contributes to these higher $\delta^{15}\text{N}$ values. These processes can explain the higher values of $\delta^{15}\text{N}$ in deeper ocean below 1200 dbar, where the contribution of AA is insignificant and where $\delta^{18}\text{O}$ of nitrate was similar than the deep ocean average of ~2‰ (Peters et al., 2018).

The range of $\delta^{15}\text{N}_{\text{NO}_3^-}$ values found during FLUXES II was in line with the range (2-7‰) found in the Atlantic Ocean by Marconi et al. (2015). The increase of $\delta^{18}\text{O}_{\text{NO}_3^-}$ without a parallel increase in the $\delta^{15}\text{N}$ of nitrate in domain A suggests the co-occurrence of assimilation and nitrification processes, which produce the raising of $\delta^{18}\text{O}$ while the $\delta^{15}\text{N}_{\text{NO}_3^-}$ remain constant. Both processes are part of the N cycle, therefore their co-occurrence has no effect on the $\delta^{15}\text{N}$ of nitrate in the same water parcel (Sigman et al.,

2009; Casciotti et al., 2011; Marconi et al., 2015; Deman et al., 2021). However, for O atoms, both processes have different patterns, because nitrification act as a source of O to nitrate and assimilation acts as sink of O, altering $\delta^{18}\text{O}_{\text{NO}_3^-}$ (Sigman et al., 2009; Casciotti et al., 2011; Deman et al., 2021).

These processes explain the high $\delta^{18}\text{O}_{\text{NO}_3^-}$ values at depths below 250 dbar. But it is non-clear how these processes can explain the increase of $\delta^{18}\text{O}_{\text{NO}_3^-}$ down to 400 dbar. This increase of $\delta^{18}\text{O}_{\text{NO}_3^-}$ was also found by Marconi et al. (2015) in other regions of the Atlantic Ocean (60°W), without a clear explanation, and by Fawcett et al. (2015) and Deman et al. (2021) in higher Atlantic latitudes, who suggested that it can occurs by the transport of the nitrate with assimilation isotopic signal by the circulation.

4.4.2 Isotopic imprints in the nitrate of the different water masses of the CVFZ

In the FLUXES I cruise, the profiles of archetype $\delta^{15}\text{N}_{\text{NO}_3^-}$ and $\delta^{18}\text{O}_{\text{NO}_3^-}$ followed the same patterns as those found by Marconi et al. (2015) in the Atlantic Ocean. Archetype values of $\delta^{15}\text{N}_{\text{NO}_3^-}$ and $\delta^{18}\text{O}_{\text{NO}_3^-}$ found in the shallower central water masses in the CVFZ are not significantly different from the mean values found by Marconi et al. (2019) at $\leq 20^\circ\text{N}$ ($5.34\text{‰} \pm 1.47$ and $2.70\text{‰} \pm 2.37$, respectively). Archetype $\delta^{15}\text{N}_{\text{NO}_3^-}$ of ENACW at the CVFZ was higher than the $\delta^{15}\text{N}_{\text{NO}_3^-}$ in its formation area of 4.41‰ (Deman et al., 2021). This was especially noticeable in ENACW₁₂ with 5.6‰ at the CVFZ. Both ENACW and SACW presented similar $\delta^{15}\text{N}_{\text{NO}_3^-}$ values to those found by Marconi et al. (2015) between $4.5\text{--}5.2\text{‰}$ for ENACW and $4.8\text{--}5.5\text{‰}$ for SACW respectively in $20\text{--}40^\circ\text{N}$, $20\text{--}70^\circ\text{W}$.

Archetype $\delta^{15}\text{N}_{\text{NO}_3^-}$ and $\delta^{18}\text{O}_{\text{NO}_3^-}$ of AA in the CVFZ were slightly lower than the mean values in the source region of this water mass ($\delta^{15}\text{N}$ 6.2‰ ; $\delta^{18}\text{O}$ 3.5‰ ; nitrate concentration $20.6 \mu\text{mol kg}^{-1}$ (Sigman et al., 1999; Marconi et al., 2019), while a noticeable increase occurs in the concentration of nitrate from the source region to the CVFZ. This is because of two reasons; first, the aging of AA from the source to the study regions, which could explain the decrease of $\delta^{18}\text{O}_{\text{NO}_3^-}$ by nitrate regeneration with low $\delta^{18}\text{O}$ (Rafter et al., 2013; Marconi et al., 2015; Casciotti, 2016; Deman et al., 2021); and second, because the AA in the CVFZ is not a pure water mass but it intensely mixed with water masses with

lower $\delta^{15}\text{N}_{\text{NO}_3^-}$ and $\delta^{18}\text{O}_{\text{NO}_3^-}$. Marconi et al. (2015, 2019) found even lower $\delta^{15}\text{N}_{\text{NO}_3^-}$ and $\delta^{18}\text{O}_{\text{NO}_3^-}$ values in AA, around 5.4‰ and 1.9‰ in the North Atlantic, suggesting that the regenerated nitrate, and sinking of organic matter with low $\delta^{15}\text{N}_{\text{NO}_3^-}$ from N_2 fixation in the mid-depth counteracts the continuous import of higher $\delta^{15}\text{N}_{\text{NO}_3^-}$ from the Southern Ocean as it flows northward in the Atlantic. On the contrary, the MW in its formation region had a $\delta^{15}\text{N}_{\text{NO}_3^-}$ and $\delta^{18}\text{O}_{\text{NO}_3^-}$ values of 3‰ and 2‰ respectively and nitrate concentration of $11.2 \mu\text{mol kg}^{-1}$ (Pantoja et al., 2002), being our archetype values higher in the CVFZ (5.4‰, 2.2‰, $\sim 25 \mu\text{mol kg}^{-1}$). These higher values are related with the influence of AA and the low volume of MW sampled in the study area during the FLUXES I cruise (3.1%; Chapter 2). High $\delta^{15}\text{N}_{\text{NO}_3^-}$ and $\delta^{18}\text{O}_{\text{NO}_3^-}$ values were also reported for MW in the Atlantic Ocean by Marconi et al. (2015, 2019).

Marconi et al. (2019) found that in Equatorial and North Atlantic waters (0-60°N), the $\delta^{15}\text{N}$ of regenerated nitrate in a given range of latitude was similar for different water masses, which is expected for regenerated nitrate derived mainly from sinking PON than *in situ* DON remineralization, and suggest that the remineralization of sinking N increases the $\delta^{15}\text{N}$ of nitrate in NADW as it flows southward. These patterns were also shown in the different WT present in CVFZ, suggesting that regenerated nitrate was primarily derived from sinking PON, which supports the conclusion of the previous chapters on the greater importance of sinking POM than DON and suspended PON for nitrate production in the interior ocean.

Average archetype values of $\delta^{15}\text{N}_{\text{NO}_3^-}$ and $\delta^{18}\text{O}_{\text{NO}_3^-}$ and nitrate concentration found in the deep ocean were similar for the three WTs and were in agreement with the characteristic values of $\delta^{15}\text{N}_{\text{NO}_3^-}$ and $\delta^{18}\text{O}_{\text{NO}_3^-}$ in deep ocean water, which range between 3 and 6 ‰ with a global average of 4.8‰ (Montoya, 2008; Rafter et al., 2013; Fernandez et al., 2014; Marconi et al., 2015) for $\delta^{15}\text{N}$ and ~ 2 ‰ for $\delta^{18}\text{O}$. Suggesting that in deeper layers the circulation and mixing equilibrate the $\delta^{15}\text{N}$ and $\delta^{18}\text{O}$ of nitrogen pools in these WT.

4.4.3 Dominant nitrogen cycle processes along the four transects of FLUXES I

In FLUXES I, when each transect was considered separately, at depths below 200 dbar, in the domain of the shallower central waters, while $\delta^{15}\text{N}_{\text{NO}_3^-}$ showed similar values

along the four transects, $\delta^{18}\text{O}_{\text{NO}_3^-}$ showed lower values in the transects near the coast, i.e. the Northern and Eastern transects. Nitrate assimilation by phytoplankton rises proportionally the $\delta^{15}\text{N}$ and $\delta^{18}\text{O}$ of the remaining nitrate (Sigman et al., 2009; Rafter et al., 2013; Marconi et al., 2015; Casciotti, 2016; Rafter et al., 2019), while decoupling of the $\delta^{15}\text{N}$ and $\delta^{18}\text{O}$ of nitrate has been associated to the isotopic imprints of nitrification in the euphotic zone, which can overprint the isotopic signal of nitrate assimilation with a contribution of higher $\delta^{18}\text{O}_{\text{NO}_3^-}$ respect to $\delta^{15}\text{N}_{\text{NO}_3^-}$ (Sigman et al., 2009; Casciotti et al., 2011; Rafter et al., 2013; Fawcett et al., 2015). The co-occurrence of assimilation and nitrification processes in the euphotic zone increase the $\delta^{18}\text{O}_{\text{NO}_3^-}$ more than $\delta^{15}\text{N}_{\text{NO}_3^-}$ (Fawcett et al., 2015; Rafter et al., 2019). $\delta^{15}\text{N}$ of regenerated nitrate have similar values of $\delta^{15}\text{N}$ in suspended particulate organic N (Casciotti, 2016; Sigman and Fripiat, 2019). While higher values of $\delta^{18}\text{O}_{\text{NO}_3^-}$ are associate to assimilation processes, lower values of $\delta^{18}\text{O}$ are associated with regenerated nitrate.

As nitrate regenerates, it may have higher or lower $\delta^{15}\text{N}$ values than the isotopic values of suspended PON. However, $\delta^{18}\text{O}$ is not dependent on regeneration (Montoya, 2008; Rafter et al., 2013; Fawcett et al., 2015; Sigman and Fripiat, 2019). On the one hand, the lower values of $\delta^{18}\text{O}_{\text{NO}_3^-}$ at depths below 200 dbar and in the shallower central waters of the Northern and Eastern transects could be related with the higher contribution of suspended PON to the organic matter remineralization, than in the Southern and Western transects. This result was in line with the higher PON concentration found at surface layers in the Northern and Eastern transect (Chapter 2) with higher percentage of suspended PON contributing to the remineralization in the Norther and Eastern transects ($\geq 10\%$) than in the Western and Southern transects ($\leq 4\%$), being furthermore, the remineralization of PON in mesopelagic layers higher in the Northern (3.9%) than in the Southern (1.4%) transect.

On the other hand, the higher values of $\delta^{18}\text{O}_{\text{NO}_3^-}$ at deeps below 200 dbar, in the shallower central waters of the Southern and Western transects, suggest the imprints of the co-occurrence of nitrate assimilation and nitrification. Generally, in low latitudes where surface nitrate consumption tends to be most often complete, complete assimilation process tends to be dominant. However, around 125-175 dbar, an exception could occur. In this layer, which constitute a transition zone from the thermocline to the euphotic zone, partial nitrate assimilation followed by nitrification could occurs, reaching $\delta^{18}\text{O}_{\text{NO}_3^-}$ (Knapp et al., 2008; Sigman et al., 2009; Fawcett et al., 2015).

4.5 Conclusion

$\delta^{15}\text{N}_{\text{NO}_3^-}$ and $\delta^{18}\text{O}_{\text{NO}_3^-}$ in the CVFZ are strongly influenced by biogeochemical and water mass mixing processes. In the 30-200 dbar depth range, the observed low $\delta^{15}\text{N}$ of nitrate was associated with the regeneration of the low $\delta^{15}\text{N}$ of PON acquired through N_2 fixation. Relatively high O_2 concentration in the CVFZ supports the lack of denitrification in this region. Thus, the high $\delta^{15}\text{N}_{\text{NO}_3^-}$ values in intermediate waters, suggest that this isotopic imprint of nitrate was imported: these high values were related to the nitrate partial assimilation that occurs in the source region of AA, which is transported towards the mid-Atlantic Ocean. This produces the introduction of nitrate with high $\delta^{15}\text{N}_{\text{NO}_3^-}$ and $\delta^{18}\text{O}_{\text{NO}_3^-}$, importing these isotopic signatures, which in addition could experience some modifications as it flows northward. The $\delta^{15}\text{N}_{\text{NO}_3^-}$ and $\delta^{18}\text{O}_{\text{NO}_3^-}$ distributions and archetype values for each WT obtained in this chapter, suggest that the locally regenerated nitrate in the CVFZ was mainly derived from sinking POM.

Chapter 5

General discussion

5.1 Water mass definitions in the Cape Verde Frontal Zone

The water masses composition of the North Atlantic Ocean has been thoroughly studied for decades (Zenk et al., 1991; Perez-Rodríguez et al., 2001; Martinez-Marrero et al., 2008; Pelegri and Peña-Izquierdo, 2015; Pastor et al., 2015). Different authors define distinct water masses or used diverse initial thermohaline and chemical properties to define those water masses (Perez-Rodríguez et al., 2001; Pastor et al., 2012; Lønborg and Álvarez-Salgado, 2014). The water mass definitions used in this PhD thesis and their thermohaline and chemical characteristics are briefly discussed below.

The ENACW has been defined by two water types, the warm (subtropical) ENACW_15 and the cold (subpolar) ENACW_12. We took their physical and chemical properties from Álvarez and Álvarez-Salgado (2009) and Lønborg and Álvarez-Salgado (2014) for ENACW_15 and from Perez-Rodríguez et al. (2001) and Álvarez and Álvarez-Salgado (2009) for ENACW_12. The physical and chemical properties of Madeira Mode Water were also taken from Álvarez and Álvarez-Salgado (2009) and Lønborg and Álvarez-Salgado (2014).

SACW is also defined by two water types, the warm SACW_18 and the cold SACW_12. In this case, their physical and chemical characteristics were not taken from the literature, that usually define this water mass in its formation area in the South Atlantic Subtropical gyre. In this PhD thesis we decided to define the average physical and chemical characteristics of these WTs in the Eastern Equatorial Atlantic, in a box from 5° N–5° S and from 20 to 30 °W from the World Ocean Atlas (2013). This region was chosen to account only for the transformations experienced for these WTs as they are transported from the equatorial region to the CVFZ by the Mauritanian current and, therefore, avoid all the biogeochemical transformations experienced by this water mass from the Subtropical South Atlantic to the Eastern Equatorial Atlantic.

The same reasoning was applied to the definition of the Antarctic Intermediate water (AAIW). This water mass originates in the Drake passage, and its initial characteristics undergoes substantial physical mixing and biogeochemical transformations as it flows northward, following the South Atlantic Current, the South Equatorial Current and the Equatorial Current System before reaching the CVFZ. For this reason, instead of using the pure AAIW we took again the physical and chemical properties of this water mass in the Eastern Equatorial Atlantic box that we defined to characterise SACW. The AAIW at this

source region is really strongly modified AAIW, so we did not name it AAIW but modified AA.

The characteristic of Subpolar Mode Water (SPMW) where taken from Perez et al. (2001) and Álvarez and Álvarez-Salgado (2009). In the case of the Mediterranean water mass (MW), many authors refer to its characteristics when it flows out of the Strait of Gibraltar, and name it as Mediterranean Overflow water (MOW). However, due to its high salinity, the MW is denser than the surrounding Atlantic water, subducting when it enters the Atlantic Ocean. Intense mixing with ENACW occurs during MOW subduction down to about 1200 dbar (Pelegrí and Peña Izquierdo, 2015). Therefore, the characteristics of the MW should be taken at 1200 dbar in the Atlantic ocean near the Gulf of Cadiz, when the dilution with ENACW in a proportion 2.5 : 1 stops and the MW becomes stable.

Finally, concerning the deep waters, while some authors, e.g. Pastor et al. (2012), grouped all deep WTs under the generic denomination of North Atlantic Deep Water (NADW), In this PhD thesis we identified 3 WTs: LSW, UNEADW and LNEADW with contrasting origin and degrees of mixing with Antarctic Bottom waters as shown by their contrasting silicate concentrations (19.5 ± 0.4 ; 34.8 ± 0.3 and $44.4 \pm 0.3 \mu\text{mol kg}^{-1}$, respectively) (Pérez-Rodríguez et al., 2001; Álvarez and Álvarez-Salgado, 2009)

5.2 The importance of correcting water mass mixing to obtain reliable -O₂:N:P:Si nutrient ratios

Despite the use of the single linear correlation among dissolved oxygen and inorganic nutrients to obtain -O₂:N:P:Si ratios is generalised, in this PhD Thesis we have shown that these ratios maybe not reliable in areas where contrasting water masses of different origins and biogeochemical histories meet, as the CVFZ. In these cases, it is important to separate the contribution of water mass mixing from the biogeochemical process that take place during that mixing. For epipelagic waters below the pycnocline, we decided to apply a multiple linear correlation in which salinity was used to correct the effect of mixing, while on meso- and bathypelagic layers we used the water mass proportions (x_{ij}) to discount the effect of mixing to estimate the -O₂:N:P:Si stoichiometry of organic matter mineralization.

To show this, Table 5.1 summarises the notable differences in the slopes of the single (salinity or X_{ij} not considered) as compared with the multiple (salinity or X_{ij} included) correlations between AOU, NO_3^- , HPO_4^{2-} and SiO_4H_4 .

The AOU: NO_3^- coefficient represent the $-\text{O}_2$:N ratios of organic matter mineralization. When the effect of mixing was correct with salinity during FLUXES I, the $-\text{O}_2$:N ratios was closer to canonical Redfield ratio in epipelagic waters, while at meso- and bathypelagic layers both slopes were similar to the Redfield ratio (Table 5.1). During FLUXES II, this correction contributed to increase $-\text{O}_2$:N ratio from 6.7 to 8.3, much closer to the canonical Redfield ratio in epipelagic waters, while in meso- and bathypelagic waters produce the opposite effect. This suggested strong preferential nitrogen remineralization at both layers in FLUXES II.

This correction was also noticeable when the contribution of mixing was separate from mineralization processes in the $-\text{O}_2$:P ratios. In FLUXES I, corrected $-\text{O}_2$:P ratios in epipelagic waters were in agreement with the Redfield ratio, while this correction at meso- and bathypelagic layers, showed closer but still higher values than the Redfield ratio, suggesting preferential remineralization of P over N. On the contrary, in FLUXES II the corrected $-\text{O}_2$:P ratios were higher than the Redfield ratio in epipelagic waters, while they were in agreement with the Redfield ratio at meso- and bathypelagic layers.

When correcting for the effect of mixing with salinity during FLUXES I, the N:P ratios increase from 17.9 ± 0.2 to 20.0 ± 0.7 in epipelagic waters, and from 17.3 ± 0.1 to 18 ± 0.7 in meso- and bathypelagic layers, being in both cases higher than the canonical Redfield ratio. This suggests preferential P remineralization compared to N in both layers during FLUXES I. For FLUXES II, the correction decreases the N:P molar ratio of epipelagic water being closer but higher than Redfield ratio. However, in meso- and bathypelagic waters, if this correction is not applied, the N:P ratio would be 14, pointing to a preferential N remineralization compared to P, while in reality, when the correction is applied, this N:P ratio was 16, being in consonance with the Redfield ratio (Redfield et al., 1963; Anderson and Sarmiento, 1994; Anderson, 1995).

The corrected N:Si ratios, at epipelagic layers in FLUXES I and in FLUXES II, became closer but still higher than canonical Redfield ratios, reflecting the faster regeneration of N over Si. Note that silicate was one of the variables used to define the WTs present in CVFZ,

to run the OMP. For this reason, the N:Si ratios were non-calculated in meso- and bathypelagic layers.

In summary, to avoid erroneous deviations from the canonical Redfield ratios, correction of water mass mixing using salinity or water mass proportions as explanatory variables in multiple linear correlations between dissolved oxygen and inorganic nutrients is strongly recommended.

Table 5.1. Coefficients of the lineal regression (subsurface epipelagic layers) and multiple correlation (with salinity for epipelagic and with the WT proportions (X_{ij}) for meso- and bathypelagic) of AOU and NO_3^- regression coefficient of each variable with NO_3^- or HPO_4^{2-} and with HPO_4^{2-} or SiO_2 , respectively, and for each cruise.

			Without correction	WM- corrected
FLUXES I	Epipelagic	AOU vs NO_3^-	7.1 ± 0.1	9.1 ± 0.2
		AOU vs HPO_4^{2-}	126.0 ± 3.2	153.3 ± 6.8
		NO_3^- vs HPO_4^{2-}	17.9 ± 0.2	20.0 ± 0.7
		NO_3^- vs SiO_4H_4	3.4 ± 0.1	2.6 ± 0.2
	Meso- Bathypelagic	AOU vs NO_3^-	9.8 ± 0.2	9.2 ± 0.3
		AOU vs HPO_4^{2-}	205 ± 1	196 ± 1
		NO_3^- vs HPO_4^{2-}	17.3 ± 0.1	18 ± 0.7
FLUXES II	Epipelagic	AOU vs NO_3^-	6.7 ± 0.1	8.3 ± 0.3
		AOU vs HPO_4^{2-}	135.9 ± 3.8	200.0 ± 9.6
		NO_3^- vs HPO_4^{2-}	20.9 ± 0.4	18 ± 1
		NO_3^- vs SiO_4H_4	3.4 ± 0.1	2.3 ± 0.2
	Mesopelagic	AOU vs NO_3^-	9.3 ± 0.1	7.6 ± 0.1
		AOU vs HPO_4^{2-}	172 ± 1	151 ± 1
		NO_3^- vs HPO_4^{2-}	14.3 ± 0.3	16.1 ± 0.8

5.3 Differences in $-\text{O}_2$:N:P:Si stoichiometry between FLUXES I and II

In epipelagic waters below the pycnocline, both FLUXES I and II presented significant deviation from the Redfield stoichiometry, being the N:P:Si ratios significantly higher than the canonical values of 16: 1: 1 in both cruises (Table 5.1). The N:P ratios indicate preferential remineralization of P, while the N:Si ratios showed the faster mineralization of N than Si during the mineralization of sinking POM in both cruises (Redfield et al., 1963; Anderson and Sarmiento, 1994; Anderson, 1995; Kudela and

Dugdale, 2000; Álvarez-Salgado et al., 2014), The deviation of the N:P ratio was higher in FLUXES I (20) than in FLUXES II (18). Noticeably, while the $-O_2:N$ ratio was Redfieldian during FLUXES I, it was significantly lower during FLUXES II, suggesting that in epipelagic waters below the pycnocline preferential mineralization of N compared to C occurs. This was also supported by the higher C:N molar ratios of PON in epi and mesopelagic layers in FLUXES II (see chapters 2 and 3). In summary, preferential mineralization of P over N, and of N over C and Si compared to the Redfield stoichiometry takes place, with some significant differences between the two cruises. Considering that the cruises were occupied in different times of the year (FLUXES I in mid summer and FLUXES II in late autumn) and have a very different spatial coverage (30 NM resolution in FLUXES I vs. 5 NM in FLUXES II), such differences are not surprising.

In meso- and bathypelagic waters both cruises showed very contrasting $-O_2:N:P$ ratios of organic matter mineralization (Table 5.1). During FLUXES I, the $-O_2:N$ ratios followed the Redfield ratio, while the $-O_2:P$ ratio was much higher than the canonical Redfield value. As a result, the N:P ratio was significantly higher than the Redfield ratio of 16. On the contrary, during FLUXES II the $-O_2:N$ ratios was significantly lower than the Redfield ratio while the $-O_2:P$ ratio was in agreement with the canonical Redfield value of 150-170 and the N:P ratio was Redfieldian (Redfield et al., 1963; Anderson, 1995) (Table 5.2). These marked deviation from the Redfield stoichiometry suggest a preferential remineralization of P in FLUXES I, and a strong preferential N remineralization in FLUXES II (Redfield et al., 1963; Anderson and Sarmiento, 1994; Anderson, 1995; Hupe and Karstensen, 2000; Kudela and Dugdale, 2000; Osterroht and Thomas, 2000). Differences between FLUXES I and II are likely related to the different geographic coverage of the cruises. To test if the observed differences could be associated to the different depth ranges covered in FLUXES I (0-4000 dbar) and FLUXES II (0-1500 dbar), correlation with X_{ij} and AOU were also run for the depth range 0-1500 db in FLUXES I and the $-O_2:N:P$ ratios continued to be different between the two cruises.

5.4 Organic nitrogen contribution to NO_3^- production in the CVFZ

In epipelagic waters below the pycnocline, DON mineralization contributed more to NO_3^- production than PON: 17% in FLUXES I and 33% in FLUXES II. Conversely, the contribution of PON to NO_3^- production was higher in FLUXES I (8%) than in FLUXES

II (2.7%) (Table 5.2). These differences were also observed in the contributions of POC to the oxygen demand, being lower in FLUXES II (4%,) than in FLUXES I (10%) (Table 5.2). In addition, in FLUXES I, was also noticeable the higher contribution of POM in epipelagic waters than in the meso- and bathypelagic layers.

These differences of DON and PON contribution were likely related with the above mentioned different spatial resolution of both cruises and also to seasonality, being the intensity of upwelling higher in November. Production of new DOM is often N-poor relative to C, with elevated C:N ratios measured during and immediately after diatom blooms. (Søndergaard, M. et al., 2000). Furthermore, as upwelling intensity increases, there is an increase in exported POM, which would explain the higher POM contribution to the mineralization in subsurface layers in FLUXES I cruise.

Table 5.2. Coefficients of the multiple correlation of PON, POC, DON and DOC regression coefficient of each variable with AOU, and NO_3^- . The correction with salinity in epipelagic layers in DON and DOC parameters in FLUXES II non-were significantly and the coefficients in these cases are represented as lineal regression

Epipelagic layer	FLUXES I				FLUXES II			
	AOU	%	NO_3^-	%	AOU	%	NO_3^-	%
PON	-		-0.081 ± 0.008	8.1	-		-0.027 ± 0.004	2.7
POC	-0.076 ± 0.007	10			-0.030 ± 0.006	4.4		
DON	-		-0.17 ± 0.02	17	-		-0.33 ± 0.1	32
DOC	-0.17 ± 0.01	24			-0.15 ± 0.01	21		
Mesopelagic layer								
PON	-0.003 ± 0.001		-0.0210 ± 0.0004	2.1	-		-	
POC	-0.032 ± 0.005	4.5			-		-	
DON	-0.013 ± 0.004		-0.156 ± 0.02	15.7	-		-	
DOC	-0.026 ± 0.01	3.6			-		-	

The limited contribution of DON and mostly PON to NO_3^- production in the CVFZ, which suggest that NO_3^- is locally produced during the mineralization of sinking POM, has also been supported by the results obtained from a marine snow catcher (MSC) deployed at some selected stations during FLUXES I. Our results show that 75 to 84% of the particles captured at 50 dbar depth by the MSC did not settled after 24 h of incubation, and can be therefore exported offshore by the currents in the area (Fig. 5.1).

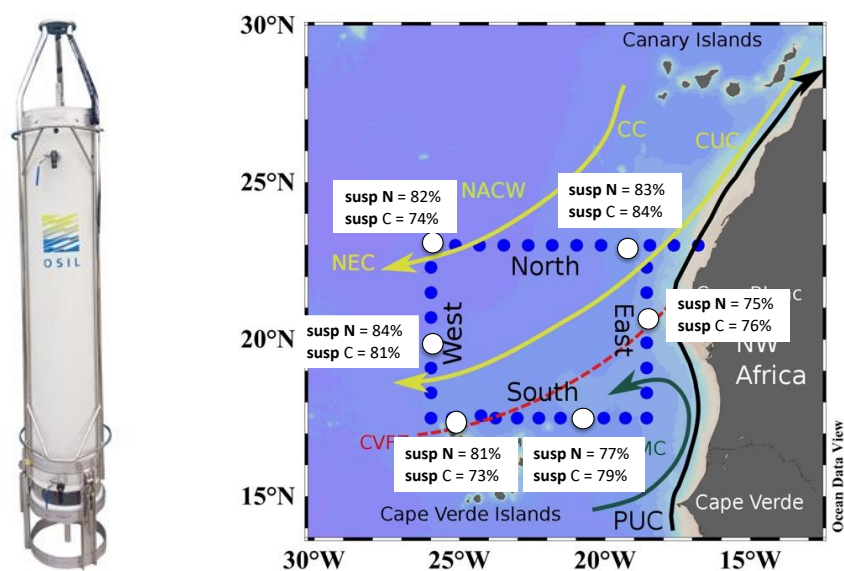


Figure 5.1. Marine snow catcher (MSC) (left) and map of the FLUXES I cruise with results from the MSC. The white dots represent the 6 stations (4, 12, 16, 20, 26 and 33) where the MSC was deployed. The white squares summarises the percentage of suspended particulate nitrogen (N) and carbon (C) at each stn. The MSC (100 litres of water) was deployed at 50 dbar. After recovery the MSC, this remained upright on deck for 24 hours. After 24 hours, the top 95L were slowly emptied by the tap. then, the upper part of the MSC was separated to the bottom part. This bottom section contains the remaining 5L of seawater with the fast-sinking particles, while the slow-sinking or buoyant particles remained in the upper part. We took 10L from the upper part and 5L from the lower part and filter them through GF/F filters for the analysis of POC and PON by high temperature catalytic oxidation (see Chapter 2).

5.5 Revisiting the isotopic determination of NH_4^+

NH_4^+ concentrations in the water column of the CVFZ turned out to be very low, usually less than $0.1 \mu\text{mol kg}^{-1}$, except in the surroundings of the DCM (with values ranging from 0.11 to $2.0 \mu\text{mol kg}^{-1}$, see Figures 2.6c and 3.8c of Chapters 2 and 3, respectively). Determination of $\delta^{15}\text{N}$ of NH_4^+ would have been interesting to resolve the processes of assimilation or oxidation that this N from experiences at the DCM of the CVFZ, due to the large differences in the rates of enzymatic reaction with molecules containing heavy and

light isotopes, i.e. kinetic isotope effect associate to both processes: $\varepsilon=5\%$ or lower for assimilation and $\varepsilon=14\text{--}19\%$ for oxidation (Casciotti et al., 2003; Fawcett et al., 2015).

To determine the $\delta^{15}\text{N}$ of NH_4^+ in FLUXES I and II, seawater samples were taken directly from the Niskin bottles in borosilicate vials of 12 mL, previously poisoned with saturated HgCl_2 and refrigerated at 4 °C until analysis in the base lab. Samples were treated with the method described by Liu et al. (2014), which consists of two steps for the conversion of NH_4^+ into N_2O , as summarized in Figure 5.2 and Table 5.3 and explained in detail in annex I.

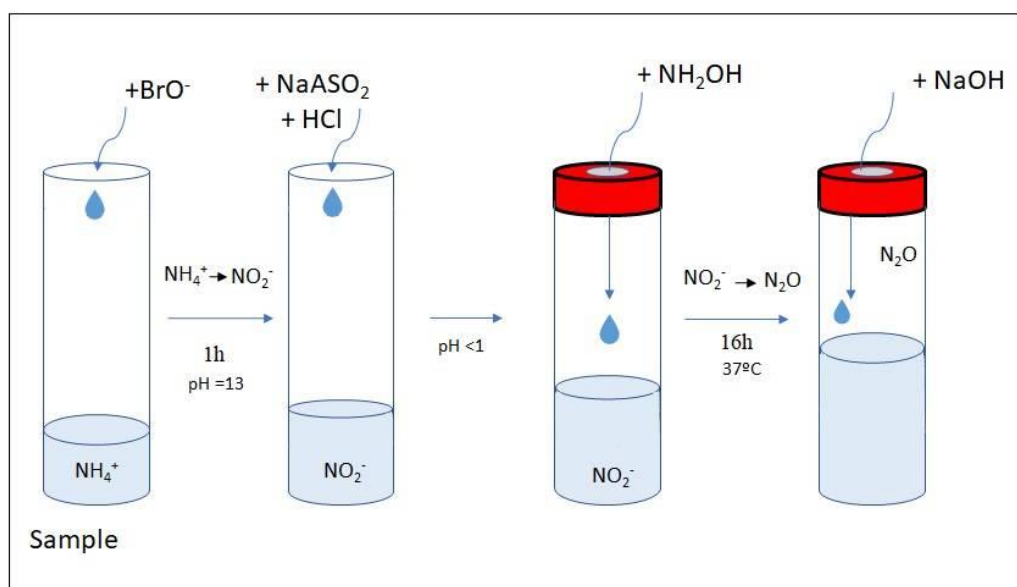


Figure 5.2. Liu et al. (2014) summarized method. The first step (NH_4^+ to NO_2^-) and the second step (NO_2^- to N_2O)

Table 5.3. Reactions involves in the different steps of Liu et al. (2014), method protocol.

Step	Reaction
1	$\text{BrO}^- + \text{NH}_4^+ + 2\text{OH}^- \rightarrow \text{NO}_2^- + 3\text{H}_2\text{O} + 3\text{Br}^-$
2	$\text{NH}_2\text{OH} + \text{HNO}_2 \rightarrow \text{N}_2\text{O} + 2\text{H}_2\text{O}$

Liu et al. (2014) indicated that this method was reliable, and can work effectively for low NH_4^+ concentration and small sample volumes (< 4 mL) in soil KCl extracts and probably seawater samples. However, Zhang et al. (2010) suggested that, even if the reproducibility of BrO^- method for sea water could be carried out in samples with NH_4^+ concentrations over the working range ($0.5 \mu\text{mol kg}^{-1}$); The range of $0.5\text{--}20 \mu\text{mol kg}^{-1}$ in deionizer water and $10 \mu\text{mol kg}^{-1}$ in seawater is recommended for more reliable and precise

values. Furthermore, we have found that, for the low concentration of NH_4^+ in the study area, together with a series of problems running the Liu et al. (2014) protocol, the results obtained by this method were unreliable in our case.

Liu et al. (2014) found that under optimal reaction conditions the oxidation efficiency of NH_4^+ into N_2O is $> 90\%$ in samples with NH_4^+ concentrations of $0.5\text{--}20\ \mu\text{mol kg}^{-1}$ in deionize water and $0.5\text{--}10\ \mu\text{mol kg}^{-1}$ in fresh and sea water. However, we have found that although this efficiency may indeed be 90% , the efficiency of the oxidation of NH_4^+ into NO_2^- is not linear respect to time for the BrO^- reaction (Fig. 5.3). To check the efficiency of the oxidation step, we exposed a solution of NH_4^+ $12\ \mu\text{mol kg}^{-1}$ in deionize water, to different reaction times (30, 60 and 90 minutes) with BrO^- . After 60 minutes, we found that about 25% of the initial NH_4^+ still remained in the sample and, at the same time, about 9% of the initial NH_4^+ was oxidized to NO_3^- rather than to N_2O (Fig 5.3). This reflects an acceptable conversion factor, but in NO_2^- and also NO_3^- nitrogen forms.

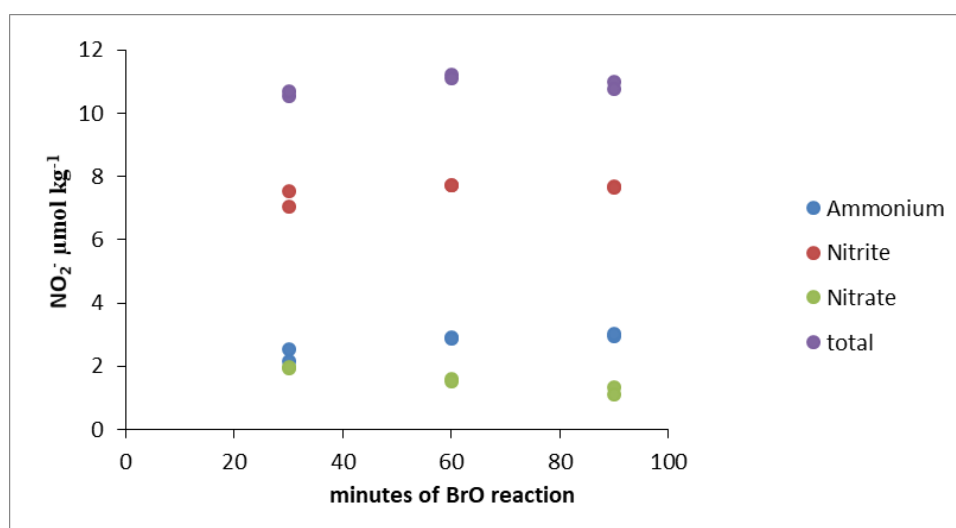


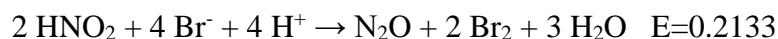
Figure 5.3. Concentration of nitrite ($\mu\text{mol kg}^{-1}$) measured in the first step of Liu et al. (2014) method according to the reaction time of BrO^- in minutes, for samples of $12\ \mu\text{mol kg}^{-1}$ of NH_4^+ in deionized water.

In addition, the excess of BrO^- added to carry out the oxidation of NH_4^+ to NO_2^- can react with the hydroxylamine reagent to form N_2O . Hydroxylamine is necessary to reduce the NO_2^- to N_2O in the second step. So, to avoid the reaction between BrO^- and hydroxylamine, a volume of NaAsO_2 have to be added (Liu et al., 2014) to neutralize the BrO^- excess, before adding the hydroxylamine reagent.

This addition, follow the reaction:



In this intermediate step, we found that in the highly acidic condition necessary for NO_2^- conversion to N_2O in the second step (pH ~ 0.42), the Br^- formed by NaAsO_2 addition can react with the NO_2^- from the NH_4^+ oxidation and form N_2O without hydroxylamine addition (Fig. 5.4):



The N_2O produced increases at higher temperature and longer reaction time (12 hours reaction at 50°C produce up to $5 \mu\text{mol kg}^{-1}$ of N_2O). Due to the low NH_4^+ concentration this reaction could produce an undesirable isotopic fractionation, which could do the obtained data unreliable.

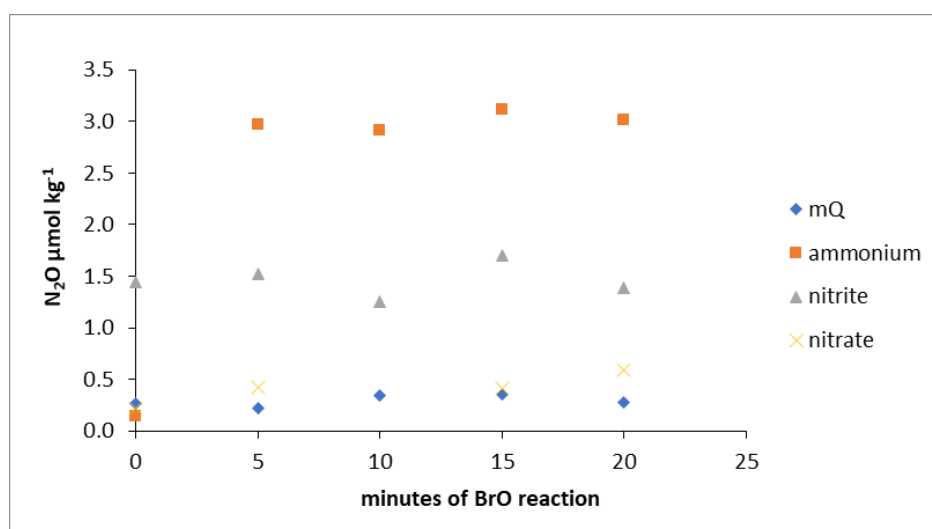


Figure 5.4. N_2O ($\mu\text{mol kg}^{-1}$) obtained in the second step of Liu et al. (2014) method, without the NH_2OH addition. Different solution at $10 \mu\text{mol kg}^{-1}$ of ammonium, nitrite and nitrate, were run for different times of reaction with BrO^- (minutes) (First step), then after the addition of NaAsO_2 and HCl , the samples were placed into a thermostatic bath at 37°C for 20 minutes, without NH_2OH addition to evaluate the N_2O produced. In addition, this figure showed that without BrO^- reaction time and being immediately neutralised with NaAsO_2 and HCl , the $\mu\text{mol kg}^{-1}$ of N_2O obtained in ammonium and nitrate reagent were close to zero, suggesting that these reagents didn't have any traces of NO_2^- .

Despite this method was applicable to the standard solution in deionized water, when the seawater samples with low NH_4^+ concentration were analysed, the obtained data were unreliable, due the associate isotopic fractionation effects. Finally, due the describe laboratory problems, the generally low NH_4^+ concentration at the CVFZ, the small number of stations with $\geq 0.5 \mu\text{mol kg}^{-1}$ (~ 10) and the unreliable data obtained, $\delta^{15}\text{N}$ of NH_4^+ were not considered in this PhD thesis.

Chapter 6

Conclusions

1. The distributions of DIN, DON and suspended PON in the epipelagic layer of the CVFZ are dictated by the position of the front and its interaction with meso- and submeso-scale structures as meanders, cyclonic and anticyclonic eddies, and the Cape Blanc Giant Filament.
2. The distributions of DIN, DON and PON in the intermediate and deep waters of the CVFZ are mainly dictated by water mass mixing and remineralization processes from the source regions of these water masses to the CVFZ.
3. The CVFZ dynamics reflects the importance of the vertical vs. horizontal flows of organic matter in the Canary Current EBUE. The offshore region of this EBUE act as a buffer zone where the stoichiometry of the organic matter exported to the gyres is modified, making it N poorer.
4. The N:P:Si molar ratio of inorganic nutrients in the surface mixed layer points to a severe N limitation to net primary production in the CVFZ and the epipelagic waters below the pycnocline show a preferential elemental organic matter mineralization in the order $P > N > C$ compared with the canonical Redfield stoichiometry.
5. Preferential elemental organic matter mineralization occurs also in mesopelagic waters of the CVFZ, with N been preferentially mineralised during FLUXES I and P during FLUXES II, as compared with the canonical Redfield stoichiometry
6. N limitation in the surface mixed layer and preferential N mineralisation in the waters below the pycnocline led to high C:N molar ratios compared with the canonical Redfield ratio, which increase with depth in the meso- and bathypelagic layers.
7. DON and suspended PON contributed only to about 18% of the local nitrate production in the meso- and bathypelagic layers CVFZ. The remaining 82% was due to sinking organic N exported from the Mauritanian upwelling.
8. The distributions of $\delta^{15}\text{N}_{\text{NO}_3^-}$ and $\delta^{18}\text{O}_{\text{NO}_3^-}$ and the archetype values obtained for each water mass in the CVFZ also support that the locally regenerated nitrate was mainly derived from sinking POM.
9. $\delta^{15}\text{N}_{\text{NO}_3^-}$ and $\delta^{18}\text{O}_{\text{NO}_3^-}$ in the CVFZ are strongly influenced by biogeochemical and mixing processes. Local processes of organic N mineralization affected significantly the isotopic composition. Furthermore, the high $\delta^{15}\text{N}_{\text{NO}_3^-}$ values in intermediate waters are related with the partial nitrate assimilation that occurs in Antarctic Intermediate Water, and the subsequent transport of this water mass towards mid-Atlantic waters.

Supplementary material

Chapter 2: Large-scale variability of nitrogen species in the Cape Verde Frontal Zone (NW Africa).

- ❖ Hydrographic setting of the Cape Vert Frontal Zone
 - Figure S1
 - Figure S2

- ❖ Biogeochemical variability in epi-, meso- and bathypelagic waters of the CVFZ
 - Figure S3
 - Figure S4

Chapter 3: Meso- and submeso-scale variability of nitrogen species in the Cape Verde Frontal Zone (NW Africa).

- ❖ Nitrogen biogeochemistry in the CVF in November 2017
 - Figure S5
 - Figure S6

Chapter 4: Nitrate in Cape Verde Frontal Zone: an isotopic approach

- ❖ $\delta^{15}\text{N}$ and d^{18}O in the interior ocean (>200 dbar)
 - Table S1
 - Figure S7

Chapter 2: Influence of large-scale dynamics in the nitrogen of Cape Verde Frontal Zone (NW Africa).

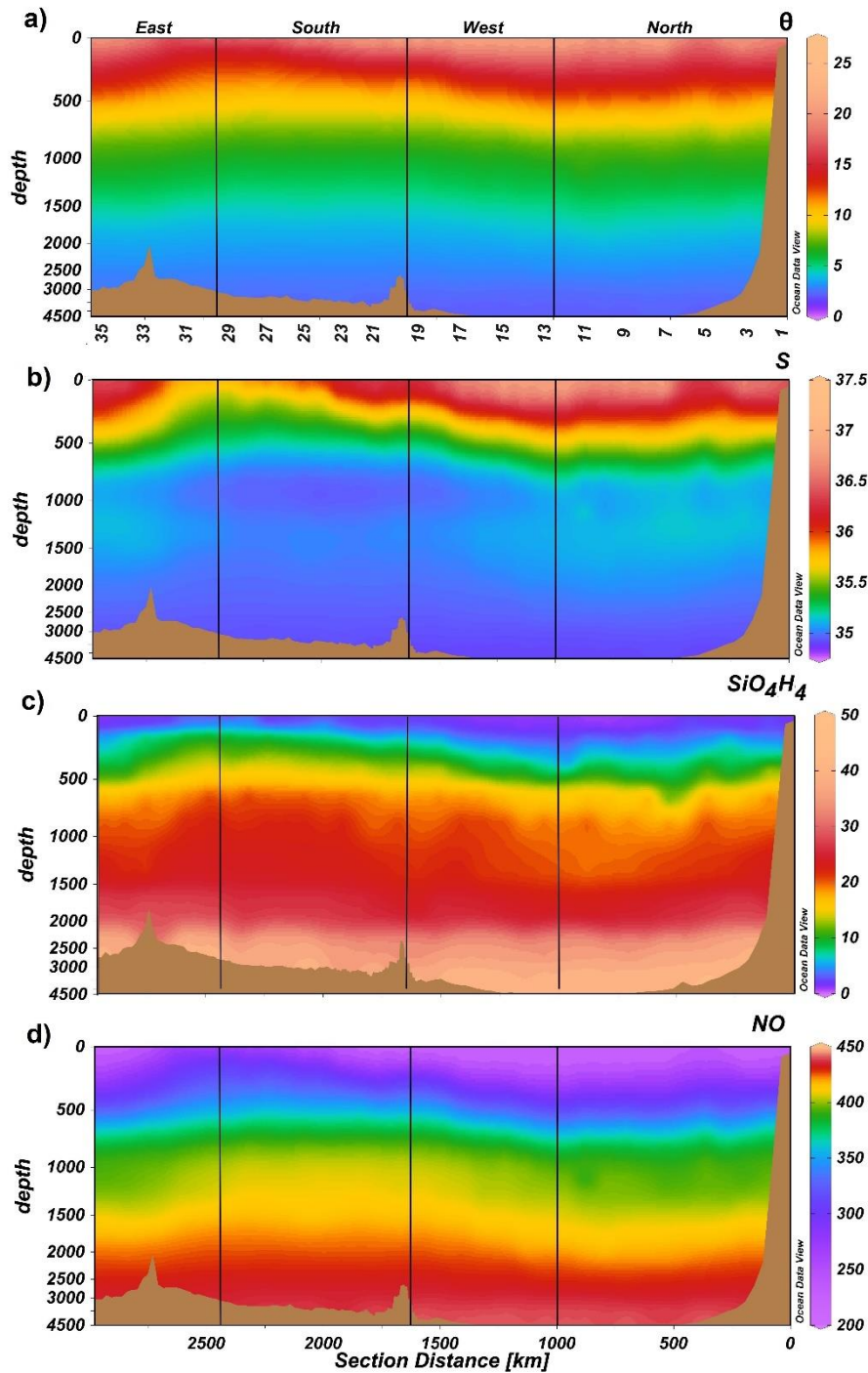


Figure S1. Full depth distributions of potential temperature (θ) in $^{\circ}\text{C}$ (a), salinity (S) (b), silicate (SiO_4) in $\mu\text{mol kg}^{-1}$ (c), and NO in $\mu\text{mol kg}^{-1}$ (d) derived from CTD measurements at 1 dbar vertical resolution during FLUXES I. θ and S were measured directly with the CTD, while SiO_4H_4 and NO values were reconstructed by fitting the measured water sample concentrations to a non-linear combination of variables directly measured with the CTD (θ , S , O_2). Note that the depth scale is not linear. Vertical back lines represent the corners of the FLUXES hydrographic box. Produced with Ocean Data View (Schlitzer, 2017).

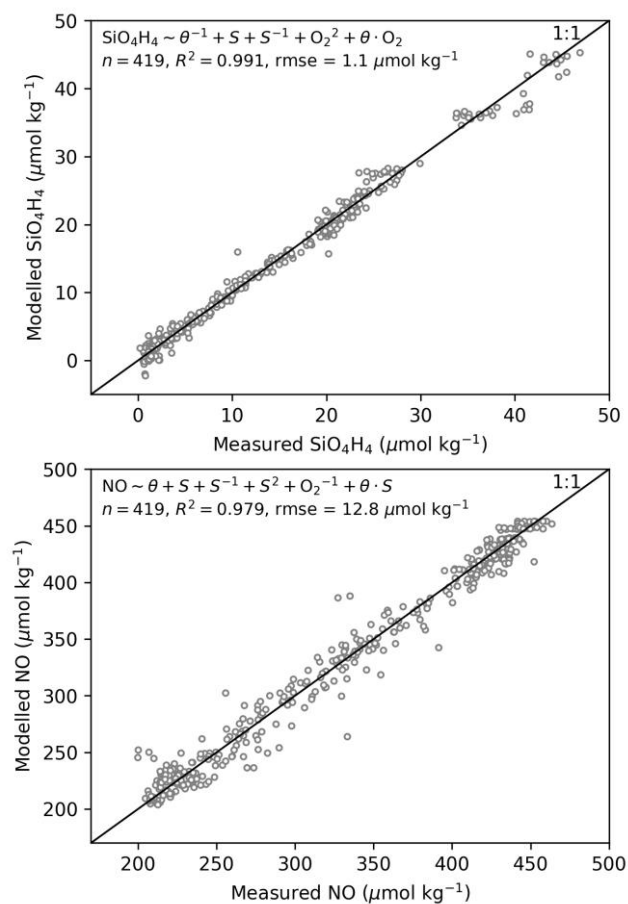


Figure S2. Fits of the measured NO and SiO₄H₄ concentrations to a non-linear combination of CTD measured variables (θ , S , O_2). Different combinations were tried and only the highly significant terms (according to their p -value < 0.001) were retained. The adjusted- R^2 and the root-mean-square error are reported as indicators of the goodness of the fit

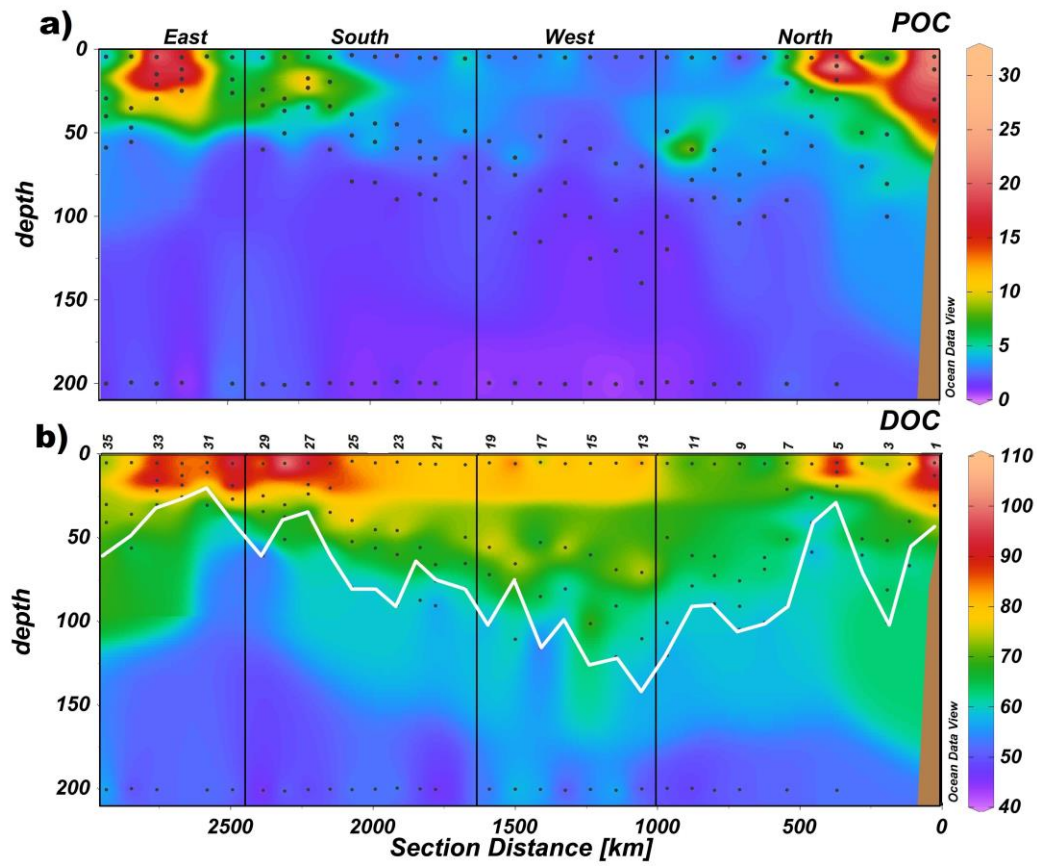


Figure S3. Distributions of POC in $\mu\text{mol L}^{-1}$ (a) and DOC in $\mu\text{mol L}^{-1}$ (b) in the epipelagic layer during the FLUXES I cruise, dots represent samples, vertical black lines represent the corners of the FLUXES I hydrographic box. White line in b represent the base of DCM. The x-axis shows the station number (a) or section distance in km (b). Produced with Ocean Data View (Schlitzer, 2017).

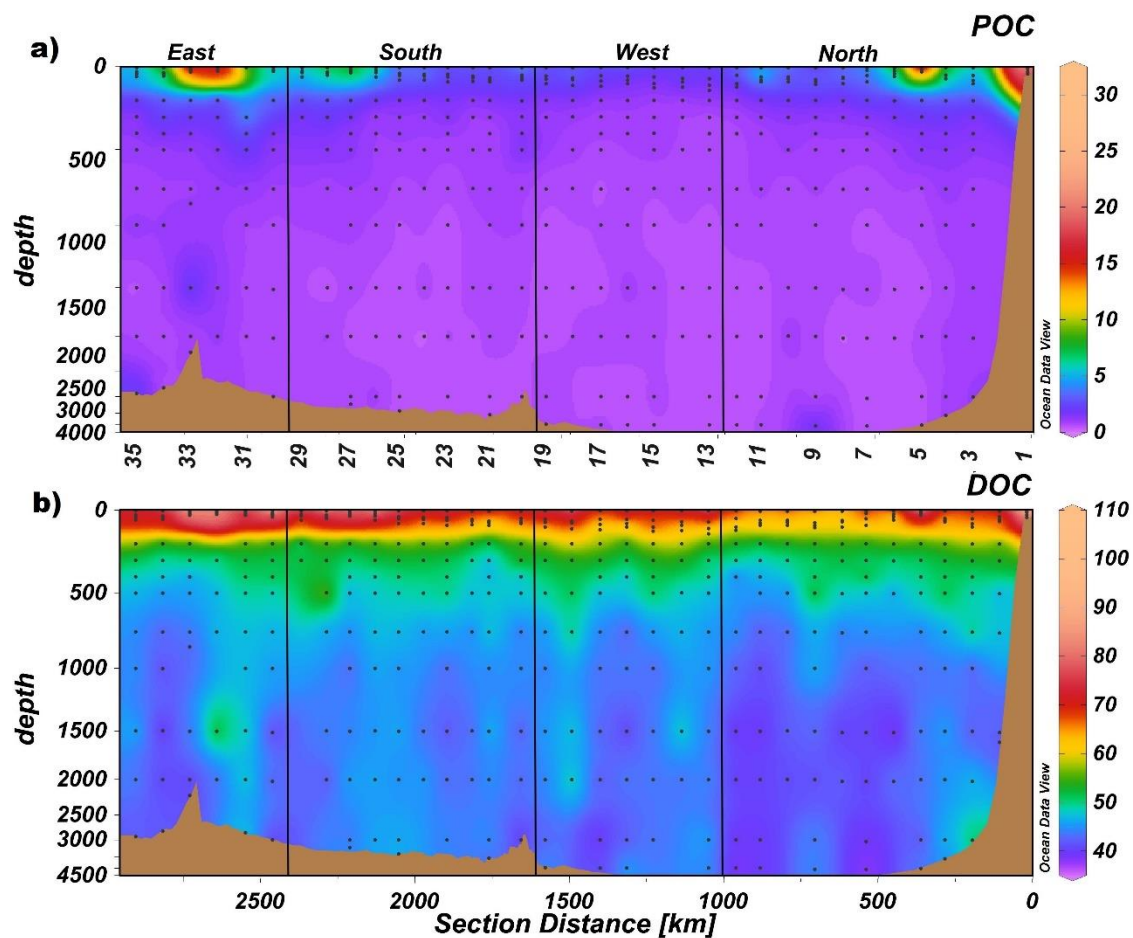


Figure S4. Full depth distributions of POC in $\mu\text{mol L}^{-1}$ (a) and DOC in $\mu\text{mol L}^{-1}$ (b) during the FLUXES I cruise. Dots represent samples and vertical black lines represent the corners of the FLUXES I hydrographic box. Note that depth scale is not linear. The x-axis shows the station number (a) or section distance in km (b). Note that depth scale is non-linear. Produced with Ocean Data View (Schlitzer, 2017).

Chapter 3: Meso- and submeso-scale variability of nitrogen species in the Cape Verde Frontal Zone

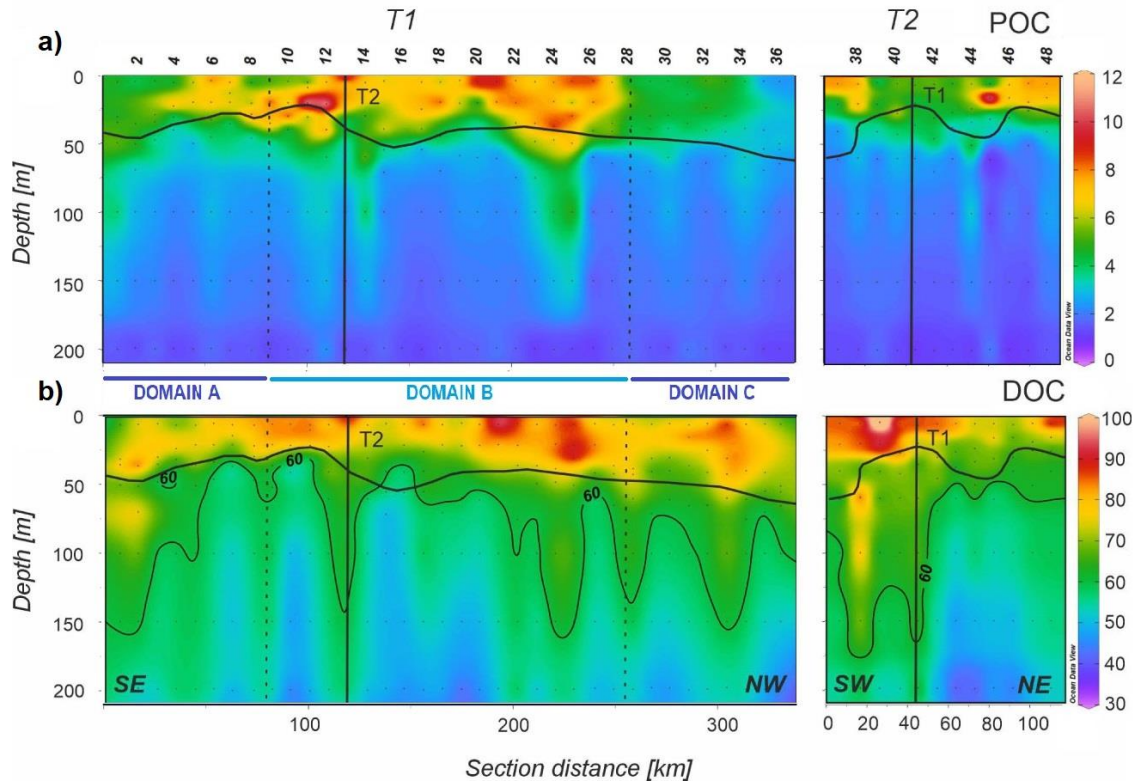


Figure S5. Distributions POC in $\mu\text{mol L}^{-1}$ (a) and DOC in $\mu\text{mol L}^{-1}$ (b) in the epipelagic layer during the FLUXES II cruise along T1 (left) and T2 (right). T1 is divided into three domains (A-C) separated by vertical dotted lines at stn 9 and 28. Vertical black lines show the position of the orthogonal transects T2 and T1, respectively. Horizontal black line shows the position of the pycnocline. Section distance is counting from southeast (SE) to northwest (NW) in T1 and from southwest (SW) to northeast (NE) in T2. Produced with Ocean Data View (Schlitzer, 2017).

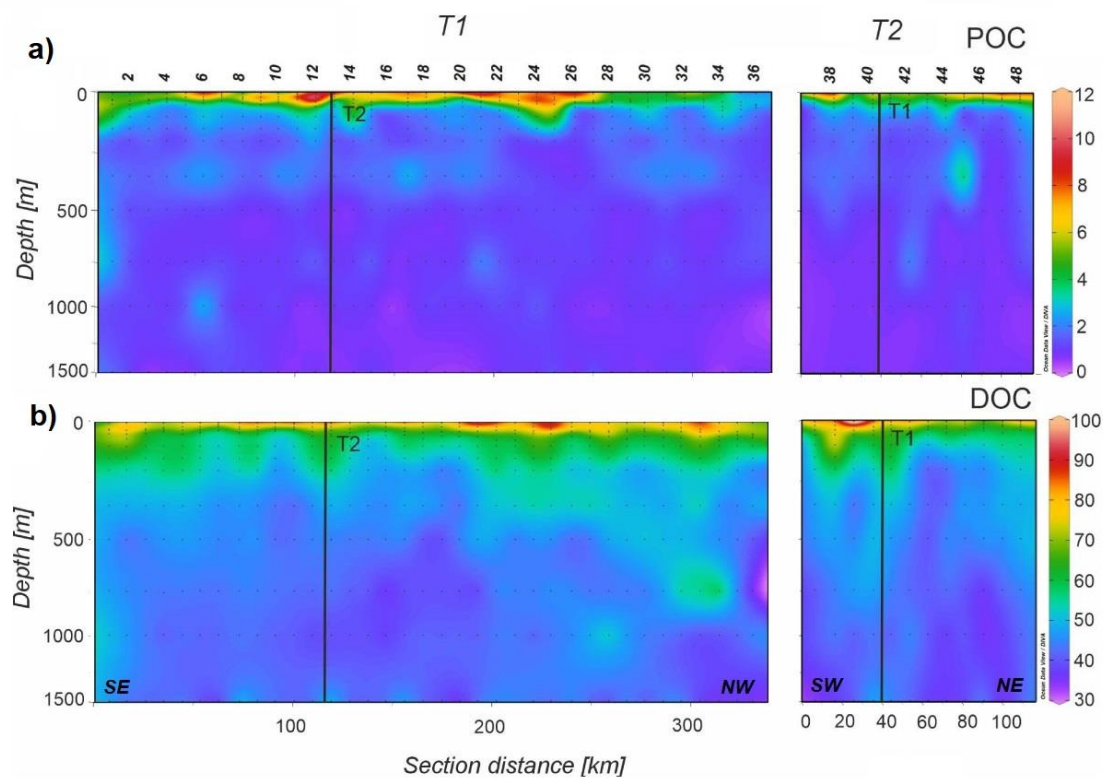


Figure S6. Distributions POC in $\mu\text{mol L}^{-1}$ (a) and DOC in $\mu\text{mol L}^{-1}$ (b) in the mesopelagic layer during the FLUXES II cruise along T1 (left) and T2 (right). Vertical black lines show the position of the orthogonal transects T2 and T1, respectively. Section distance is counting from southeast (SE) to northwest (NW) in T1 and from southwest (SW) to northeast (NE) in T2. Produced with Ocean Data View (Schlitzer, 2017).

Chapter 4: Nitrate in Cape Verde Frontal Zone: an isotopic approach

Table S1. Average \pm SE of nitrate $\delta^{15}\text{N}$ and $\delta^{18}\text{O}$ (‰) in Northern, Western, Southern and Eastern transects of FLUXES I.

	Northern		Western		Southern		Eastern	
WT	$\delta^{15}\text{N}$	$\delta^{18}\text{O}$	$\delta^{15}\text{N}$	$\delta^{18}\text{O}$	$\delta^{15}\text{N}$	$\delta^{18}\text{O}$	$\delta^{15}\text{N}$	$\delta^{18}\text{O}$
SACW_18	3.9 ± 1.3	2.5 ± 1.0	3.9 ± 0.7	4.8 ± 1.4	5.9 ± 0.5	6.8 ± 0.5	4.8 ± 0.4	3.2 ± 1.0
MMW	3.5 ± 2.3	1.7 ± 1.4	3.7 ± 0.6	3.9 ± 1.1	4.2 ± 0.5	6.2 ± 0.5	n.s	n.s
ENACW_15	4.1 ± 0.4	1.9 ± 0.3	4.7 ± 0.6	2.9 ± 0.5	4.8 ± 0.3	6.1 ± 0.6	4.7 ± 0.4	2.6 ± 0.7
SACW_12	5.3 ± 1.3	2.2 ± 0.6	6.1 ± 1.0	4.2 ± 0.7	5.5 ± 0.3	4.5 ± 0.4	5.3 ± 0.3	3.1 ± 0.4
ENACW_12	5.4 ± 0.4	2.1 ± 0.6	6.3 ± 0.6	4.1 ± 0.5	6.3 ± 0.2	4.6 ± 0.3	5.4 ± 0.2	2.9 ± 0.4
SPMW	5.5 ± 0.5	1.9 ± 0.2	6.6 ± 0.9	3.5 ± 0.5	5.9 ± 0.2	4.1 ± 0.5	5.7 ± 0.7	1.9 ± 0.4
AA	5.6 ± 0.5	2.0 ± 0.3	6.4 ± 1.5	3.3 ± 0.6	6.0 ± 0.2	3.6 ± 0.4	5.8 ± 1.0	2.1 ± 0.3
MW	5.4 ± 0.5	2.0 ± 0.7	5.2 ± 2.8	2.2 ± 0.8	4.9 ± 0.6	2.5 ± 0.7	5.6 ± 2.2	2.0 ± 0.4
LSW	5.3 ± 0.3	1.8 ± 0.3	5.0 ± 0.8	2.2 ± 0.4	5.5 ± 0.2	2.7 ± 0.3	5.9 ± 0.7	2.1 ± 0.2
UNEADW	5.3 ± 0.2	2.0 ± 0.5	5.1 ± 1.2	2.2 ± 0.4	5.3 ± 0.2	2.7 ± 0.4	5.8 ± 0.2	2.4 ± 0.4
LNEADW	5.8 ± 0.2	2.2 ± 0.4	5.2 ± 1.5	2.7 ± 0.6	5.5 ± 0.5	2.9 ± 0.6	n.s	n.s

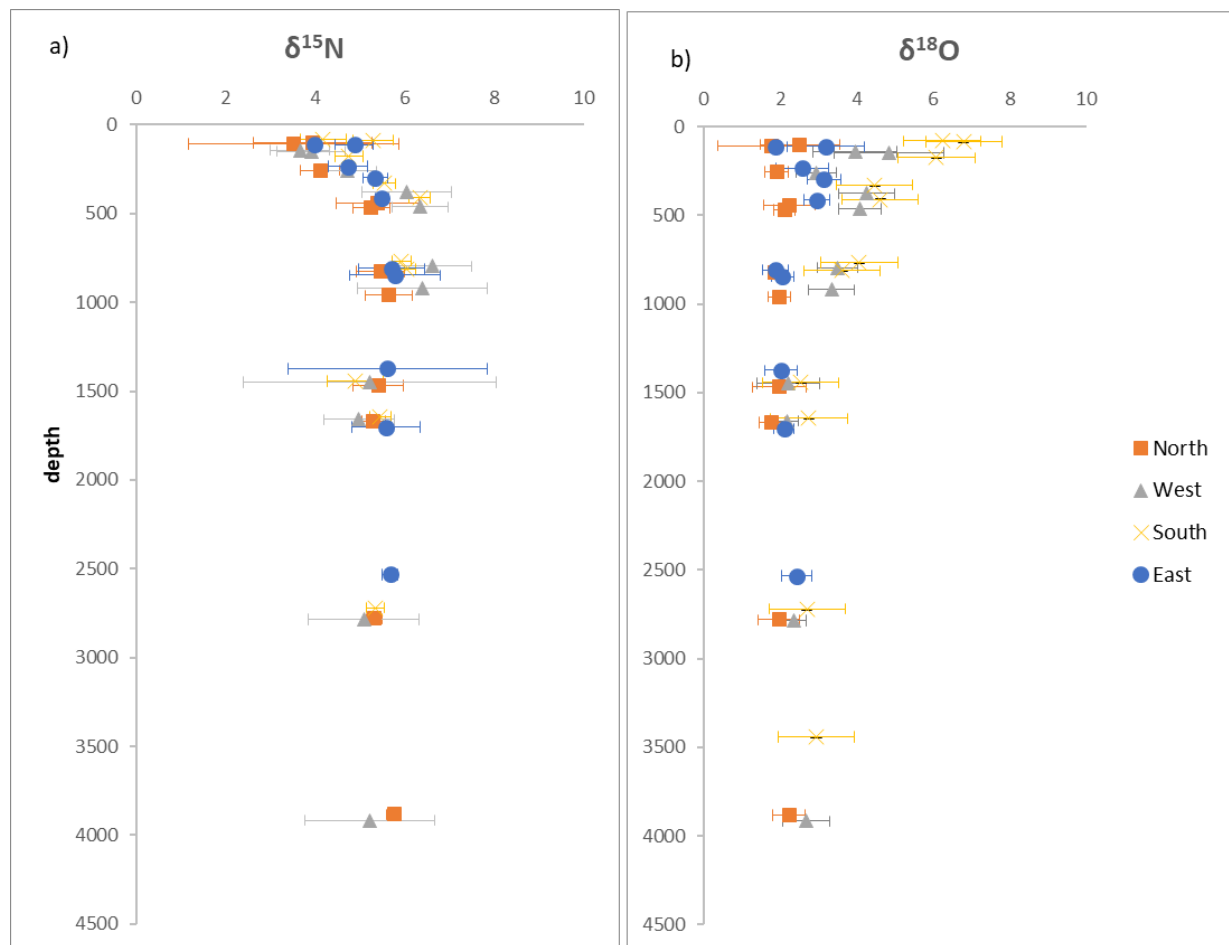


Figure S7. Distributions of the $\delta^{15}\text{N}_{\text{NO}_3^-}$ (a) and $\delta^{18}\text{O}_{\text{NO}_3^-}$ (‰) (b) of the water masses present in the Northern, Western, Southern and Eastern transects in CVFZ during FLUXES I cruise with SE.

Annexe

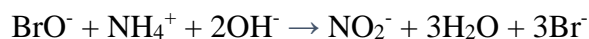
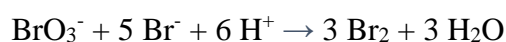
Analytical determination of $\delta^{15}\text{N}$ of NH_4^+

The determination of the $\delta^{15}\text{N}$ of NH_4^+ was carried out following the method of Liu et al. (2014). It consists of two steps, which involve two primary reactions:

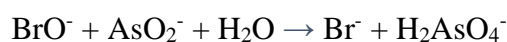
Oxidation of NH_4^+ to NO_2^-

Reduction of NO_2^- to N_2O

For the first step, they used the bromide oxidation method described by Zhang et al. (2007). A stock solution of bromate/bromide was made by dissolving in 250 mL of deionized water (DIW), 0.6 g of sodium bromate (NaBrO_3) and 5 g of sodium bromide (NaBr). This solution is stable for 6 months. The working solution has to be prepared daily due the instability of BrO^- , through the mixing of 1 mL of stock solution with 50 mL of DIW, followed by 3 mL of HCl 6M. This mixture needs to react in the dark for 5 minutes to produced Br_2 , and then 50 mL of NaOH 10M are added rapidly to produced BrO^- . Therefore, the reactions involved in the first step were:



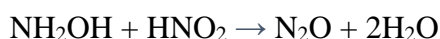
Liu et al. (2014) used 2.5 to 5 mL of laboratory $(\text{NH}_4)_2\text{SO}_4$ solution with varied concentrations of 5 to 80 μM and then add 0.25 or 0.5 mL of BrO^- working solution (volume ratio of BrO^- and Laboratory $(\text{NH}_4)_2\text{SO}_4$ was 1:10). After 30 minutes 0.5 mL of sodium arsenite (NaAsO_2) was added. We used 12 mL headspace borosilicate vials as reaction vessels, pipetting 4 mL of water samples, adjusting the volume of BrO^- working and sodium arsenite to this volume of samples. In addition, the time of BrO^- reaction prior to add sodium arsenite, were 60 minutes of time reaction with vigorously horizontal shaking at room temperature as proposed by Felix et al. (2013). The arsenite reagent was made dissolving 5.1 g of sodium arsenite (NaAsO_2) in 100 mL of deionized water and was used to remove the excess of BrO^- after the NH_4^+ oxidation, following this reaction:



To optimize the NH_4^+ oxidation yield and minimize the isotopic fractionation, the optimal NH_4^+ concentration range used of 0.5 to 20 μM in deionized water and 0.5 to 10 μM in fresh water, because beyond these range undesirable isotope fractionations could

appear. Under optimal reaction time and BrO^- amount Zhang et al. (2007) had an oxidation efficiency above 90%. In this regard, an almost complete oxidation from NH_4^+ to NO_2^- is necessary to reduce undesired isotope fractionation.

The second step consisted of the reduction of NO_2^- to N_2O with hydroxylamine hydrochloride ($\text{NH}_2\text{OH}\cdot\text{HCl}$). The $\text{NH}_2\text{OH}\cdot\text{HCl}$ reagent stock solution was made dissolving 0.2778 g of $\text{NH}_2\text{OH}\cdot\text{HCl}$ in 100 mL of deionized water, this solution is stable for 1 week. The working solution was made daily adding 3 mL of the stock solution to 500 mL of deionized water. The reaction involved in this step was



Liu et al. (2014) conducted several experiments to optimize the experimental parameters for maximizing the NO_2^- reduction yield, finding that the reaction rate of NO_2^- reduction was highly dependent on pH, increasing rapidly the reaction rate at $\text{pH} < 1$. So, to correct the different pH needed for the second step ($\text{pH} < 1$) from the alkaline solution produced during the NH_4^+ oxidation step (pH around 13), a volume of 0.5 mL of HCl 6M was added to each sample. Afterwards, the vials were crimp sealed and working solution of NH_2OH was added to each sample with a syringe, the reduction efficiency increased at molar ratio of NO_2^- to NH_2OH at 1:2, The reaction took place on the shaker at elevated temperature (37°C), with a time of incubation of 16 h. The optimal NO_2^- concentration range of 15 to 50 μM , being the reduction efficiency of 90%. Then, 0.5 mL of 10 M NaOH was injected with a syringe to stop the reaction by making the solution basic (Liu et al., 2014).

To corroborate the consistency of the method, eliminate analytical variation by any deviation in the IRMS response, and calibrate the $\delta^{15}\text{N}$ NH_4^+ of the samples for the calculation of the true $\delta^{15}\text{N}$ for NH_4^+ , three international standards with known $\delta^{15}\text{N}$ NH_4^+ (USGS 25, 30‰, USGS 26, $\delta^{15}\text{N}$ 53‰, IAEA 20, $\delta^{15}\text{N}$ 20‰) and another laboratory ($(\text{NH}_4)_2\text{SO}_4$ (-0.52‰) were used, and were treated with the same protocol than the samples. For this, 4 mL of 15 μM international standard solution prepared in deionized water, were added into the 12 mL reaction vials. In the same way a laboratory NaNO_2 standards named IACT 9 and IACT 10 ($\delta^{15}\text{N}$ -8.08‰ and -37.8‰ respectively and determined by IRMS) were running to check the efficiency of the reduction of NO_2^- to N_2O .

As described by Stevens and Laughlin (1994), the two atoms present in the final N_2O product measured, provided from NH_4^+ of sampled and for reagent, with the

combination of one N atom from the NH_4^+ and the other from the NH_2OH reagent. This fact could be reflected in the slope of the relationship between $\delta^{15}\text{N}$ of NH_4^+ international standard and the $\delta^{15}\text{N}$ of the measured N_2O , which will be 0.5 (Zhang et al., 2007; Liu et al., 2014). In addition, the intercept reflects the combination of isotopic fractionation related with the NH_4^+ oxidation and initial $\delta^{15}\text{N}$ of the reagent (NH_2OH).

The calibration equation is:

$$\delta^{15}\text{N}_{\text{NH}_4^+ \text{ sample}} = \frac{\delta^{15}\text{N}_{\text{N}_2\text{O sample}} - \text{intercept}}{\text{slope}}$$

The relationship between the assigned $\delta^{15}\text{N}$ NH_4^+ and measured $\delta^{15}\text{N}$ N_2O was significant and linear (Fig. AI.1). The N_2O peak measured of the laboratory IACT 9 and IACT 10 standards (NaNO_2), showed nearly the same height as the N_2O produced from NH_4^+ . In addition, the $\delta^{15}\text{N}$ of these reagents were in the regression line generated by international NH_4^+ standards, suggesting that the oxidation of NH_4^+ to NO_2^- was nearly complete and there were not any isotopic fractionation during NH_4^+ oxidation (Fig. AI.1).

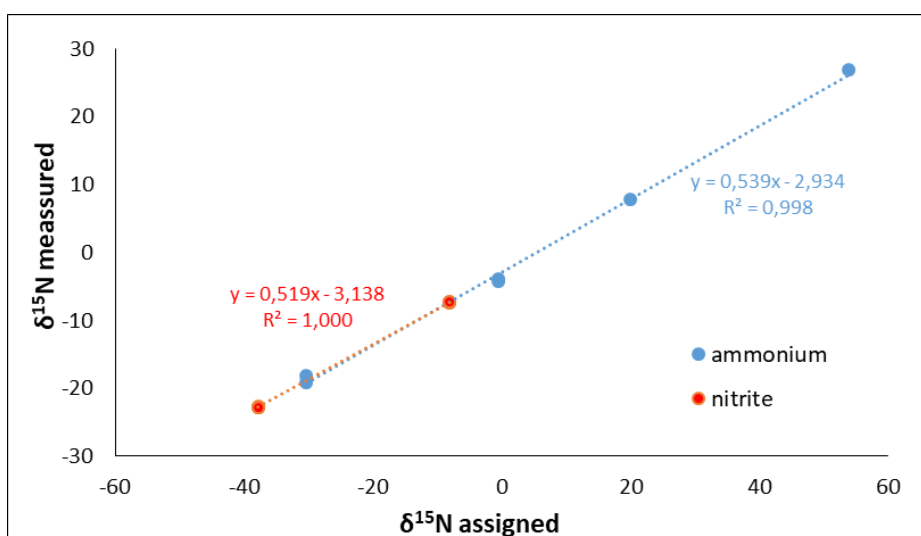


Figure AI.1. Correlations between the $\delta^{15}\text{N}$ - N_2O and the $\delta^{15}\text{N}$ assigned for the four Ammonium and two nitrite standards used, in deionized water.

References

References

- Abrahams, A., Schlegel, R.W., Smit, A.J., 2021. Variation and Change of Upwelling Dynamics Detected in the World's Eastern Boundary Upwelling Systems. *Front Mar Sci* 8, 626411. <https://doi.org/10.3389/FMARS.2021.626411/BIBTEX>
- Alonso-González, I.J., Arístegui, J., Vilas, J.C., Hernández-Guerra, A., 2009. Lateral POC transport and consumption in surface and deep waters of the Canary Current region: A box model study. *Global Biogeochem Cycles* 23, GB2007. <https://doi.org/10.1029/2008GB003185>
- Alpers, W., Brandt, P., Lazar, A., Dagorne, D., Sow, B., Faye, S., Hansen, M.W., Rubino, A., Poulain, P.M., Brehmer, P., 2013. A small-scale oceanic eddy off the coast of West Africa studied by multi-sensor satellite and surface drifter data. *Remote Sens Environ* 129, 132–143. <https://doi.org/10.1016/j.rse.2012.10.032>
- Altabet, M.A., 1988. Variations in nitrogen isotopic composition between sinking and suspended particles: implications for nitrogen cycling and particle transformation in the open ocean. *Deep Sea Research Part A. Oceanographic Research Papers* 35, 535–554. [https://doi.org/10.1016/0198-0149\(88\)90130-6](https://doi.org/10.1016/0198-0149(88)90130-6)
- Altabet, M.A., 2006. Isotopic tracers of the marine nitrogen cycle: Present and past. *Handbook of Environmental Chemistry, Volume 2: Reactions and Processes 2 N*, 251–293. https://doi.org/10.1007/698_2_008/COVER
- Altabet, M.A., Francois, R., 1994. Sedimentary nitrogen isotopic ratio as a recorder for surface ocean nitrate utilization. *Global Biogeochem Cycles* 8, 103–116. <https://doi.org/10.1029/93GB03396>
- Álvarez, M., Álvarez-Salgado, X., 2009. Chemical tracer transport in the eastern boundary current system of the North Atlantic. *Cienc Mar* 35, 123–139. <https://doi.org/10.7773/cm.v35i2.1438>
- Álvarez, M., Brea, S., Mercier, H., Álvarez-Salgado, X. A. (2014). Mineralization of biogenic materials in the water masses of the South Atlantic Ocean. I: Assessment and results of an optimum multiparameter analysis. *Progress in Oceanography*, 123, 1-23.
- Álvarez-Salgado, X., Arístegui, J., 2015. Organic matter dynamics in the Canary Current. L. Valdés, I. Déniz-González (Eds.), *Oceanographic and biological features in the Canary Current Large Marine Ecosystem*, IOC-UNESCO, Paris (2015), pp. 151-160 (IOC Technical Series No. 115).
- Álvarez-Salgado, X., Nieto-Cid, M., Álvarez, M., Pérez, F., Morin, P., Mercier, H., 2013. New insights on the mineralization of dissolved organic matter in central, intermediate, and deep water masses of the northeast North Atlantic. *Limnol Oceanogr* 58, 681–696. <https://doi.org/10.4319/lo.2013.58.2.0681>
- Álvarez-Salgado, X.A., Álvarez, M., Brea, S., Mèmery, L., Messias, M.J., 2014. Mineralization of biogenic materials in the water masses of the South Atlantic Ocean. II: Stoichiometric ratios and mineralization rates. *Prog Oceanogr* 123, 24–37. <https://doi.org/10.1016/J.POCEAN.2013.12.009>

References

- Álvarez-Salgado, X.A., Arístegui, J., Barton, E.D., Hansell, D.A., 2007. Contribution of upwelling filaments to offshore carbon export in the subtropical Northeast Atlantic Ocean. *Limnol Oceanogr* 52, 1287–1292. <https://doi.org/10.4319/lo.2007.52.3.1287>
- Álvarez-Salgado, X.A., Doval, M.D., Borges, A. V., Joint, I., Frankignoulle, M., Woodward, E.M.S., Figueiras, F.G., 2001. Off-shelf fluxes of labile materials by an upwelling filament in the NW Iberian Upwelling System. *Prog Oceanogr* 51, 321–337. [https://doi.org/10.1016/S0079-6611\(01\)00073-8](https://doi.org/10.1016/S0079-6611(01)00073-8)
- Álvarez-Salgado, X.A., Miller, A.E.J., 1998. Simultaneous determination of dissolved organic carbon and total dissolved nitrogen in seawater by high temperature catalytic oxidation: conditions for precise shipboard measurements. *Mar Chem* 62, 325–333. [https://doi.org/10.1016/S0304-4203\(98\)00037-1](https://doi.org/10.1016/S0304-4203(98)00037-1)
- Álvarez-Salgado, X.A., Nieto-Cid, M., Gago, J., Brea, S., Castro, C.G., Doval, M.D., Pérez, F.F., 2006. Stoichiometry of the degradation of dissolved and particulate biogenic organic matter in the NW Iberian upwelling. *J Geophys Res* 111, C07017. <https://doi.org/10.1029/2004JC002473>
- Anderson, L.A., 1995. On the hydrogen and oxygen content of marine phytoplankton. *Deep-Sea Research Part I* 42, 1675–1680. [https://doi.org/10.1016/0967-0637\(95\)00072-E](https://doi.org/10.1016/0967-0637(95)00072-E)
- Anderson, L. A., and Sarmiento, J. L. (1994). Redfield ratios of remineralization determined by nutrient data analysis. *Global biogeochemical cycles*, 8(1), 65-80.
- Antoine, D., Andre, J.M., Morel, A., 1996. Oceanic primary production: 2. Estimation at global scale from satellite (Coastal Zone Color Scanner) chlorophyll. *Global Biogeochem Cycles* 10, 57–69. <https://doi.org/10.1029/95GB02832>
- Arístegui, J., Barton, E., Montero, M., García-Muñoz, M., Escáñez, J., 2003. Organic carbon distribution and water column respiration in the NW Africa-Canaries Coastal Transition Zone. *Aquatic Microbial Ecology* 33, 289–301.
- Arístegui, J., Barton, E., Tett, P., Montero, M., García-Muñoz, M., Basterretxea, G., Cussatlegras, A., Ojeda, A., De Armas, D., 2004. Variability in plankton community structure, metabolism, and vertical carbon fluxes along an upwelling filament (Cape Juby, NW Africa). *Prog Oceanogr* 62, 95–113.
- Arístegui, J., Barton, E.D., Álvarez-Salgado, X.A., Santos, A., Figueiras, F.G., Kifani, S., Hernández-León, S., Mason, E., Machú, E., Demarcq, H., 2009. Sub-regional ecosystem variability in the Canary Current upwelling. *Prog Oceanogr* 83, 33–48. <https://doi.org/10.1016/j.pcean.2009.07.031>
- Arístegui, J., Duarte, C., Agustí, S., Doval, M., Álvarez-Salgado, X., Hansell, D.A., 2002. Dissolved Organic Carbon Support of Respiration in the Dark Ocean. *Science* 298:1,967.
- Arístegui, J., Montero, M., Hernández-Hernández, N., Alonso-González, I., Baltar, F., Calleja, M.L., Duarte, C.M., 2020. Variability in Water-Column Respiration and Its Dependence on Organic Carbon Sources in the Canary Current Upwelling Region. *Front Earth Sci (Lausanne)* 8, 349. <https://doi.org/10.3389/feart.2020.00349>

- Auger, P. A., Gorgues, T., Machu, E., Aumont, O., Brehmer, P. 2016. What drives the spatial variability of primary productivity and matter fluxes in the north-west African upwelling system? A modelling approach. *Biogeosciences*, 13(23), 6419–6440.
- Bachmann, J., Heimbach, T., Hassenrück, C., Kopprio, G.A., Iversen, M.H., Grossart, H.P., Gärdes, A., 2018. Environmental drivers of free-living vs. particle-attached bacterial community composition in the Mauritania upwelling system. *Front Microbiol* 9, 417435. <https://doi.org/10.3389/FMICB.2018.02836/BIBTEX>
- Bacon, M.P., Anderson, R.F., 1982. Distribution of thorium isotopes between dissolved and particulate forms in the deep sea. *J Geophys Res Oceans* 87, 2045–2056. <https://doi.org/10.1029/JC087IC03P02045>
- Bakun, A., 1990. Global climate change and intensification of coastal ocean upwelling. *Science* 247, 198–201. <https://doi.org/10.1126/SCIENCE.247.4939.198>
- Bakun, A., Black, B.A., Bograd, S.J., García-Reyes, M., Miller, A.J., Rykaczewski, R.R., Sydeman, W.J., 2015. Anticipated Effects of Climate Change on Coastal Upwelling Ecosystems. *Curr Clim Change Rep* 1, 85–93. <https://doi.org/10.1007/S40641-015-0008-4/FIGURES/2>
- Bakun, A., Field, D.B., Redondo-Rodriguez, A., Weeks, S.J., 2010. Greenhouse gas, upwelling-favorable winds, and the future of coastal ocean upwelling ecosystems. *Glob Chang Biol* 16, 1213–1228. <https://doi.org/10.1111/J.1365-2486.2009.02094.X>
- Bakun, A., Nelson, C. S. 1991. The seasonal cycle of wind-stress curl in subtropical eastern boundary current regions. *Journal of Physical Oceanography*, 21(12), 1815–1834.
- Baltar, F., Arístegui, J., Gasol, J.M., Sintes, E., Herndl, G.J., 2009. Evidence of prokaryotic metabolism on suspended particulate organic matter in the dark waters of the subtropical North Atlantic. *Limnol Oceanogr* 54, 182–193. <https://doi.org/10.4319/LO.2009.54.1.0182>
- Barceló-Llull, B., Sangrà, P., Pallàs-Sanz, E., Barton, E.D., Estrada-allis, S.N., Martínez-Marrero, A., Aguiar-Gonzalez, B., Grisolla, D., Gordo, C., Rodríguez-Santana, Á., Marrero-Díaz, Á., Arístegui, J., 2017. Anatomy of a subtropical intrathermocline eddy. *Deep Sea Res 1 Oceanogr Res Pap* 124, 126–139.
- Barth, J., Collins, C., Hickey B, 2002. West coast oceanography: Implications for ballast water exchange. Draft report.
- Barton, E., Arístegui, J., Tett, P., Cantón, M., García- Braun, J., Hernández-León, S., Nykjaer, L., Almeida, C., Almunia, J., Ballesteros, S., Basterretxea, G., Escánez, J., García-Weil, L., Hernandez-Guerra, A., López-Laatzén, F., Molina, R., Montero, M., Navarro-Pérez, E., Rodríguez, J., Van Lenning, K., Wild, K., 1998. The transition zone of the Canary Current upwelling region. *Prog Oceanogr* 41, 455–504.
- Benazzouz, A., Mordane, S., Orbi, A., Chagdali, M., Hilmi, K., Atillah, A., Lluís Pelegrí, J., Hervé, D., 2014. An improved coastal upwelling index from sea surface temperature using satellite-based approach – The case of the Canary Current upwelling system. *Cont Shelf Res* 81, 38–54. <https://doi.org/10.1016/J.CSR.2014.03.012>

References

- Benítez-Barrios, V. M., Pelegrí, J. L., Hernández-Guerra, A., Lwiza, K. M. M., Gomis, D., Vélez-Belchí, P., Hernández-León, S. 2011. Three-dimensional circulation in the NW Africa coastal transition zone. *Progress in Oceanography*, 91(4), 516-533.
- Berner, R.A., 2006. Geological nitrogen cycle and atmospheric N₂ over Phanerozoic time. *Geology* 34, 413–415. <https://doi.org/10.1130/G22470.1>
- Bertrand, J., Bonin, P., Caumette, P., Gattuso, J., 2015. *Environmental Microbiology: Fundamentals and Applications*. <https://doi.org/10.1007/978-94-017-9118-2>
- Bettencourt, J.H., Rossi, V., Renault, L., Haynes, P., Morel, Y., Garçon, V., 2020. Effects of upwelling duration and phytoplankton growth regime on dissolved-oxygen levels in an idealized Iberian Peninsula upwelling system. *Nonlinear Process Geophys* 27, 277–294. <https://doi.org/10.5194/NPG-27-277-2020>
- Bode, A., Botas, J. A., Fernandez, E. 1997. Nitrate storage by phytoplankton in a coastal upwelling environment. *Marine Biology*, 129, 399-406.
- Bonnet, S., Dekaezemacker, J., Turk-Kubo, K.A., Moutin, T., Hamersley, R.M., Grosso, O., Zehr, J.P., Capone, D.G., 2013. Aphotic N₂ Fixation in the Eastern Tropical South Pacific Ocean. *PLoS One* 8, e81265. <https://doi.org/10.1371/journal.pone.0081265>
- Bower, A.S., Serra, N., Ambar, I., 2002. Structure of the Mediterranean Undercurrent and Mediterranean Water spreading around the southwestern Iberian Peninsula. *J Geophys Res Oceans* 107, 25–1. <https://doi.org/10.1029/2001JC001007>
- Boyd, P., Claustre, H., Levy, M., Siegel, D., Weber, T., 2019. Multi-faceted particle pumps drive carbon sequestration in the ocean. *Nature* 568, 327–336.
- Brandes, J.A., Devol, A.H., 2002. A global marine-fixed nitrogen isotopic budget: Implications for Holocene nitrogen cycling. *Global Biogeochem Cycles* 16, 67–1. <https://doi.org/10.1029/2001GB001856>
- Brandes, J.A., Devol, A.H., Deutsch, C., 2007. New developments in the marine nitrogen cycle. *Chem Rev* 107, 577–589.
- Brea, S., Alvarez Salgado, X.A, Alvarez, M., Perez, F., Memery, L., Mercier, H., Messias, M. J. (2004). Nutrient mineralization rates and ratios in the eastern South Atlantic-art. no. C05030. *Journal of Geophysical Union-Research C-Oceans*, 109(C5).
- Broecker, W.S., 1974. NO a conservative water–mass tracer. *Earth Planet. Sci. Lett.* 23 100–107.
- Brzezinski, M.A., 1985. The Si:C:N ratio of marine diatoms: interspecific variability and the effect of some environmental variables1. *j phycol* 21, 347–357. <https://doi.org/10.1111/j.0022-3646.1985.00347.x>
- Buchwald, C., Casciotti, K.L., 2010. Oxygen isotopic fractionation and exchange during bacterial nitrite oxidation. *Limnol Oceanogr* 55, 1064–1074. <https://doi.org/10.4319/LO.2010.55.3.1064>

- Burgoa, N., Machín, F., Marrero-Díaz, S., Rodríguez-Santana, A., Martínez-Marrero, A., Arístegui, J., Duarte, C., 2020. Mass, nutrients and dissolved organic carbon (DOC) lateral transports off northwest Africa during fall 2002 and spring 2003 Item Type Article. *Ocean Sci.* 16, 483–511. <https://doi.org/10.5194/os-16-483-2020>
- Burgoa, N., Machín, F., Rodríguez-Santana, Á., Marrero-Díaz, Á., Álvarez-Salgado, X.A., Fernández-Castro, B., Gelado-Caballero, M.D., Arístegui, J., 2021. Cape Verde Frontal Zone in summer 2017: Lateral transports of mass, dissolved oxygen and inorganic nutrients. *Ocean Science* 17, 769–788. <https://doi.org/10.5194/OS-17-769-2021>
- Campbell, W.H., Kinghorn, J.R., 1990. Functional domains of assimilatory nitrate reductases and nitrite reductases. *Trends Biochem Sci* 15, 315–319. [https://doi.org/10.1016/0968-0004\(90\)90021-3](https://doi.org/10.1016/0968-0004(90)90021-3)
- Canfield, D.E., Glazer, A.N., Falkowski, P.G., 2010. The evolution and future of Earth's nitrogen cycle. *Science* 330, 192–6. <https://doi.org/10.1126/science.1186120>
- Capone, D.G., Bronk, D.A., Mulholland, M.R., Carpenter, E., 2008. *Nitrogen in the Marine Environment*. Elsevier.
- Capone, D.G., Hutchins, D.A., 2013. Microbial biogeochemistry of coastal upwelling regimes in a changing ocean. *Nature Geoscience* 2013 6:9 6, 711–717. <https://doi.org/10.1038/ngeo1916>
- Capone, D. G., Zehr, J. P., Paerl, H. W., Bergman, B., Carpenter, E. J. 1997. *Trichodesmium*, a globally significant marine cyanobacterium. *Science*, 276(5316), 1221-1229.
- Cardoso, C., Caldeira, R.M.A., Relvas, P., Stegner, A., 2020. Islands as eddy transformation and generation hotspots: Cabo Verde case study. *Prog Oceanogr* 184, 102271. <https://doi.org/10.1016/j.pocean.2020.102271>
- Carlson, C., Hansell, D., Nelson, N., Siegel, D., 2010. Dissolved organic carbon export and subsequent remineralization in the mesopelagic and bathypelagic realms of the North Atlantic basin. *Deep Sea Research Part II* 57, 1433–1445.
- Carpenter, E. J., Montoya, J. P., Burns, J., Mulholland, M. R., Subramaniam, A., Capone, D. G. (1999). Extensive bloom of a N₂-fixing diatom/cyanobacterial association in the tropical Atlantic Ocean. *Marine Ecology Progress Series*, 185, 273-283.
- Carr, M.E., Kearns, E.J., 2003. Production regimes in four Eastern Boundary Current systems. *Deep Sea Research Part II: Topical Studies in Oceanography* 50, 3199–3221. <https://doi.org/10.1016/J.DSR2.2003.07.015>
- Casciotti, K., 2009. Inverse kinetic isotope fractionation during bacterial nitrite oxidation. *Geochimica et Cosmochimica Acta* 73, 2061–2076. <https://doi.org/10.1016/J.GCA.2008.12.022>
- Casciotti, K.L., 2016. Nitrogen and Oxygen Isotopic Studies of the Marine Nitrogen Cycle. *Ann Rev Mar Sci* 8, 379–407. <https://doi.org/10.1146/annurev-marine-010213-135052>

References

- Casciotti, K.L., Buchwald, C., McIlvin, M., 2013. Implications of nitrate and nitrite isotopic measurements for the mechanisms of nitrogen cycling in the Peru oxygen deficient zone. *Deep Sea Res 1 Oceanogr Res Pap* 80, 78–93. <https://doi.org/10.1016/J.DSR.2013.05.017>
- Casciotti, K.L., Buchwald, C., Santoro, A.E., Frame, C., 2011. Assessment of Nitrogen and Oxygen Isotopic Fractionation During Nitrification and Its Expression in the Marine Environment. *Methods Enzymol* 486, 253–280. <https://doi.org/10.1016/B978-0-12-381294-0.00011-0>
- Casciotti, K.L., Sigman, D.M., Hastings, M.G., Böhlke, J.K., Hilkert, A., 2002. Measurement of the oxygen isotopic composition of nitrate in seawater and freshwater using the denitrifier method. *Anal Chem* 74, 4905–4912. <https://doi.org/10.1021/AC020113W/ASSET/IMAGES/LARGE/AC020113WF00005.JPEG>
- Chaigneau, A., Eldin, G., Dewitte, B., 2009. Eddy activity in the four major upwelling systems from satellite altimetry (1992–2007). *Prog Oceanogr* 83, 117–123. <https://doi.org/10.1016/J.POCEAN.2009.07.012>
- Chavez, F.P., Messié, M., 2009. A comparison of Eastern Boundary Upwelling Ecosystems. *Prog Oceanogr* 83, 80–96. <https://doi.org/10.1016/J.POCEAN.2009.07.032>
- Chen, Y., Chen, M., Chen, J., Fan, L., Zheng, M. and Qiu, Y. (2022) Dual isotopes of nitrite in the Amundsen Sea in summer. *Science of The Total Environment* 843, 157055.
- Church, M.J., Ducklow, H.W., Karl, D.M., 2002. Multiyear increases in dissolved organic matter inventories at Station ALOHA in the North Pacific Subtropical Gyre. *Limnol Oceanogr* 47, 1–10. <https://doi.org/10.4319/lo.2002.47.1.0001>
- Clark, D.R., Widdicombe, C.E., Rees, A.P., Woodward, E., 2016. The significance of nitrogen regeneration for new production within a filament of the Mauritanian upwelling system. *Biogeosciences* 13, 2873–2888. <https://doi.org/10.5194/bg-13-2873-2016>
- Cline, J. D., & Kaplan, I. R. 1975. Isotopic fractionation of dissolved nitrate during denitrification in the eastern tropical North Pacific Ocean. *Marine Chemistry*, 3(4), 271–299
- Codispoti, L.A., 2007. An oceanic fixed nitrogen sink exceeding 400 Tg N a⁻¹ vs the concept of homeostasis in the fixed-nitrogen inventory. *Biogeosciences* 4, 233–253. <https://doi.org/10.5194/BG-4-233-2007>
- Coplen, T.B. 1996 New guidelines for reporting stable hydrogen, carbon, and oxygen isotope-ratio data. *Geochimica et Cosmochimica Acta* 60, 3359–3360.
- Dekaezemacker, J., Bonnet, S., Grosso, O., Moutin, T., Bressac, M., Capone, D.G., 2013. Evidence of active dinitrogen fixation in surface waters of the eastern tropical South Pacific during El Niño and la Niña events and evaluation of its potential nutrient controls. *Global Biogeochem Cycles* 27, 768–779. <https://doi.org/10.1002/GBC.20063>
- Dekas, A. E., Poretsky, R. S., Orphan, V. J. (2009). Deep-sea archaea fix and share nitrogen in methane-consuming microbial consortia. *Science*, 326(5951), 422–426.

- Del Giorgio, P., Duarte, C., 2002. Respiration in the open ocean. *Nature* 420, 379–384.
- Deman, F., Fonseca-Batista, D., Roukaerts, A., García-Ibáñez, M.I., Le Roy, E., Thilakaratne, E.P.D.N., Elskens, M., Dehairs, F., Fripiat, F., 2021. Nitrate Supply Routes and Impact of Internal Cycling in the North Atlantic Ocean Inferred From Nitrate Isotopic Composition. *Global Biogeochem Cycles* 35, e2020GB006887. <https://doi.org/10.1029/2020GB006887>
- Demarcq, H., Somoue, L., 2015. Phytoplankton and primary productivity off Northwest Africa, in: *Oceanographic and Biological Features in the Canary Current Large Marine Ecosystem*, p. pp. 161–174.
- Deutsch, C., Sarmiento, J.L., Sigman, D.M., Gruber, N., Dunne, J.P., 2007. Spatial coupling of nitrogen inputs and losses in the ocean. *Nature* 2006 445:7124 445, 163–167. <https://doi.org/10.1038/nature05392>
- Deutsch, C., Weber, T. (2012). Nutrient ratios as a tracer and driver of ocean biogeochemistry. *Annual review of marine science*, 4, 113–141.
- Devol, A.H., 2015. Denitrification, Anammox, and N₂ Production in Marine Sediments. *Marine of Science* 7, 403–423. <https://doi.org/10.1146/annurev-marine-010213-135040>
- Devries, T., Primeau, F., Deutsch, C., 2012. The sequestration efficiency of the biological pump. *Geophys Res Lett* 39, 13601. <https://doi.org/10.1029/2012GL051963>
- Diercks, A.R., Asper, V.L., 1997. In situ settling speeds of marine snow aggregates below the mixed layer: Black Sea and Gulf of Mexico. *Deep Sea Research Part I: Oceanographic Research Papers* 44, 385–398. [https://doi.org/10.1016/S0967-0637\(96\)00104-5](https://doi.org/10.1016/S0967-0637(96)00104-5)
- Dole M 1936 The relative atomic weight of oxygen in water and air. A discussion of the atmospheric distribution of the oxygen isotopes and of the chemical standard of atomic weights. *J Chem Phys* 4:268–275.
- Doval, M.D., Álvarez-Salgado, X.A., Gasol, J.M., Lorenzo, L.M., Mirón, I., Figueiras, F.G., Pedrós-Alió, C., 2001. Dissolved and suspended organic carbon in the Atlantic sector of the Southern Ocean. Stock dynamics in upper ocean waters. *Mar Ecol Prog Ser* 223, 27–38. <https://doi.org/10.3354/MEPS223027>
- Du, E., Terrer, C., Pellegrini, A.F.A., Ahlström, A., van Lissa, C.J., Zhao, X., Xia, N., Wu, X., Jackson, R.B., 2020. Global patterns of terrestrial nitrogen and phosphorus limitation. *Nat Geosci* 13, 221–226. <https://doi.org/10.1038/S41561-019-0530-4>
- Duce, R.A., LaRoche, J., Altieri, K., Arrigo, K.R., Baker, A.R., Capone, D.G., Cornell, S., Dentener, F., Galloway, J., Ganeshram, R.S., Geider, R.J., Jickells, T., Kuypers, M.M., Langlois, R., Liss, P.S., Liu, S.M., Middelburg, J.J., Moore, C.M., Nickovic, S., Oschlies, A., Pedersen, T., Prospero, J., Schlitzer, R., Seitzinger, S., Sorensen, L.L., Uematsu, M., Ulloa, O., Voss, M., Ward, B., Zamora, L., 2008. Impacts of atmospheric anthropogenic nitrogen on the open ocean. *Science* 320, 893–897.
- Elser, J.J., Bracken, M.E.S., Cleland, E.E., Gruner, D.S., Harpole, W.S., Hillebrand, H., Ngai, J.T., Seabloom, E.W., Shurin, J.B., Smith, J.E., 2007. Global analysis of nitrogen and

References

- phosphorus limitation of primary producers in freshwater, marine and terrestrial ecosystems. *Ecol Lett* 10, 1135–1142. <https://doi.org/10.1111/J.1461-0248.2007.01113.X>
- Epstein S, Mayeda T 1953 Variation of ^{18}O content of waters from natural sources. *Geochim Cosmochim Acta* 4:213–224.
- Estapa, M.L., Siegel, D.A., Buesseler, K.O., Stanley, R.H.R., Lomas, M.W., Nelson, N.B., 2015. Decoupling of net community and export production on submesoscales in the Sargasso Sea. *Global Biogeochem Cycles* 29, 1266–1282. <https://doi.org/10.1002/2014GB004913>
- Eugster, O., Gruber, N., 2012. A probabilistic estimate of global marine N-fixation and denitrification. *Global Biogeochem Cycles* 26. <https://doi.org/10.1029/2012GB004300>
- Fawcett, S.E., Ward, B.B., Lomas, M.W., Sigman, D.M., 2015. Vertical decoupling of nitrate assimilation and nitrification in the Sargasso Sea. *Deep Sea Research Part I: Oceanographic Research Papers* 103, 64–72. <https://doi.org/10.1016/J.DSR.2015.05.004>
- Faye, S., Lazar, A., Sow, B.A., Gaye, A.T., 2015. A model study of the seasonality of sea surface temperature and circulation in the Atlantic North-eastern Tropical Upwelling System. *Front Phys* 3, 140513. <https://doi.org/10.3389/FPHY.2015.00076/BIBTEX>
- Felix, J., Elliott, E. M., Gish, T. J., McConnell, L. L., Shaw, S. L. 2013. Characterizing the isotopic composition of atmospheric ammonia emission sources using passive samplers and a combined oxidation-bacterial denitrifier approach. *Rapid Communications in Mass Spectrometry*, 27(20), 2239-2246
- Fernandez, C., Farías, L., Ulloa, O., 2011. Nitrogen Fixation in Denitrified Marine Waters. *PLoS One* 6, e20539. <https://doi.org/10.1371/JOURNAL.PONE.0020539>
- Fernández-Castro, B., Mouriño-Carballido, B., Álvarez-Salgado, X. A. 2019. Non-redfieldian mesopelagic nutrient remineralization in the eastern North Atlantic subtropical gyre. *Progress in Oceanography*, 171, 136-153.
- Fernandez, A., Marañón, E., Bode, A. 2014. Large-scale meridional and zonal variability in the nitrogen isotopic composition of plankton in the Atlantic Ocean. *Journal of plankton research*, 36(4), 1060-1073.
- Fischer, G., Karakaş, G., 2009. Sinking rates and ballast composition of particles in the Atlantic Ocean: implications for the organic carbon fluxes to the deep ocean. *Biogeosciences* 6, 85–102. <https://doi.org/10.5194/bg-6-85-2009>
- Fischer, G., Reuter, C., Karakas, G., Nowald, N., Wefer, G., 2009. Offshore advection of particles within the Cape Blanc filament, Mauritania: Results from observational and modelling studies. *Prog Oceanogr* 83, 322–330. <https://doi.org/10.1016/j.pocean.2009.07.023>
- Fischer, G., Romero, O., Merkel, U., Donner, B., Iversen, M., Nowald, N., Ratmeyer, V., Ruhland, G., Klann, M., Wefer, G., 2016. Deep ocean mass fluxes in the coastal upwelling off Mauritania from 1988 to 2012: variability on seasonal to decadal timescales. *Biogeosciences* 13, 3071–3090. <https://doi.org/10.5194/bgd-12-17643-2015>

- Fischer, G., Romero, O., Toby, E., Iversen, M., Donner, B., Mollenhauer, G., Nowald, N., Ruhland, G., Klann, M., Hamady, B., Wefer, G., 2019. Changes in the Dust-Influenced Biological Carbon Pump in the Canary Current System: Implications From a Coastal and an Offshore Sediment Trap Record Off Cape Blanc, Mauritania. *Global Biogeochem Cycles* 33, 1100–1128. <https://doi.org/10.1029/2019GB006194>
- Fowler, D., Steadman, C.E., Stevenson, D., Coyle, M., Rees, R.M., Skiba, U.M., Sutton, M.A., Cape, J.N., Dore, A.J., Vieno, M., Simpson, D., Zaehle, S., Stocker, B.D., Rinaldi, M., Facchini, M.C., Flechard, C.R., Nemitz, E., Twigg, M., Erisman, J.W., Butterbach-Bahl, K., Galloway, J.N., 2015. Effects of global change during the 21st century on the nitrogen cycle. *Atmos Chem Phys* 15, 13849–13893. <https://doi.org/10.5194/ACP-15-13849-2015>
- Fry, B., 2006. Stable Isotope Ecology. *Stable Isotope Ecology*. <https://doi.org/10.1007/0-387-33745-8>
- Fulweiler, R., Nixon, S., Buckley, B., 2007. Reversal of the net dinitrogen gas flux in coastal marine sediments. *Nature*.
- Gabric, A.J., Garcia, L., Van Camp, L., Nykjaer, L., Eifler, W., Schrimpf, W., 1993. Offshore export of shelf production in the Cape Blanc (Mauritania) giant filament as derived from coastal zone color scanner imagery. *J Geophys Res* 98, 4697–4712. <https://doi.org/10.1029/92JC01714>
- Galloway, J.N., Dentener, F.J., Capone, D.G., Boyer, E.W., Howarth, R.W., Seitzinger, S.P., Asner, G.P., Cleveland, C.C., Green, P.A., Holland, E.A., Karl, D.M., Michaels, A.F., Porter, J.H., Townsend, A.R., Vöosmarty, C.J., 2004. Nitrogen Cycles: Past, Present, and Future. *Biogeochemistry* 70, 153–226. <https://doi.org/10.1007/s10533-004-0370-0>
- Gattuso, J.-P., Frankignoulle, M., Wollast, R., 1998. Carbon and Carbonate metabolism in coastal aquatic ecosystems. *Annu Rev Ecol Syst* 29, 405–434. <https://doi.org/10.1146/annurev.ecolsys.29.1.405>
- Gebbie, G., Huybers, P., 2010. Total Matrix Intercomparison: A Method for Determining the Geometry of Water-Mass Pathways. *J Phys Oceanogr* 40, 1710–1728. <https://doi.org/10.1175/2010JPO4272.1>
- Geider, R.J., La Roche, J., 2002. Redfield revisited: variability of C[ratio] N[ratio] P in marine microalgae and its biochemical basis. *Eur J Phycol* 37, 1–17. <https://doi.org/10.1017/S0967026201003456>
- Glibert, P.M., Wilkerson, F.P., Dugdale, R.C., Raven, J.A., Dupont, C.L., Leavitt, P.R., Parker, A.E., Burkholder, J.M., Kana, T.M., 2016. Pluses and minuses of ammonium and nitrate uptake and assimilation by phytoplankton and implications for productivity and community composition, with emphasis on nitrogen-enriched conditions. *Limnol Oceanogr* 61, 165–197. <https://doi.org/10.1002/LNO.10203>
- Granger, J., Sigman, D.M., Lehmann, M.F., Tortell, P.D., 2008. Nitrogen and oxygen isotope fractionation during dissimilatory nitrate reduction by denitrifying bacteria. *Limnol Oceanogr* 53, 2533–2545. <https://doi.org/10.4319/LO.2008.53.6.2533>

References

- Granger, J., Sigman, D.M., Needoba, J.A., Harrison, P.J., 2004. Coupled nitrogen and oxygen isotope fractionation of nitrate during assimilation by cultures of marine phytoplankton. *Limnol Oceanogr* 49, 1763–1773. <https://doi.org/10.4319/LO.2004.49.5.1763>
- Granger, J., Sigman, D.M., Rohde, M.M., Maldonado, M.T., Tortell, P.D., 2010. N and O isotope effects during nitrate assimilation by unicellular prokaryotic and eukaryotic plankton cultures. *GeCoA* 74, 1030–1040. <https://doi.org/10.1016/J.GCA.2009.10.044>
- Grokovf, T., Mohr, W., Baustian, T., Schunck, H., Gill, D., Kuypers, M.M.M., Lavik, G., Schmitz, R.A., Wallace, D.W.R., Laroche, J., 2012. Doubling of marine dinitrogen-fixation rates based on direct measurements. *Nature* 2012 488:7411 488, 361–364. <https://doi.org/10.1038/nature11338>
- Gruber, N., 2004. The Dynamics of the Marine Nitrogen Cycle and its Influence on Atmospheric CO₂ Variations. *The Ocean Carbon Cycle and Climate* 97–148. https://doi.org/10.1007/978-1-4020-2087-2_4
- Gruber, N., 2008. The Marine Nitrogen Cycle: Overview and Challenges. In *Nitrogen in the Marine Environment*. D.G. Capone, D.A. Bronk, M.R. Mulholland, and E.J. Carpenter (eds). Amsterdam, The Netherlands: Elsevier, pp. 1– 50.
- Gruber, N., Galloway, J., 2008. An Earth-system perspective of the global nitrogen cycle. *Nature*.
- Gruber, N., Sarmiento, J.L., 1997. Global patterns of marine nitrogen fixation and denitrification. *Global Biogeochem Cycles* 11, 235–266. <https://doi.org/10.1029/97GB00077>
- Hallstrøm, S., Benavides, M., Salamon, E.R., Arístegui, J., Riemann, L., 2022. Activity and distribution of diazotrophic communities across the Cape Verde Frontal Zone in the Northeast Atlantic Ocean. *Biogeochemistry* 2022 160:1 160, 49–67. <https://doi.org/10.1007/S10533-022-00940-W>
- Hansell, D.A, Carlson, C.A, 2001. Biogeochemistry of total organic carbon and nitrogen in the Sargasso Sea: control by convective overturn. *Deep Sea Research Part II: Topical Studies in Oceanography* 48, 1649–1667. [https://doi.org/10.1016/S0967-0645\(00\)00153-3](https://doi.org/10.1016/S0967-0645(00)00153-3)
- Hansell, D.A, Carlson, C.A, 2013. Localized refractory dissolved organic carbon sinks in the deep ocean. *Global Biogeochem Cycles* 27, 705–710. <https://doi.org/10.1002/gbc.20067>
- Hansell, D.A, Carlson, C.A, 2014. *Biogeochemistry of marine dissolved organic matter*. Academic Press
- Hansell, D.A, Carlson, C.A, Repeta, D., Schlitzer, R., 2009. Dissolved organic matter in the ocean: A controversy stimulates new insights. *Oceanography* 22, 202–211.
- Hansell, D.A, Carlson, C.A, Schlitzer, R., 2012. Net removal of major marine dissolved organic carbon fractions in the subsurface ocean. *Global Biogeochem Cycles* 26, GB1016. <https://doi.org/10.1029/2011GB004069>
- Hansell, D.A., Carlson, C.A., Amon, R.M.W., Álvarez-Salgado, X.A., Yamashita, Y., Romera-Castillo, C., Bif, M.B., 2021. Compilation of dissolved organic matter (DOM) data

- obtained from the global ocean surveys from 1994 to 2020. <https://doi.org/10.25921/S4F4-YE35>
- Hansen, H., Koroleff, F., 1999. *Methods of Seawater Analysis*, 3rd, Completely Revised and Extended Edition, Ed. by K. Grashoff et al (Wiley, Weinheim, 1999), pp. 149–228.
- Helmke, P., Romero, O., Fischer, G., 2005. Northwest African upwelling and its effect on offshore organic carbon export to the deep sea. *Global Biogeochem Cycles* 19, GB4015. <https://doi.org/10.1029/2004GB002265>
- Henriksen, K., Blackburn, T.H., Lomstein, B.A., McRoy, C.P., 1993. Rates of nitrification, distribution of nitrifying bacteria and inorganic N fluxes in northern Bering-Chukchi shelf sediments. *Cont Shelf Res* 13, 629–651. [https://doi.org/10.1016/0278-4343\(93\)90097-H](https://doi.org/10.1016/0278-4343(93)90097-H)
- Hernández-Hernández, N., Arístegui, J., Montero, M.F., Velasco-Senovilla, E., Baltar, F., Marrero-Díaz, Á., Martínez-Marrero, A., Rodríguez-Santana, Á., 2020. Drivers of Plankton Distribution Across Mesoscale Eddies at Submesoscale Range. *Front Mar Sci* 7, 667. <https://doi.org/10.3389/FMARS.2020.00667/BIBTEX>
- Hill, J.K., Wheeler, P.A., 2002. Organic carbon and nitrogen in the northern California current system: comparison of offshore, river plume, and coastally upwelled waters. *Prog Oceanogr* 53, 369–387.
- Holm-Hansen, O., Lorenzen, C.J., Holmes, R.W., Strickland, J.D.H., 1965. Fluorometric Determination of Chlorophyll. *ICES Journal of Marine Science* 30, 3–15. <https://doi.org/10.1093/icesjms/30.1.3>
- Hooper, A. B., Vannelli, T., Bergmann, D. J., Arciero, D. M. 1997. Enzymology of the oxidation of ammonia to nitrite by bacteria. *Antonie van Leeuwenhoek*, 71, 59-67.
- Hopkinson, C., Vallino, J., 2005. Efficient export of carbon to the deep ocean through dissolved organic matter. *Nature* 433, 142–145.
- Hort, M., Hansteen for discussions, T., Bouabdellah, M., Chaieb, M., Garbe-Schönberg, D., Harris, C., Hauff, F., Jadid, M., Fernandez Soler, J.M., Milhi, M., Moukadiri, A., Rau, D., Sticklus, J., Dalsgaard, T., Canfield, D.E., Petersen, J., Thamdrup, B., Acuña-González, J., 2003. N₂ production by the anammox reaction in the anoxic water column of Golfo Dulce, Costa Rica. *Nature* 422:6932 422, 606–608. <https://doi.org/10.1038/nature01526>
- Hosegood, P., Nightingale, P., Rees, A., Widdicombe, C., Woodward, E., Clark, D., Torres, R., 2017. Nutrient pumping by submesoscale circulations in the mauritanian upwelling system. *Prog Oceanogr* 159, 223–236.
- Houlton, B. Z., Morford, S. L., Dahlgren, R. A. 2018. Convergent evidence for widespread rock nitrogen sources in Earth's surface environment. *Science*, 360(6384), 58-62.
- Hu, H., Bourbonnais, A., Larkum, J., Bange, H.W., Altabet, M.A., 2016. Nitrogen cycling in shallow low-oxygen coastal waters off Peru from nitrite and nitrate nitrogen and oxygen isotopes. *Biogeosciences* 13, 1453–1468. <https://doi.org/10.5194/BG-13-1453-2016>
- Hupe, A., Karstensen, J., 2000. Redfield stoichiometry in Arabian Sea subsurface waters. *Global Biogeochem Cycles* 14, 357–372. <https://doi.org/10.1029/1999GB900077>

References

- Hutchins, D.A., Capone, D.G., 2022. The marine nitrogen cycle: new developments and global change. *Nature Reviews Microbiology* 2022 20:7 20, 401–414. <https://doi.org/10.1038/s41579-022-00687-z>
- Iuculano, F., Álvarez-Salgado, X., Otero, J., Catalá, T., Sobrino, C., Duarte, C., Agustí, S., 2019. Patterns and drivers of UV absorbing chromophoric dissolved organic matter in the euphotic layer of the open ocean. *frontier in Marine Science* 6, 320.
- Iversen, M., Nowald, N., Ploug, H., Jackson, G., Fischer, G., 2010. High resolution profiles of vertical particulate organic matter export off Cape Blanc, Mauritania: Degradation processes and ballasting effects. *Deep-Sea Research Part I* 57, 771–784.
- Jackson, G.A., Williams, P.M., 1985. Importance of dissolved organic nitrogen and phosphorus to biological nutrient cycling. *Deep Sea Research Part A, Oceanographic Research Papers* 32, 223–235. [https://doi.org/10.1016/0198-0149\(85\)90030-5](https://doi.org/10.1016/0198-0149(85)90030-5)
- Jerusalén-Lleó, E., Nieto-Cid, M., Fuentes-Santos, I., Dittmar, T., Álvarez-Salgado, X.A., 2023. Solid phase extraction of ocean dissolved organic matter with PPL cartridges: efficiency and selectivity. *Front Mar Sci* 10, 652. <https://doi.org/10.3389/FMARS.2023.1159762>
- Jickells, T.D., Buitenhuis, E., Altieri, K., Baker, A.R., Capone, D., Duce, R.A., Dentener, F., Fennel, K., Kanakidou, M., LaRoche, J., Lee, K., Liss, P., Middelburg, J.J., Moore, J.K., Okin, G., Oschlies, A., Sarin, M., Seitzinger, S., Sharples, J., Singh, A., Suntharalingam, P., Uematsu, M., Zamora, L.M., 2017. A reevaluation of the magnitude and impacts of anthropogenic atmospheric nitrogen inputs on the ocean. *Global Biogeochem Cycles* 31, 289–305. <https://doi.org/10.1002/2016GB005586>
- Kaneko, M. and Poulson, S.R. (2013) The rate of oxygen isotope exchange between nitrate and water. *Geochimica et Cosmochimica Acta* 118, 148-156.
- Karakaş, G., Nowald, N., Blaas, M., Marchesiello, P., Frickenhaus, S., Schlitzer, R., 2006. High-resolution modeling of sediment erosion and particle transport across the northwest African shelf. *J Geophys Res* 111, C06025. <https://doi.org/10.1029/2005JC003296>
- Karstensen, J., Tomczak, M., 1998. Age determination of mixed water masses using CFC and oxygen data. *J Geophys Res* 103, 18599–18609. <https://doi.org/10.1029/98JC00889>
- Kemeny, P.C., Weigand, M.A., Zhang, R., Carter, B.R., Karsh, K.L., Fawcett, S.E. and Sigman, D.M. (2016) Enzyme-level interconversion of nitrate and nitrite in the fall mixed layer of the Antarctic Ocean. *Global Biogeochemical Cycles* 30, 1069-1085.
- Kendall, C., Caldwell, E.A., 1998. Fundamentals of Isotope Geochemistry. *Isotope Tracers in Catchment Hydrology* 51–86. <https://doi.org/10.1016/B978-0-444-81546-0.50009-4>
- Kérouel, R., Aminot, A., 1997. Fluorometric determination of ammonia in sea and estuarine waters by direct segmented flow analysis. *Mar Chem* 57, 265–275. [https://doi.org/10.1016/S0304-4203\(97\)00040-6](https://doi.org/10.1016/S0304-4203(97)00040-6)
- Kim, H., 2016. Review of inorganic nitrogen transformations and effect of global climate change on inorganic nitrogen cycling in ocean ecosystems. *Ocean Science Journal* 51, 159–167. <https://doi.org/10.1007/S12601-016-0014-Z/METRICS>

- Klein, B., Siedler, G. 1989. On the origin of the Azores Current. *Journal of Geophysical Research: Oceans*, 94(C5), 6159-6168.
- Knapp, A.N., DiFiore, P.J., Deutsch, C., Sigman, D.M., Lipschultz, F., 2008. Nitrate isotopic composition between Bermuda and Puerto Rico: Implications for N₂ fixation in the Atlantic Ocean. *Global Biogeochem Cycles* 22, 3014. <https://doi.org/10.1029/2007GB003107>
- Knapp, A.N., Sigman, D.M., Lipschultz, F., 2005. N isotopic composition of dissolved organic nitrogen and nitrate at the Bermuda Atlantic Time-series Study site. *Global Biogeochem Cycles* 19, 1–15. <https://doi.org/10.1029/2004GB002320>
- Körtzinger, A., Koeve, W., Kähler, P., Mintrop, L., 2001. C : N ratios in the mixed layer during the productive season in the northeast Atlantic Ocean. *Deep Sea Research Part I: Oceanographic Research Papers* 48, 661–688. [https://doi.org/10.1016/S0967-0637\(00\)00051-0](https://doi.org/10.1016/S0967-0637(00)00051-0)
- Kudela, R.M., Dugdale, R.C., 2000. Nutrient regulation of phytoplankton productivity in Monterey Bay, California. *Deep Sea Research Part II: Topical Studies in Oceanography* 47, 1023–1053. [https://doi.org/10.1016/S0967-0645\(99\)00135-6](https://doi.org/10.1016/S0967-0645(99)00135-6)
- Kuypers, M.M.M., Silekers, A.O., Lavik, G., Schmid, M., Jørgensen, B.B., Kuenen, J.G., Sinninghe Damsté, J.S., Strous, M., Jetten, M.S.M., 2003. Anaerobic ammonium oxidation by anammox bacteria in the Black Sea. *Nature* 2003 422:6932 422, 608–611. <https://doi.org/10.1038/nature01472>
- Landrum, J.P., Altabet, M.A., Montoya, J.P., 2011. Basin-scale distributions of stable nitrogen isotopes in the subtropical North Atlantic Ocean: Contribution of diazotroph nitrogen to particulate organic matter and mesozooplankton. *Deep Sea Research Part I: Oceanographic Research Papers* 58, 615–625. <https://doi.org/10.1016/J.DSR.2011.01.012>
- Lane, G.A. and Dole, M. 1956. Fractionation of oxygen isotopes during respiration. *Science* 123, 574-576.
- Langdon, C., 2010. Determination of dissolved oxygen in seawater by winkler titration using the amperometric technique. In: Hood, E.M., Sloyan, B.M., Sabine, C. (Eds.), *GO-SHIP Repeat Hydrography Manual: A Collection of Expert Reports and Guidelines*. IOCCP Report no. 14, ICPO Publication Series no. 134.
- Letscher, Robert T, Hansell, D.A., Carlson, C.A., Lumpkin, R., Knapp, A.N., 2013. Dissolved organic nitrogen in the global surface ocean: Distribution and fate. *Global Biogeochem Cycles* 27, 141–153. <https://doi.org/10.1029/2012GB004449>
- Lévy, M., Ferrari, R., Franks, P.J.S., Martin, A.P., Rivière, P., 2012. Bringing physics to life at the submesoscale. *Geophys Res Lett* 39. <https://doi.org/10.1029/2012GL052756>
- Li, Q.P., Hansell, D.A., Zhang, J.-Z., 2008. Underway monitoring of nanomolar nitrate plus nitrite and phosphate in oligotrophic seawater. *Limnol Oceanogr Methods* 6, 319–326. <https://doi.org/10.4319/lom.2008.6.319>
- Liu, K. K. (1979). *Geochemistry of inorganic nitrogen compounds in two marine environments: The Santa Barbara Basin and the ocean off Peru*. University of California, Los Angeles.

References

- Liu, D., Fang, Y., Tu, Y., Pan, Y., 2014. Chemical Method for Nitrogen Isotopic Analysis of Ammonium at Natural Abundance. *Anal Chem* 86, 3787–3792. <https://doi.org/10.1021/ac403756u>
- Lomas, M.W., Lipschultz, F., 2006. Forming the primary nitrite maximum: Nitrifiers or phytoplankton? *Limnol Oceanogr*. <https://doi.org/10.4319/lo.2006.51.5.2453>
- Lønborg, C. and, Álvarez-Salgado, X.A, 2014. Tracing dissolved organic matter cycling in the eastern boundary of the temperate North Atlantic using absorption and fluorescence spectroscopy. *Deep-Sea Research I* 85, 35–46.
- Lovecchio, E., Gruber, N., Münnich, M., 2018. Mesoscale contribution to the long-range offshore transport of organic carbon from the Canary Upwelling System to the open North Atlantic. *Biogeosciences* 15, 2018–5061. <https://doi.org/10.3929/ethz-b-000286944>
- Lovecchio, E., Gruber, N., Münnich, M., Lachkar, Z., 2017. On the long-range offshore transport of organic carbon from the Canary Upwelling System to the open North Atlantic. *Biogeosciences* 14, 3337–3369. <https://doi.org/10.3929/ethz-b-000190480>
- Machín, F., Pelegrí, J.L., 2009. Northward Penetration of Antarctic Intermediate Water off Northwest Africa. *J Phys Oceanogr* 39, 512–535. <https://doi.org/10.1175/2008JPO3825.1>
- Mahaffey, C., Michaels, A.F., Capone, D.G., 2005. The conundrum of marine N₂ fixation. *Am J Sci* 305, 546–595. <https://doi.org/10.2475/AJS.305.6-8.546>
- Mahaffey, C., Williams, R.G., Wolff, G.A., Anderson, W.T., 2004. Physical supply of nitrogen to phytoplankton in the Atlantic Ocean. *Global Biogeochem Cycles* 18. <https://doi.org/10.1029/2003GB002129>
- Mahaffey, C., Williams, R. G., Wolff, G. A., Mahowald, N., Anderson, W., Woodward, M. (2003). Biogeochemical signatures of nitrogen fixation in the eastern North Atlantic. *Geophysical Research Letters*, 30(6).
- Maita, Y., Yanada, M., 1990. Vertical distribution of total dissolved nitrogen and dissolved organic nitrogen in seawater. *Geochem J* 24, 245–254. <https://doi.org/10.2343/geochemj.24.245>
- Marconi, D., Kopf, S., Rafter, P.A., Sigman, D.M., 2017. Aerobic respiration along isopycnals leads to overestimation of the isotope effect of denitrification in the ocean water column. *Geochim Cosmochim Acta* 197, 417–432. <https://doi.org/10.1016/J.GCA.2016.10.012>
- Marconi, D., Weigand, M.A., Rafter, P.A., McIlvin, M.R., Forbes, M., Casciotti, K.L., Sigman, D.M., 2015. Nitrate isotope distributions on the US GEOTRACES North Atlantic cross-basin section: Signals of polar nitrate sources and low latitude nitrogen cycling. *Mar Chem* 177, 143–156. <https://doi.org/10.1016/J.MARCHEM.2015.06.007>
- Marconi, D., Weigand, M.A., Sigman, D.M., 2019. Nitrate isotopic gradients in the North Atlantic Ocean and the nitrogen isotopic composition of sinking organic matter. *Deep Sea Research Part I: Oceanographic Research Papers* 145, 109–124. <https://doi.org/10.1016/J.DSR.2019.01.010>

- Margeson, J. H., Suggs, J. C., Midgett, M. R. (1980). Reduction of nitrate to nitrite with cadmium. *Analytical Chemistry*, 52(12), 1955-1957.
- Mariotti, A. (1983) Atmospheric nitrogen is a reliable standard for natural ^{15}N abundance measurements. *Nature* 303, 685.
- Mariotti, A., Germon, J.C., Hubert, P., Kaiser, P., Letolle, R., Tardieux, A. and Tardieux, P. (1981) Experimental determination of nitrogen kinetic isotope fractionation: Some principles; illustration for the denitrification and nitrification processes. *Plant and Soil* 62, 413-430
- Martínez-Marrero, A., Rodríguez-Santana, A., Hernández-Guerra, A., Fraile-Nuez, E., López-Laatzén, F., Vélez-Belchí, P., Parrilla, G., 2008. Distribution of water masses and diapycnal mixing in the Cape Verde Frontal Zone. *Geophys Res Lett* 35, L07609. <https://doi.org/10.1029/2008GL033229>
- Martiny, A.C., Pham, C.T.A., Primeau, F.W., Vrugt, J.A., Moore, J.K., Levin, S.A., Lomas, M.W., 2013. Strong latitudinal patterns in the elemental ratios of marine plankton and organic matter. *Nature Geoscience* 2013 6:4 6, 279–283. <https://doi.org/10.1038/ngeo1757>
- McCarthy, M. D., Hedges, J. I., Benner, R. (1998). Major bacterial contribution to marine dissolved organic nitrogen. *Science*, 281(5374), 231-234.
- McCartney, M.S., 1992. Recirculating components to the deep boundary current of the northern North Atlantic. *Prog Oceanogr* 29, 283–383. [https://doi.org/10.1016/0079-6611\(92\)90006-L](https://doi.org/10.1016/0079-6611(92)90006-L)
- McIlvin, M.R., Altabet, M.A., 2005. Chemical conversion of nitrate and nitrite to nitrous oxide for nitrogen and oxygen isotopic analysis in freshwater and seawater. *Anal Chem* 77, 5589–5595. https://doi.org/10.1021/AC050528S/SUPPL_FILE/AC050528S_S.PDF
- Meeder, E., Mackey, K., Paytan, A., Shaked, Y., Iluz, D., Stambler, N., Rivlin, T., Post, A., Lazar, B., 2012. Nitrite dynamics in the open ocean—clues from seasonal and diurnal variations. *Mar Ecol Prog Ser* 453, 11–26. <https://doi.org/10.3354/meps09525>
- Mehta, M.P., Butterfield, D.A., Baross, J.A., 2003. Phylogenetic diversity of nitrogenase (*nifH*) genes in deep-sea and hydrothermal vent environments of the Juan de Fuca Ridge. *Appl Environ Microbiol* 69, 960–970. <https://doi.org/10.1128/AEM.69.2.960-970.2003/ASSET/41691955-AFF5-4726-8338-7F274A8EAD88/ASSETS/GRAPHIC/AM0231562006.JPEG>
- Meunier, T., Barton, E., Barreiro, B., Torres, R., 2012. Upwelling filaments off cap blanc: Interaction of the NW african upwelling current and the cape verde frontal zone eddy field? *J Geophys Res* 117, C08031. <https://doi.org/10.1029/2012JC007905>
- Mills, M. M., Arrigo, K. R. (2010). Magnitude of oceanic nitrogen fixation influenced by the nutrient uptake ratio of phytoplankton. *Nature Geoscience*, 3(6), 412-416.
- Mignot, A., Claustre, H., Uitz, J., Poteau, A., D’Ortenzio, F., Xing, X., 2014. Understanding the seasonal dynamics of phytoplankton biomass and the deep chlorophyll maximum in oligotrophic environments: A Bio-Argo float investigation. *Global Biogeochem Cycles* 28, 856– 876. <https://doi.org/10.1002/2013GB004781>

References

- Miyake, Y., and Wada, E. 1967. The abundance ratio of $^{15}\text{N}/^{14}\text{N}$ in marine environments. *Rec. Oceanogr. Works Jpn*, 9, 37-53.
- Mittelstaedt, E., 1991. The ocean boundary along the northwest African coast: Circulation and oceanographic properties at the sea surface. *Prog Oceanogr*.
- Montoya, J., 2008. Nitrogen stable isotopes in marine environments, in: *Nitrogen in the Marine Environment*. pp. 1277–1302. <https://doi.org/10.1029/2009GB003767>
- Montoya, J. P., Carpenter, E. J., Capone, D. G. (2002). Nitrogen fixation and nitrogen isotope abundances in zooplankton of the oligotrophic North Atlantic. *Limnology and Oceanography*, 47(6), 1617-1628.
- Moore, C.M., Mills, M.M., Arrigo, K.R., Berman-Frank, I., Bopp, L., Boyd, P.W., Galbraith, E.D., Geider, R.J., Guieu, C., Jaccard, S.L., Jickells, T.D., La Roche, J., Lenton, T.M., Mahowald, N.M., Marañón, E., Marinov, I., Moore, J.K., Nakatsuka, T., Oschlies, A., Saito, M.A., Thingstad, T.F., Tsuda, A., Ulloa, O., 2013. Processes and patterns of oceanic nutrient limitation. *Nat Geosci* 6, 701–710. <https://doi.org/10.1038/NGEO1765>
- Morrow, R., Birol, F., Griffin, D., Sudre, J., 2004. Divergent pathways of cyclonic and anticyclonic ocean eddies. *Geophys Res Lett* 31, 1–5. <https://doi.org/10.1029/2004GL020974>
- Mulholland, M.R., Lomas, M.W., 2008. Nitrogen Uptake and Assimilation. *Nitrogen in the Marine Environment* 303–384. <https://doi.org/10.1016/B978-0-12-372522-6.00007-4>
- Muller-Karger, F.E., Varela, R., Thunell, R., Luerssen, R., Hu, C., Walsh, J.J., 2005. The importance of continental margins in the global carbon cycle. *Geophys Res Lett* 32, 1–4. <https://doi.org/10.1029/2004GL021346>
- Nagai, T., Gruber, N., Frenzel, H., Lachkar, Z., McWilliams, J.C., Plattner, G.K., 2015. Dominant role of eddies and filaments in the offshore transport of carbon and nutrients in the California Current System. *J Geophys Res Oceans* 120, 5318–5341. <https://doi.org/10.1002/2015JC010889>
- Niewiadomska, K., Claustre, H., Prieur, L., D’Ortenzio, F., 2008. Submesoscale physical-biogeochemical coupling across the Ligurian current (northwestern Mediterranean) using a bio-optical glider. *Limnol Oceanogr* 53, 2210–2225. https://doi.org/10.4319/LO.2008.53.5_PART_2.2210
- Nowald, N., Fischer, G., Ratmeyer, V., Iversen, M., Reuter, C., Wefer, G., 2009. In-situ sinking speed measurements of marine snow aggregates acquired with a settling chamber mounted to the Cherokee ROV. *OCEANS '09 IEEE Bremen: Balancing Technology with Future Needs*. <https://doi.org/10.1109/OCEANSE.2009.5278186>
- Nowald, N., Iversen, M., Fischer, G., Ratmeyer, V., Wefer, G., 2015. Time series of in-situ particle properties and sediment trap fluxes in the coastal upwelling filament off Cape Blanc, Mauritania. *Prog Oceanogr* 137, 1–11. <https://doi.org/10.1016/j.pcean.2014.12.015>
- Nowald, N., Karakas, G., Ratmeyer, V., Fischer, G., Schlitzer, R., Davenport, R.A., Wefer, G., 2006. Distribution and transport processes of marine particulate matter off Cape Blanc (NW-Africa): results from vertical camera profiles. *Ocean Sci. Discuss* 3, 903–938.

- Ohde, T., Fiedler, B., Körtzinger, A., 2015. Spatio-temporal distribution and transport of particulate matter in the eastern tropical North Atlantic observed by Argo floats. *Deep-Sea Research Part I* 102, 26–42.
- Olivar, M., Sabatés, A., Pastor, M., Pelegrí, J.L., 2016. Water masses and mesoscale control on latitudinal and cross-shelf variations in larval fish assemblages off NW Africa. *Deep Sea Res 1 Oceanogr Res Pap* 117, 120–137. <https://doi.org/10.1016/j.dsr.2016.10.003>
- Omand, M., D'Asaro, E., Lee, C., 2015. Eddy-driven subduction exports particulate organic carbon from the spring bloom. *Science*
- Osterroht, C., Thomas, H., 2000. New production enhanced by nutrient supply from non-Redfield remineralisation of freshly produced organic material. *Journal of Marine Systems* 25, 33–46. [https://doi.org/10.1016/S0924-7963\(00\)00007-5](https://doi.org/10.1016/S0924-7963(00)00007-5)
- Pantoja, S., Repeta, D.L., Sachs, J.P., Sigman, D.M., 2002. Stable isotope constraints on the nitrogen cycle of the Mediterranean Sea water column. *Deep-Sea Res. I* 49 (9), 1609–1621.
- Pastor M, Velez-Velchí P, Hernández-Guerra, A., 2015. Water masses in the Canary Current Large Marine Ecosystem.
- Pastor, M., Pelegrí, J.L., Hernández-Guerra, A., Font, J., Salat, J., Emelianov, M., 2008. Water and nutrient fluxes off Northwest Africa. *Cont Shelf Res* 28, 915–936. <https://doi.org/10.1016/J.CSR.2008.01.011>
- Pastor, M., Peña-Izquierdo, J., Pelegrí, J., Marrero-Díaz, A., 2012. Meridional changes in water mass distributions off NW Africa during November 2007/2008. *Cienc Mar* 38, 223– 244. <https://doi.org/10.7773/cm.v38i1B.1831>
- Pegliasco, C., Chaigneau, A., Morrow, R., 2015. Main eddy vertical structures observed in the four major Eastern Boundary Upwelling Systems. *J Geophys Res Oceans* 120, 6008–6033. <https://doi.org/10.1002/2015JC010950>
- Pelegrí J, Benazzouz A, 2015. Oceanographic and biological features in the Canary Current Large Marine Ecosystem, Chap. 3.4, Coastal Upwelling off north-west Africa, IOC Technical Series, 115.
- Pelegrí, J.L., Arístegui, J., Cana, L., González-Dávila, M., Hernández-Guerra, A., Hernández-León, S., Marrero-Díaz, A., Montero, M.F., Sangrà, P., Santana-Casiano, M., 2005. Coupling between the open ocean and the coastal upwelling region off northwest Africa: water recirculation and offshore pumping of organic matter. *Journal of Marine Systems* 54, 3–37. <https://doi.org/10.1016/j.jmarsys.2004.07.003>
- Pelegrí, J.L., Peña-Izquierdo, J., 2015. Easter boundary currents off North'West Africa. *Oceanographic and Biological Features in the Canary Current Large Marine Ecosystem* 3 (3): 81-92, IOC Technical Series 115 81-92 IOC Technical Series.
- Pelegrí, J.L., Peña-Izquierdo, J., Machín, F., Meiners, C., Presas-Navarro, C., 2017. Oceanography of the cape Verde Basin and Mauritanian slope waters. *Deep-Sea Ecosystems Off Mauritania: Research of Marine Biodiversity and Habitats in the Northwest African Margin* 119–153. https://doi.org/10.1007/978-94-024-1023-5_3/FIGURES/23

References

- Peña-Izquierdo, J., Pelegrí, J.L., Pastor, M. V., Castellanos, P., Emelianov, M., Gasser, M., Salvador, J., Vázquez-Domínguez, E., 2012. El sistema de corrientes de talud continental entre Cabo Verde y las Islas Canarias. *Sci Mar* 76, 65–78. <https://doi.org/10.3989/SCIMAR.03607.18C>
- Pérez-Rodríguez, P., Pelegrí, J., Marrero-Díaz, A., 2001. Dynamical characteristics of the Cape Verde frontal zone. *Marine science* 65, 241–250.
- Peters, B.D., Lam, P.J., Casciotti, K.L., 2018. Nitrogen and oxygen isotope measurements of nitrate along the US GEOTRACES Eastern Pacific Zonal Transect (GP16) yield insights into nitrate supply, remineralization, and water mass transport. *Mar Chem* 201, 137–150. <https://doi.org/10.1016/J.MARCHEM.2017.09.009>
- Pilskaln, C.H., Lehmann, C., Paduan, J.B., Silver, M.W., 1998. Spatial and temporal dynamics in marine aggregate abundance, sinking rate and flux: Monterey Bay, central California. *Deep Sea Research Part II: Topical Studies in Oceanography* 45, 1803–1837. [https://doi.org/10.1016/S0967-0645\(98\)80018-0](https://doi.org/10.1016/S0967-0645(98)80018-0)
- Piñango, A., Azar, E., Wallner-Kersanach, M., da Costa Machado, E., Martins, G., Peterle, T., de Rezende, C.E., da Graça Baumgarten, M., 2023. Influence of the ITCZ and OMZ on the isotopic composition of suspended particulate matter in the western tropical North Atlantic. *Journal of Marine Systems* 237, 103803. <https://doi.org/10.1016/J.JMARSYS.2022.103803>
- Rafter, P., Bagnell, A., Marconi, D., Devries, T., 2019. Global trends in marine nitrate N isotopes from observations and a neural network-based climatology. *Biogeosciences* 16, 2617–2633. <https://doi.org/10.5194/BG-16-2617-2019>
- Rafter, P.A., Difiore, P.J., Sigman, D.M., 2013. Coupled nitrate nitrogen and oxygen isotopes and organic matter remineralization in the Southern and Pacific Oceans. *J Geophys Res Oceans* 118, 4781–4794. <https://doi.org/10.1002/JGRC.20316>
- Rafter, P.A., Sigman, D.M., 2016. Spatial distribution and temporal variation of nitrate nitrogen and oxygen isotopes in the upper equatorial Pacific Ocean. *Limnol Oceanogr* 61, 14–31. <https://doi.org/10.1002/LNO.10152>
- Redfield, A.C., Ketchum, B., Richards, F., 1963. The influence of organisms on the composition of seawater. In “The Sea” (Hill, M. N., ed.). Vol. 2, Wiley-Interscience, New York. pp. 26–77.
- Repeta, D.J., 2015. Chemical Characterization and Cycling of Dissolved Organic Matter, in: *Biogeochemistry of Marine Dissolved Organic Matter: Second Edition*. Elsevier Inc., pp. 21–63. <https://doi.org/10.1016/B978-0-12-405940-5.00002-9>
- Riley, J.S., Sanders, R., Marsay, C., Le Moigne, F.A.C., Achterberg, E.P., Poulton, A.J., 2012. The relative contribution of fast and slow sinking particles to ocean carbon export. *Global Biogeochem Cycles* 26. <https://doi.org/10.1029/2011GB004085>
- Ríos, A.F., Fraga, F., Pérez, F.F., Figueiras, F.G., 1998. Chemical composition of phytoplankton and Particulate Organic Matter in the Ría de Vigo (NW Spain). *Sci Mar* 3, 257–271. <https://doi.org/10.3989/SCIMAR.1998.62N3257>

- Rosman, K.J.R., Taylor, P.D.P., 1998. Isotopic Compositions of the Elements 1997. *J Phys Chem Ref Data* 27, 1275–1287. <https://doi.org/10.1063/1.556031>
- Roussenov, V., Williams, R.G., Mahaffey, C., Wolff, G.A., 2006. Does the transport of dissolved organic nutrients affect export production in the Atlantic Ocean? *Global Biogeochem Cycles* 20, n/a-n/a. <https://doi.org/10.1029/2005GB002510>
- Sambrotto, R.N., Savidge, G., Robinson, C., Boyd, P., Takahashi, T., Karl, D.M., Langdon, C., Chipman, D., Marra, J., Codispoti, L., 1993. Elevated consumption of carbon relative to nitrogen in the surface ocean. *Nature* 1993 363:6426 363, 248–250. <https://doi.org/10.1038/363248a0>
- Sanchez-Vidal, A., Ann Wynn-Edwards, C., Yang, W., Fischer, G., Neuer, S., Ramondenc, S., Müller, T.J., Donner, B., Ruhland, G., Ratmeyer, V., Meinecke, G., Nowald, N., Klann, M., Wefer, G., 2020. Long-Term Changes of Particle Flux in the Canary Basin Between 1991 and 2009 and Comparison to Sediment Trap Records Off Mauritania. *Sediment Trap Records Off Mauritania. Front. Earth Sci* 8, 280. <https://doi.org/10.3389/feart.2020.00280>
- Sanders, R., Henson, S.A., Koski, M., De La Rocha, C.L., Painter, S.C., Poulton, A.J., Riley, J., Salihoglu, B., Visser, A., Yool, A., Bellerby, R., Martin, A.P., 2014. The Biological Carbon Pump in the North Atlantic. *Prog Oceanogr* 129, 200–218. <https://doi.org/10.1016/J.POCEAN.2014.05.005>
- Sangrà, P., 2015. Canary Islands eddies and coastal upwelling filaments off North-west Africa.
- Sangrà, P., Pascual, A., Rodríguez-Santana, Á., Machín, F., Mason, E., McWilliams, J.C., Pelegrí, J.L., Dong, C., Rubio, A., Arístegui, J., Marrero-Díaz, Á., Hernández-Guerra, A., Martínez-Marrero, A., Auladell, M., 2009. The Canary Eddy Corridor: A major pathway for long-lived eddies in the subtropical North Atlantic. *Deep Sea Res 1 Oceanogr Res Pap* 56, 2100–2114. <https://doi.org/10.1016/j.dsr.2009.08.008>
- Santana-Falcón, Y., Mason, E., Arístegui, J., 2020. Offshore transport of organic carbon by upwelling filaments in the Canary Current System. *Prog Oceanogr* 186, 102322. <https://doi.org/10.1016/j.pocean.2020.102322>
- Sarmiento, J. L., and Bryan, K. 1982. An ocean transport model for the North Atlantic. *Journal of Geophysical Research: Oceans*, 87(C1), 394-408.
- Sarmiento, J.L., and Gruber, N., 2006. Ocean biogeochemical dynamics, chapter 1. ocean biogeochemical dynamics.
- Schlitzer, R., 2017. Ocean Data View. Ocean Data View.
- Schneider, B., Schlitzer, R., Fischer, G., Nöthig, E.M., 2003. Depth-dependent elemental compositions of particulate organic matter (POM) in the ocean. *Global Biogeochem Cycles* 17. <https://doi.org/10.1029/2002GB001871>
- Sigman, D., Altabet, M., McCorkle, D., Francois, R., Fischer, G. 1999. The $\delta^{15}\text{N}$ of nitrate in the Southern Ocean: Consumption of nitrate in surface waters. *Global Biogeochemical Cycles*, 13(4), 1149-1166.

References

- Sigman, D., Casciotti, K., 2001. Nitrogen isotopes in the ocean, academia.edu. Encyclopedia of ocean sciences.
- Sigman, D., Fripiat, F., 2019. Nitrogen Isotopes in the Ocean. Encyclopedia of Ocean Sciences 263–278. <https://doi.org/10.1016/B978-0-12-409548-9.11605-7>
- Sigman, D., Karsh, K., Casciotti, K., 2009. Ocean process tracers: nitrogen isotopes in the ocean.
- Sipler, R.E., Bronk, D.A., 2015. Dynamics of Dissolved Organic Nitrogen. Biogeochemistry of Marine Dissolved Organic Matter: Second Edition 127–232. <https://doi.org/10.1016/B978-0-12-405940-5.00004-2>
- Smil V, 2004. Enriching the Earth: Fritz Haber, Carl Bosch, and the Transformation of World Food Production, MIT Press: Cambridge. ed.
- Smith, J.M., Chavez, F.P., Francis, C.A., 2014. Ammonium Uptake by Phytoplankton Regulates Nitrification in the Sunlit Ocean. PLoS One 9, e108173. <https://doi.org/10.1371/JOURNAL.PONE.0108173>
- Solomonson, L.P., Barber, M.J., 1990. Assimilatory nitrate reductase: Functional properties and regulation. Annu Rev Plant Physiol Plant Mol Biol 41, 225–253. <https://doi.org/10.1146/ANNUREV.PP.41.060190.001301>
- Søndergaard, M., Williams, P. J. L. B., Cauwet, G., Riemann, B., Robinson, C., Terzic, S., Malcom, E., Woodward, S., Worm, J. (2000). Net accumulation and flux of dissolved organic carbon and dissolved organic nitrogen in marine plankton communities. Limnology and Oceanography, 45(5), 1097–1111.
- Stevens, R. J., Laughlin, R. J. (1994). Determining nitrogen-15 in nitrite or nitrate by producing nitrous oxide. Soil Science Society of America Journal, 58(4), 1108–1116.
- Stramma, L., Schott, F., 1999. The mean flow field of the tropical Atlantic Ocean. Deep-Sea Research II 46, 279–303.
- Sy, A., Rheint, M., Lazier, J.R.N., Koltermann, K.P., Meincke, J., Putzka, A., Bersch, M., 1997. Surprisingly rapid spreading of newly formed intermediate waters across the North Atlantic Ocean. Nature 1997 386:6626 386, 675–679. <https://doi.org/10.1038/386675a0>
- Talley, L., McCartney, M., 1982. Distribution and circulation of Labrador Sea Water. J. Phys. Oceanogr., 12 1189–1205.
- Tiedemann, M., Fock, H., Döring, J., Bonaventure-Badji, L., Möllmann, C., 2018. Water masses and oceanic eddy regulation of larval fish assemblages along the Cape Verde Frontal Zone. Journal of Marine Systems 183, 42–55.
- Tomczak, M., 1999. Some historical, theoretical and applied aspects of quantitative water mass analysis. J Mar Res 57, 275–303. <https://doi.org/10.1357/002224099321618227>
- Torres-Valdés, S., Roussenov, V.M., Sanders, R., Reynolds, S., Pan, X., Mather, R., Landolfi, A., Wolff, G.A., Achterberg, E.P., Williams, R.G., 2009. Distribution of dissolved organic nutrients and their effect on export production over the Atlantic Ocean. Global Biogeochem Cycles 23. <https://doi.org/10.1029/2008GB003389>

- Twomey, L.J., Waite, A.M., Pez, V., Pattiaratchi, C.B., 2007. Variability in nitrogen uptake and fixation in the oligotrophic waters off the south west coast of Australia. *Deep Sea Res 2 Top Stud Oceanogr* 54, 925–942. <https://doi.org/10.1016/j.dsr2.2006.10.001>
- UNESCO, 1985. The International System of Units (SI) in Oceanography. UNESCO Tech. Papers Mar. Sci. 45 1–59. <https://doi.org/10.25607/OBP-666>
- UNESCO, 1986. Progression Oceanographic Tables and Standards 1983–1986. Work and Recommendations of the UNESCO/SCOR/ICES/IAPSO Joint Panel. UNESCO Technical Papers in Marine Science 50.
- Urey HC. 1947. The thermodynamic properties of isotopic substances. *J Chem Soc* 1947:562.
- Van Aken, H.M., 2000. The hydrography of the mid-latitude northeast Atlantic Ocean: I: The deep water masses. *Deep Sea Research Part I: Oceanographic Research Papers* 47, 757–788. [https://doi.org/10.1016/S0967-0637\(99\)00092-8](https://doi.org/10.1016/S0967-0637(99)00092-8)
- Van Camp, L., Nykjaer, L., Mittelstaedt, E., Schlittenhardy, P., 1991. Upwelling and boundary circulation off Northwest Africa as depicted by infrared and visible satellite observations. *Prog Oceanogr* 26, 357–402.
- Van der Jagt, H., Friese, C., Stuut, J.B.W., Fischer, G., Iversen, M.H., 2018. The ballasting effect of Saharan dust deposition on aggregate dynamics and carbon export: Aggregation, settling, and scavenging potential of marine snow. *Limnol Oceanogr* 63, 1386–1394. <https://doi.org/10.1002/LNO.10779>
- Vanzella, A., Guerrero, M. A., Jones, R. D. 1989. Effect of CO and light on ammonium and nitrite oxidation by chemolithotrophic bacteria. *Marine ecology progress series*. Oldendorf, 57(1), 69-76.
- Verdugo, P., Alldredge, A.L., Azam, F., Kirchman, D.L., Passow, U., Santschi, P.H., 2004. The oceanic gel phase: a bridge in the DOM-POM continuum. *Mar Chem* 92, 67–85. <https://doi.org/10.1016/j.marchem.2004.06.017>
- Von Appen, W.J., Strass, V.H., Bracher, A., Xi, H., Hörstmann, C., Iversen, M.H., Waite, A.M., 2020. High-resolution physical-biogeochemical structure of a filament and an eddy of upwelled water off northwest Africa. *Ocean Science* 16, 253–270. <https://doi.org/10.5194/OS-16-253-2020>
- Voss, M., Bange, H.W., Dippner, J.W., Middelburg, J.J., Montoya, J.P., Ward, B., 2013. The marine nitrogen cycle: Recent discoveries, uncertainties and the potential relevance of climate change. *Philosophical Transactions of the Royal Society B: Biological Sciences* 368. <https://doi.org/10.1098/RSTB.2013.0121>
- Wada, E., and Hattori, A. 1978. Nitrogen isotope effects in the assimilation of inorganic nitrogenous compounds by marine diatoms. *Geomicrobiology Journal*, 1(1), 85-101.
- Wang, Y., Lin, Z., He, L., Huang, W., Zhou, J., He, Q., 2019. Simultaneous partial nitrification, anammox and denitrification (SNAD) process for nitrogen and refractory organic compounds removal from mature landfill leachate: Performance and metagenome-based microbial ecology. *Bioresour Technol* 294, 122166. <https://doi.org/10.1016/J.BIORTECH.2019.122166>

References

- Ward, B. B. 2008. Phytoplankton community composition and gene expression of functional genes involved in carbon and nitrogen assimilation 1. *Journal of phycology*, 44(6), 1490-1503.
- Ward, B. B., and Jensen, M. M. 2014. The microbial nitrogen cycle. *Frontiers in microbiology*, 5, 553
- Ward, B.B., Olson, R.J., Perry, M.J., 1982. Microbial nitrification rates in the primary nitrite maximum off southern California. *Deep Sea Research Part A, Oceanographic Research Papers* 29, 247–255. [https://doi.org/10.1016/0198-0149\(82\)90112-1](https://doi.org/10.1016/0198-0149(82)90112-1)
- Weber, T.S., Deutsch, C., 2010. Ocean nutrient ratios governed by plankton biogeography. *Nature* 2010 467:7315 467, 550–554. <https://doi.org/10.1038/nature09403>
- Winter Mark, 1999. WebElements, <https://www.webelements.com>. [WWW Document]. URL https://www.webelements.com/nitrogen/compound_properties.html.
- Wollast, R., Mackenzie, F. T., Chou, L. 1993. Working Group 2: Interactions of the Cycles of C, N, P and S in the Recent Past (The Quaternary) and Present. In *Interactions of C, N, P and S Biogeochemical Cycles and Global Change* (pp. 495-500). Springer Berlin Heidelberg.
- World Ocean Atlas, 2013. <https://www.nodc.noaa.gov/OC5/woa13>
- Yang, S., Gruber, N., 2016. The anthropogenic perturbation of the marine nitrogen cycle by atmospheric deposition: Nitrogen cycle feedbacks and the 15N Haber-Bosch effect. *Global Biogeochem Cycles* 30, 1418–1440. <https://doi.org/10.1002/2016GB005421>
- Yoshikawa, C., Makabe, A., Shiozaki, T., Toyoda, S., Yoshida, O., Furuya, K., Yoshida, N., 2015. Nitrogen isotope ratios of nitrate and N* anomalies in the subtropical South Pacific. *Geochemistry, Geophysics, Geosystems* 16, 1439–1448. <https://doi.org/10.1002/2014GC005678>
- Zakem, E.J., Al-Haj, A., Church, M.J., Van Dijken, G.L., Dutkiewicz, S., Foster, S.Q., Fulweiler, R.W., Mills, M.M., Follows, M.J., 2018. Ecological control of nitrite in the upper ocean. *N*
- Zehr, J.P., and Capone, D.G., 2020. Changing perspectives in marine nitrogen fixation. *Science* 368. <https://doi.org/10.1126/SCIENCE.AAY9514>
- Zenk, W., Klein, B., Schroder, M., 1991. Cape Verde Frontal Zone. *Deep Sea Research Part A* 38, S505–S530. [https://doi.org/10.1016/S0198-0149\(12\)80022-7](https://doi.org/10.1016/S0198-0149(12)80022-7)
- Zhang, L., Altabet, M. A., Wu, T., Hadas, O. 2007. Sensitive measurement of NH₄⁺ 15N/14N (δ¹⁵NH₄⁺) at natural abundance levels in fresh and saltwaters. *Analytical Chemistry*, 79(14), 5297-5303.
- Zhang, X., Ward, B.B., Sigman, D.M., 2020. Global Nitrogen Cycle: Critical Enzymes, Organisms, and Processes for Nitrogen Budgets and Dynamics. *Chem Rev* 120, 5308–5351. https://doi.org/10.1021/ACS.CHEMREV.9B00613/ASSET/IMAGES/LARGE/CR9B00613_0002.JPEG

- Zouiten, H., Díaz, C.Á., Gómez, A.G., Cortezón, J.A.R., Alba, J.G., 2013. An advanced tool for eutrophication modeling in coastal lagoons: Application to the Victoria lagoon in the north of Spain. *Ecol Modell* 265, 99–113. <https://doi.org/10.1016/J.ECOLMODEL.2013.06.009>



**Nitrogen Cycling in the
Cape Verde Frontal Zone (NW Africa):
Elemental and isotopic characterization.**

Sara Valiente Rodríguez
PhD Thesis 2023

